

ResearchOnline@JCU

This file is part of the following reference:

Meehan, Michael Thomas (2015) *Dark matter relic abundance in non-standard cosmological scenarios*. PhD thesis, James Cook University.

Access to this file is available from:

<http://researchonline.jcu.edu.au/41213/>

The author has certified to JCU that they have made a reasonable effort to gain permission and acknowledge the owner of any third party copyright material included in this document. If you believe that this is not the case, please contact

*ResearchOnline@jcu.edu.au and quote
<http://researchonline.jcu.edu.au/41213/>*

Dark Matter Relic Abundance in Non-Standard Cosmological Scenarios

by

Michael Thomas Meehan BSc (Hons) JCU

A thesis submitted in partial fulfillment for the
degree of Doctor of Philosophy

in the
College of Science, Technology and Engineering

JAMES COOK UNIVERSITY

August 2015

Acknowledgements

First and foremost, I would like to thank my supervisor, Prof. Ian Whittingham. Not only is he the reason I have set down this path, but he is most certainly the reason I have reached the end of it. His passion for physics and his devotion to his students have made this experience extremely rewarding. I truly could not have asked for a better supervisor.

I would also like to mention his incredible wife, Annie, whose constant kind words and encouragement have been instrumental throughout my studies.

My thanks also goes to all of the Maths and Physics department faculty members whose doors are *always* open. I would also like to thank the support staff, in particular Melissa Norton, for helping me with countless forms and other organizational duties.

Thank you to Danny and Greg and all of the other post-graduate students who have made this PhD such an enjoyable experience. To Danny and Greg in particular for their help with my many computing-related enquiries.

Finally I would like to thank my parents for all of their support and patience and to my Aunt Marie for proof reading a very early draft of this manuscript.

Most importantly, I would like to thank my wonderful partner Melanie whose love and devotion have gotten me to this point. I couldn't have done it without you.

Statement on the Contribution of Others

I, Michael Thomas Meehan, declare that this thesis titled, 'Dark Matter Relic Abundance in Non-Standard Cosmological Scenarios' and the work presented in it have in major part been undertaken by myself. Where I have consulted the published work of others, this is always clearly attributed. The role of my supervisor, Prof. Ian Whittingham, was to suggest and design the project as well as helping with the analysis and interpretation of results. He also provided editorial assistance with the two publications that arose from this work (based on the results contained in chapters 5 and 6 respectively):

- M. T. Meehan and I. B. Whittingham, *Asymmetric dark matter in braneworld cosmology*, JCAP **1412** (2014), 034.
- M. T. Meehan and I. B. Whittingham, *Dark matter relic density in Gauss-Bonnet braneworld cosmology*, JCAP **1412** (2014), 034.

and with producing the final draft of this thesis. Additionally, he has also provided editorial assistance with an upcoming publication (based on the results in chapter 4)

- M. T. Meehan and I. B. Whittingham, *Revised relic abundance calculations in scalar-tensor gravity models*, (in preparation).

Abstract

The relic abundance of symmetric dark matter particles (where particle χ and antiparticle $\bar{\chi}$ are identical and therefore self-annihilating) and asymmetric dark matter particles (where $\chi \neq \bar{\chi}$) is calculated in several non-standard cosmological scenarios that predict a modified Hubble expansion rate in the pre-Big Bang Nucleosynthesis (BBN) era. The Boltzmann rate equation describing the time evolution of the dark matter number density is solved to accurately quantify the level of enhancement (or suppression) of the dark matter relic abundance with respect to the standard cosmology result. In terms of the dark matter particle interactions, we adopt a model independent approach and choose a generic form for the annihilation cross section $\langle\sigma v\rangle = a + bT/m_\chi$ (where T is the temperature of the universe and m_χ is the dark matter particle mass), calculating results for both the s - ($b = 0$) and p - ($a = 0$) wave annihilation cases. The solution method incorporated the numerical considerations outlined in the recent paper by Steigman *et al* (2012) for precise calculations of relic abundances, such as maintaining the temperature dependence of the number of entropic degrees of freedom $g_*(T)$. Furthermore, knowing the present dark matter density, $\Omega_{\text{DM}}h^2 = 0.1188 \pm 0.0010$, is a precisely measured quantity, the relic abundance calculations are inverted to determine the annihilation cross section, $\langle\sigma v\rangle$, required to provide the observed density. A comparison of these results with observational bounds on $\langle\sigma v\rangle$, such those derived using the Fermi-LAT gamma ray data, enables deviations from the standard expansion history in the pre-BBN era to be constrained.

The four non-standard cosmological scenarios considered fall into two broad categories: gravity supplemented with a scalar field (kination phase quintessence dark energy and scalar-tensor gravity) and higher dimensional universe models (Randall-Sundrum type II and Gauss-Bonnet braneworlds). We find that those models that predict a faster (slower) expansion rate in the early universe lead to dark matter relic abundances that are enhanced (suppressed) by up to several orders of magnitude. More specifically, of the four models considered, three predicted faster expansion rates at early times with only the Gauss-Bonnet braneworld model admitting both faster and slower pre-BBN expansion rates. Hence, the kination phase quintessence, scalar-tensor gravity and Randall-Sundrum type II braneworld models all predicted an enhanced dark matter relic abundance whilst the Gauss-Bonnet braneworld model allowed for either enhanced or suppressed relic abundances. Furthermore, the level of enhancement (or suppression) increased with the amount of deviation from the standard expansion law at the time of dark matter decoupling so that the braneworld scenarios, which predicted the fastest expansion rates, provided the greatest levels of enhancement of the order $\sim 10^6$ for particle mass $m_\chi = 100$ GeV. Additionally, we found that the enhancement was larger

for p -wave annihilating particles since the freeze-out process occurred more rapidly in this case.

We also found that previous calculations that failed to properly account for the temperature variation in the number of degrees of freedom incurred errors of up to a factor of two, with the larger errors arising for smaller particle masses ($m_\chi < 10$ GeV) and for those models in which the freeze-out process took longer to occur (e.g. braneworld models). Moreover, for scalar-tensor gravity, we found that, although large deviations from the standard expansion history at the time of dark matter decoupling were possible, the stringent constraints imposed by BBN calculations excluded these regions of parameter space, ensuring the modified expansion rate was nearly coincident with the standard expansion law. Accordingly, the relic abundance in these models only increased by a factor of 2–3 which is in stark contrast to the several orders of magnitude enhancement factors reported in Catena *et al* (2004).

The calculations for the Gauss-Bonnet braneworld model extend the study by Okada and Okada (2009) who assumed that the energy scale associated with the Gauss-Bonnet correction term, m_α , was equal to that associated with the brane tension, m_σ , so that the pre-BBN expansion rate was slower than the standard cosmological model and the relic abundance was suppressed. We consider the more plausible case $m_\alpha \geq m_\sigma$ and find that the relic density is typically enhanced for $m_\alpha > m_\sigma$ and that, in the limit $m_\alpha \gg m_\sigma$, the familiar Randall-Sundrum type behaviour is recovered.

The annihilation cross section required to produce the observed dark matter density was found to be enhanced by several orders of magnitude in the kination phase quintessence and braneworld scenarios, allowing current Fermi-LAT gamma ray data to directly probe significant portions of parameter space.

Finally, in the context of asymmetric dark matter models, we found that the modified decoupling predicted in non-standard cosmological models can either 'wash out' or amplify the asymmetry between the majority and minority dark matter components depending on whether the early time expansion rate is faster or slower than the standard expansion law respectively. Interestingly, in the former case, the relic density of the asymmetric dark matter species depends on the annihilation cross section, $\langle\sigma v\rangle$, rather than the asymmetry parameter, C , so that it behaves like symmetric dark matter in this sense. This leads to the intriguing prospect that the enhanced annihilation cross section required to provide the observed dark matter density can compensate for the suppressed abundance of the minority dark matter component and produce an observable detection signal. This result, which is contrary to the usual expectation that the asymmetric annihilation rate is negligible due to the exponentially suppressed abundance of the minority component, can be achieved for a wide range of parameter values within the kination

phase quintessence and braneworld scenarios (and even for particular parameter values within the scalar-tensor gravity scenario).

The findings presented in this thesis extend, and in several cases challenge, existing results in the literature and also provide important insights for the planning and interpretation of both present and future dark matter experiments.

Contents

Acknowledgements	i
Statement on the Contribution of Others	ii
Abstract	iii
Contents	vi
List of Tables	ix
List of Figures	x
1 Dark Matter and Cosmology: An Overview	1
1.1 Introduction	1
1.2 Standard cosmology	2
1.3 Dark energy	7
1.3.1 What is dark energy?	7
1.3.2 Dark energy models	8
1.4 Dark matter	10
1.4.1 What is dark matter?	10
1.4.2 Candidates	11
1.4.3 Asymmetric dark matter	15
1.4.4 Thermal relic abundance	16
1.4.5 The search for dark matter	17
1.4.6 Constraints	19
1.5 Non-standard cosmologies	21
1.6 Relic abundance calculations	23
1.6.1 Modified expansion history	23
1.6.2 Constraints on non-standard scenarios	24
1.6.3 Implications for dark matter candidates	24
1.6.4 Implications for dark matter searches	25
1.7 Outline	26
2 Relic Density	29
2.1 Introduction	29

2.2	Symmetric dark matter	30
2.2.1	Boltzmann equation	30
2.2.2	Approximate solution	35
2.3	Constraints	38
2.4	Asymmetric dark matter	39
2.4.1	Motivation	39
2.4.2	Boltzmann equation	40
2.4.3	Density evolution	42
2.4.4	Approximate solution	44
2.4.5	Constraints	45
2.4.6	Asymmetric detection signal	46
2.5	Summary	48
3	Quintessence Dark Energy Models	50
3.1	Introduction	50
3.2	Kination	52
3.3	Symmetric dark matter	56
3.4	Asymmetric dark matter	63
3.5	Summary	66
4	Scalar-Tensor Gravity	68
4.1	Introduction	68
4.2	Conformal transformations	71
4.2.1	Jordan and Einstein frames	71
4.2.2	Connection with other modified gravity theories	74
4.3	Cosmological equations	75
4.4	Scalar field dynamics	77
4.5	Modified expansion rate	81
4.6	Constraints	82
4.7	Symmetric dark matter	87
4.8	Asymmetric dark matter	90
4.9	Non-universal scalar-tensor theories	91
4.9.1	Visible and Dark Jordan frames	91
4.9.2	Boltzmann equation	93
4.10	Summary	94
5	Randall-Sundrum Braneworlds	96
5.1	Introduction	96
5.2	Randall-Sundrum II model	98
5.3	Symmetric dark matter	100
5.4	Asymmetric dark matter	108
5.5	Summary	111
6	Gauss-Bonnet Braneworlds	113
6.1	Introduction	113
6.2	Gauss-Bonnet Braneworlds	114
6.3	Symmetric Dark Matter	118
6.4	Asymmetric Dark Matter	122

6.5	Summary	125
7	Discussion and Outlook	127
7.1	Context of project and investigations undertaken	127
7.2	Overview of methods used	130
7.3	Results of investigation	132
7.4	Outlook	136
7.5	Future work	138
	Bibliography	139
A	Review of General Relativity	161
A.1	Geodesics	161
A.2	Cosmology	162
B	Thermodynamics of the Early Universe	166
B.1	Equilibrium	166
B.2	Entropy	168
C	Rate Equation for Relic Abundance	173
C.1	Relativistic Boltzmann equation	173
C.2	Collision term	175
D	Lagrangian Field Theory	178
D.1	Euler-Lagrange equations	178
D.2	Lagrangian formalism for a scalar field	179
D.3	Einstein's field equations from a variational principle	181
E	Equations of Scalar-tensor gravity	183
E.1	Jordan frame field equations	183
E.2	Conformal transformation to the Einstein frame	184
E.3	Einstein frame field equations	186
F	Braneworld Field Equations	188
F.1	Field equations	188
F.2	Cosmological solution	190

List of Tables

7.1	Ratio of the relic density in non-standard cosmological scenarios to the corresponding result in the standard cosmological model.	134
B.1	Properties of the Standard Model particles.	170
B.2	Relativistic degrees of freedom.	171

List of Figures

1.1	Fermi-LAT constraints on the dark matter annihilation cross section . . .	20
2.1	Evolution of the comoving number density for varying annihilation cross sections.	33
2.2	Evolution of the annihilation rate for varying annihilation cross sections. .	35
2.3	Required annihilation cross section as a function of WIMP mass in the standard cosmological scenario.	38
2.4	Required annihilation cross section as a function of WIMP mass in the standard cosmological scenario compared with the Fermi-LAT constraints. .	39
2.5	Evolution of the comoving number density for an asymmetric dark matter species in the standard cosmological scenario.	43
2.6	Iso-abundance contours in the $(\langle\sigma v\rangle, m_{100}C)$ plane for varying WIMP mass in the standard cosmological scenario.	45
2.7	Asymmetric damping factor.	48
3.1	Evolution of the comoving number density in the kination domination scenario for s -wave annihilating particles.	56
3.2	Evolution of the comoving number density in the kination domination scenario for p -wave annihilating particles.	57
3.3	Dark matter relic density enhancement in the kination domination scenario. .	59
3.4	Comparison of the numerical and analytical solutions for the dark matter relic density enhancement in the kination domination scenario (s -wave). .	60
3.5	Comparison of the numerical and analytical solutions for the dark matter relic density enhancement in the kination domination scenario (p -wave). .	61
3.6	Required annihilation cross section in the kination domination scenario (s -wave).	61
3.7	Required annihilation cross section in the kination domination scenario (p -wave).	62
3.8	Required annihilation cross section in the kination domination scenario compared to Fermi-LAT constraints.	63
3.9	Evolution of the comoving number density for an asymmetric dark matter species in the kination domination scenario	64
3.10	Iso-abundance contours in the $(\langle\sigma v\rangle, C)$ plane in the kination domination scenario (s -wave).	65
3.11	Iso-abundance contours in the $(\langle\sigma v\rangle, C)$ plane in the kination domination scenario (p -wave).	65
4.1	Relativistic kick function $\Sigma(T)$	79
4.2	Equation of state parameter	80

4.3	Scalar field evolution in scalar-tensor gravity models	80
4.4	Ratio of the scalar-tensor and standard expansion rates at the time of dark matter decoupling	82
4.5	Allowed region in the (β, φ_{*in}) parameter space satisfying the Cassini bounds	83
4.6	Comparison of the scalar-tensor predictions with Big-Bang Nucleosynthesis constraints	84
4.7	Allowed region in the (β, φ_{*in}) parameter space satisfying the Cassini bounds and the bounds from BBN calculations	85
4.8	Dark matter relic abundance enhancement in scalar-tensor gravity models	88
4.9	Required annihilation cross section in scalar-tensor gravity model (s -wave)	89
4.10	Required annihilation cross section in scalar-tensor gravity model (p -wave)	89
4.11	Iso-abundance contours in the $(\langle\sigma v\rangle, C)$ plane in the scalar-tensor gravity scenario	90
5.1	Evolution of the comoving number density in the RSII braneworld scenario for s -wave annihilating particles.	100
5.2	Evolution of the comoving number density in the RSII braneworld scenario for p -wave annihilating particles.	101
5.3	Evolution of the annihilation rate in the RSII braneworld model.	102
5.4	Dark matter relic density enhancement in the RSII braneworld scenario.	103
5.5	Comparison of the numerical and analytical solutions for the dark matter relic density enhancement in the RSII braneworld scenario (s -wave).	105
5.6	Comparison of the numerical and analytical solutions for the dark matter relic density enhancement in the RSII braneworld scenario (p -wave).	106
5.7	Required annihilation cross section in the RSII braneworld scenario (s -wave).	107
5.8	Required annihilation cross section in the RSII braneworld scenario (p -wave).	107
5.9	Required annihilation cross section in the RSII braneworld scenario compared to Fermi-LAT constraints.	109
5.10	Iso-abundance contours in the $(\langle\sigma v\rangle, C)$ plane in the RSII braneworld scenario (s -wave).	109
5.11	Iso-abundance contours in the $(\langle\sigma v\rangle, C)$ plane in the RSII braneworld scenario (p -wave).	110
6.1	Modified expansion rate in the Gauss-Bonnet braneworld scenario	117
6.2	Dark matter relic abundance enhancement/suppression in the Gauss-Bonnet braneworld scenario (s -wave)	120
6.3	Required annihilation cross section in the Gauss-Bonnet braneworld scenario (s -wave)	122
6.4	Iso-abundance contours in the $(\langle\sigma v\rangle, C)$ plane in the Gauss-Bonnet braneworld scenario for $m_\chi = 100$ GeV	124
6.5	Iso-abundance contours in the $(\langle\sigma v\rangle, C)$ plane in the Gauss-Bonnet braneworld scenario for $m_\chi = 10$ GeV	125
7.1	Ratio of the relic density in non-standard cosmological scenarios to the corresponding result in the standard cosmological model.	133

B.1 Entropic degrees of freedom 171

Chapter 1

Dark Matter and Cosmology: An Overview

1.1 Introduction

The field of cosmology has now reached precision level. With the latest release of the Planck satellite data [1], coupled with other astrophysical and cosmological observations, the constituents of our universe have been measured to percent-level accuracy [2]. However, it is somewhat disconcerting that these same observations reveal that around 95% of the total energy density of the universe is in the form of *dark matter* and *dark energy*: two mysterious components, of unknown nature and origin. Despite considerable effort from both the theoretical and observational community to elucidate the nature of dark matter and dark energy, separately responsible for the clustering of matter on large scales and the accelerated expansion of the universe, respectively,¹ little progress has been made. As such, the dark matter and dark energy problems now stand as two of the greatest challenges facing modern physics.

Moreover, the theory of General Relativity (upon which the standard cosmological model is based) is expected to break down in the ultraviolet limit [4] and attempts to develop a quantum theory of gravity appear to have stalled [5]. Arguably the leading contender, string theory (or M-theory) [6, 7] has thus far struggled to connect theory and observation. For the most part, this is because the predictions of string theory and its conjectures for the structure of space and time only manifest at extremely high energies (or equivalently, extremely small distances). In this way, cosmology offers an exciting route to advance our understanding of the fundamental laws of nature. The tremendous energies reached during the very earliest moments of the universe — energies that are

¹Despite the common adjective, dark energy and dark matter are *a priori* unrelated (see e.g. [3]).

simply inaccessible in current (or near-future) terrestrial laboratories — provide a fertile hunting ground to test many of the exotic ideas proposed by unified field theories (see e.g. [8]).

The present investigation of dark matter relic abundances connects these various themes by considering non-standard cosmological models that are motivated by the dark energy problem and unified field theories and their affects on early universe phenomenology.

In this chapter we review the standard cosmological model (section 1.2) and discuss in detail its two primary ingredients, namely, dark energy (section 1.3) and dark matter (section 1.4). We pay particular attention to dark matter theory, candidates, and observations since this will serve as important background material for the remainder of this thesis. In section 1.5 we introduce the non-standard cosmological scenarios that will be the focus of our study and give details surrounding their general features and underlying motivation. In section 1.6 we discuss how dark matter relic abundance calculations can be used as a valuable tool to extract elusive details about the nature of dark matter and the physics of the early universe. Finally, in section 1.7, we summarize the important concepts and provide an outline for the remaining chapters.

1.2 Standard cosmology

The standard Big Bang model of cosmology asserts that the universe began in an incredibly hot and dense state which we call the Big Bang; experienced a short period of exponential expansion (i.e. *inflation* [9–11]);² and has continued to expand and cool ever since. Among several notable achievements, the Big Bang model successfully predicts the properties and features of the relic radiation leftover from the early stages of the universe (at the time when charged electrons and protons combined to form neutral hydrogen and the universe became transparent to radiation) known as the cosmic microwave background (CMB). Additionally, Big Bang Nucleosynthesis (BBN) [14], a process that occurs at $t \sim 200$ s, correctly predicts the primordial abundances of the light elements D, ^3He , ^4He and ^7Li — abundances that span nine orders of magnitude! Lastly, the Big Bang model also predicts that matter, under the combined influence of its mutual gravitational attraction, will form galaxies, clusters, and the other large scale structures that we observe today.

²The inflationary scenario is an extension of the original Big Bang model that naturally sets the initial conditions thus solving several problems of the standard cosmological model including the *Horizon* and *Flatness* problems [12, 13].

The Big Bang model is based upon Einstein's theory of General Relativity which is summarized in his field equations [15] (see Appendix A),³

$$R_{\mu\nu} - \frac{1}{2}g_{\mu\nu}R + g_{\mu\nu}\Lambda = 8\pi GT_{\mu\nu}, \quad (1.1)$$

where $R_{\mu\nu}$ is the Ricci tensor, $R = g^{\mu\nu}R_{\mu\nu}$ is the Ricci scalar constructed from the metric tensor $g_{\mu\nu}$, and $T_{\mu\nu}$ is the energy-momentum tensor that encompasses the distribution of mass and energy throughout spacetime. Λ is the cosmological constant and G is Newton's gravitational constant which we will use interchangeably with the Planck mass $M_{\text{Pl}} = G^{-1/2} = 1.2209 \times 10^{19}$ GeV.

Observations of large-scale structure and the CMB reveal that on large scales ($\gtrsim 10$ Mpc) the universe is homogeneous and isotropic [2]. This allows us to describe the spacetime interval ds using the Robertson-Walker metric:

$$ds^2 = g_{\mu\nu}dx^\mu dx^\nu = -dt^2 + a^2(t) \left[\frac{d\xi^2}{1 - k\xi^2} + \xi^2 d\theta^2 + \xi^2 \sin^2 \theta d\phi^2 \right] \quad (1.2)$$

where t is cosmic time, $a(t)$ is the cosmic scale factor normalized to 1 at the present epoch t_0 (i.e. $a(t_0) = 1$), and ξ , θ and ϕ are spatial coordinates. The curvature of spacetime is parameterized via k , which is equal to $+1$, 0 and -1 for spherical, flat and hyperbolic geometries respectively.

Modeling the matter fields as an idealized fluid, devoid of shear-viscous, bulk viscous and heat-conductive properties, we can write the energy-momentum tensor, $T_{\mu\nu}$, in the perfect fluid form

$$T_{\mu\nu} = (\rho + p)u_\mu u_\nu + pg_{\mu\nu}, \quad (1.3)$$

where ρ and p are the total energy density and pressure of the fluid respectively and $u_\mu = g_{\mu\nu}u^\nu = g_{\mu\nu}dx^\nu/d\tau$ is the fluid's four-velocity (where τ is the proper time). Under the conditions of isotropy and homogeneity, we have that ρ and p are functions of the cosmic time only, i.e. $\rho \equiv \rho(t)$ and $p \equiv p(t)$.

Solving Einstein's field equations for the Robertson-Walker metric (1.2) and inserting the energy-momentum tensor (1.3), we obtain the Friedmann(-Lemaître) equations [16, 17]

³Note that we are working in natural units where $c = \hbar = k_B = 1$. In these units mass, energy and temperature are given in terms of GeV and time and length are given in terms of GeV^{-1} . To convert back to standard SI units we can use the conversion factors: $1 \text{ s} = 1.51926689 \times 10^{24} \text{ GeV}$; $1 \text{ m} = 5.06772886 \times 10^{15} \text{ GeV}^{-1}$; and $1 \text{ K} = 8.6173078 \times 10^{-14} \text{ GeV}$. We also work with the *Lorentzian* metric $(-, +, +, +)$ and use the definition for the Ricci tensor given in (A.14).

for the evolution of the scale factor $a(t)$ (see Appendix A):

$$\frac{\dot{a}^2}{a^2} + \frac{k}{a^2} = \frac{8\pi G}{3}\rho + \frac{\Lambda}{3}, \quad (1.4)$$

$$\frac{\ddot{a}}{a} = -\frac{4\pi G}{3}(\rho + 3p) + \frac{\Lambda}{3}, \quad (1.5)$$

where an overdot denotes differentiation with respect to t . Combining the two Friedmann equations we can also derive the continuity equation

$$\dot{\rho}_i + 3\frac{\dot{a}}{a}(\rho_i + p_i) = 0, \quad (1.6)$$

which holds separately for each (non-interacting) fluid component i .

If we assume each fluid component is barotropic, their pressure and energy density are related through $p_i = w_i\rho_i$, where w_i is the equation of state parameter for each fluid. We can then integrate (1.6) to get

$$\rho_i(t) = \rho_i(t_0) \exp\left[-3\int_{t_0}^t H(1+w_i) dt\right], \quad (1.7)$$

where we have introduced the Hubble parameter $H \equiv \dot{a}/a$. If we further assume that w_i is constant, then this expression reduces to

$$\rho_i = \rho_i^0 \left(\frac{a}{a_0}\right)^{-3(1+w_i)}, \quad (1.8)$$

where we have used a sub(super)script '0' to denote parameters evaluated at the present time t_0 , e.g. $a_0 \equiv a(t_0)$.

The basic fluid components in the standard cosmological model are:

- Relativistic matter and radiation: $w_r = 1/3$,

$$\rho_r = \rho_r^0 \left(\frac{a_0}{a}\right)^4, \quad (1.9)$$

- Non-relativistic (pressureless) matter: $w_m = 0$,

$$\rho_m = \rho_m^0 \left(\frac{a_0}{a}\right)^3, \quad (1.10)$$

- Cosmological constant: $w_\Lambda = -1$,

$$\rho_\Lambda = \rho_\Lambda^0, \quad (1.11)$$

where the cosmological constant energy density is defined as

$$\rho_\Lambda = \frac{\Lambda}{8\pi G}. \quad (1.12)$$

Substituting these results back into the first Friedmann equation (1.4) gives

$$H^2 \equiv \frac{\dot{a}^2}{a^2} = \frac{8\pi G}{3} \left[\rho_r^0 \left(\frac{a_0}{a}\right)^4 + \rho_m^0 \left(\frac{a_0}{a}\right)^3 + \rho_\Lambda \right] - \frac{k}{a^2}. \quad (1.13)$$

We can rewrite the Friedmann equation in dimensionless form if we introduce the density parameters

$$\Omega_i \equiv \frac{\rho_i}{\rho_{\text{crit}}} \quad (1.14)$$

where ρ_{crit} is known as the *critical density* and is given by

$$\rho_{\text{crit}} = \frac{3H^2}{8\pi G}. \quad (1.15)$$

In terms of the density parameters Ω_i , the Friedmann equation (1.4) becomes

$$1 + \frac{k}{a^2 H^2} = \sum_i \Omega_i \quad (1.16)$$

where the index i runs over the relativistic, non-relativistic and cosmological constant fluid components. This result clearly indicates that the curvature of the universe is directly related to the total energy density. When $\Omega_{\text{tot}} \equiv \sum_i \Omega_i = 1$ the curvature vanishes; when $\Omega_{\text{tot}} > 1$, the universe is positively curved ($k = +1$); and when $\Omega_{\text{tot}} < 1$, the universe is negatively curved ($k = -1$). Hence, the critical density, ρ_{crit} , is the density required to ensure the geometry of the universe is flat.

At the present epoch ($t = t_0$), ρ_{crit} has a value of [18]

$$\begin{aligned} \rho_{\text{crit}}^0 &= \frac{3H_0^2}{8\pi G} = 1.054 \times 10^{-5} h^2 \text{ GeV/cm}^3, \\ &= 8.097 \times 10^{-47} h^2 \text{ GeV}^4 \end{aligned} \quad (1.17)$$

where $h = 0.6774 \pm 0.0046$ [2] is defined via the present value of the Hubble constant, $H_0 = 100h \text{ km/s/Mpc}$. Inflationary theory predicts that the curvature of the universe is vanishingly small so that the total energy density is equal to the critical density, i.e. $\Omega_{\text{tot}} = 1$. This prediction has been confirmed by observations of the CMB [2] combined with several other datasets, with the most recent value given by $\Omega_{\text{tot}} = 1.000 \pm 0.005$.

Returning to the Friedmann equation (1.13), we see that the scale dependence of the various fluid components ensures the universe evolves through three distinct expansion eras: at early times ($a \ll 1$) the energy density of the universe is dominated by radiation

with $H \sim \rho_r \sim a^{-4}$; the universe then experiences a matter dominated era with $H \sim \rho_m \sim a^{-3}$; and then at late times the cosmological constant term dominates. Indeed, observations show that the equation of state of the universe at the present epoch is $w = -1.019_{-0.080}^{+0.075}$ [19], consistent with a cosmological constant.

Finally, the age of the universe, t_0 , can be calculated using (1.13):

$$t_0 = \frac{1}{H_0} \int_0^1 \frac{dx}{x \sqrt{\Omega_r^0 x^{-4} + \Omega_m^0 x^{-3} + \Omega_\Lambda}} \quad (1.18)$$

where $x = a/a_0$, and depends on the magnitude of the various density components Ω_i^0 as well as present value of the Hubble parameter H_0 .

Assuming the standard cosmological model, with a non-zero cosmological constant, the present energy densities of the various components are given by (68% C.L.) [2]

$$\begin{aligned} \Omega_m^0 &= 0.3089 \pm 0.0062, \\ \Omega_\Lambda &= 0.6911 \pm 0.0062, \end{aligned} \quad (1.19)$$

with Ω_m^0 being the present (non-relativistic) matter density and Ω_Λ the present energy density associated with the cosmological constant Λ . Note that the present value of the radiation density, which scales as $\Omega_r \sim a^{-4}$, is negligible.

The total matter density Ω_m can be decomposed into the separate contributions from the baryonic, Ω_b , and dark (see section 1.4), Ω_{DM} , matter sectors. The associated *physical densities* $\Omega_i h^2$ are

$$\begin{aligned} \Omega_b h^2 &= 0.02230 \pm 0.00014, \\ \Omega_{DM} h^2 &= 0.1188 \pm 0.0010. \end{aligned} \quad (1.20)$$

The baryonic (standard matter) component $\Omega_b h^2$ is composed overwhelmingly of protons and neutrons but, more generally, of composites of three quarks.⁴ Importantly, $\Omega_b h^2$ counts all baryonic particles, including those that may act as dark matter, i.e. baryonic states that are non-luminous (see section 1.4.2).

The standard cosmological model, based upon Einstein's General Relativity and a non-zero cosmological constant, is known as the Λ CDM (Λ + Cold Dark Matter)⁵ model and, through repeated confirmation by experiment, has now been established as the 'concordance' model of cosmology.

⁴The contribution from the other Standard Model fermions, the leptons (point-like particles, e.g. e^\pm , ν 's) and mesons (quark-antiquark composites, e.g. π^\pm , K^0), is negligible.

⁵The dark matter is assumed to be 'cold' (i.e. non-relativistic), in order to properly explain the growth of large scale structure.

1.3 Dark energy

1.3.1 What is dark energy?

Over a decade ago, two teams studying the luminosity of distant type Ia supernovae [20, 21], independently discovered that the universe is expanding at an accelerated rate! This landmark discovery directly contradicts the expectation that the expansion should be decelerating due to the gravitational attraction of matter and indicates the primary fluid component in the total energy density budget must have a negative equation of state since, from equation (1.5), $\ddot{a} > 0$ implies $w < -1/3$. This mysterious fluid, which acts as a sort of repulsive gravity, has been dubbed *dark energy*.

Prior to the discovery of the accelerated expansion of the universe, the prevailing cosmological model posited that the present energy density of the universe was due to non-relativistic matter and was equal to the critical density, i.e. $\Omega_m^0 = 1$. Even at the time, this model (which was motivated by inflation) was known to contain serious tensions between theory and experiment. In particular, taking $(\Omega_m, \Omega_\Lambda) = (1, 0)$ in (1.18) gives an estimate for the age of the universe of 9.3 Gyr; comparing this with the ages of the oldest stars, which were calculated to be over 13 Gyr old, implied that the universe was younger than the objects within it! Several other anomalies including galaxy number counts, the missing matter problem and measurements of the Hubble constant also plagued the $\Omega_m^0 = 1$ cosmological model.

To resolve these issues, it was suggested that Einstein's cosmological constant Λ may have a non-zero value and could in fact represent a significant fraction of the energy density of the universe [22–24]. Including a non-zero cosmological constant term, for which $w_\Lambda = -1$, in the Friedmann equations (1.4) and (1.5), ensures the universe is expanding faster now than in the recent past. This would mean, for example, it takes longer for the universe to reach its present radius, thereby increasing the age estimate above the lower bound placed by observation — indeed substituting in the observed values $(\Omega_m, \Omega_\Lambda) \approx (0.3, 0.7)$ gives $t_0 \approx 13.8$ Gyr.

Thus the evidence for an exotic fluid with a negative equation of state, or dark energy, existed well before the discovery of the accelerated expansion of the universe. Furthermore, more recent results, including those arising from analysis of the CMB, baryon acoustic oscillations (BAO) and gravitational lensing have further strengthened the case for dark energy (for recent reviews see [25] and [26]).

1.3.2 Dark energy models

A number of models exist in the literature to explain the late-time accelerated expansion including exotic fluids with a negative equation of state and modifications to General Relativity (see section 1.5). Here, we very briefly mention the two leading exotic fluid models.

- Λ : Cosmological constant/Vacuum energy

The simplest, and currently favoured model for the accelerated expansion is dark energy modeled by a cosmological constant, Λ . This term was originally introduced by Einstein [27] to produce static solutions to his field equations (1.1) only to be discarded upon Hubble's discovery of the expanding universe [28].

Although it originally appeared as a mathematical device devoid of a physical interpretation, the cosmological constant term was shown by Zel'dovich [29] to be mathematically equivalent to the vacuum energy density of spacetime:

$$\langle \rho_{\text{vac}} \rangle = T_{\mu}^{\nu} = (8\pi G)^{-1} \text{diag}(-\Lambda, \Lambda, \Lambda, \Lambda). \quad (1.21)$$

However, the problem with this interpretation is that the total sum of zero point energies $\frac{1}{2}\hbar\omega$ of the quantum fields is infinite! Even if we truncate the integral,

$$\rho_{\text{vac}} = \frac{1}{2\pi} \int_0^{M_{\text{Pl}}} d^3p \frac{1}{2} \sqrt{|\vec{p}|^2 + m^2} \sim 10^{76} \text{ GeV}^4, \quad (1.22)$$

at the Planck scale $M_{\text{Pl}} = 1.22 \times 10^{19} \text{ GeV}$, the theoretical energy density is still some 123 orders of magnitude larger than the observed value, $\rho_{\Lambda} \sim 10^{-47} \text{ GeV}^4$! This is modestly known as the fine-tuning problem. Unless some symmetry is introduced to cancel the vacuum contributions to an extraordinarily fine precision, the cosmological constant model loses much of its theoretical motivation [30].

Moreover, the cosmological constant model fails to explain why, if the magnitudes of the vacuum energy density ($\rho_{\Lambda} \sim \text{const.}$) and the matter density ($\rho_{\text{m}} \sim a^{-3}$) differ by many orders of magnitude throughout the history of the universe, these two values are of the same order today. This is known as the coincidence problem and arises because the accelerated expansion is a recent (in cosmological terms) phenomena.

Nevertheless, the cosmological constant model not only provides the simplest model of dark energy, but it is also the best fit to all of the available data. As such, the cosmological constant remains the preferred model for dark energy [31–33].

- Quintessence

The natural extension of the cosmological constant model is to replace Λ by a time-varying scalar field $\phi \equiv \phi(t)$; this class of models is known as quintessence [34–37]. In quintessence models of dark energy, the scalar field is non-interacting and evolves according to (see Appendix D)

$$\ddot{\phi} + 3H\dot{\phi} + \frac{\partial V}{\partial \phi} = 0, \quad (1.23)$$

where $V(\phi)$ is the self-interaction potential. In order to reproduce the accelerated expansion at late times, the equation of state of the scalar field,

$$w_\phi = \frac{\dot{\phi}^2/2 - V(\phi)}{\dot{\phi}^2/2 + V(\phi)}, \quad (1.24)$$

must satisfy $w_\phi < -1/3$. This condition is realized if the potential energy, $V(\phi)$, dominates over the kinetic energy, $\dot{\phi}^2/2$, so that $V \gg \dot{\phi}^2/2$ (i.e. if the field is *slow-rolling*). In this instance the equation of state parameter $w_\phi \approx -1$ at late times and the quintessence field mimics the cosmological constant.

For simple choices of the potential V , the presence of so-called tracking solutions allows the field, for a wide range of initial conditions, to approach a common evolutionary path where the field energy density remains sub-dominant during most of the cosmological evolution [38, 39]. This tracking mechanism resolves the fine-tuning problem associated with the cosmological constant model, but fails to explain why the field comes to dominate today. Therefore the coincidence problem remains unaddressed.

A major issue with different models of dark energy is that it is often difficult to distinguish between them experimentally. Many are purposely designed to reproduce the standard expansion history in the early universe and to mimic the behaviour of a cosmological constant ($w \approx -1$) at late times. Unless observations show that the equation of state parameter deviates from $w = -1$, or that it contains some time dependence, the degeneracy between these models may never allow us to determine the true nature of dark energy.

1.4 Dark matter

1.4.1 What is dark matter?

As early as the 1930s, astronomers [40, 41] noticed that the motions of stars and galaxies in gravitationally bound systems could not be explained in terms of luminous matter alone. In particular, by measuring the velocity dispersion of galaxies in the Coma cluster, Zwicky [41] used the virial theorem⁶ to show that the galaxies are moving too quickly to remain gravitationally bound, suggesting that the observed luminous matter only represents a small fraction of the total matter present. These observations were reinforced in the 1970s when Rubin *et al* [42] studied the rotation curves of nearby galaxies, which trace the rotational velocity of stars and clouds of gas as a function of distance from the galactic centre. According to Newtonian dynamics, the rotational velocity obeys the relation

$$v(r) = \sqrt{\frac{Gm(r)}{r}}, \quad (1.26)$$

where G is Newton's gravitational constant and $m(r)$ is the total mass contained within the radius r . Since most of the luminous matter contained in galaxies is concentrated in the galactic nucleus, the rotation curves are expected to fall as $v \propto 1/\sqrt{r}$ outside the central bulge (i.e. the stars should follow Keplerian orbits). However, the observed rotation curves are flat ($v(r) \sim \text{const}$) out to large distance. This indicates the presence of a large halo of non-luminous matter whose density scales as $\rho(r) \propto 1/r^2$.

This 'missing matter' is called dark matter, which is non-luminous and only interacts with ordinary matter gravitationally (and possibly via the weak force or other numerically weak scale interactions). Dark matter is needed to explain the clustering of matter on large scales and is roughly five times more abundant than standard baryonic matter (i.e. matter made of protons and neutrons) [43–45]. Aside from the observations just mentioned, further evidence for dark matter comes from gravitational lensing of distant galaxies by foreground galactic clusters, X-rays from hot plasma in clusters, the ratio of the first two acoustic peaks in the angular decomposition of the anisotropies in the CMB, and the power spectrum of the density perturbations of gravitational clustering into galaxies, clusters and superclusters. Although several of these observations can be explained by alternative theories of gravity, such as MODified Newtonian Mechanics (MOND) [46], no unified framework is capable of reproducing *all* of the observational data with the level of precision supplied by the dark matter hypothesis.

⁶The virial theorem relates the average kinetic energy of a system, $\langle T \rangle$, to the average potential energy, $\langle U \rangle$,

$$\langle T \rangle = -\frac{1}{2}\langle U \rangle. \quad (1.25)$$

1.4.2 Candidates

Despite the overwhelming evidence for the existence of dark matter, dark matter particles have never been observed directly and a convincing description of their particle nature remains elusive. That said, it *is* known that a viable dark matter candidate (denoted χ) should satisfy the following criteria (see also [47])

1. Its interaction with electromagnetic radiation must be sufficiently suppressed — otherwise the particle would emit or reflect light and would not count as dark matter.
2. It must be stable on cosmological time scales — if the dark matter particle had a lifetime less than the present age of the universe, it would have already decayed into lighter particles and would fail to explain the observed dark matter density.
3. It must have the correct relic density — this ensures that the dark matter isn't overproduced with reference to the observed relic density. This final criteria will be examined in greater detail in section 1.6.3.

We also know from modeling the growth of large scale structures that the data favour cold (non-relativistic) dark matter particles for which the most popular theoretical candidates are WIMPs (Weakly Interacting Massive Particles) with masses in the range $m_\chi \sim 10 - 1000$ GeV. Below we list some prominent dark matter candidates with particular focus on the supersymmetric neutralino, which is by far the most extensively studied dark matter candidate.

- Standard Model

Firstly, it would be remiss of us not to mention that dark matter candidates arise within the Standard Model of particle physics. Indeed, baryonic dark matter exists in the form of objects with null or negligible luminosity, such as black holes, Jupiters, brown dwarfs, etc. These Massive Compact Halo Objects (MACHOs) satisfy the criteria given above and as such play the role of dark matter. Furthermore, neutrinos, which only experience the weak nuclear force, can also be categorized as dark matter.

However, both microlensing surveys [48] and predictions from Big Bang Nucleosynthesis, whose calculations are sensitive to the total baryon density, limit the contribution of MACHOs to the overall dark matter density to be $\lesssim 8\%$. Similarly, the contribution from neutrinos is limited by neutrino mass measurements so that their overall contribution to the total dark matter density is expected to

be negligible also. Moreover, since these particles are 'hot' (i.e. relativistic) relics, an excess of neutrinos would spoil the standard hierarchical paradigm of structure formation.⁷ Therefore, although a portion of the dark matter density can be explained by known particles, combined dark matter observations provide strong motivation for physics beyond the Standard Model.

- SuperSymmetry (SUSY)

A promising proposal for physics beyond the Standard Model is provided by SuperSymmetry (SUSY) [49–51]. Supersymmetric models introduce a new symmetry of nature that relates bosonic integral (fermionic half integral) spin particles to fermionic half integral (bosonic integral) spin superpartners — thereby doubling the particle spectrum. SUSY theories address several outstanding problems of the Standard Model: supersymmetry protects the successful low energy Standard Model theory from being swamped by divergent corrections from higher energy scales,⁸ i.e. it solves the *hierarchy problem*. Moreover, SUSY unifies the gauge coupling constants at high energies (opening the door for Grand Unified Theories) and is an essential ingredient in many field theories attempting to unify the strong and electro-weak forces with gravity, e.g. string theory.

Significantly, in SUSY theories in which R -parity is conserved,⁹ the Lightest Supersymmetric Particle (LSP) is stable; if, in addition, the LSP is neutral, then it provides a viable dark matter candidate [52, 53]. By far the most extensively studied SUSY candidate is the lightest neutralino, χ , which is a spin $\frac{1}{2}$ Majorana fermion (i.e. it is its own antiparticle, $\bar{\chi} = \chi$).

The neutralino is the linear combination

$$\chi = N_{11}\tilde{B} + N_{12}\tilde{W}_3 + N_{13}\tilde{H}_1^0 + N_{14}\tilde{H}_2^0, \quad (1.27)$$

where the b -ino (\tilde{B}) and the W -ino (\tilde{W}_3) are the supersymmetric partners of the Standard Model gauge bosons B and W_3 , and \tilde{H}_1^0 and \tilde{H}_2^0 are two neutral *Higgs*-inos. The coefficients N_{1i} are taken from the diagonalized neutralino mass matrix and can be used to specify the neutralino's *gaug*-ino or *Higgs*-ino fraction. For example, if $|N_{11}| \gtrsim 0.99$, we would say that the neutralino is b -ino like. Similarly, if $|N_{12}|$ or $\sqrt{|N_{13}|^2 + |N_{14}|^2}$ are $\gtrsim 0.99$, the neutralino is said to be W -ino or

⁷Theories of structure formation based on hot dark matter particles proceed in a top-down fashion, with larger structures forming first and then fragmenting into smaller sub-structures. This picture conflicts with the observation that the Milky Way galaxy appears to be older than the Local Group and actually provides the strongest constraint on the sum of the neutrino masses.

⁸By introducing additional bosonic degrees of freedom, the masses of scalar particles (such as the Higgs boson) are protected from quadratic radiative corrections induced by the enormous difference between the electro-weak scale, $M_{\text{EW}} \sim 10^2$ GeV, and the Planck scale, $M_{\text{Pl}} \sim 10^{19}$ GeV.

⁹ R is a Z_2 quantum number with $R = +1$ for Standard Model particles and $R = -1$ for their supersymmetric partners, or *sparticles*.

Higgs-ino like respectively. The *gaug*-ino fraction of the neutralino, which depends on the various SUSY model parameters (along with the particular SUSY model), strongly influences its properties and in particular the nature and strength of its interactions; several public packages [54–56] (see also chapter 16 of [43]) are available to routinely calculate many of the important particle parameters including the neutralino annihilation cross section and thermal relic density.

Supersymmetry also provides several other dark matter candidates including the sneutrino and axino, which are the supersymmetric partners of the neutrino and axion (see later) respectively; details of possible supersymmetric explanations for the dark matter problem can be found in the excellent review by Jungman *et al* [57] and the more recent review [58].

A number of ongoing collider experiments, most notably the Large Hadron Collider (LHC) at CERN, are searching for signatures of supersymmetry in the collisions of high energy particles. So far no such signature has been observed and some would argue that the outlook for the simplest SUSY models is looking tenuous [59]. As no SUSY particles have been found with masses equal to their non-SUSY partners, these models all assume the SUSY symmetry is broken by adding terms to the Lagrangian, thus generating a SUSY mass spectrum. In order to naturally solve the hierarchy problem within the framework of supersymmetry, the masses of the SUSY particles must be around the TeV scale. However, cumulated data taken from the LHC is starting to exclude a large portion of this mass range, thereby removing much of the original motivation for introducing supersymmetry in the first place [60, 61].

LHC bounds on SUSY theories in which R-parity is conserved and the lightest stable SUSY particle, the neutralino (1.27), is the cold dark matter candidate are very model dependent. The different variants of the minimal SUSY extension of the standard model (MSSM) studied range from the constrained MSSM (CMSSM) model which assumes that, at the grand unification scale, all scalars have a universal (soft) SUSY-breaking mass m_0 , the gauginos have a universal mass $m_{1/2}$ and all trilinear couplings have a universal value A_0 , resulting in five free parameters, to the phenomenological MSSM (pMSSM) model in which no grand unification is assumed and there are 10 free parameters. The bounds on CMSSM masses depend on the sign of the coupling μ between the Higgs doublets (\tilde{H}_1 and \tilde{H}_2). For the CMSSM the LHC Run 1 places lower bounds of 1810 GeV ($\mu > 0$) and 3540 GeV ($\mu < 0$) on gluinos, 1620 GeV ($\mu > 0$) and 6300 GeV ($\mu < 0$) on right-handed squarks, 750 GeV ($\mu > 0$) and 4100 GeV ($\mu < 0$) for the lighter stop squark, 340 GeV ($\mu > 0$) and 4930 GeV ($\mu < 0$) for the lighter stau slepton, and 935 GeV ($\mu > 0$) for the lightest neutralino [62]. The best-fit pMSSM values are 2880 GeV

for gluinos, 4360 GeV for stop squarks, 440 GeV for sleptons and 160 GeV for the neutralino [63].

- Other candidates

In addition to those just mentioned, there are many other hypothetical particles that, for a certain parameter range, could provide a viable dark matter candidate. For example, the axion, which was introduced by Peccei and Quinn [64] to solve the Strong CP problem in quantum chromodynamics (QCD),¹⁰ is extremely weakly interacting and, if sufficiently produced in the early universe, could play the role of dark matter. Alternatively, the dark matter could be made of a new *sterile* generation of neutrinos [66] that are separate from the *active* neutrino generations of the Standard Model and only experience gravitational interactions. A more exotic possibility is that dark matter is comprised of primordial black holes which are thought to have formed during the very early moments of the universe.

It is interesting that quite often these candidates have been introduced for ulterior motives, removed from dark matter considerations, and many arise naturally in other areas of physics. For a more complete list of possible dark matter candidates we refer the reader to the comprehensive reviews by Bertone *et al* [67], Feng [68] and the monograph [43].

It is important to keep in mind that the total dark matter density need not be composed entirely of a single species and that several of the candidates listed above can contribute. As such, the relic density bound (1.20) only places a firm upper bound on the contribution from each component; candidates with relic densities lower than this bound are still acceptable but must be supplemented with dark matter species — as in the case of neutrinos, for example.

Given the plethora of dark matter candidates, coupled with the transient state of Supersymmetry and physics beyond the Standard Model in light of incoming LHC data, throughout this thesis we remain agnostic about the identity of the dark matter particle only assuming that it is produced thermally in the early universe (see section 1.4.4). In other words, we focus on the cosmological aspect of the problem and leave the particle physics details to experts in the field.

¹⁰The Strong CP problem relates to the stringent constraints on C(harge conjugation)P(arity symmetry) violating processes in strong interactions despite the presence of CP violating terms in the QCD Lagrangian [65].

1.4.3 Asymmetric dark matter

The majority of dark matter models assume symmetric dark matter for which the particles are Majorana fermions with $\chi = \bar{\chi}$, i.e. they are self-conjugate. Given that most known particles are not Majorana, it is reasonable to consider asymmetric dark matter models in which the particle χ and antiparticle $\bar{\chi}$ are distinct, i.e. $\chi \neq \bar{\chi}$, and to assume an asymmetry between the number densities of the dark matter particles and antiparticles [69–71]. Indeed, a similar asymmetry exists in the baryonic matter sector between the number of observed baryons n_b and antibaryons $n_{\bar{b}}$. This baryonic asymmetry is

$$\eta_b = \frac{n_B}{n_\gamma} = \frac{n_b - n_{\bar{b}}}{n_\gamma} \approx 6 \times 10^{-10}, \quad (1.28)$$

where n_γ is the number density of photons. Several models have been proposed [69, 70] that relate the asymmetries in the baryonic and dark sectors. These models typically assume [72] either a primordial asymmetry in one sector which is transferred to the other sector, or that both asymmetries are generated by the same physical process such as the decay of a heavy particle. Kaplan *et al.* [73] consider a baryonic $B - L$ (where B and L are the baryon number and lepton number respectively) asymmetry generated by baryogenesis at high temperatures that is transferred to the dark matter sector by interactions arising from higher dimension operators which then decouple at a temperature above the dark matter mass and freeze in the asymmetry.¹¹ If the asymmetries in the dark and baryonic matter sectors share a common origin then their number densities will be related $n_{\text{DM}} \sim n_b$, as will their densities $\Omega_{\text{DM}} \sim (m_\chi/m_b)\Omega_b$ [69, 70, 73]. This could explain the approximate equality of the observed dark and baryonic abundances ($\Omega_{\text{DM}}/\Omega_b \sim 5$) and suggests a dark matter particle mass in the range $m_\chi \sim 5 - 15$ GeV. Interestingly, this mass range is favored by a number of observational datasets [75–77], providing further motivation for asymmetric dark matter.

Cosmological, astrophysical and collider constraints on light thermal dark matter ($m_\chi \sim 1$ MeV - 10 GeV) have been examined by [78] for both symmetric and asymmetric models of dark matter and [79] have considered flavour constraints on, and collider signatures of, asymmetric dark matter produced by decays of supersymmetric particles in the minimal supersymmetric Standard Model (MSSM).

¹¹Asymmetric dark matter has been considered in the context of composite dark matter. For example, [74] propose a model based upon technicolour in which techniparticles with charge -2 formed from techniquarks bind with ${}^4\text{He}^{++}$ to produce neutral dark matter. The excess of the charge -2 techniparticles over their antiparticles is related to the baryon relic density.

1.4.4 Thermal relic abundance

A popular framework for the origin of dark matter is provided by the thermal relic scenario in which the dark matter particles are produced through thermal scatterings of background particles in the cosmic bath,

$$\chi\bar{\chi} \leftrightarrow X\bar{X} \quad (1.29)$$

where $(\bar{X})X$ are the background (anti)particles. At early times, when the temperature of the universe is high, frequent interactions keep the dark matter particles in equilibrium with the background, i.e. $n_\chi \approx n_\chi^{\text{eq}}$ where n_χ and n_χ^{eq} are the dark matter number density and equilibrium number density respectively. As the universe expands and cools the dark matter interaction rate drops below the expansion rate and the particles fall out of equilibrium. At this point, both creation and annihilation processes cease, and the number density redshifts with expansion; the remaining 'relic' particles constitute the dark matter density we observe today. This process is known as particle freeze-out and, for non-relativistic dark matter particles, typically occurs at $T_f \approx m_\chi/23$ (where m_χ is the dark matter particle mass) — that is, during the very early moments of the universe.¹²

The dark matter number density n_χ is governed by the relativistic Boltzmann equation (for symmetric dark matter) [80]¹³

$$\frac{dn_\chi}{dt} + 3Hn_\chi = -\langle\sigma v\rangle \left[n_\chi^2 - (n_\chi^{\text{eq}})^2 \right], \quad (1.30)$$

where H is the expansion rate of the universe and $\langle\sigma v\rangle$ is the thermal average of the annihilation cross section σ times the relative velocity v . In the literature, $\langle\sigma v\rangle$ is often referred to as simply the annihilation cross section.

The present dark matter density, determined from the asymptotic solution of (1.30), is extremely sensitive to the timing of dark matter decoupling. Due to the Boltzmann suppression factor in the equilibrium number density (for temperatures below the dark matter rest mass, $n_\chi^{\text{eq}} \sim e^{-m_\chi/T}$), the longer the dark matter particles remain in equilibrium the lower their number densities are at freeze-out. Thus species with larger interaction cross sections which maintain thermal contact longer, freeze out with diminished abundances. Alternatively, cosmological scenarios that predict a faster expansion rate during the decoupling phase lead to earlier particle freeze-out and enhanced relic abundances.

¹²Alternatively, there are several particles, including the neutrino, that freeze-out with relativistic thermal distributions.

¹³The corresponding expression for an asymmetric dark matter species, $\chi \neq \bar{\chi}$, is given in section 2.4 (see (2.33)-(2.34)).

In the standard radiation dominated scenario the dark matter relic density can be approximated by (see section 2.2.2)¹⁴

$$\Omega_{\text{DM}} h^2 \simeq 0.12 \left(\frac{2 \times 10^{-26} \text{ cm}^3 \text{ s}^{-1}}{\langle \sigma v \rangle} \right), \quad (1.31)$$

so that a dark matter particle with a weak scale interaction cross section $\sigma \sim G_{\text{F}}^2 m_{\chi}^2$, for which $\sigma v \sim 10^{-26} \text{ cm}^3 \text{ s}^{-1}$, will freeze-out with an abundance that matches the presently observed value (1.20). This is known as the WIMP miracle and strongly motivates thermal WIMP dark matter.¹⁵

We briefly mention that alternative scenarios to explain the origin of dark matter exist in which the dark matter is produced through the decay of a heavier species. In this case the Boltzmann equation (1.30) becomes¹⁶

$$\frac{dn_{\chi}}{dt} + 3Hn_{\chi} = -\langle \sigma v \rangle \left[n_{\chi}^2 - (n_{\chi}^{\text{eq}})^2 \right] + N_D, \quad (1.32)$$

where N_D is an additional source term. Further, it is possible that the dark matter particles either do not, or only partially thermalize in the early universe, in which case the Boltzmann equation (1.30) does not apply. In this thesis we will always assume that dark matter is produced thermally in the early universe and that (1.30) is valid. For further details on non-thermal dark matter scenarios see for instance [82–84].

1.4.5 The search for dark matter

The weakly interacting nature of dark matter particles makes them exceedingly difficult to detect experimentally [85]. One approach, known as *direct* detection, is to search for dark matter particles scattering off Standard Model particles inside a laboratory. Since our solar system (and galaxy) is embedded in a vast halo of dark matter, dark matter particles should be continuously streaming through our terrestrial atmosphere and dark matter interactions may occur at a detectable level. To maximize the likelihood of detection, the detector is made from a high density target nucleus and is usually placed deep underground (in a low background environment) so as to avoid contamination from other (more strongly interacting) background signals. Experiments of this type have been ongoing for over a decade with several groups [86, 87] reporting an irreducible

¹⁴The expression (1.31) assumes that dark matter annihilations are dominated by s -wave processes so that the thermally averaged annihilation cross section $\langle \sigma v \rangle = \text{constant}$. For the more general expression see section 2.2.2.

¹⁵Although the relation (1.31) is often referred to as ‘miraculous’, it has been argued that the correct thermal abundance can be obtained for dark matter candidates that have neither weak scale masses nor weak scale interactions [81].

¹⁶Again, this equation is only valid for symmetric dark matter particles $\chi = \bar{\chi}$.

signal above background with the correct annual modulation (which arises due to Earth's motion around the Sun). Unfortunately, these results are disputed by more sensitive experiments [88–91] and the origin of the signal remains unclear (for further details see the recent review by Schumann [92]).

Of particular relevance for our study are *indirect* dark matter experiments. These surveys search for the products of dark matter annihilations (or decays), e.g.

$$\chi\bar{\chi} \rightarrow \gamma\gamma, e^+e^-, \nu\bar{\nu}, b\bar{b}, W^+W^- \dots \quad (1.33)$$

and can therefore be used to place constraints on the dark matter annihilation cross section $\langle\sigma v\rangle$ — the same quantity used in the relic abundance calculation (1.30).¹⁷

Many space-borne [94–96] and ground based experiments [97, 98] are currently underway with target sites including dark matter sub-halos, dwarf spheroidal galaxies, and even our own Sun [99]. Again, several interesting results, including anomalous gamma ray signals [100–102], with possible dark matter interpretations have been identified [77, 103–110]. Specifically, we mention cosmic ray observations by the PAMELA collaboration who measured a rising positron fraction $e^+/(e^+ + e^-)$ up to energies of ~ 5 GeV [111, 112]. This measurement, which was later extended to higher energies by the Alpha Magnetic Spectrometer (AMS) instrument [113], is above that expected from astrophysical sources and cannot be explained by modifying cosmic ray propagation models. Furthermore, the most recent data release from the AMS-02 collaboration [114] found that above ~ 200 GeV, the positron fraction no longer increases, which, along with other measurements, implies that high energy positrons have a different origin to that of electrons. Therefore, either additional uncatalogued astrophysical sources (such as pulsars) are present [115], or, the rising positron fraction can be interpreted in terms of annihilating dark matter [104, 116, 117].

We stress that a dark matter interpretation of the rising positron fraction requires large boost factors (up to three orders of magnitude larger) of either the local dark matter density or the dark matter annihilation cross section via e.g. Sommerfeld enhancement [118] or some other mechanism (see later). Hence, despite the excitement surrounding these anomalous signals, no conclusive determination can yet be made.¹⁸

Finally, it is also possible that dark matter could be produced through Standard Model particle interactions in high energy particle accelerators such as the LHC (this is the inverse process to what is observed in indirect detection experiments). In this case,

¹⁷This is in contrast to the direct detection experiments mentioned above that probe the WIMP-nucleon scattering cross $\sigma_{\chi N \rightarrow \chi N}$, which is related to the annihilation cross section $\sigma_{\chi\bar{\chi} \rightarrow X\bar{X}}$ (where the X 's are Standard Model particles) by a model-dependent crossing symmetry [93].

¹⁸For recent reviews on the status of indirect dark matter searches see [119, 120].

because the dark matter particles interact so weakly, they would easily escape the accelerator’s detectors. However, their presence could be deduced via missing transverse momentum and the nature of the dark matter particle and its interactions could be reconstructed from analyzing the collision. So far, no excess of events above Standard Model expectations has been found, but it is hoped that dark matter signatures may appear as the LHC pushes towards its 14 TeV design capacity in the coming years.

In summary, despite a number of exciting observations with potential dark matter interpretations, the situation remains far from conclusive. However, with several existing and upcoming experiments [121, 122] beginning to probe the weak scale interaction region predicted by generic relic abundance calculations (see for example figure 1.1), a definitive signal is expected soon.

1.4.6 Constraints

Although very little data is available regarding the nature of the dark matter particle, the observed dark matter density (1.20) does place a firm *upper* bound on the relic abundance of any dark matter species (keep in mind, lower abundances are certainly permissible). Further, since the relic abundance is inversely related to the annihilation cross section $\langle\sigma v\rangle$, the observed dark matter density can be used to place a firm *lower* bound on the dark matter annihilation cross section. For example, if the magnitude of $\langle\sigma v\rangle$ is too small, the species does not effectively annihilate in the early universe, and decouples with an abundance that exceeds the presently observed value. Therefore, relic abundance calculations, in conjunction with the observed dark matter density, provide an important test for dark matter models (see section 1.6.3).

In addition, the *lack* of an observed signal using the detection methods described above, allows one to place constraints on the strength of dark matter interactions. For our purposes, we will focus on indirect detection observations which place direct constraints on the dark matter annihilation cross section $\langle\sigma v\rangle$. More specifically, the indirect detection measurements can be used to place constraints on the velocity independent, or *s*-wave, component of the thermally averaged annihilation cross section. Since the present velocity of the dark matter particles is negligible ($v/c \sim 10^{-3}$), any velocity dependent terms in the non-relativistic expansion of the annihilation cross section [123, 124],¹⁹

$$\langle\sigma v\rangle = a + b\langle v\rangle^2 + c\langle v\rangle^4 + \dots, \quad (1.34)$$

¹⁹The successive terms in the expansion $\langle\sigma v\rangle = \sum_n c_n \langle v\rangle^{2n}$ where $v \sim T^{1/2}$ correspond to *s*-wave ($n = 0$) annihilation, *p*-wave ($n = 1$) annihilation, etc.

will not contribute to dark matter annihilations in the late time universe. Therefore these terms are immune to indirect detection experiments.

In this thesis we primarily refer to the constraints derived from the gamma ray data [125] which were obtained from observations of 25 dwarf spheroidal satellite galaxies of the Milky Way using the Large Area Telescope (LAT) on board the Fermi space satellite. The Fermi-LAT constraints, which are shown in figure 1.1 for dark matter particles annihilating predominantly through a particular annihilation channel, are competitive with those determined using the AMS-02 positron data [126],²⁰ measurements of the isotropic gamma ray background [127, 128], and CMB data [129–134].²¹

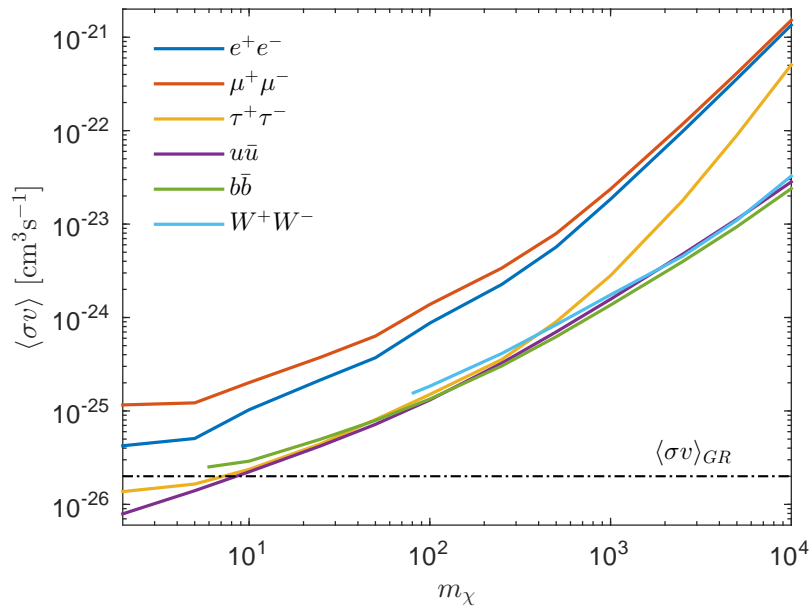


FIGURE 1.1: Upper limits on the dark matter annihilation cross section $\langle\sigma v\rangle$ as a function of WIMP mass m_χ for different annihilation channels derived from the Fermi-LAT gamma ray data. We have also indicated the annihilation cross section required to produce the correct thermal relic abundance in the standard cosmological scenario, $\langle\sigma v\rangle_{GR}$ (dot-dashed black curve).

In figure 1.1 we have superimposed the (approximate) annihilation cross section required to produce the observed relic density in the standard (GR) cosmological scenario, $\langle\sigma v\rangle_{GR}$ (dot-dashed black curve). Remember that this curve represents the lower bound derived from calculations of the dark matter relic abundance. Comparing this result with the Fermi-LAT constraints we see that indirect detection experiments are already beginning to probe the canonical annihilation cross section expected from standard thermal relic abundance calculations. In fact, dark matter particles with masses $m_\chi \lesssim 10$ GeV, that

²⁰The constraints determined using the AMS-02 positron observations are in fact the most stringent available. However, this set only constrains the annihilation cross section into leptonic final states, so we choose to use the more complete set given by the Fermi-LAT dwarf spheroidal data [125] in our analysis.

²¹For additional publications constraining the dark matter annihilation cross section, see for instance [135–138].

primarily annihilate through the $\tau^+\tau^-$ or $u\bar{u}$ annihilation channels, are excluded by these constraints.

We must stress, however, that the Fermi-LAT constraints only apply if the dark matter particle annihilates predominantly through one of the annihilation channels considered. In the general case, multiple (possibly non-Standard Model) annihilation channels are accessible and these constraints can be evaded. We will therefore use the Fermi-LAT data to simply illustrate how the annihilation constraints can be applied to the calculations undertaken in this thesis and avoid making absolutist claims about the viability of particular theories in the face of these constraints.

1.5 Non-standard cosmologies

The standard Λ CDM model has been remarkably successful in explaining all astrophysical and cosmological observations. However, all of the data collected so far, such as the information extracted from, e.g. the cosmic microwave background (CMB), baryon acoustic oscillations (BAO) or large-scale structure (LSS), originates from cosmological events that occur at times when the temperature of the universe has cooled to the order of an \sim MeV or below. Indeed, the earliest available probe of the Big Bang model is Big Bang Nucleosynthesis, which occurs at a temperature of ~ 1 MeV.²² The evolution of the universe prior to this event is relatively unconstrained and it is only assumed that the standard radiation dominated expansion regime can be extrapolated back to the inflationary epoch. It's possible, therefore, that the actual evolution deviates from the predictions of the standard cosmological model.

There are several compelling reasons for considering extensions of the standard Λ + Cold Dark Matter model. Perhaps most obvious is that $\sim 95\%$ of the total energy budget in the Λ CDM model is of unknown nature and origin. Although dark matter and dark energy both provide excellent fits to the available observational data, no experimental verification of either component exists. Moreover, the requirement of an exotic fluid with a negative equation of state (dark energy) to explain the late time accelerated expansion of the universe appears especially ad-hoc given the leading model, the cosmological constant (Λ) model, lacks physical motivation and has limited predictive power. Other dark energy models have been proposed, but many fail to match the observational

²²Recently, the BICEP2 collaboration released measurements of B -mode polarization imprinted in the CMB [139] which the authors speculated was evidence of primordial tensor perturbations (i.e. gravitational waves generated during the inflationary period). However, a subsequent joint analysis of the BICEP2/Keck Array and Planck data [140] indicates the B -mode signal reported by BICEP2 is most likely due to dust in our galaxy.

successes of the Λ model, and others still suffer from the same fine-tuning and coincidence problems. Lastly, General Relativity in its present form cannot be renormalized, and therefore precludes a quantum description. Any attempts to unify the fundamental forces of nature must therefore appeal to a more fundamental theory of gravity.

Here we will consider several non-standard cosmological scenarios that address the issues just mentioned. In particular, we focus on scenarios that predict a modified expansion history in the pre-BBN era:

- Quintessential kination models

Quintessence models of dark energy are typically introduced to explain the late time accelerated expansion of the universe with the energy density of the field expected to remain sub-dominant at early times (see the discussion on tracker solutions in the section 1.3.2). However, it is possible that the dynamics of the field may lead to a phase of *kination domination*, where the kinetic energy of the scalar field dominates over the potential energy. If this occurs at sufficiently early times, the quintessence field would dominate, modifying the expansion history from that predicted by the standard cosmological model [141, 142]. This scenario, known as quintessential kination, is an interesting example of how dark energy, a late time phenomena, may influence the physics of the early universe.

- Scalar-tensor gravity

An extension of the quintessence scenario is provided by scalar-tensor gravity models which incorporate a coupling between the scalar field, φ , and the metric field, $g_{\mu\nu}$ [143–146]. These models arise naturally in string theory and other unified field theories and represent a departure from standard General Relativity.

The coupling between the scalar field and the metric introduces a new long range force between material objects and is therefore subject to strict bounds from laboratory and solar system tests of gravity. Fortunately, scalar-tensor models exhibit an attraction mechanism towards General Relativity [147, 148] so that the scalar field relaxes towards a state where the two are coincident for a wide range of initial conditions. This allows for large deviations from the standard cosmological history at early times whilst still respecting the observational constraints from BBN and post-BBN processes, e.g. CMB and BAO.

- Braneworlds

Braneworld models are inspired by string theory (and M-theory) which postulates that there are additional spacetime dimensions beyond the four (three spatial + time) that we naturally experience. Within this framework our universe is modeled as a four-dimensional surface (the *brane*) embedded in a higher dimensional

spacetime; matter (in this case both dark and baryonic) is confined to the surface of the brane whereas gravity leaks into the higher dimensions. This provides a possible explanation as to why gravity is so much weaker than the other forces of nature.

Depending on the particular set-up, the extra dimensions can be either large [149, 150] or small [151], and are only accessible in either the high [149, 150] or low energy limits [152]. Therefore, cosmological scenarios based on the braneworld paradigm have interesting phenomenological consequences for both the early and late time evolution of the universe.

1.6 Relic abundance calculations

1.6.1 Modified expansion history

Most relic abundance calculations assume that, at the time of dark matter decoupling, the universe is radiation dominated with $H^2 \simeq 8\pi G\rho_r/3$ (see (1.4)), where ρ_r is the radiation energy density. In this case, particle freeze-out occurs around $T_f \approx m_\chi/23$ and the relic abundance is (approximately) given by the canonical result (1.31). However, if we modify our assumptions about the expansion rate of the universe in the pre-BBN era, and in particular at the time of dark matter decoupling, particle freeze-out will be affected and the dark matter relic abundance will be modified.

Early works by Barrow [153] and Kamionkowski and Turner [154] showed that the dark matter relic abundance can be enhanced in cosmological scenarios with anisotropic expansion [153, 154] or suppressed in scenarios where the energy density at the time of decoupling is dominated by some non-relativistic species [154]. Later, Salati [142] considered a simple quintessential kination scenario (see the description in the previous section) and showed that the relic abundance of dark matter may be enhanced by up to several orders of magnitude with respect to the canonical result. Since then, many similar works investigating dark matter relic abundances in non-standard cosmological scenarios have appeared (see for example [155–159]). In general, it is found that scenarios that predict a faster expansion rate at the time of dark matter decoupling lead to accelerated particle freeze-out and, due to the Boltzmann suppression factor, an enhanced dark matter relic density. Conversely, a slower expansion rate at the time of dark matter decoupling delays freeze-out leading to a suppressed relic abundance.

Since the relic abundance (i.e. the present dark matter density $\Omega_{\text{DM}}h^2$ given in (1.20)) is a precisely measured quantity, we can use the results of relic abundance calculations to constrain the parameters of non-standard cosmological scenarios and the properties

of dark matter particle candidates. In this way, relic abundance calculations offer an exciting probe of beyond the standard model physics and exemplify the strong interplay between particle physics and cosmology.

1.6.2 Constraints on non-standard scenarios

As mentioned previously, the earliest available constraint on the expansion rate of the universe is provided by Big Bang Nucleosynthesis, a process that occurs when $T \sim 1$ MeV. All other observational constraints, such as those imposed by the CMB and LSS, relate to events that occur much later on. In fact, the number of detectable signals from the pre-BBN era is limited. However, dark matter decoupling occurs at temperatures $T_f \approx m_\chi/23$ which, for dark matter particles with mass $m_\chi \gtrsim \mathcal{O}(100)$ MeV, is greater than the BBN temperature. Hence, dark matter relic abundance calculations, which rely on data from times much earlier than BBN, can therefore be used as a novel observational probe of early universe physics (see for instance [153, 160, 161]).

The role of relic abundance calculations becomes even more significant when one considers that many alternative cosmological models are constructed (or at least constrained) to collapse towards the standard cosmological model prior to the onset of BBN. Subsequently, in the low energy regime, the non-standard models mimic the standard model and the predictions of the two are degenerate. Hence, relic abundance calculations may be one of the few probes capable of discriminating these theories from the standard Λ CDM model.²³

1.6.3 Implications for dark matter candidates

The ignorance surrounding the dark matter particle and its properties suggests that the role of relic abundance calculations can also be viewed from the inverse perspective. Recall that, for a dark matter candidate to be considered viable, it must be produced with the correct thermal abundance. Those candidates that are overproduced are rejected, and those that are underproduced are often overlooked. However, this assignment is performed assuming that the standard cosmological model holds during the era of dark matter decoupling. If we relax this assumption and consider a non-standard expansion law during the decoupling era, the dark matter relic density will be modified and the distinction between those candidates that are viable and those that are not will be moderated.

²³This idea can be connected back to the concept introduced in the opening section, that the early universe can be treated as a sort of cosmic laboratory, reaching energies that other experiments simply don't have access to.

We can be more specific if we recall that the dark matter relic abundance is inversely related to the annihilation cross section, as in (1.31) (note that a similar relationship holds in other cosmological scenarios also). As an example, take the neutralino, whose annihilation cross section, and in turn its relic density, depends sensitively on its gaugino fraction (see section 1.4.2): *b*-ino like neutralinos typically possess an annihilation cross section weaker than the canonical WIMP value ($\langle\sigma v\rangle \sim 10^{-26} \text{ cm}^3\text{s}^{-1}$) and are therefore overproduced in the standard cosmological model; conversely, *W*-ino and *Higgs*-ino like neutralinos have stronger annihilation cross sections, thus leading to a heavily suppressed relic abundance.²⁴ In fact, Arkani-Hamed *et al* [162] argued that the observed dark matter density is only obtained if the SUSY parameters are fine-tuned so that the gaugino fraction lies right on the boundary between pure *b*-ino and pure *W*-ino or *Higgs*-ino.

This fine-tuning can be alleviated in non-standard cosmological models. For example, those cosmologies that predict a slower expansion rate during dark matter decoupling, and as a result a suppressed dark matter relic abundance, could rescue pure *b*-ino neutralinos. Alternatively, scenarios that predict a faster expansion rate and an enhanced relic abundance could revive *W*-ino and *Higgs*-ino like neutralinos. Therefore, given the lack of available data from times prior to BBN, the relic density bound applied to dark matter candidates should be considered provisional.

More generally, the existence of a viable dark matter candidate with the correct relic abundance is often used to appraise the various incarnations of Supersymmetric extensions of the Standard Model. If the relic density bound can be evaded in non-standard cosmological scenarios, in that the observed dark matter density can be obtained with an annihilation cross section that differs from the canonical thermal WIMP value, the viability of SUSY models must be reevaluated. Moreover, the relic density bound is regularly used to inform directed searches for Supersymmetry at the LHC [163] and could therefore be pointing experimentalists in the wrong direction.

1.6.4 Implications for dark matter searches

If the relic density bound can be evaded, and the interaction strength of the dark matter particle can be vastly different from the canonical thermal WIMP value, the implications for the planning and interpretation of present and future dark matter searches are far reaching [164]. In section 1.4.5 we saw that indirect detection experiments are beginning to probe the weak scale annihilation cross section predicted by generic relic abundance

²⁴The annihilation cross section of *W*-ino and *Higgs*-ino like neutralinos is usually larger because for these neutralino types a greater number of annihilation channels are accessible. Moreover there are often several sparticles which are degenerate in mass leading to additional co-annihilations.

calculations, and it's possible that additional data taken from both present and future generation experiments may exclude the thermal WIMP region entirely. Since the relic dark matter density places a firm lower bound on the dark matter annihilation cross section, one interpretation of this result is that the thermal relic explanation for dark matter is not appropriate and that other dark matter production mechanisms should be investigated. Alternatively, this observation could point to new physics in the era prior to BBN; a null result from indirect dark matter searches could indicate that the expansion rate of the universe at the time of dark matter decoupling is slower than that predicted by the standard cosmological model as such a scenario could accommodate an annihilation cross section smaller than the thermal WIMP value.

On the other hand, the anomalous PAMELA data discussed in section 1.4.5 could be naturally explained in a non-standard cosmological scenario that requires an enhanced annihilation cross section. There we mentioned that a dark matter interpretation of the rising positron fraction requires an annihilation cross section which is up to three orders of magnitude larger than the standard thermal WIMP value. In the standard cosmological model, such a large cross section would severely deplete the present relic abundance of dark matter, in conflict with the observed density. However, non-standard cosmological scenarios can easily accommodate the enhanced annihilation cross section required to generate the observed positron excess and still produce the observed dark matter density (see for example [165]).²⁵

Furthermore, since the dark matter annihilation cross section, $\langle\sigma_{\chi\bar{\chi}\rightarrow X\bar{X}v}\rangle$, is related to the scattering cross section, $\langle\sigma_{\chi X\rightarrow\chi Xv}\rangle$, through crossing symmetry [93], the modified dark matter relic abundance has similar implications for direct dark matter searches as well.

1.7 Outline

The aim of this thesis is to compute the relic abundance of both symmetric and asymmetric dark matter particles in a variety of non-standard cosmological scenarios and determine the enhancement (or suppression) factors with respect to the corresponding value in the standard scenario. We also invert the problem, and determine the magnitude of the annihilation cross section required to produce the observed relic density (1.20) and compare the results to the upper limits derived from the Fermi-LAT gamma ray data. In this way we derive constraints on the various non-standard cosmology model

²⁵In this instance we should be careful because both antiproton and gamma ray data constrain the dark matter annihilation cross section into particular final states (see figure 1.1). A dark matter interpretation therefore requires a dark matter particle that annihilates preferentially into leptons, i.e. one that is *leptophilic* (see for example [166]).

parameters as a function of the dark matter particle properties. Additionally, where possible, we derive approximate analytical solutions for the dark matter density and the required annihilation cross section and compare our findings to the numerical data. We also discuss the predicted detection signal in each of these scenarios and their prospects for future detection. Lastly, we briefly mention the possible implications for SuperSymmetric particle models.

The outline is as follows:

In chapter 2 we review the freeze-out scenario and the explanation for the origin of dark matter before introducing the Boltzmann rate equation that is used to determine the present dark matter density. We then study the evolution of the dark matter number density in the standard cosmological scenario and highlight several of the key ingredients that influence dark matter decoupling. Importantly, we derive an approximate analytical solution for the relic abundance that can be applied to non-standard cosmological models.

In chapter 3 we apply the formalism developed in chapter 2 to quintessential kination models. Although the dark matter relic abundance in the quintessential kination scenario has been considered previously by several authors [142, 157, 167–169], we use this simple example to illustrate many of the generic features that are common to other non-standard cosmological scenarios that predict a modified expansion rate at early times. In doing so, we review a number of the key findings presented in the literature and evaluate the validity of the existing results in light of updated computational considerations [170].

In chapter 4 we investigate scalar-tensor models of gravity and critically examine the existing studies by Catena *et al* [156, 159, 171, 172] and the several follow up papers based on their results [173–175]. We find that, for a more common choice of the scalar coupling, which had recently been subjected to detailed BBN studies [176], the relic abundance is only slightly modified from its canonical value. This is in stark contrast to the several orders magnitude enhancement factors reported by the Catena group.²⁶ To conclude, we briefly discuss the relic abundance of dark matter in non-universal scalar tensor models, where the scalar interaction with the dark and baryonic sectors is distinct, and suggest possible avenues for further investigation.

In chapters 5 and 6 we study the relic abundance of dark matter in braneworld cosmological scenarios. Chapter 5 is dedicated to Randall-Sundrum type II braneworld cosmology and we show how the enhanced expansion rate in this scenario, which at early times evolves as $H \propto \rho$, amplifies the dark matter relic abundance. Then, in

²⁶A preliminary account of this investigation was presented in [177].

chapter 6 we consider an extension of the Randall-Sundrum braneworld model that incorporates a higher order curvature correction, known as the Gauss-Bonnet term, in the bulk action integral. We challenge the previous investigation by Okada and Okada [158] of dark matter relic abundances in the Gauss-Bonnet braneworld scenario which concluded that the relic density is diminished in this scenario. We show that this result is atypical of Gauss-Bonnet braneworld models, and that, in general, the model predicts an enhanced dark matter density. The results and discussion in these chapters have been expanded from our publications [178] and [179] respectively.

Finally, in chapter 7 we summarize our findings and point out the key differences and similarities between each of the non-standard scenarios considered and discuss the potential for future observations to discriminate between them. We also suggest potential directions for future work.

Chapter 2

Relic Density

2.1 Introduction

A natural framework for the origin of dark matter is provided by the thermal relic scenario: at early times the dark matter (anti)particles $(\bar{\chi})\chi$ are held in equilibrium through frequent interactions with the background thermal bath. At temperatures well above the rest mass of the dark matter particle, m_χ , creation and annihilation processes are balanced and the dark matter number density behaves as (see Appendix B)

$$n_\chi^{\text{eq}}(T \gg m_\chi) = g_\chi \frac{3\zeta(3)}{4\pi^2} T^3, \quad (2.1)$$

where g_χ is the number of internal degrees of freedom of the dark matter particle and the Riemann zeta function is $\zeta(3) \simeq 1.202$. Remembering that the temperature is (roughly) related to the scale factor by $T \sim a^{-1}$, we see that in this regime the number of particles in a comoving volume, $N_\chi = n_\chi a^3$, is conserved.

However, as the universe expands and cools, and the temperature drops below m_χ , creation processes are Boltzmann suppressed; here, the background particles are no longer energetic enough to create $\chi\bar{\chi}$ pairs and the dark matter number density decays exponentially;

$$n_\chi^{\text{eq}}(T \ll m_\chi) = g_\chi \left(\frac{m_\chi T}{2\pi} \right)^{3/2} e^{-m_\chi/T}. \quad (2.2)$$

Eventually, through annihilation and expansion, the dark matter density becomes so diluted that $\chi\bar{\chi}$ interactions cease, at which point the number density simply redshifts

with expansion.¹ This process is known as particle freeze-out, and the surviving 'relic' particles constitute the dark matter density we observe today.² Remarkably, the freeze-out mechanism, which can be applied more broadly to relativistic and non-relativistic particles, not only explains the present dark matter density, but also encompasses the successful predictions of Big Bang Nucleosynthesis, neutrino decoupling as well as the era of recombination [80].

In the next section we introduce the Boltzmann rate equation describing the time evolution of the dark matter number density, discuss how the expansion history of the universe and dark matter annihilation cross section determine the present dark matter density, and derive an approximate solution to the Boltzmann equation that we can apply to general cosmological scenarios. In section 2.3 we use the observed dark matter density to constrain the dark matter annihilation cross section as a function of the WIMP mass and compare our results with the Fermi-LAT data. In section 2.4 we extend our discussion to the case of asymmetric dark matter. Finally, in section 2.5 we summarize the major ideas.

2.2 Symmetric dark matter

2.2.1 Boltzmann equation

The dark matter phase space distribution function $f_\chi(x^\mu, p^\mu)$ obeys the Boltzmann equation [80]

$$\hat{L}[f_\chi(x^\mu, p^\mu)] = \hat{C}[f_\chi(x^\mu, p^\mu)]. \quad (2.3)$$

\hat{L} is the relativistic Liouville operator describing the trajectory of the distribution function through phase space, given by

$$\hat{L} \equiv p^\alpha \frac{\partial}{\partial x^\alpha} - \Gamma_{\beta\gamma}^\alpha p^\beta p^\gamma \frac{\partial}{\partial p^\alpha}, \quad (2.4)$$

where $\Gamma_{\beta\gamma}^\alpha$ are the affine connections of the Robertson-Walker spacetime (see Appendix A). \hat{C} is the collision operator for the process $\chi\bar{\chi} \leftrightarrow X\bar{X}$ (see Appendix C).

¹Although interactions of the type $\chi\bar{\chi} \leftrightarrow X\bar{X}$ (where the X 's are Standard Model particles) have been extinguished, and the dark matter species has chemically decoupled, $\chi X \leftrightarrow \chi X$ interactions persist, since the target density for the scattering process, $n_X \sim T^3$, remains large. Therefore, kinetic decoupling, which occurs when the dark matter particles cease to exchange momentum efficiently with the background, occurs much later [180].

²For early work on the subject of thermal relics and their cosmic abundances see [52, 53, 123, 154, 181–201]

For a homogeneous and isotropic distribution function $f_\chi(x^\mu, p^\mu) = f_\chi(E, t)$, the evolution of the dark matter number density,

$$n_\chi(t) = \frac{g_\chi}{(2\pi)^3} \int d^3p f_\chi(E, t), \quad (2.5)$$

is obtained by taking the zeroth moment of the Boltzmann equation (2.3), to give [185, 202] (see Appendix C for a complete derivation)³

$$\frac{dn_\chi}{dt} = -3Hn_\chi - \langle\sigma v\rangle \left[n_\chi^2 - (n_\chi^{\text{eq}})^2 \right], \quad (2.6)$$

where $H \equiv \dot{a}/a$ is the expansion rate of the universe, $\langle\sigma v\rangle$ is the thermally averaged annihilation cross section times relative velocity (frequently referred to in the literature as simply the annihilation cross section) and n_χ^{eq} is the equilibrium number density. In the non-relativistic limit we can expand $\langle\sigma v\rangle$ in powers of the relative velocity, $\langle v^2 \rangle \sim T/m_\chi$ [198]:

$$\langle\sigma v\rangle = a + \frac{bT}{m_\chi} + \dots \quad (2.7)$$

where we identify the first (constant) term with s -wave scattering, the second term with p -wave scattering and so on.⁴ The quantity $\langle\sigma v\rangle$ depends on the specific dark matter particle model and incorporates the particle physics aspect of the problem.

In deriving (2.6) we have assumed (i) the dark matter particles maintain kinetic equilibrium throughout chemical decoupling (see earlier footnote) (ii) the dark matter annihilation products rapidly reach thermal equilibrium with the cosmic background and (iii) that the chemical potential μ_χ is negligible.⁵

Each term in the Boltzmann equation (2.6) can be understood as follows: the first term on the right hand side, $-3Hn_\chi$, is a dilution term arising from the expansion of the universe; and the two terms $-\langle\sigma v\rangle n_\chi^2$ and $\langle\sigma v\rangle (n_\chi^{\text{eq}})^2$ correspond to the loss and gain of particles through annihilation and creation respectively. In the absence of particle interactions, $\langle\sigma v\rangle = 0$, the solution of (2.6) is $n_\chi \propto a^{-3}$ so that the number of particles in a comoving volume is conserved. Note that the creation and annihilation terms contain the square of the number density because we have assumed (for now) that the dark matter species is self-conjugate with $\chi = \bar{\chi}$.

We can scale out the expansion of the universe by working with the fiducial quantity $Y \equiv n_\chi/s$, where $s = 2\pi^2 g_{*s}(T) T^3/45$ is the entropy density and $g_{*s}(T)$ is the number of

³The Boltzmann rate equation can also be derived in a non-rigorous fashion by invoking the general principle of detailed balance (see [203]).

⁴The expansion (2.7) breaks down near the formation of a resonance or at the opening of a new annihilation channel [199].

⁵There are several exceptions that will modify the calculation of the dark matter relic density, including the effects of coannihilations and resonances etc. [200, 201] which will not be considered here.

entropic degrees of freedom (see Appendix B). In an isentropic expansion, the entropy in a comoving volume is conserved, i.e. $d(sa^3) = 0$, and $s \propto a^{-3}$. Therefore, the quantity $Y \sim n_\chi a^3$ may be interpreted as the *comoving number density*.

Rewriting the time derivative of n_χ in terms of Y , and substituting in the entropy conservation relation, $\dot{s} = -3Hs$, we get

$$\dot{n}_\chi + 3Hn_\chi = s\dot{Y}. \quad (2.8)$$

The Boltzmann equation now reads

$$\frac{dY}{dt} = -s\langle\sigma v\rangle [Y^2 - Y_{\text{eq}}^2], \quad (2.9)$$

where $Y_{\text{eq}} = n_{\text{eq}}/s$. It is also convenient to write the evolution equation in terms of the dimensionless variable $x \equiv m_\chi/T$, which is related to t via

$$\frac{dx}{dt} = -\frac{x}{T} \frac{dT}{dt}. \quad (2.10)$$

Using the relationship (B.34) between the temperature T and the scale factor a ,

$$\frac{a}{a_0} = \left[\frac{g_s(T_0)}{g_s(T)} \right]^{1/3} \frac{T_0}{T}, \quad (2.11)$$

we have

$$-\frac{da}{a} = \zeta(T) \frac{dT}{T}, \quad (2.12)$$

where $\zeta(T)$ is a temperature dependent function related to the change in $g_{*s}(T)$, given by

$$\zeta(T) = 1 + \frac{1}{3} \frac{d \ln(g_{*s}(T))}{d \ln T}. \quad (2.13)$$

Finally, substituting (2.10) and (2.12) into (2.9) we get

$$\frac{dY}{dx} = -\frac{s\langle\sigma v\rangle}{xH} \zeta(T) [Y^2 - Y_{\text{eq}}^2]. \quad (2.14)$$

This is the form of the Boltzmann equation that we will most commonly work with throughout this thesis.

Note that since the number of relativistic degrees of freedom, $g_{*\rho}$, and the number of entropic degrees of freedom, g_{*s} , only differ when a particle crosses a mass threshold for $T \gtrsim 10^{-3}$ GeV (see Appendix B), when integrating (2.14) we assume that $g_{*\rho} = g_{*s}$. Hence, unless either of these quantities appears explicitly in an analytic expression, we will adopt the notation $g_* \equiv g_{*\rho} = g_{*s}$.

In figure 2.1 we show the evolution of the comoving number density, Y , (normalized to its value at very high temperatures, $x_i \ll 1$) as a function of x for several annihilation cross sections, $\langle\sigma v\rangle$, in the standard cosmological scenario. At early times, Y closely tracks its equilibrium value $Y_{\text{eq}} \simeq 0.208 (g_\chi/g_{*s})$ (black curve) which, for $x \lesssim 1$, is essentially constant. As the temperature of the universe drops below the dark matter rest mass ($x \gtrsim 1$), the equilibrium density begins to decay exponentially, yet Y continues to track $Y_{\text{eq}} \simeq 0.145 (g_\chi/g_{*s}) x^{3/2} e^{-x}$. Eventually, however, Y starts to deviate significantly from Y_{eq} , this is known as the freeze-out point and roughly occurs at $x_f \equiv m_\chi/T_f \approx 23$ (where T_f is the freeze-out temperature). After freeze-out ($x \gtrsim x_f$), Y continues to decay but now much more slowly than Y_{eq} , until finally it levels out, where it is once again conserved.

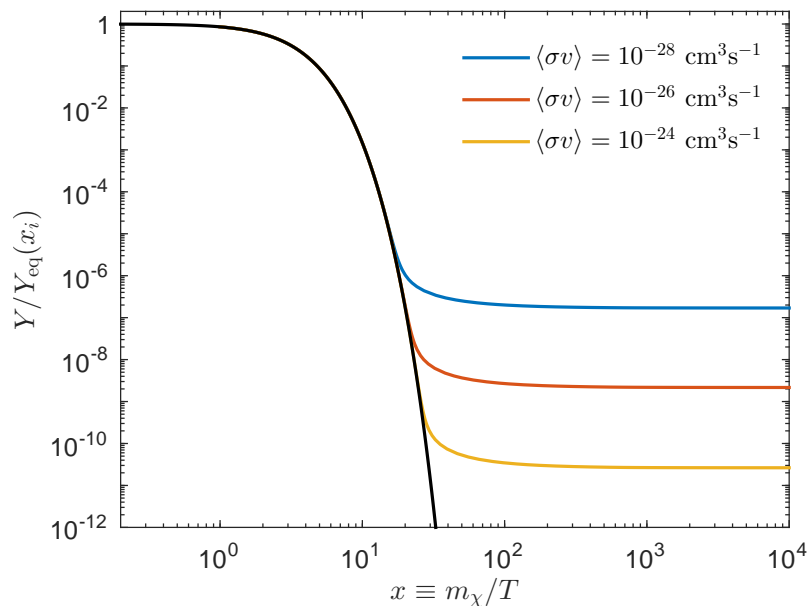


FIGURE 2.1: Evolution of the comoving number density Y as a function of x for $\langle\sigma v\rangle = 10^{-28} \text{ cm}^3\text{s}^{-1}$ (blue), $\langle\sigma v\rangle = 10^{-26} \text{ cm}^3\text{s}^{-1}$ (red) and $\langle\sigma v\rangle = 10^{-24} \text{ cm}^3\text{s}^{-1}$ (yellow). Also shown is the equilibrium density Y_{eq} (black).

The freeze-out process is not instantaneous, and it can take several decades (particularly in non-standard cosmological scenarios) before the comoving density settles towards to its asymptotic value [197]. Following the authors of [168], we therefore distinguish between two separate events: firstly, particle *freeze-out* (which we have denoted as x_f), when the comoving density no longer tracks its equilibrium value; and secondly, particle *freeze-in*, when the comoving density reaches its asymptotic value and is once again conserved. Between these two events, $Y(x)$ can decay by up to (or more than) an order of magnitude.

Since the comoving density is conserved after freeze-in, the present dark matter energy density, $\Omega_{\text{DM}}h^2$, is then obtained from the asymptotic solution of (2.14), i.e. $Y(x_0) =$

$Y(\infty)$, and

$$\Omega_{\text{DM}} h^2 = \frac{\rho_{\text{DM}}^0 h^2}{\rho_c^0} = \frac{m_\chi s_0 Y_0 h^2}{\rho_c^0}. \quad (2.15)$$

We then have, substituting in the values for the entropy density, $s_0 = 2895 \text{ cm}^{-3}$ and the critical density, $\rho_c^0 = 1.054 \times 10^{-5} h^2 \text{ GeV cm}^{-3}$,

$$\Omega_{\text{DM}} h^2 = 2.75 \times 10^8 \left(\frac{m_\chi}{\text{GeV}} \right) Y(\infty). \quad (2.16)$$

Figure 2.1 shows that the asymptotic comoving density $Y(\infty)$ depends sensitively on the timing of particle freeze-out. Since, for $x \gtrsim 1$, the equilibrium density is decaying exponentially, the longer the dark matter particles remain in equilibrium, the smaller the final abundance. Therefore, increasing the annihilation cross section $\langle \sigma v \rangle$, which extends the species thermal contact and delays freeze-out, leads to a suppressed relic abundance.

In fact, we can rewrite (2.14) in terms of the annihilation rate $\Gamma = n_\chi \langle \sigma v \rangle$ [80]:

$$\frac{d \ln Y}{d \ln x} = \frac{\Gamma}{H} \zeta(x) \left[\left(\frac{Y_{\text{eq}}}{Y} \right)^2 - 1 \right], \quad (2.17)$$

to show that the timing of particle freeze-out actually depends on the relative magnitude of the annihilation rate and the expansion rate, H . Decomposing (2.17) as

$$0 = \frac{\Gamma}{H} \zeta(x) \left[\left(\frac{Y_{\text{eq}}}{Y} \right)^2 - 1 \right] d \ln x - d \ln Y, \quad (2.18)$$

it is clear that the ratio Γ/H controls the efficiency with which the comoving density, Y , tracks the equilibrium density, Y_{eq} : for $\Gamma/H \gg 1$ (early times), the first term in (2.18) dominates and Y is driven towards Y_{eq} ; for $\Gamma/H \ll 1$ (late times), the first term is negligible and Y is conserved. These two regimes are illustrated in figure 2.2 where we compare the annihilation rate and expansion rate for the annihilation cross sections used in figure 2.1. As the annihilation rate is enhanced (with increasing $\langle \sigma v \rangle$), particle freeze-out, which very roughly occurs when $\Gamma \sim \mathcal{O}(H)$, is delayed.

Significantly, equation (2.17) (together with figure 2.2) demonstrates that freeze-out can also be affected if the expansion rate, H , is modified. Specifically, a faster (slower) expansion rate at the time of dark matter decoupling would accelerate (delay) particle freeze-out and therefore enhance (suppress) the dark matter relic abundance. This behaviour is what has motivated the present investigation and will be further explored in the following chapters.

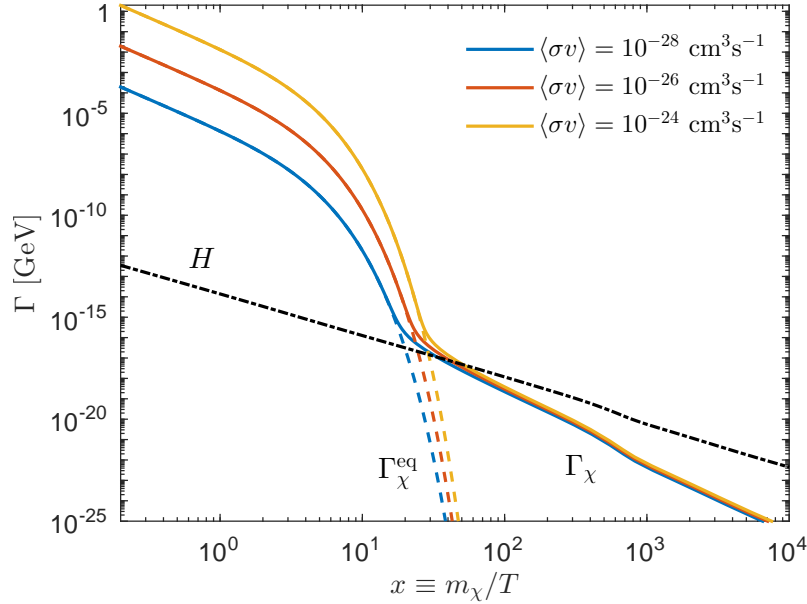


FIGURE 2.2: Annihilation rate Γ_χ for varying annihilation cross section $\langle\sigma v\rangle$ as a function of $x \equiv m_\chi/T$. The solid curves give the evolution of the actual annihilation rate $\Gamma_\chi = n_\chi\langle\sigma v\rangle$ whereas the dashed curves show the corresponding equilibrium annihilation rates $\Gamma_\chi^{\text{eq}} = n_\chi^{\text{eq}}\langle\sigma v\rangle$. The black dashed-dot line represents the expansion rate of the universe.

2.2.2 Approximate solution

The Boltzmann equation (2.14) is a particular form of the Riccati equation for which there are no closed form solutions. However, once the dark matter particles have decoupled from the thermal background and Y begins to deviate significantly from Y_{eq} , the contribution to (2.14) from the creation term is negligible and the Boltzmann equation greatly simplifies. In fact, in this regime it is possible to integrate (2.14) directly and find an approximate expression for the asymptotic comoving density $Y(\infty)$ in terms of the freeze-out point. To this end, we follow the procedure detailed in [123] (see also [80, 199] as well as [170, 204–206] for updated treatments), where the evolution of the dark matter density is broken into two distinct eras: prior to particle freeze-out (early times); and after freeze-out (late times). These two eras are separated by the freeze-out point, which we denote as $x_f \equiv T_f/m_\chi$, where T_f is the freeze-out temperature.

Before we begin, we rewrite the Boltzmann equation (2.14) as

$$\frac{dY}{dx} = -A(x) [Y^2 - Y_{\text{eq}}^2], \quad (2.19)$$

making sure to keep the coefficient $A(x)$, given by

$$A(x) = \frac{s\langle\sigma v\rangle}{xH}, \quad (2.20)$$

as general as possible. This allows us to incorporate the non-standard Hubble factors that we will encounter in the forthcoming chapters. Note also, that in (2.20) we have neglected the temperature dependence of $g_*(T)$ and set $\zeta(x) = 1$ to allow for an analytic calculation of both the freeze-out point, x_f , and asymptotic comoving density, $Y(\infty)$.

- Early times, $x \lesssim x_f$

Our initial goal is to determine the freeze-out point x_f , or equivalently, the point where the comoving density Y begins to deviate significantly from its equilibrium value Y_{eq} . We therefore introduce the parameter $\Delta \equiv Y - Y_{\text{eq}}$ which measures the deviation of Y from Y_{eq} and whose evolution is governed by (using (2.19))

$$\frac{d\Delta}{dx} = -A(x)\Delta[\Delta + 2Y_{\text{eq}}] - \frac{dY_{\text{eq}}}{dx}. \quad (2.21)$$

For small x , Y closely tracks Y_{eq} and $|\Delta'| \ll Y'_{\text{eq}}$ (where a dash denotes differentiation with respect to x), in which case we have

$$\Delta \simeq -\frac{Y'_{\text{eq}}}{A(x)(\Delta + 2Y_{\text{eq}})}. \quad (2.22)$$

The magnitude of Δ grows with increasing x until around the epoch of decoupling $\Delta \sim \mathcal{O}(Y_{\text{eq}})$. Accordingly, we define the freeze-out point via the condition⁶

$$\Delta(x_f) = cY_{\text{eq}}(x_f), \quad (2.23)$$

where $c \approx 0.6$ is a constant of order unity [123]. Using the expression for the non-relativistic equilibrium density $Y_{\text{eq}} \propto x^{3/2}e^{-x}$, we see that, in general, (2.23) will be a transcendental equation in x_f that can be solved iteratively.

- Late times, $x \gtrsim x_f$

Once the dark matter particles have decoupled, $Y \gg Y_{\text{eq}}$ and the Boltzmann equation (2.19) reduces to

$$\frac{dY}{dx} \simeq -A(x)Y^2, \quad (2.24)$$

which we can integrate from the freeze-out point, x_f , up to the present epoch ($x \rightarrow \infty$) to get

$$\frac{1}{Y(\infty)} - \frac{1}{Y(x_f)} = \int_{x_f}^{\infty} A(x) dx. \quad (2.25)$$

Since the comoving density at freeze-out $Y(x_f)$ is much larger than $Y(\infty)$ (see figure 2.1), we can safely neglect the second term on the left hand side of (2.25),

⁶Since the freeze-out process is not instantaneous (see section 2.2.1), the definition of the freeze-out point x_f is arbitrary. Following our discussion in section 2.2.1, we could have alternatively defined the freeze-out point as the point when the annihilation rate drops below the expansion rate, i.e. $\Gamma_\chi(x_f) \approx H(x_f)$. The definition (2.23) is the one that appears most frequently in the literature.

in which case the asymptotic comoving density is given by

$$\begin{aligned} Y(\infty) &\simeq \left[\int_{x_f}^{\infty} A(x) dx \right]^{-1}, \\ &\simeq \left[\int_{x_f}^{\infty} \frac{s\langle\sigma v\rangle}{xH} dx \right]^{-1}, \end{aligned} \quad (2.26)$$

where we have substituted in the definition (2.20) for $A(x)$. The approximate expression (2.26) shows that $Y(\infty)$ increases with either increasing expansion rate or decreasing annihilation cross section — reinforcing our discussion from the previous section.

To find the approximate solution in the standard radiation dominated cosmological scenario, $H = H_{GR}$, we assume the parameterization $\langle\sigma v\rangle = \sigma_n x^{-n}$, in which case the coefficient $A(x)$ becomes

$$A(x) \simeq \lambda \sigma_n x^{-n-2}, \quad (2.27)$$

where $\lambda = 0.264(g_{*s}/\sqrt{g_{*\rho}})m_\chi M_{\text{Pl}}$ and we have used the expression for the entropy density (B.30), $s \simeq 0.439 g_{*s} m_\chi^3/x^3$. Substituting this into (2.26) gives [80]

$$\begin{aligned} Y_{GR}(\infty) &\simeq \frac{(n+1)x_f^{n+1}}{\lambda \sigma_n}, \\ &\simeq \frac{3.79(n+1)x_f^{n+1}}{(g_{*s}/\sqrt{g_{*\rho}}) m_\chi M_{\text{Pl}} \sigma_n}, \end{aligned} \quad (2.28)$$

where the freeze-out point x_f is

$$x_f = \ln[(2+c)\lambda\sigma_n a c] - \left(n + \frac{1}{2}\right) \ln\{\ln[(2+c)\lambda\sigma_n a c]\}, \quad (2.29)$$

and $a = 0.145(g_\chi/g_{*s})$. In general, the freeze-out point x_f depends logarithmically on the dark matter particle mass and annihilation cross section, with $x_f \approx 23$ for typical values of these parameters (again refer to figure 2.1).

The corresponding dark matter energy density, obtained using (2.16), is

$$\Omega_{\text{DM}} h^2 \simeq \frac{1.04 \times 10^9 (n+1) x_f^{n+1}}{(g_{*s}/\sqrt{g_{*\rho}}) M_{\text{Pl}} \sigma_n}, \quad (2.30)$$

which, if we substitute in $M_{\text{Pl}} = 1.22 \times 10^{19}$ GeV, can be written⁷

$$\Omega_{\text{DM}} h^2 \simeq 0.12 \left(\frac{x_f}{23}\right) \left(\frac{2 \times 10^{-26} \text{ cm}^3 \text{ s}^{-1}}{\sigma_0}\right); \quad \text{for } n = 0, \quad (2.31)$$

⁷We have also set $g_{*s} = g_{*\rho} = 85$.

or

$$\Omega_{\text{DM}} h^2 \simeq 0.12 \left(\frac{x_f}{23} \right)^2 \left(\frac{10^{-24} \text{ cm}^3 \text{ s}^{-1}}{\sigma_1} \right); \quad \text{for } n = 1. \quad (2.32)$$

Immediately we see that the observed relic density $\Omega_{\text{DM}} h^2 \simeq 0.12$ is recovered for a weak scale annihilation cross section of the order $\langle \sigma v \rangle \approx 2 \times 10^{-26} \text{ cm}^3 \text{ s}^{-1}$ for s -wave annihilation and $\langle \sigma v \rangle \approx 10^{-24}/x \text{ cm}^3 \text{ s}^{-1}$ for p -wave annihilation. Additionally, the approximate solution (2.30) shows that the relic abundance of symmetric dark matter is inversely proportional to the dark matter annihilation cross section, $\langle \sigma v \rangle$, and roughly independent of the dark matter particle mass, m_χ (there is actually a logarithmic dependence on m_χ through the factor λ in the freeze-out value x_f).

2.3 Constraints

Solving the Boltzmann equation numerically, we can accurately calculate the annihilation cross section required to produce the observed relic abundance $\Omega_{\text{DM}} h^2 = 0.1188$. The results are shown in figure 2.3 as a function of WIMP mass m_χ and should be compared with the approximations (2.31) and (2.32).⁸ There is a noticeably sharp drop

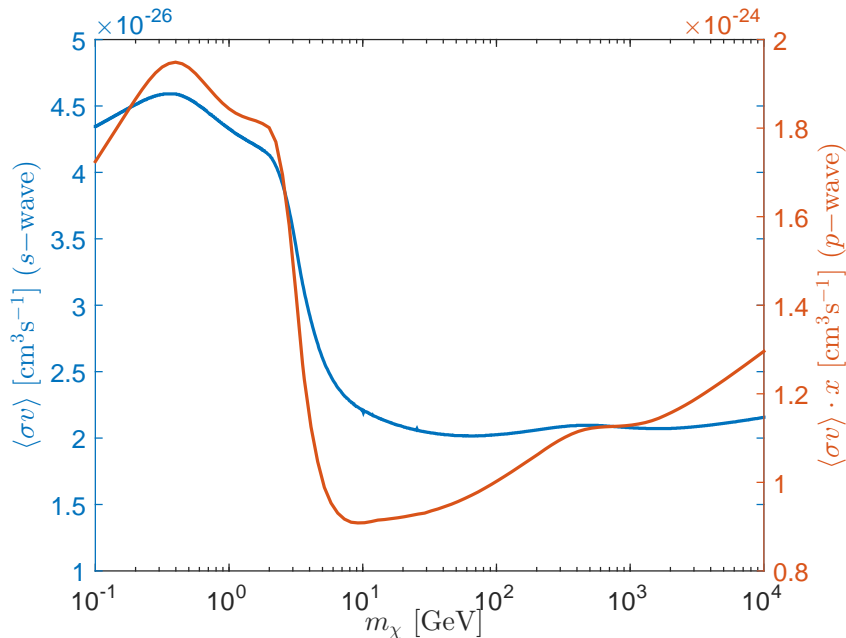


FIGURE 2.3: Required annihilation cross section as a function of WIMP mass in the standard cosmological scenario.

in $\langle \sigma v \rangle$ between $m_\chi = 1 \text{ GeV}$ and $m_\chi = 10 \text{ GeV}$; in both cases (s - and p -wave) there is more than a factor of 2 difference between the maximum and minimum values of the

⁸The same figure appears in Steigman *et al* [170] (for the s -wave case only) which we have used to benchmark our numerical scheme.

required annihilation cross section. This feature is caused by the temperature dependence of $g_*(T)$ which drops by more than an order of magnitude between $T \sim 10^3$ GeV and $T \sim 10^{-5}$ GeV [170]. This is an important effect, particularly for scenarios where the dark matter particles take a long time to freeze-in (see upcoming chapters).

In addition to the relic density observation, data is available from the Fermi Large Area Telescope (Fermi-LAT) which searches for gamma rays from satellite galaxies of the Milky Way, particularly those originating from dark matter annihilations [125] (see section 1.4.6). Depending on the annihilation channel, the gamma ray data can be used to place upper bounds on the dark matter annihilation cross section assuming the dark matter species constitutes all of the dark matter density.

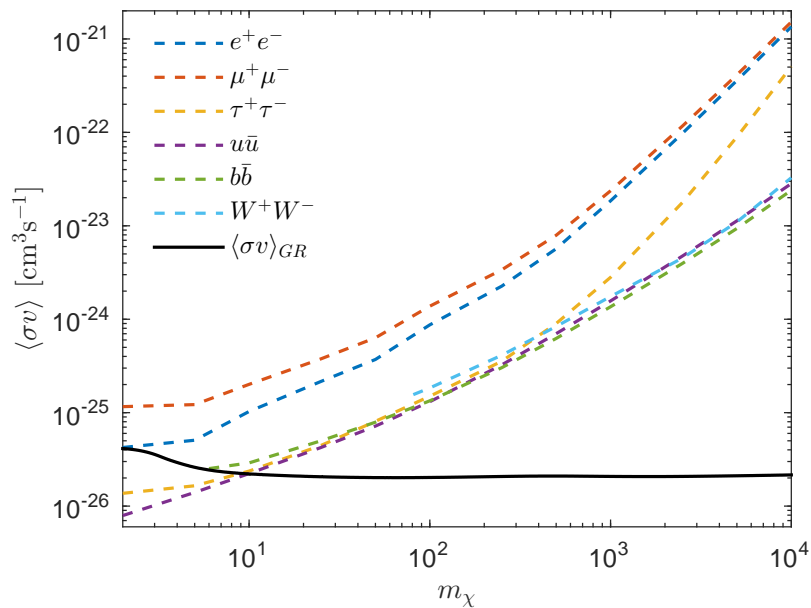


FIGURE 2.4: Required annihilation cross section as a function of WIMP mass in the standard cosmological scenario compared with the Fermi-LAT constraints [125].

In figure 2.4 we superimpose these bounds to show that the Fermi-LAT experiment is beginning to probe the low mass region of the thermal relic framework and can even exclude WIMPs with $m_\chi \lesssim 10$ GeV annihilating wholly into $\tau^+\tau^-$ or $u\bar{u}$ pairs.

2.4 Asymmetric dark matter

2.4.1 Motivation

In the previous section we investigated the relic abundance of a symmetric ($\chi = \bar{\chi}$) dark matter species. However, most fermions are not Majorana particles, so we now consider dark matter models in which $\chi \neq \bar{\chi}$ and there is an asymmetry between the number densities of the particles and antiparticles.

For symmetric dark matter we showed that the present dark matter density is determined by the annihilation cross section $\langle\sigma v\rangle$. In particular, we found that the observed dark matter density, $\Omega_{\text{DM}}h^2 = 0.1188$, is obtained for a weak scale annihilation cross section of the order $10^{-26} \text{ cm}^3\text{s}^{-1}$, with the exact value depending on the WIMP mass (see figure 2.3).

If we were to apply the same formalism to baryonic particles (such as the neutron with its strong interaction cross section, $\langle\sigma v\rangle \sim 10^{-15} \text{ cm}^3\text{s}^{-1}$), we would find the present density of ordinary matter to be negligibly small — in stark contradiction to what is observed. Fortunately, the baryonic sector is rescued by an asymmetry in the number of particles and antiparticles, with the former assumed to be slightly more abundant than the latter;⁹ hence, in the early universe, the particles annihilate away the antiparticle population, and only the excess particles remain. Therefore, the baryonic relic density is fixed by the asymmetry between the particles and antiparticles and is independent of the annihilation cross section.

This is one of the major differences between symmetric and asymmetric matter models, with the relic density determined respectively by the annihilation cross section and asymmetry. We should point out, however, that not all asymmetric models follow this simple blueprint, and that baryonic matter only behaved this way because of its strong interaction cross section and the relatively large asymmetry. In general, the role of the asymmetry actually depends on its magnitude relative to the relic density of the species, such that even within asymmetric models we can speak of two distinct regimes [207]: the *strongly* asymmetric regime, in which the antiparticle population is exponentially suppressed and the relic density is fixed by the asymmetry between particles and antiparticles (as in the baryonic sector); and the *weakly* asymmetric regime, in which the densities of the particle and antiparticle components are comparable and the relic density is determined by the annihilation cross section.

In this section we investigate the relic abundance of asymmetric dark matter and discuss in detail the criteria separating the weakly and strongly asymmetric regimes, and therefore the primary factors that determine the present dark matter density when $\chi \neq \bar{\chi}$.

2.4.2 Boltzmann equation

The Boltzmann equation introduced in section 2.2.1 can be straightforwardly generalized when the particle χ and antiparticle $\bar{\chi}$ are distinct: assuming that self-annihilations are forbidden, and that only interactions of the type $\chi\bar{\chi} \leftrightarrow X\bar{X}$ (where X 's are Standard

⁹The ratio of the observed baryonic and radiation densities suggests that $n_b - n_{\bar{b}} \approx 6 \times 10^{-10} n_\gamma$ where $(n_{\bar{b}})n_b$ and n_γ are the (anti)baryon and photon number densities respectively.

Model particles) can change the particle number, the χ and $\bar{\chi}$ number densities are governed by the coupled system [207] (see also Appendix C)

$$\frac{dn_\chi}{dt} = -3Hn_\chi - \langle\sigma v\rangle (n_\chi n_{\bar{\chi}} - n_\chi^{\text{eq}} n_{\bar{\chi}}^{\text{eq}}), \quad (2.33)$$

$$\frac{dn_{\bar{\chi}}}{dt} = -3Hn_{\bar{\chi}} - \langle\sigma v\rangle (n_\chi n_{\bar{\chi}} - n_\chi^{\text{eq}} n_{\bar{\chi}}^{\text{eq}}), \quad (2.34)$$

where, provided the dark matter particles are non-relativistic at decoupling, the equilibrium densities are given by

$$\begin{aligned} n_\chi^{\text{eq}} &= g_\chi \left(\frac{m_\chi T}{2\pi}\right)^{3/2} e^{(-m_\chi + \mu_\chi)/T}, \\ n_{\bar{\chi}}^{\text{eq}} &= g_\chi \left(\frac{m_\chi T}{2\pi}\right)^{3/2} e^{(-m_\chi - \mu_\chi)/T}. \end{aligned} \quad (2.35)$$

Here g_χ is the number of internal degrees of freedom of $\chi(\bar{\chi})$ and we have used the fact that, in equilibrium, the chemical potentials μ_χ and $\mu_{\bar{\chi}}$ satisfy $\mu_\chi = -\mu_{\bar{\chi}}$. Again we rewrite the system (2.33)-(2.34) in terms of the comoving density $Y_{\chi,\bar{\chi}} \equiv n_{\chi,\bar{\chi}}/s$ and $x \equiv m_\chi/T$:

$$\begin{aligned} \frac{dY_\chi}{dx} &= -\frac{s\langle\sigma v\rangle}{xH} \zeta(x) (Y_\chi Y_{\bar{\chi}} - Y_\chi^{\text{eq}} Y_{\bar{\chi}}^{\text{eq}}), \\ \frac{dY_{\bar{\chi}}}{dx} &= -\frac{s\langle\sigma v\rangle}{xH} \zeta(x) (Y_\chi Y_{\bar{\chi}} - Y_\chi^{\text{eq}} Y_{\bar{\chi}}^{\text{eq}}). \end{aligned} \quad (2.36)$$

Knowing that only interactions of the type $\chi\bar{\chi} \leftrightarrow X\bar{X}$ can change the particle number, we can find a connection between the particle, Y_χ , and antiparticle, $Y_{\bar{\chi}}$, comoving densities using

$$\frac{dY_\chi}{dx} = \frac{dY_{\bar{\chi}}}{dx} \quad \Rightarrow \quad \frac{d}{dx} (Y_\chi - Y_{\bar{\chi}}) = 0, \quad (2.37)$$

which allows us to write

$$Y_\chi - Y_{\bar{\chi}} = C, \quad (2.38)$$

where C is a positive constant that defines the asymmetry between the particles, χ , and antiparticles, $\bar{\chi}$.¹⁰ If the asymmetry in the dark sector is linked to the baryonic asymmetry, we would expect that $n_\chi - n_{\bar{\chi}} \approx n_b - n_{\bar{b}} \approx 6 \times 10^{-10} n_\gamma$, which, using the present entropy density $s \simeq 7.04 n_\gamma$ [18], gives an estimate for the dark sector asymmetry of $C \sim \mathcal{O}(10^{-11})$. Importantly, the relation (2.38) introduces a lower limit to the dark matter relic density, $Y_\chi + Y_{\bar{\chi}} > C$, as discussed in section 2.4.

¹⁰This notation implies that χ is the majority component and $\bar{\chi}$ the minority component.

We can substitute (2.38) into (2.36) to decouple the Boltzmann system and get

$$\begin{aligned}\frac{dY_\chi}{dx} &= -\frac{s\langle\sigma v\rangle}{xH}\zeta(x)(Y_\chi^2 - CY_\chi - P), \\ \frac{dY_{\bar{\chi}}}{dx} &= -\frac{s\langle\sigma v\rangle}{xH}\zeta(x)(Y_{\bar{\chi}}^2 + CY_{\bar{\chi}} - P),\end{aligned}\quad (2.39)$$

where

$$P \equiv Y_\chi^{\text{eq}}Y_{\bar{\chi}}^{\text{eq}} = \left(\frac{0.145 g_\chi}{g_{*s}}\right)^2 x^3 e^{-2x}.\quad (2.40)$$

Combining (2.38) with (2.35) and (2.40) we can eliminate μ_χ and obtain explicit expressions for the equilibrium densities of the χ and $\bar{\chi}$ components,

$$\begin{aligned}Y_\chi^{\text{eq}} &= \frac{C}{2} + \sqrt{\frac{C^2}{4} + P}, \\ Y_{\bar{\chi}}^{\text{eq}} &= -\frac{C}{2} + \sqrt{\frac{C^2}{4} + P}.\end{aligned}\quad (2.41)$$

The dark matter relic abundance, which is now the sum of the χ and $\bar{\chi}$ contributions, is determined by solving (2.39) in the asymptotic limit:

$$\begin{aligned}\Omega_{\text{DM}}h^2 &= \Omega_\chi h^2 + \Omega_{\bar{\chi}} h^2 \\ &= 2.75 \times 10^8 m_\chi [Y_\chi(\infty) + Y_{\bar{\chi}}(\infty)],\end{aligned}\quad (2.42)$$

where $Y_{\chi,\bar{\chi}}(\infty) \equiv Y_{\chi,\bar{\chi}}(x \rightarrow \infty)$. The formalism presented in this section does not reduce simply to the corresponding symmetric formalism in the limit $C \rightarrow 0$, as you might expect. Setting $C = 0$ in (2.38) establishes an equality between the particle and antiparticle number densities, i.e. $Y_\chi = Y_{\bar{\chi}}$ (or equivalently $n_\chi = n_{\bar{\chi}}$) but the particles and anti-particles remain distinct and their contributions to the total relic abundance must be counted separately. Consequently, for equal masses and annihilation cross sections, the relic density of an asymmetric dark matter species is around twice that of its symmetric counterpart.

2.4.3 Density evolution

Before deriving approximate analytic solutions to the system (2.39), we first discuss the evolution of the particle and antiparticle number densities for varying annihilation cross section and asymmetry.

In figure 2.5 we plot the solutions to (2.39) for the χ and $\bar{\chi}$ number densities for varying annihilation cross section (left panel) and asymmetry (right panel). In each case, the early time evolution is the same: both the χ and $\bar{\chi}$ components track their equilibrium values Y_χ^{eq} and $Y_{\bar{\chi}}^{\text{eq}}$ respectively (which for high temperatures are approximately equal,

$Y_\chi^{\text{eq}} \approx Y_{\bar{\chi}}^{\text{eq}} \gg C$) until the interaction rate drops below the expansion rate and the species decouples from the thermal background.

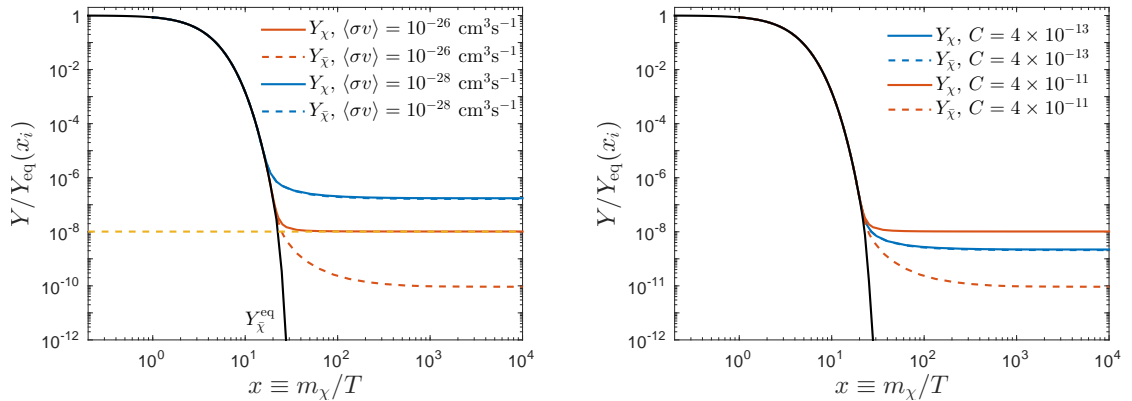


FIGURE 2.5: The evolution of the comoving number densities Y_χ (solid) and $Y_{\bar{\chi}}$ (dashed) as a function of x in the standard scenario. In the left panel we have fixed $C = 4 \times 10^{-11}$ (indicated by the dashed yellow line) and varied the annihilation cross section from $\langle\sigma v\rangle = 10^{-28} \text{ cm}^3\text{s}^{-1}$ (blue) to $\langle\sigma v\rangle = 10^{-26} \text{ cm}^3\text{s}^{-1}$ (red). In the right panel we fix the annihilation cross section at $\langle\sigma v\rangle = 10^{-26} \text{ cm}^3\text{s}^{-1}$ and vary the asymmetry from $C = 4 \times 10^{-13}$ (blue) to $C = 4 \times 10^{-11}$ (red). The results have been calculated for a WIMP with mass $m_\chi = 100 \text{ GeV}$ and $g_\chi = 2$.

The late time behaviour however is quite different, with the relative magnitudes of the (anti)particle asymptotic densities heavily dependent on the values of C and $\langle\sigma v\rangle$. By inspection, we see that when the product of the annihilation cross section and asymmetry is large, the density of the minority component $Y_{\bar{\chi}}(\infty)$ is exponentially suppressed and $Y_\chi(\infty)$ is approximately equal to the asymmetry C , i.e. $Y_\chi(\infty) \approx C \gg Y_{\bar{\chi}}(\infty)$. Conversely, when this product is small, the densities of the χ and $\bar{\chi}$ components are comparable and $Y_\chi(\infty) \approx Y_{\bar{\chi}}(\infty) \gg C$.¹¹ These two cases correspond to the weakly (blue) and strongly (red) asymmetric regimes discussed in the opening to this section.

An interesting feature of figure 2.5 is the post freeze-out evolution of the χ and $\bar{\chi}$ number densities in the strongly asymmetric case: the majority component χ (solid red) rapidly reaches its asymptotic value; whilst $Y_{\bar{\chi}}$ takes several decades to do so. As explained by [173], this is understood by noting that the annihilation rate of the majority component, $\Gamma_\chi = n_{\bar{\chi}}\langle\sigma v\rangle$, is proportional to the number density of the minority component, $n_{\bar{\chi}}$, and the annihilation rate of the minority component, $\Gamma_{\bar{\chi}} = n_\chi\langle\sigma v\rangle$, is proportional to the number density of the majority component, n_χ . Hence, after freeze-out, the particles, χ , struggle to find antiparticles, $\bar{\chi}$, with which to annihilate and Y_χ is rapidly conserved. In contrast, the antiparticles find an abundance of annihilating partners and $Y_{\bar{\chi}}$ continues to decay by several orders of magnitude before settling at its suppressed asymptotic value.

¹¹A more precise definition of what is considered large and small will be given in the next section where we derive approximate solutions to the Boltzmann system (2.39).

2.4.4 Approximate solution

Approximate asymptotic solutions to the coupled system (2.39) can be found by repeating the arguments developed in section 2.2.2 for symmetric dark matter. Recall that once the species has decoupled, the exponentially suppressed creation term, which in the asymmetric case is proportional to P , can be neglected. Therefore, (2.39) reduces to

$$\frac{dY_\chi}{dx} \simeq -A(x) [Y_\chi^2 - CY_\chi], \quad (2.43)$$

$$\frac{dY_{\bar{\chi}}}{dx} \simeq -A(x) [Y_{\bar{\chi}}^2 + CY_{\bar{\chi}}], \quad (2.44)$$

where again

$$A(x) = \frac{s\langle\sigma v\rangle}{xH}. \quad (2.45)$$

Integrating (2.43) and (2.44) directly, we find that the asymptotic densities of the χ and $\bar{\chi}$ components can be approximated by [207]

$$Y_\chi(\infty) \simeq \frac{C}{1 - \exp\{-C/Y_{(s)}(\infty)\}}, \quad (2.46)$$

$$Y_{\bar{\chi}}(\infty) \simeq \frac{C}{\exp\{C/Y_{(s)}(\infty)\} - 1}, \quad (2.47)$$

where $Y_{(s)}(\infty)$ is the asymptotic solution for the symmetric case (2.28) derived in section 2.2.2,¹²

$$Y_{(s)}(\infty) \simeq \left[\int_{x_f}^{\infty} A(x) dx \right]^{-1}. \quad (2.48)$$

The approximate solutions (2.46) and (2.47) reveal that it is the magnitude of the ratio $C/Y_{(s)}(\infty)$ that determines whether the model is either strongly or weakly asymmetric. For large values of this ratio, the contribution from the minority component $Y_{\bar{\chi}}(\infty)$ is exponentially suppressed and the density of the majority component approaches the asymmetry, $Y_\chi(\infty) \simeq C$ (e.g. the red curves in figure 2.5). When $C/Y_{(s)}(\infty)$ is small, the asymmetry C drops out of the expressions (2.46) and (2.47) and the density of the two components is comparable, $Y_\chi(\infty) \simeq Y_{\bar{\chi}}(\infty) \simeq Y_{(s)}(\infty)$ (e.g. the blue curves in figure 2.5). In each of these two limiting regimes, the total relic density (found by combining the approximations (2.47) and (2.46))

$$\Omega_{\text{DM}} h^2 \simeq 2.75 \times 10^8 m_\chi C \coth^{-1} \left(\frac{C}{Y_{(s)}(\infty)} \right), \quad (2.49)$$

¹²It is straightforward to verify that the approximations (2.46) and (2.47) satisfy (2.38).

behaves as

$$\Omega_{\text{DM}} h^2 \simeq \begin{cases} 2.75 \times 10^8 m_\chi C, & C/Y_{(s)}(\infty) \gg 1, \\ 2 \times 2.75 \times 10^8 m_\chi Y_{(s)}(\infty), & C/Y_{(s)}(\infty) \ll 1. \end{cases} \quad (2.50)$$

2.4.5 Constraints

The two limiting cases (2.50) are clearly discernible in figure 2.6, where we plot the iso-abundance contours in the $(\langle\sigma v\rangle, m_{100}C)$ plane, where m_{100} is the WIMP mass in units of 100 GeV, corresponding to the observed relic density $\Omega_{\text{DM}} h^2 = 0.1188$ for s -wave annihilating particles. For small C , the curves are vertical and the iso-abundance

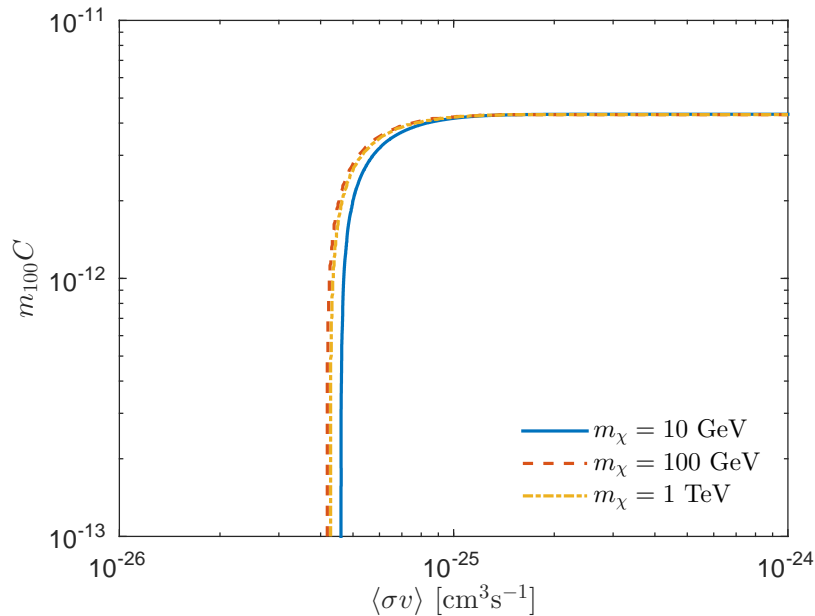


FIGURE 2.6: Iso-abundance contours in the $(\langle\sigma v\rangle, m_{100}C)$ plane for varying WIMP mass m_χ assuming an s -wave annihilation cross section.

contours are independent of the asymmetry. This is the weakly asymmetric regime where $C/Y_{(s)}(\infty) \ll 1$ and the dark matter relic abundance is fixed by the annihilation cross section $\langle\sigma v\rangle$. As the asymmetry increases so does the magnitude of the ratio $C/Y_{(s)}(\infty)$ and the contours transition into a region which is strongly asymmetric; the relic density is now fixed by the asymmetry C and is independent of the annihilation cross section. In this regime the density of the minority component is exponentially suppressed and the dark matter abundance is given by $\Omega_{\text{DM}} \sim C$.¹³

¹³There is also an intermediate region where the abundance depends on both the asymmetry and the annihilation cross section. Here the minority component freezes out shortly after the majority component and their final densities are comparable. For a discussion on each regime and their relation to the freeze-out of the χ and $\bar{\chi}$ components see [173].

The position of the vertical asymptote can be predicted using the numerical results in the previous section (with allowance for an additional factor of two to account for the separate χ and $\bar{\chi}$ contributions) where we found the required annihilation cross section as a function of mass for a symmetric dark matter species. By substituting (2.28) into (2.49) and rearranging for $\langle\sigma v\rangle$, we find that each of the iso-abundance contours is described by the relation,

$$\langle\sigma v\rangle \approx A \times 10^{-35} \frac{1}{m_\chi C} \coth^{-1} \left(\frac{\omega}{C} \right), \quad (2.51)$$

where $\omega = \Omega_{\text{DM}} h^2 / (2.75 \times 10^8 m_\chi)$, and the coefficient A varies between 1.8 and 2 as m_χ is reduced from 1000 GeV down to 10 GeV. The upper bound on the asymmetry C is $m_{100} C = 4.32 \times 10^{-12}$.

In general, if the asymptotic density for symmetric dark matter can be written

$$Y_{(s)}(\infty) \simeq \frac{\beta}{\sigma_n}, \quad (2.52)$$

the required annihilation cross section in the asymmetric case is

$$\sigma_n \simeq \frac{2\beta}{C} \coth^{-1} \left(\frac{\omega}{C} \right). \quad (2.53)$$

2.4.6 Asymmetric detection signal

It is commonly assumed that the annihilation rate of asymmetric dark matter, $\Gamma_{(a)}$, is exponentially damped due to the suppressed abundance of the minority component $\bar{\chi}$ and is therefore incapable of producing a detectable signal over the astrophysical background. Despite the significant dark matter population, the particles cannot find antiparticles with which to annihilate. However, as we showed in the previous sections, the relative abundance of the minority component may not be suppressed, and could in fact be appreciable, i.e. in the *weakly* asymmetric regime, indicating that a nominally asymmetric model could produce a detectable signal.

To compare the expected detection signals in the symmetric and asymmetric cases we first write the annihilation rate of symmetric dark matter in the standard scenario [173],

$$\Gamma_{(s)} = \frac{1}{2} \langle\sigma_s v\rangle \left(\frac{\rho_{\text{DM}}}{m_\chi} \right)^2, \quad (2.54)$$

where we now use $\langle\sigma_s v\rangle$ to denote the self annihilation cross section of the self-conjugate particles $\chi = \bar{\chi}$ which we distinguish from the annihilation cross section of the asymmetric ($\chi \neq \bar{\chi}$) particles, denoted here as $\langle\sigma v\rangle$. Additionally, ρ_{DM} is the dark matter

energy density, $\rho_{\text{DM}} = \Omega_{\text{DM}}\rho_{\text{crit}}$ (where ρ_{crit} is the critical density), and the factor of $1/2$ is necessary since the annihilating particles are identical.

When the dark matter particle and antiparticle are distinct, the annihilation rate (2.54) becomes

$$\Gamma_{(a)} = \langle\sigma v\rangle \frac{\rho_\chi \rho_{\bar{\chi}}}{m_\chi^2} = \langle\sigma v\rangle \left(\frac{\rho_{\text{DM}}}{m_\chi}\right)^2 \frac{Y_\chi Y_{\bar{\chi}}}{(Y_\chi + Y_{\bar{\chi}})^2}, \quad (2.55)$$

where $\Gamma_{(a)}$ denotes the annihilation rate for an asymmetric dark matter species. Comparing this expression to that for the symmetric case (2.54),

$$\frac{\Gamma_{(a)}}{\Gamma_{(s)}} = \frac{\langle\sigma v\rangle}{\langle\sigma_s v\rangle} \frac{2Y_\chi Y_{\bar{\chi}}}{(Y_\chi + Y_{\bar{\chi}})^2} \quad (2.56)$$

we see that the asymmetric annihilation rate picks up a damping factor γ :

$$\gamma \equiv \frac{2Y_\chi Y_{\bar{\chi}}}{(Y_\chi + Y_{\bar{\chi}})^2}, \quad (2.57)$$

induced by the asymmetry between the particles and antiparticles. Since the asymmetric annihilation cross section $\langle\sigma v\rangle$ is typically twice that of the symmetric one, then, for the trivial case, $C = 0$, the damping factor $\gamma = 1/2$ and the ratio of the asymmetric and symmetric annihilation rates (2.56) is $\Gamma_{(a)}/\Gamma_{(s)} \simeq 1$. This extreme example of *weakly* asymmetric dark matter demonstrates that the two annihilation rates can indeed be comparable.

Interestingly, once the relic density $\Omega_{\text{DM}}h^2$ has been specified, the damping factor γ can be expressed explicitly in terms of the asymmetry, C ;

$$\gamma = \frac{\omega^2 - C^2}{2\omega^2}, \quad (2.58)$$

where $\omega = \Omega_{\text{DM}}h^2/(2.75 \times 10^8 m_\chi)$. The magnitude of this factor has been plotted in figure 2.7 for different dark matter densities, showing that for small C , $\gamma \simeq 1/2$ before rapidly dropping to 0 at $C = \omega$. Importantly, for the observed dark matter density $\Omega_{\text{DM}}h^2 = 0.1188$ (solid blue curve), the damping factor $\gamma \sim \mathcal{O}(10^{-1})$ for $m_{100}C \lesssim 4 \times 10^{-12}$, and is therefore sufficiently large for a wide range of asymmetries.

In the following chapters, we will find that the annihilation cross section required to produce the observed dark matter density in non-standard cosmological scenarios is enhanced with respect to the weak scale cross section required in the standard cosmology. In this instance the modified annihilation cross section could easily compensate for the damping factor γ and even produce an enhanced asymmetric detection signal with respect to the symmetric signal in the standard scenario [173]. The details depend on

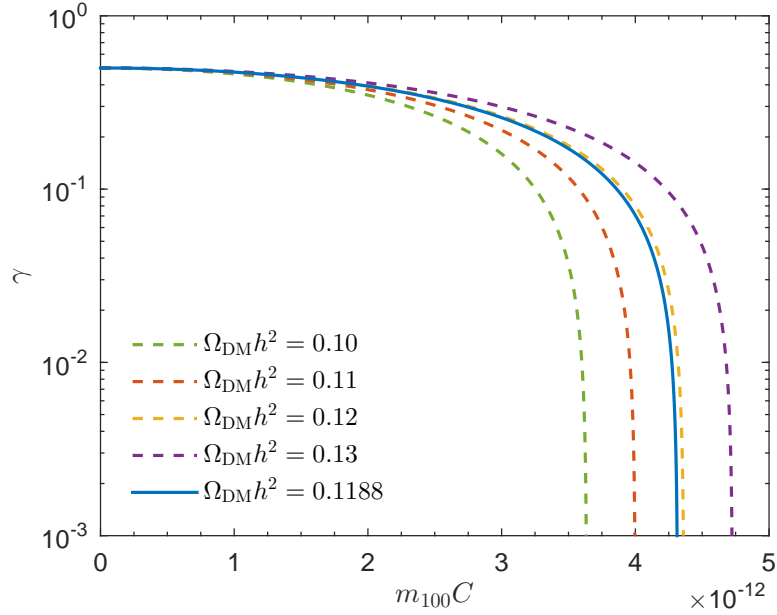


FIGURE 2.7: The asymmetric damping factor defined in (2.58) as a function of $m_{100}C$ where m_{100} is the dark matter mass in units of 100 GeV and C is the dark matter asymmetry.

the particular cosmological model so we therefore defer this discussion to the upcoming chapters.

Finally, we should compare the asymmetric detection signal to the annihilation rate inferred from the Fermi-LAT dataset. Using the same assumptions as the Fermi experiment, the predicted asymmetric detection signal will satisfy the Fermi bound if [173]

$$\frac{\Gamma_{(a)}}{\Gamma_{\text{Fermi}}} = \frac{\langle\sigma v\rangle}{\langle\sigma v\rangle_{\text{Fermi}}} \frac{2Y_{\chi}Y_{\bar{\chi}}}{(Y_{\chi}^2 + Y_{\bar{\chi}}^2)} < 1, \quad (2.59)$$

or, if

$$\gamma\langle\sigma v\rangle < \langle\sigma v\rangle_{\text{Fermi}}. \quad (2.60)$$

2.5 Summary

In this chapter we examined the thermal relic scenario, in which the dark matter particles are thermally produced in the early universe, thereby providing a natural framework for the origin of dark matter. Within this framework, the number density of a symmetric dark matter species can be modelled by a simple Boltzmann rate equation (2.6) whose primary inputs are the dark matter annihilation cross section, $\langle\sigma v\rangle$, and the expansion rate, H . The present dark matter density, which is determined by solving (2.6) in the limit $x \rightarrow \infty$, then depends sensitively on the relative magnitudes of these two parameters. In particular, in the standard cosmological scenario, in which the universe

is radiation dominated at the time of dark matter decoupling with $H \sim T^2$, the observed dark matter density, $\Omega_{\text{DM}}h^2 = 0.1188$, is recovered for a weak scale (s -wave) annihilation cross section of the order $\langle\sigma v\rangle \approx 2 \times 10^{-26} \text{ cm}^3\text{s}^{-1}$ — the so-called WIMP miracle.

More generally, for an enhanced expansion rate or reduced annihilation cross section, the dark matter relic abundance is enhanced. Whereas for a slower expansion rate or larger annihilation cross section, the relic abundance is suppressed. By approximating the asymptotic behaviour of the Boltzmann equation (2.6) we were able to derive an analytical solution for the present dark matter density in a general cosmological setting.

In section 2.4 we generalized these results to asymmetric dark matter models which introduce a new 'asymmetry parameter' C , characterizing the excess in the number of particles over antiparticles in a comoving volume. While it is generally thought that the present antiparticle population is negligible, and that the relic density in asymmetric models is determined by the asymmetry parameter, in some cases the annihilation cross section, $\langle\sigma v\rangle$, can play a significant role and the asymmetric dark matter models can behave like symmetric dark matter in this sense. As an extension of this result, we also highlighted the potential of asymmetric dark matter models to produce an amplified detection signal in non-standard cosmological scenarios compared to the symmetric signal in the standard cosmology.

In the next chapter we will apply the formalism and concepts developed here to a simple extension of the standard cosmological model in which the cosmological constant is replaced by a non-interacting scalar field and use this simple model to highlight some of the generic features common to other non-standard cosmologies.

Chapter 3

Quintessence Dark Energy Models

3.1 Introduction

In the previous chapter we discussed the decoupling of dark matter in the early universe and introduced the formalism necessary to calculate the dark matter relic abundance today. In doing so we showed that the timing of particle decoupling, which roughly occurs when the dark matter annihilation rate drops below the expansion rate of the universe, determines the present dark matter density. In this, and the following chapters, we investigate the relic abundance of dark matter in non-standard cosmological scenarios that predict a modified expansion rate at early times, and use the observed dark matter density to constrain any deviations from the standard expansion history.

As a first example, we consider the simplest extension of the standard cosmological model, so-called quintessence models, where the cosmological constant Λ is replaced by a non-interacting, spatially homogeneous scalar field, $\phi(t)$. The total action of the system is

$$S_{\text{tot}} = \int_{\mathcal{M}} d^4x \sqrt{-g} L_{\text{tot}} \quad (3.1)$$

where

$$L_{\text{tot}} = L_{\text{EH}} + L_{\phi} + L_{\text{mat}}. \quad (3.2)$$

Here g is the determinant of the metric tensor $g_{\mu\nu}$ and the integral is taken over the four dimensional spacetime manifold \mathcal{M} . The Einstein-Hilbert Lagrangian $L_{\text{EH}} = R/2\kappa^2$, where R is the Ricci scalar and $\kappa^2 = 8\pi G$, generates the standard Einstein field equations

of General Relativity (see Appendix D), the scalar field Lagrangian is

$$L_\phi = -\frac{1}{2}g^{\mu\nu}\partial_\mu\phi\partial_\nu\phi - V(\phi), \quad (3.3)$$

where $-\frac{1}{2}g^{\mu\nu}\partial_\mu\phi\partial_\nu\phi$ and $V(\phi)$ correspond to the kinetic and potential energies respectively of the scalar field, and the Standard Model matter fields, Ψ_m , are incorporated through $L_{\text{mat}} \equiv L_{\text{mat}}[g_{\mu\nu}, \Psi_m]$.

Provided the potential energy dominates over the kinetic energy (i.e. the field is slow-rolling), the quintessence field can mimic the behaviour of a cosmological constant in the present epoch and successfully reproduce the predictions of the standard cosmological model. Interestingly, the early time evolution of the field is far less constrained, and it is possible that ϕ could undergo a period of *kination domination*, where the kinetic energy dominates over the potential energy and the energy density of the field scales as $\rho_\phi \sim a^{-6}$ (see next section). In this case, the quintessence field would dominate the energy budget of the universe at sufficiently early times, thereby enhancing the expansion rate with respect to the standard scenario.¹

Previously we showed that if the expansion rate of the universe is enhanced during the era of dark matter decoupling, particle freeze-out is accelerated and the dark matter relic abundance is enhanced. In the kination scenario, the early time expansion rate can be several orders of magnitude larger than the standard expansion rate, which, as first pointed out by Salati [142], following a suggestion by Joyce [141, 213–215], and Rosati [167], can have dramatic implications for the predicted relic abundance. In particular, Salati [142] was able to derive an approximate analytical solution for the Boltzmann equation by parameterizing the quintessence contribution to the total energy density through the *kination parameter* η_ϕ , which he defines as the ratio of the quintessence and photon energy densities evaluated at the time of Big Bang Nucleosynthesis (see below). Using this result he estimated that the dark matter relic density in the kination scenario is enhanced by up to $\sim 10\sqrt{\eta_\phi}m_\chi$, which can amount to $\mathcal{O}(10^3 - 10^4)$ for typical values of η_ϕ and m_χ .

Subsequent investigations by Profumo and Ullio [168] and Pallis *et al* [157, 216–218] gave more detailed treatments, introducing additional parameters to model the quintessence field contribution, and arrived at similar conclusions. Furthermore, both groups concluded that a single parameter (similar to the η_ϕ defined by Salati [142]) is sufficient to model the kination effects. These papers are also amongst several others [169, 219–223] that have considered the implications for specific dark matter particle models.

¹For further background on quintessence models of dark energy see [34, 35, 38, 39, 208–212] as well as the recent review [37].

In [224], Guo and Zhang adopted a model-independent approach, assuming the thermally averaged annihilation cross section could be approximated by $\langle\sigma v\rangle = \sigma_0$, and used the observed dark matter density to constrain the dark matter annihilation cross section in the kination scenario. They found that $\langle\sigma v\rangle$ can be enhanced by up to several orders of magnitude (depending on the WIMP mass) and suggested that these results could help to explain the rising positron fraction measured by the PAMELA [95, 112] experiment.

More recently, Gelmini *et al* [173] and Iminniyaz and Chen [225] studied the kination effects on asymmetric dark matter models and found an analogous enhancement for the particle and antiparticle abundances and, equivalently, the required annihilation cross section. Notably, Gelmini *et al* [173] realized that the enhanced annihilation cross section required to explain the observed dark matter density can compensate for the (typically) suppressed abundance of the minority dark matter component, so that, contrary to general belief, the annihilation rate of asymmetric dark matter in the kination scenario could exceed that of symmetric dark matter in the standard cosmology. This effect, which was demonstrated for both kination and scalar-tensor models, will be discussed in more detail below.

In the next section we introduce a simple kination domination scenario, whose deviation from the standard cosmology is parameterized by a single number, the so-called *kination parameter*, η_ϕ , as done in the original paper by Salati [142]. Then, in section 3.3, we numerically calculate the relic density enhancement factor for a symmetric dark matter species in the kination scenario and compare our findings to both existing results and the approximate formulas given in [142], which we re-derive using the formalism developed in the previous chapter. We also use the latest observational value for the dark matter energy density, $\Omega_{\text{DM}}h^2 = 0.1188 \pm 0.0010$, to constrain the thermally averaged annihilation cross section, $\langle\sigma v\rangle$, for varying η_ϕ for both *s*-wave and *p*-wave dominated processes and compare our results to those presented in [224]. Finally, we repeat this exercise for asymmetric dark matter models in section 3.4, highlighting the potentially enhanced detection signal of asymmetric dark matter, before summarizing our results in section 3.5.

3.2 Kination

In this section we investigate how the expansion rate of the universe is modified in the presence of a quintessence field undergoing a period of kination domination. To do so, we need to determine the energy density of the quintessence field, ρ_ϕ , and how it evolves with time.

The energy density, ρ_ϕ , and pressure, p_ϕ , of the quintessence field can be obtained by first writing the energy momentum tensor of ϕ (see Appendix D for details),

$$\begin{aligned} T_{\mu\nu}^\phi &= -\frac{2}{\sqrt{-g}} \frac{\delta(\sqrt{-g}L_\phi)}{\delta g^{\mu\nu}}, \\ &= \partial_\mu\phi\partial_\nu\phi - g_{\mu\nu} \left[\frac{1}{2}g^{\alpha\beta}\partial_\alpha\phi\partial_\beta\phi + V(\phi) \right] \end{aligned} \quad (3.4)$$

in the perfect fluid form, $T_{\mu\nu}^\phi = (\rho_\phi + p_\phi)u_\mu^\phi u_\nu^\phi + p_\phi g^{\mu\nu}$, where u_μ^ϕ is the corresponding four velocity. We then have, assuming a homogeneous field $\phi \equiv \phi(t)$,

$$\begin{aligned} \rho_\phi &= \frac{1}{2}\dot{\phi}^2 + V(\phi), \\ p_\phi &= \frac{1}{2}\dot{\phi}^2 - V(\phi). \end{aligned} \quad (3.5)$$

The scaling of the scalar field energy density ρ_ϕ can be determined from the quintessence field continuity equation

$$\dot{\rho}_\phi + 3H(\rho_\phi + p_\phi) = 0, \quad (3.6)$$

which is derived from the equation of motion (see Appendix D),

$$\ddot{\phi} + 3H\dot{\phi} + \frac{\partial V}{\partial\phi} = 0, \quad (3.7)$$

and the expressions for ρ_ϕ and p_ϕ given in (3.5).

We can rewrite the continuity equation as

$$\dot{\rho}_\phi + 3H\rho_\phi(1 + w_\phi) = 0, \quad (3.8)$$

where

$$w_\phi \equiv \frac{p_\phi}{\rho_\phi} = \frac{\dot{\phi}^2/2 - V(\phi)}{\dot{\phi}^2/2 + V(\phi)}. \quad (3.9)$$

The equation of state parameter, w_ϕ , varies between $-1 \leq w_\phi \leq 1$, with the upper and lower limits realized when $\dot{\phi}^2 \ll 2V$ and $\dot{\phi}^2 \gg 2V$, respectively. The first case ($w_\phi = -1$) is the cosmological constant behaviour desired at late times whereas the second case ($w_\phi = 1$) is the kination phase described in the introduction. From (3.8), for $w_\phi = 1$, we see that $\rho_\phi \propto a^{-6}$ during the kination phase.

Quintessence models of dark energy can be separated into two distinct classes known as *thawing* and *freezing* models respectively. In the thawing class, the field has been frozen by Hubble damping at a value displaced from its minimum until recently, when it starts to roll towards the minimum. In freezing models the field was already rolling down towards the minimum but slows considerably as the gradient of the potential flattens

out. For these cases, which are realized for different types of potential $V(\phi)$, the equation of state parameter, w_ϕ , is evolving away from and towards $w_\phi \approx -1$ respectively.

Kination domination, in which the energy density of the quintessence field dominates over the background at early times, belongs to the freezing class of quintessence dark energy models. Kination is difficult to achieve in generic freezing models with inverse power law potentials, $V(\phi) \sim \phi^{-n}$, because the field overshoots the tracking solution and remains frozen at an energy density less than the critical one [142, 167]. However, this problem can be alleviated by considering different self-interaction potentials (such as the potential $V(\phi) \sim \exp(M/\phi)$ introduced by Salati [142]) or models with multiple scalar fields or couplings to matter [167].

Here, rather than attempting to construct specific realizations of a kination domination scenario through specially designed potentials $V(\phi)$, we simply assume that a kination period exists and that the appropriate tracking behaviour is restored in time to produce the desired accelerated expansion today. In this case we need not concern ourselves with the late time dynamics induced by the particular form of the potential function (see for example [226–228]) because we are considering a cosmological setting where the role of $V(\phi)$ is marginalized (i.e. $\rho_\phi \simeq \dot{\phi}^2/2 \gg V(\phi)$).

Adding the extra contribution from the quintessence field ϕ , the early time expansion rate becomes

$$\begin{aligned} H_Q^2 &= \frac{8\pi}{3M_{\text{Pl}}^2} (\rho_r + \rho_\phi) \\ &= H_{GR}^2 \left(1 + \frac{\rho_\phi}{\rho_r} \right), \end{aligned} \quad (3.10)$$

where H_{GR} is the expansion rate in the standard (radiation-dominated) scenario. We can parameterize the scalar field contribution through the *kination parameter* η_ϕ , which we define as the ratio of the scalar field energy density, ρ_ϕ , to that of the background photon energy density, ρ_γ , at the time of Big Bang Nucleosynthesis $T_B = 1 \text{ MeV}$ [142],

$$\eta_\phi \equiv \left. \frac{\rho_\phi}{\rho_\gamma} \right|_{T=T_B} \leq 1 \quad (3.11)$$

where the upper limit is enforced to ensure that the kination period does not disturb the successful predictions of BBN. Inserting (3.11) and the expression for the radiation energy density $\rho_r = \pi^2 g_{*\rho}(T) T^4/30$, into (3.10), we can rewrite the Friedmann equation as

$$H_Q^2 = H_{GR}^2 [1 + Z_Q(T)] \quad (3.12)$$

where²

$$Z_Q \equiv \frac{\rho_\phi}{\rho_r} = \frac{2}{g_{*\rho}(T)} \eta_\phi \left[\frac{g_{*s}(T)}{g_{*s}(T_B)} \right]^2 \left(\frac{T}{T_B} \right)^2. \quad (3.13)$$

Since $Z_Q = \rho_\phi/\rho_\gamma$ grows roughly as T^2 , large deviations from the standard expansion law are possible at early times — even for $\eta_\phi \leq 1$. In fact, taking $\eta_\phi = 1$, corresponding to $\rho_\phi/\rho_\gamma = 1$ at $T = 1$ MeV, leads to a value of $\rho_\phi/\rho_\gamma = 10^6$ at $T = 1$ GeV.

The quintessence contribution to the overall energy density must be cosmologically relevant at the time of dark matter decoupling in order to modify the relic abundance from the canonical result. Thus we require that $Z_Q(T_f) \gtrsim 1$, where T_f is the freeze-out temperature. Substituting this condition into (3.13) and rearranging, we find that the minimum value of η_ϕ relevant to the present discussion is therefore

$$\eta_\phi > \eta_\phi^{\min} \sim 10^{-6}/T_f^2. \quad (3.14)$$

For values less than this lower bound, the standard expansion law is restored prior to dark matter decoupling and the freeze-out process is unaffected.

Importantly, the temperature dependence of $Z_Q(T)$, which grows roughly as T^2 , also implies that the kination effects will be mass dependent, since decoupling occurs at roughly $T_f \approx m_\chi/23$. Therefore, heavier mass particles, that freeze-out at higher temperatures, will experience greater deviations from the standard expansion history during the decoupling process. Using $T_f \approx m_\chi/23$, we can then rewrite (3.14) as

$$\eta_\phi > \eta_\phi^{\min} \sim 10^{-4}/m_\chi^2. \quad (3.15)$$

This theme will recur for other non-standard cosmologies, where the decoupling effects are amplified as the dark matter mass is increased, and is a consequence of the mass dependence of the freeze-out temperature. This should be compared with the standard cosmology result where the relic abundance is roughly independent of mass.

²In deriving (3.13) we have used the relationship (B.34) between the scale factor a and temperature T ,

$$\frac{a}{a_i} = \left[\frac{g_{*s}(T_i)}{g_{*s}(T)} \right]^{1/3} \frac{T_i}{T}$$

where T_i is some reference temperature which, in this case, we have chosen as $T_i = T_B$.

3.3 Symmetric dark matter

In section 2.2.1 we showed that the evolution of the (comoving) symmetric dark matter number density $Y \equiv n_\chi/s$ is governed by the Boltzmann equation (2.14),

$$\frac{dY}{dx} = -\frac{s\langle\sigma v\rangle}{xH}\zeta(x)(Y^2 - Y_{\text{eq}}^2), \quad (3.16)$$

where $\langle\sigma v\rangle$ is the dark matter annihilation cross section, $\zeta(x)$ is a temperature dependent function (2.13) related to the change in the number of degrees of freedom $g_*(T)$, H is the Hubble factor, and the evolution parameter is $x \equiv m_\chi/T$.

Taking $H = H_Q$, where H_Q is the kination expansion rate given in (3.12), we numerically solve the Boltzmann equation for different values of η_ϕ . The results are shown in figures 3.1 and 3.2 for the s - and p -wave cases respectively. In each figure we have chosen the annihilation cross section that reproduces the observed relic density in the standard cosmological scenario, namely, $\langle\sigma v\rangle \approx 2 \times 10^{-26} \text{ cm}^3\text{s}^{-1}$ for s -wave and $\langle\sigma v\rangle \approx 10^{-24}/x \text{ cm}^3\text{s}^{-1}$ for p -wave.

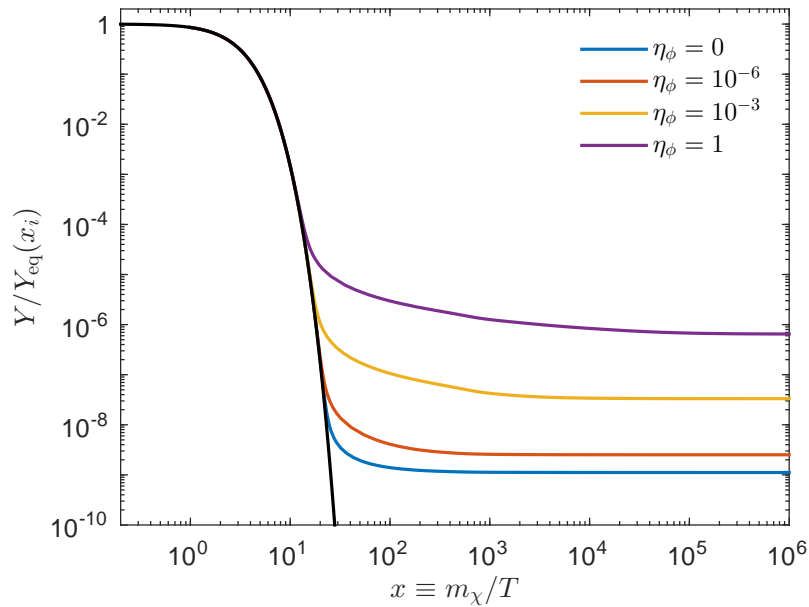


FIGURE 3.1: Evolution of the comoving density Y for varying η_ϕ as a function of $x \equiv m_\chi/T$ for s -wave annihilation. The results have been calculated for a dark matter particle with $m_\chi = 100 \text{ GeV}$, $g_\chi = 2$ and $\langle\sigma v\rangle = 2 \times 10^{-26} \text{ cm}^3\text{s}^{-1}$.

Figures 3.1 and 3.2 show that, as the value of η_ϕ is increased, particle decoupling occurs at successively earlier epochs and the resulting asymptotic density, $Y(\infty)$, is enhanced. Compared to the standard cosmology result, $\eta_\phi = 0$ (blue curve), $Y(\infty)$ for the s -wave case is enhanced by a factor of roughly 2, 30 and 580 for $\eta_\phi = 10^{-6}$, 10^{-3} and 1 respectively. This is due to the enhanced expansion rate in the kination scenario which

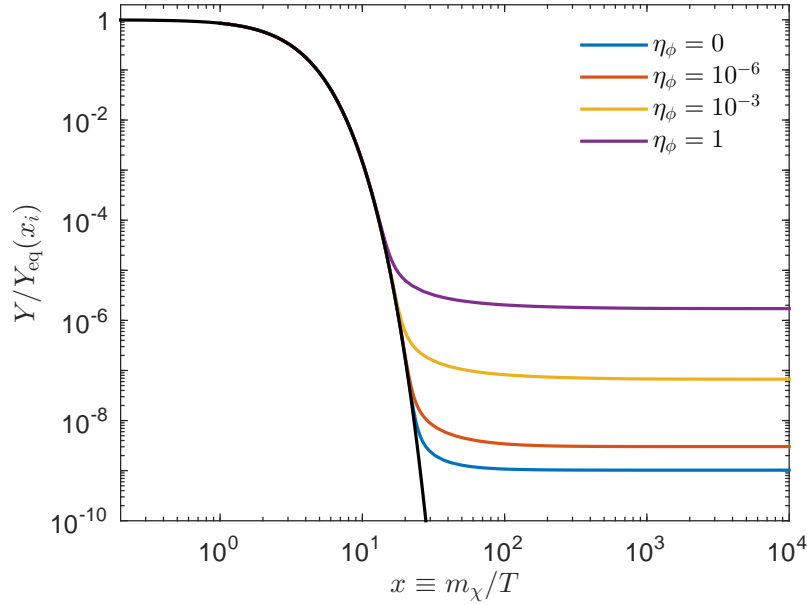


FIGURE 3.2: Same as figure 3.1 but for a p -wave dominated annihilation cross section, $\langle\sigma v\rangle = 10^{-24}/x \text{ cm}^3\text{s}^{-1}$.

increases with increasing η_ϕ . These factors increase to 3, 65 and 1680 for the p -wave case (figure 3.2).

We can estimate the asymptotic comoving density in the kination scenario using the approximate solution to (3.16) derived in section 2.2.2:

$$Y(\infty) \simeq \left[\int_{x_f}^{\infty} \frac{s\langle\sigma v\rangle}{xH} dx \right]^{-1}. \quad (3.17)$$

First, we rewrite the Friedmann equation (3.12) in terms of the dimensionless parameter x ,

$$H_Q^2 = H_{GR}^2 \left[1 + \left(\frac{x_t}{x} \right)^2 \right], \quad (3.18)$$

where x_t can be thought of as the transition point between the kination and standard expansion regimes and is given by³

$$x_t^2 = Z_Q \left(\frac{m_\chi}{T} \right)^2 = \frac{2}{g_{*\rho}(T)} \eta_\phi \left[\frac{g_{*s}(T)}{g_{*s}(T_B)} \right]^2 \frac{m_\chi^2}{T_B^2}. \quad (3.19)$$

Then, substituting (3.18) back into (3.17), along with the expression for the entropy density $s \simeq 0.439 g_{*s} m_\chi^3/x^3$ and the parameterization $\langle\sigma v\rangle = \sigma_n x^{-n}$, we have

$$Y(\infty) \simeq \left[\lambda \sigma_n \int_{x_f}^{\infty} \frac{x^{-n-1}}{\sqrt{x^2 + x_t^2}} dx \right]^{-1}, \quad (3.20)$$

³In Salati's paper [142] the transition point is replaced by the variable α , which is related to x_t via $\alpha = x_t^2$.

where $\lambda \simeq 0.264(g_{*s}/\sqrt{g_{*p}})m_\chi M_{\text{Pl}}$ (see section 2.2.2) is now evaluated at the kination freeze-out point x_f^Q , given by

$$x_f^Q \simeq \ln[(2+c)\lambda\sigma_n ac/x_t] - \left(n - \frac{1}{2}\right) \ln\{\ln[(2+c)\lambda\sigma_n ac/x_t]\}. \quad (3.21)$$

Evaluating (3.20) in the limit $x_t \gg x_f$ (i.e. assuming freeze-out occurs deep in the kination era) we get [142]

$$Y(\infty) \simeq \frac{x_t}{\lambda\sigma_0 \ln(2x_t/x_f^Q)}; \quad n = 0 \text{ (s-wave)}, \quad (3.22)$$

and

$$Y(\infty) \simeq \frac{x_t x_f^Q}{\lambda\sigma_1}; \quad n = 1 \text{ (p-wave)}. \quad (3.23)$$

Using the definition (3.19) of the transition point x_t , we see that the asymptotic comoving density scales roughly as $Y(\infty) \sim \sqrt{\eta_\phi}/\ln(\sqrt{\eta_\phi})$ and $Y(\infty) \sim \sqrt{\eta_\phi}$ for the s - and p -wave cases respectively. Therefore, the relic density grows slightly faster w.r.t η_ϕ in the p -wave case, as confirmed by our numerical results.

From the asymptotic solution of the Boltzmann equation (3.16) we can determine the present dark matter density in the kination scenario using (see section 2.2.1)

$$\Omega_{\text{DM}}^Q h^2 = 2.75 \times 10^8 m_\chi Y(\infty), \quad (3.24)$$

which we compare with the standard cosmology result in figure 3.3 for both the s - (solid) and p - (dashed) wave cases. The results in this figure are in close agreement with those presented in Chung *et al* [219].

For small values of the kination parameter, η_ϕ , the relic abundance in the kination scenario, Ω_{DM}^Q , is equal to the standard result, Ω_{DM}^{GR} . In this region, the kination period has ended and the standard expansion rate has been restored prior to dark matter decoupling, in which case freeze-out is unaffected. As the value of η_ϕ is increased, the quintessence contribution to the expansion rate becomes significant: dark matter decoupling is accelerated and the relic abundance is enhanced. The level of enhancement grows monotonically with increasing η_ϕ , reaching values of $\mathcal{O}(10^3)$ and $\mathcal{O}(10^4)$ in the s - and p -wave cases respectively, for the allowed range of $\eta_\phi \lesssim 1$ and the masses shown, $m_\chi \in \{10, 100, 1000\}$ GeV. Furthermore, the value at which the kination parameter becomes effective matches the estimate given in section 3.2, namely, $\eta_\phi^{\text{min}} \sim 10^{-4}/m_\chi^2$, and is the same for both the s - and p -wave cases.

Significantly, the level of enhancement is mass dependent, as we predicted in the previous section. The relic density of heavier mass particles increases by a greater factor, for fixed

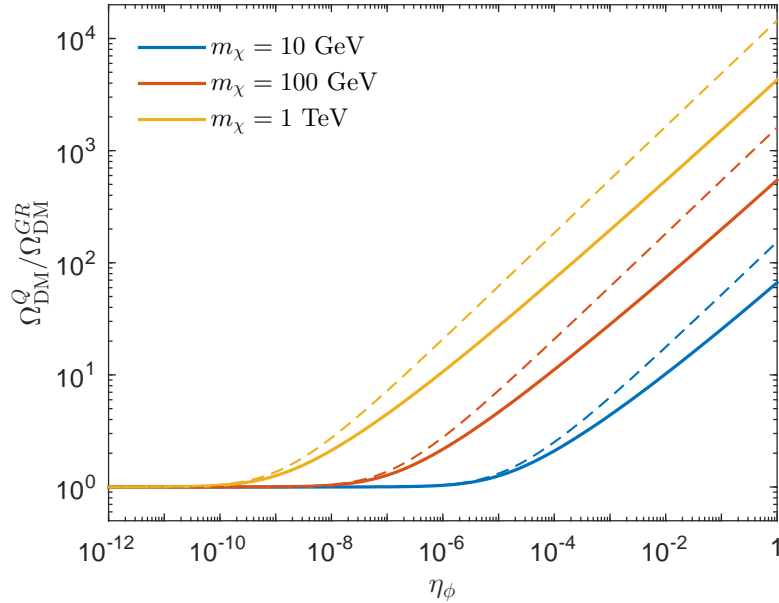


FIGURE 3.3: Ratio of the relic abundance in the kination domination scenario and the corresponding abundance in the standard scenario as a function of η_ϕ for varying WIMP mass. The results have been calculated for both s - (solid) and p -wave (dashed) cases with $\langle\sigma v\rangle = 10^{-25} \text{ cm}^3\text{s}^{-1}$ and $\langle\sigma v\rangle = 10^{-23}/x \text{ cm}^3\text{s}^{-1}$ respectively.

η_ϕ , because these particles freeze-out at higher temperatures when the deviation from the standard expansion law, $Z_Q(T)$, is greater. Therefore, we should be careful when reporting enhancement factors in a given cosmological scenario without reference to the WIMP masses considered, as is often done in the literature.

We can find an analytical estimate for the increase in relic abundance between the kination and standard cosmological scenarios by comparing the approximate solutions (3.22) and (3.23) to the corresponding expressions for the asymptotic density in the standard scenario (2.28). Doing so, we find that the dark matter relic abundance in a kination dominated scenario is boosted by a factor

$$\frac{\Omega_{\text{DM}}^Q}{\Omega_{\text{DM}}^{\text{GR}}} \simeq \frac{x_t}{x_f^{\text{GR}} \ln(2x_t/x_f^Q)}; \quad (s\text{-wave}), \quad (3.25)$$

and

$$\frac{\Omega_{\text{DM}}^Q}{\Omega_{\text{DM}}^{\text{GR}}} \simeq \frac{x_t x_f^Q}{2(x_f^{\text{GR}})^2}; \quad (p\text{-wave}), \quad (3.26)$$

where x_f^{GR} is the freeze-out value in the standard scenario (2.29) and x_f^Q is the freeze-out value in the quintessence model (3.21). These expressions show that the level of enhancement is roughly independent of the annihilation cross section $\langle\sigma v\rangle$ (neglecting the logarithmic dependence in x_f^Q and x_f^{GR}). We have confirmed this assertion numerically by increasing and decreasing the annihilation cross sections used in figure 3.3 by an order

of magnitude, in which case the ratio $\Omega_{\text{DM}}^{\text{Q}}/\Omega_{\text{DM}}^{\text{GR}}$ only changes by 10 – 15%. That said, we emphasize that the expressions (3.25) and (3.26) are only valid if freeze-out occurs deep in the kination dominated expansion era ($x_t \gg x_f$); if the standard expansion rate is restored prior to dark matter decoupling the relic abundance saturates to the standard result.

By approximating the standard and quintessence freeze-out values as $x_f^{\text{GR}} \sim 20$ and $x_f^{\text{Q}} \sim 10$ respectively, we reproduce Salati’s estimate [142], that the enhancement factor varies approximately as $\Omega_{\text{DM}}^{\text{Q}}/\Omega_{\text{DM}}^{\text{GR}} \sim 10\sqrt{\eta_{\phi}}m_{\chi}$ for both the s - and p -wave cases.

In figures 3.4 and 3.5 we compare the approximate expressions (dashed curves with crosses) for the enhancement factor given in (3.25) and (3.26) for the s - and p - wave cases respectively, with the numerical results (solid curves) presented in figure 3.3. We find that there is very good agreement between the approximate and numerical results for $\eta_{\phi} \gtrsim 10^{-3}/m_{\chi}^2$ for s -wave and for $\eta_{\phi} \gtrsim 10^{-1}/m_{\chi}^2$ for p -wave. Below these limits however, the approximate results begin to diverge from the numerical results.

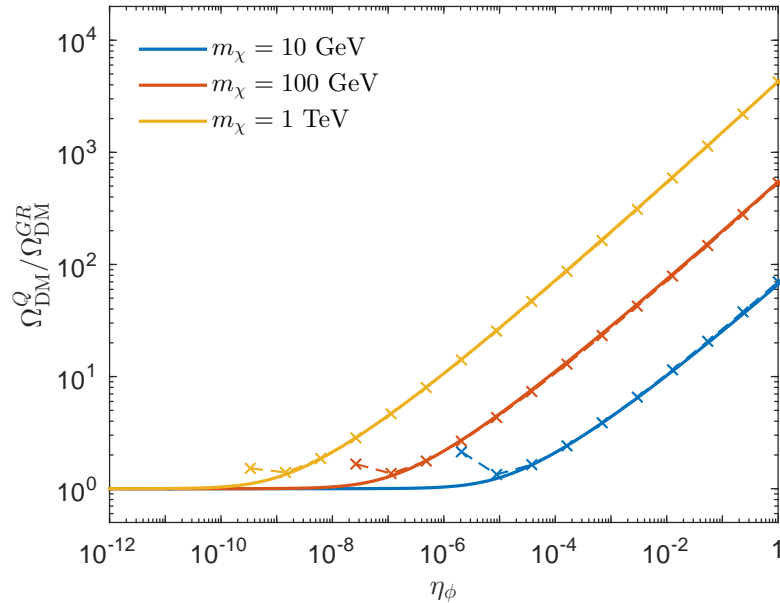
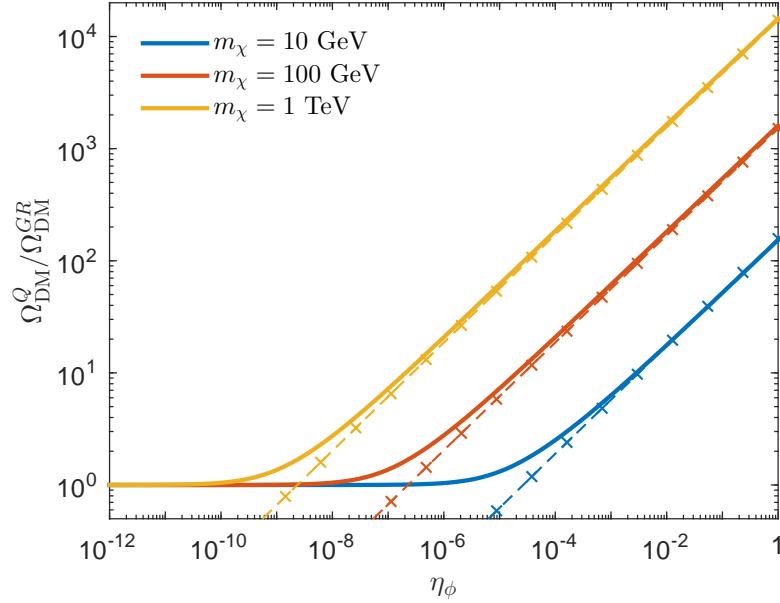


FIGURE 3.4: Comparison of the numerical (solid) and analytical (dashed with crosses) values for the kination enhancement ratio $\Omega_{\text{DM}}^{\text{Q}}/\Omega_{\text{DM}}^{\text{GR}}$ for the s -wave case using the same parameter values as figure 3.3.

In figures 3.6 (s -wave) and 3.7 (p -wave), we use the observed dark matter density, $\Omega_{\text{DM}}h^2 = 0.1188$, to constrain the annihilation cross section $\langle\sigma v\rangle$ as a function of the WIMP mass for varying η_{ϕ} . We have performed the calculation by considering both fixed $g_*(T) = 106.75^4$ (dashed curves), as done in Guo *et al* [224], and by maintaining the full temperature dependence of $g_*(T)$ (solid curves). Furthermore, we have chosen the mass

⁴Recall that we have assumed that $g_{*\rho} = g_{*s} = g_*$.

FIGURE 3.5: Same as figure 3.4 but for p -wave annihilation.

range $m_\chi \in [10^{-1}, 10^4]$ GeV so as to illustrate the effects of varying g_* for small WIMP masses [170] and, also, to utilize the full range of data collected by Fermi-LAT [125] (see figure 3.8).

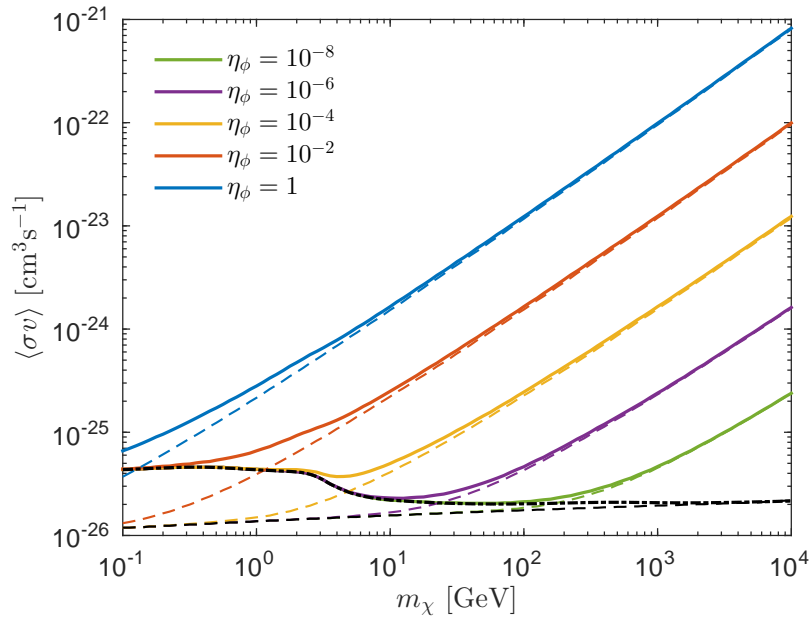
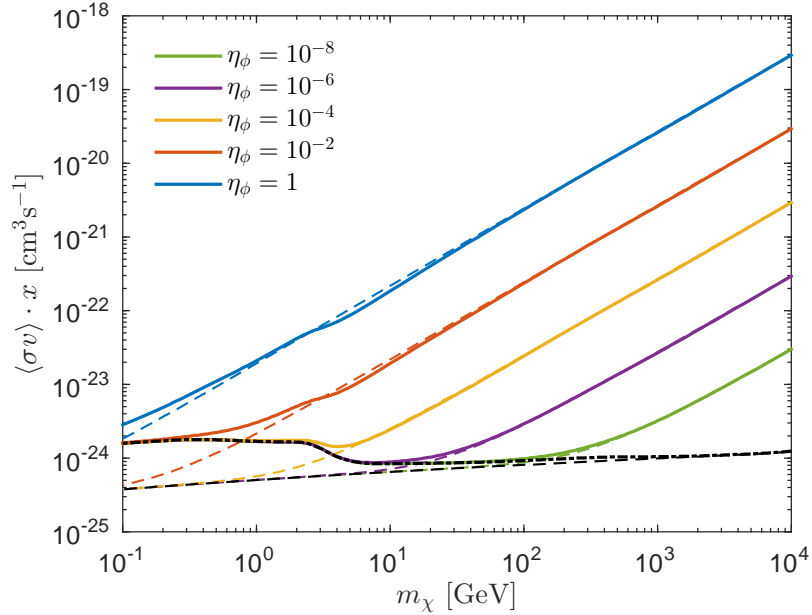


FIGURE 3.6: Required s -wave annihilation cross section in the kination domination scenario as a function of WIMP mass m_χ for varying η_ϕ . The solid and dashed curves correspond respectively to temperature dependent $g_*(T)$ and $g_*(T)$ fixed at 106.75. For reference, we have also included the standard cosmology result for both varying (dot-dashed black curve) and fixed (dashed black curve) $g_*(T)$.

Figures 3.6 and 3.7 show that the required annihilation cross section in the kination scenario can be enhanced by several orders of magnitude w.r.t. the standard results

FIGURE 3.7: Same as figure 3.6 but for p -wave annihilation.

(dot-dashed black curves) derived in the previous chapter. The level of enhancement for the annihilation cross sections, for fixed m_χ and η_ϕ , is roughly the same as we found for the relic density. This is because there is an (almost) inverse relationship between Ω_{DM}^Q and $\langle\sigma v\rangle$.

Using (3.25) and (3.26) we can approximate (to within a few percent) the required annihilation cross section in the regime $x_t \gg x_f$ ($\eta_\phi \gg 10^{-4} m_\chi^{-2}$) by

$$\sigma_0 \simeq 2.75 \times 10^8 \frac{m_\chi x_t}{\lambda \Omega_{\text{DM}} h^2 \ln(2x_t/x_f^Q)} \text{ GeV}^{-2}; \quad s\text{-wave} \quad (3.27)$$

and

$$\sigma_1 \simeq 2.75 \times 10^8 \frac{m_\chi x_t x_f^Q}{\lambda \Omega_{\text{DM}} h^2} \text{ GeV}^{-2}; \quad p\text{-wave}. \quad (3.28)$$

Since the freeze-out point x_f^Q depends on the annihilation cross section σ_n , these expressions must be solved iteratively in order to estimate the required annihilation cross section accurately.

Also, figures 3.6 and 3.7 show that neglecting the temperature dependence of $g_*(T)$ makes little difference for larger WIMP masses, regardless of the value of η_ϕ . However, for WIMP masses $m_\chi \lesssim 10 - 100$ GeV, the results for varying $g_*(T)$ and fixed g_* begin to diverge and the difference can grow to a factor of a few when $m_\chi \sim 0.1$ GeV.

Finally, in figure 3.8, we have imposed the upper limits to the dark matter annihilation cross section derived from the latest Fermi-LAT gamma ray data [125] for the s -wave results calculated in figure 3.6. Interestingly, the Fermi-LAT data is capable of excluding

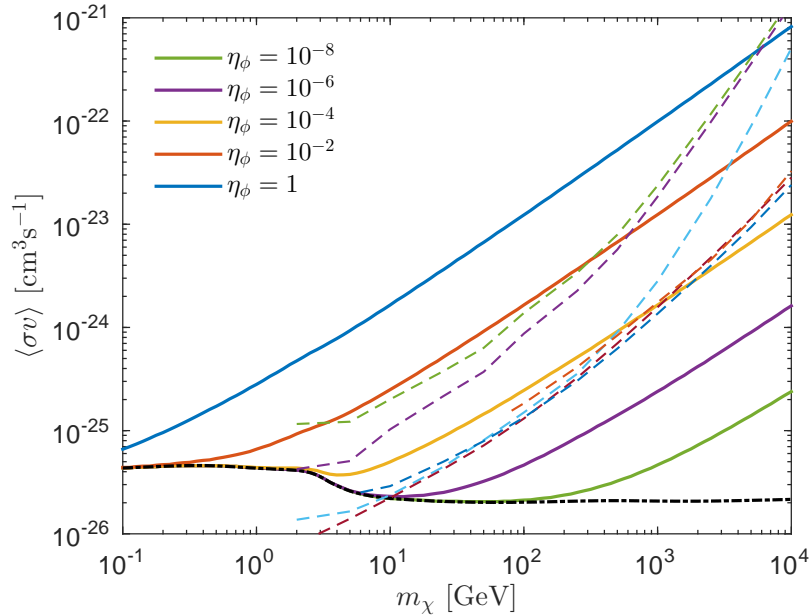


FIGURE 3.8: Required annihilation cross section in the quintessence scenario as a function of WIMP mass for varying η_ϕ . We have also included the standard cosmology result (dashed black) for reference as well as the Fermi-LAT constraints for the e^+e^- (dashed purple), $\mu^+\mu^-$ (dashed green), $\tau^+\tau^-$ (dashed light blue), $u\bar{u}$ (dashed maroon), $b\bar{b}$ (dashed blue) and W^+W^- (dashed red) annihilation channels.

the $\eta_\phi \approx 1$ case for all values of the WIMP mass m_χ , for each of the annihilation channels considered. Also, for a WIMP with $m_\chi \lesssim 1000$ GeV, the $\mu^+\mu^-$ and $b\bar{b}$ constraints exclude values of the kination parameter $\eta_\phi \gtrsim 10^{-2}$ and $\eta_\phi \gtrsim 10^{-4}$ respectively. However, larger values of η_ϕ are acceptable for heavier WIMP masses where the Fermi-LAT constraints are less stringent.⁵

3.4 Asymmetric dark matter

In this section we extend our analysis of the dark matter relic abundance to asymmetric dark matter particles ($\chi \neq \bar{\chi}$) using the Boltzmann equations (3.16) introduced in the previous chapter

$$\begin{aligned} \frac{dY_\chi}{dx} &= -\frac{s\langle\sigma v\rangle}{xH}\zeta(x)(Y_\chi^2 - CY_\chi + P), \\ \frac{dY_{\bar{\chi}}}{dx} &= -\frac{s\langle\sigma v\rangle}{xH}\zeta(x)(Y_{\bar{\chi}}^2 + CY_{\bar{\chi}} + P). \end{aligned} \quad (3.29)$$

Recall that $C \equiv Y_\chi - Y_{\bar{\chi}}$ characterizes the asymmetry between the majority dark matter component χ and the minority component $\bar{\chi}$, $P \equiv Y_\chi^{\text{eq}}Y_{\bar{\chi}}^{\text{eq}} \simeq (0.145g_\chi/g_{*s})^2 x^3 e^{-2x}$ and

⁵It is important to keep in mind that the Fermi-LAT constraints only apply if the dark matter particle annihilates primarily into the annihilation channels considered and can be evaded if other final states are accessible.

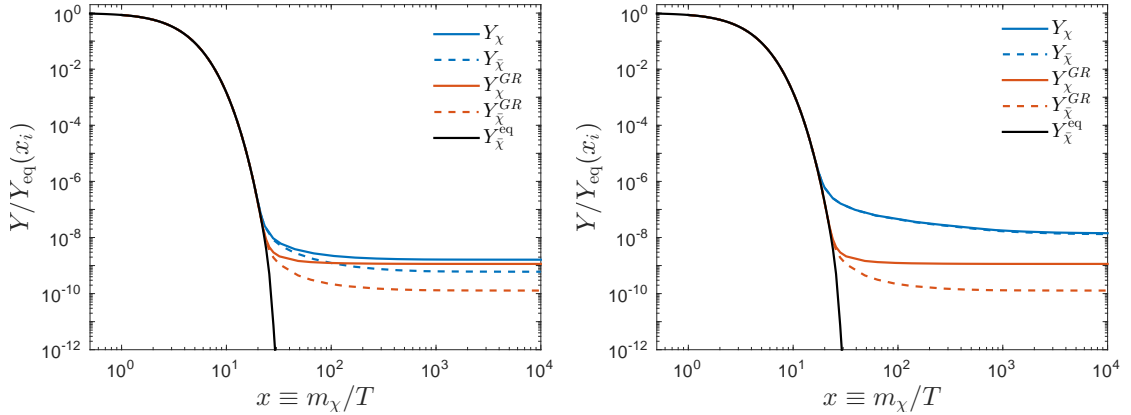


FIGURE 3.9: Evolution of the comoving number densities Y_χ (solid blue) and $Y_{\bar{\chi}}$ (dashed blue) as a function of x in the kination domination scenario with $\eta = 10^{-6}$ (left panel) and $\eta = 10^{-3}$ (right panel). The results have been calculated for an asymmetry $C = 4 \times 10^{-12}$ and a WIMP with mass $m_\chi = 100$ GeV, $g_\chi = 2$ and annihilation cross section $\langle\sigma v\rangle = 5 \times 10^{-26}$ cm³s⁻¹. Shown for reference are the comoving densities of the majority and minority components in the standard cosmology (red curve) as well as the equilibrium density Y_χ^{eq} (black curve).

the total dark matter density is the sum of the χ and $\bar{\chi}$ asymptotic densities

$$\Omega_{\text{DM}} h^2 = 2.75 \times 10^8 m_\chi (Y_\chi(\infty) + Y_{\bar{\chi}}(\infty)). \quad (3.30)$$

We begin by numerically solving the system (3.29) and studying the evolution of the asymmetric number densities in the kination domination scenario. The results are shown in figure 3.9 where we compare the evolution of the χ and $\bar{\chi}$ densities in the kination scenario for $\eta_\phi = 10^{-6}$ (left panel) and $\eta_\phi = 10^{-3}$ (right panel) with their evolution in the standard cosmology.

As a consequence of the enhanced relic density induced by the kination period, the asymmetry between the χ and $\bar{\chi}$ components is effectively ‘washed out’, and, as the value of η_ϕ is increased from $\eta_\phi = 10^{-6}$ to $\eta_\phi = 10^{-3}$, the densities of the two components become (almost) indistinguishable. Hence, increasing η_ϕ , which decreases the ratio $C/Y_{(s)}(\infty)$ for fixed C , drives the model towards the weakly asymmetric regime, where the dark matter relic density is determined by the annihilation cross section and is independent of the asymmetry.

In figures 3.10 (s -wave) and 3.11 (p -wave) we also plot the iso-abundance contours corresponding to $\Omega_{\text{DM}} h^2 = 0.1188$ in the $(\langle\sigma v\rangle, C)$ plane for varying η_ϕ . As the value of η_ϕ is increased, each curve is shifted to the right, towards higher annihilation cross sections (the position of the vertical asymptotes should be compared with the results in figures 3.6 and 3.7 for the s - and p -wave cases respectively). By substituting (3.22) and (3.23) into (2.49) and rearranging for σ_n , we find that in the limit $x_t \gg x_f$, the

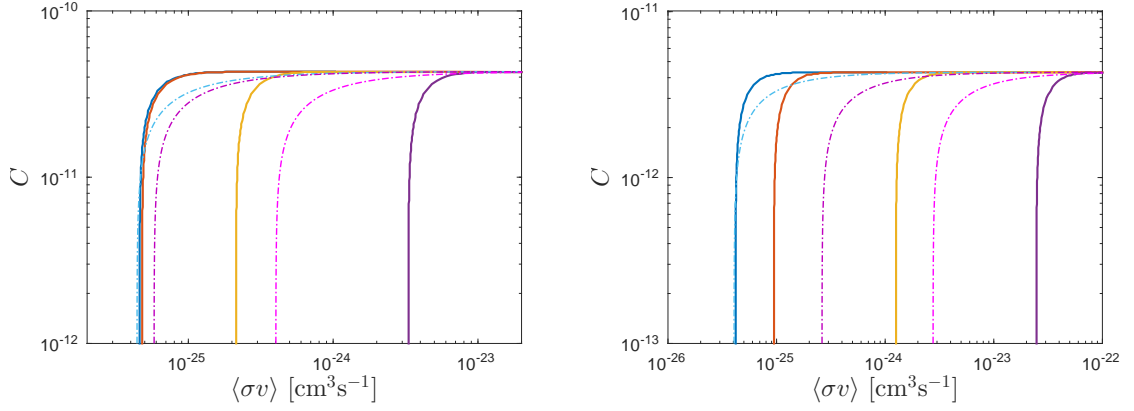


FIGURE 3.10: Iso-abundance contours in the $(\langle\sigma v\rangle, C)$ plane corresponding to the observed dark matter abundance $\Omega_{\text{DM}}h^2 = 0.1188$ for $m_\chi = 10$ GeV (left) and $m_\chi = 100$ GeV (right). The contours shown are for $\eta_\phi = 10^{-6}$ (solid red curve), $\eta_\phi = 10^{-3}$ (solid yellow curve) and $\eta_\phi = 1$ (solid purple curve). Also shown is the standard cosmology result (solid blue curve). We have superimposed the constraints derived from the Fermi-LAT gamma ray data [125] with the regions below the dark purple and magenta (dot-dashed) curves excluded for the $\mu^+\mu^-$ and $b\bar{b}$ annihilation channels respectively. We have also indicated the region (below the dot-dashed blue curve) for which the asymmetric detection signal in the kination domination scenario exceeds the symmetric signal in the standard scenario.

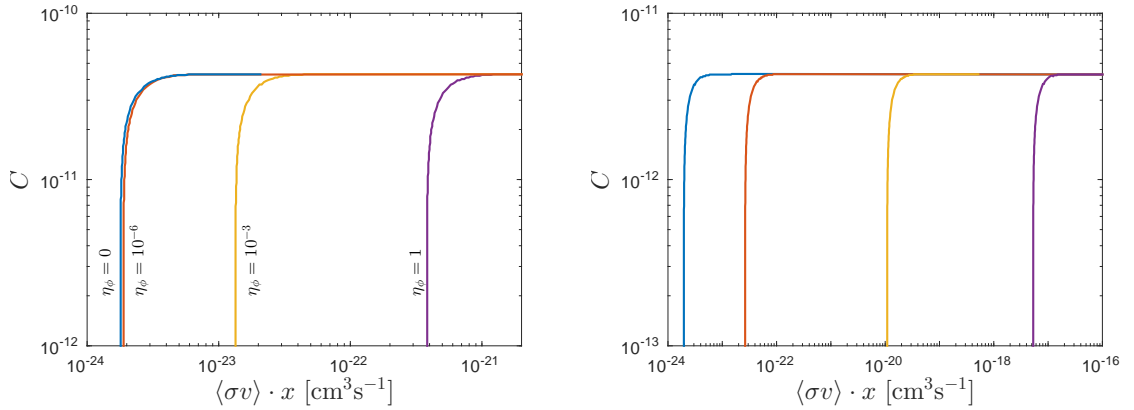


FIGURE 3.11: Same as figure 3.10 but for p -wave annihilation.

iso-abundance contours are described by

$$\sigma_0 \simeq \frac{2x_t}{\lambda C \ln(2x_t/x_f^Q)} \coth^{-1}\left(\frac{\omega}{C}\right); \quad s\text{-wave} \quad (3.31)$$

and

$$\sigma_1 \simeq \frac{2x_t x_f^Q}{\lambda C} \coth^{-1}\left(\frac{\omega}{C}\right); \quad p\text{-wave} \quad (3.32)$$

where $\omega = \Omega_{\text{DM}}h^2/(2.75 \times 10^8 m_\chi)$. These results generally agree with those presented in Iminniyaz and Chen [225]. However, they neglected the temperature dependence of $g_*(T)$ and therefore their results differ by up to a factor of two for small WIMP masses

(i.e. $m_\chi = 100$ MeV), as discussed in section 3.3.⁶

The increased annihilation cross section of the asymmetric dark matter particles in the kination domination scenario gives rise to an interesting prospect pointed out by [173]: the enhanced $\langle\sigma v\rangle$ could potentially compensate for the suppressed density of the minority dark matter component, so that the asymmetric annihilation rate, and in turn the indirect detection signal, may be greater than the corresponding signal for symmetric dark matter in the standard cosmology. Symbolically, if we use Γ_Q and Γ_{GR} to denote the annihilation rates in the quintessence and standard scenarios respectively, it is possible that $\Gamma_Q(\chi \neq \bar{\chi}) > \Gamma_{GR}(\chi = \bar{\chi})$. This condition, which is contrary to the usual expectation that the asymmetric detection signal is negligible, can be realized if

$$\langle\sigma v\rangle_{GR} < \gamma\langle\sigma v\rangle_Q \quad (3.34)$$

where $\langle\sigma v\rangle_{GR}$ is the required annihilation cross section for symmetric dark matter in the standard cosmology and $\langle\sigma v\rangle_Q$ is the annihilation cross section of asymmetric dark matter in the kination scenario. The damping factor $\gamma \leq 1/2$, which arises from the asymmetry between the particles, χ , and antiparticles, $\bar{\chi}$, was derived in section 2.4.6

$$\gamma \equiv \frac{2Y_\chi Y_{\bar{\chi}}}{(Y_\chi + Y_{\bar{\chi}}^2)} = \frac{\omega^2 - C^2}{2\omega^2}. \quad (3.35)$$

We must also ensure that the quintessence annihilation rate satisfies the Fermi-LAT constraints so that the desired region becomes

$$\langle\sigma v\rangle_{GR} < \gamma\langle\sigma v\rangle_Q < \langle\sigma v\rangle_{\text{Fermi}} \quad (3.36)$$

where $\langle\sigma v\rangle_{\text{Fermi}}$ is the upper limit on $\langle\sigma v\rangle$ derived from the Fermi-LAT data. This region, indicated in figure 3.10, lies between the dot-dashed blue and the dot-dashed purple (magenta) curves for the $\mu^+\mu^-$ ($b\bar{b}$) annihilation channels.

3.5 Summary

In this chapter we studied dark matter decoupling in quintessence models of dark energy that undergo a period of kination domination in the early universe. We reproduced

⁶Care should be taken comparing our results to those presented in Imminiyaz [225]. They define the kination parameter as the ratio of the quintessence and *radiation* energy densities (rather than the photon energy density) at a temperature T_0 (different from T_B). To convert between our results (or equivalently Salati's results) and Imminiyaz, we can use

$$\tilde{\eta}_\phi = \frac{2}{g_{*\rho}} \left[\frac{g_{*s}(T_0)}{g_{*s}(T_B)} \right]^2 \left(\frac{T_0}{T_B} \right)^2 \eta_\phi, \quad (3.33)$$

where $\tilde{\eta}_\phi$ is the Imminiyaz definition for the kination parameter and η_ϕ is the Salati definition used here.

and verified the results presented in Salati [142] and Rosati [167] who showed that the enhanced expansion rate predicted by the kination scenario led to earlier particle freeze-out and an enhanced relic abundance. In particular, we verified that the kination effects are amplified for increasing WIMP mass, m_χ , and that the ratio of the relic densities in the kination and standard scenarios roughly scales as $\Omega_{\text{DM}}^Q/\Omega_{\text{DM}}^{GR} \sim 10\sqrt{\eta_\phi}m_\chi$, where η_ϕ is the kination parameter defined in (3.11). We also determined the annihilation cross section required to produce the observed dark matter density for both the s - and p - wave cases, and compared our results to Guo and Zhang [224] who had previously considered the s - wave case only. We then used the Fermi-LAT gamma ray data [125] to constrain the allowed range of η_ϕ as a function of WIMP mass and found that the maximal value of the kination parameter permitted by BBN constraints, $\eta_\phi = 1$, is excluded for each of the annihilation channels considered.

Furthermore, in asymmetric dark matter models we verified the findings of Iminniyaz and Chen [225] and Gelmini *et al* [173] that the enhanced expansion rate in the kination scenario can 'wash out' the asymmetry between the particles and antiparticles, driving the model towards the weakly asymmetric regime discussed in 2.4, where the density of the particle and antiparticle components is comparable and the relic density is fixed by $\langle\sigma v\rangle$. Consequently, the enhanced annihilation cross section required in the kination scenario is capable of producing an amplified annihilation signal with respect to the symmetric signal in the standard cosmological scenario. This result, which is contrary to the usual expectation that the asymmetric detection signal is negligible, is realized for the region indicated in figure 3.10.

More generally, by studying dark matter decoupling in kination domination scenarios, we have introduced some of the generic features common to non-standard cosmological models that predict an enhanced expansion rate during the era of dark matter decoupling (e.g. enhanced relic density, detection signal). That said, quintessence models of dark energy, in which the scalar field is non-interacting and must be extremely light ($|m_\phi| = \sqrt{V''(\phi)}/2 \lesssim H_0 \approx 10^{-33} \text{ eV}$)⁷ in order to drive the accelerated expansion of the universe, are mostly motivated by phenomenological considerations, and should only be considered as toy models. In the next chapter we consider scalar-tensor theories of gravity, in which the scalar field ϕ is coupled to the metric tensor $g_{\mu\nu}$. This construction appears in the low energy limit of string theory and thus provides a more plausible theoretical framework than the simple quintessence models considered here.

⁷The dash corresponds to differentiation with respect to ϕ .

Chapter 4

Scalar-Tensor Gravity

4.1 Introduction

In the previous chapter we demonstrated how a non-standard expansion law at the time of dark matter decoupling can modify particle freeze-out and in turn the dark matter relic abundance. This was illustrated in the context of quintessential kination models where the enhanced expansion rate at early times led to a relic abundance that was enhanced by up to several orders of magnitude. Although this scenario provides an interesting example of how dark energy phenomenology can influence early universe physics, it can be argued that quintessence models themselves appear rather contrived, particularly given that ultra-light non-interacting scalar fields are rarely encountered in other areas of physics.

A more natural way to introduce an ultra-light scalar field is within the framework of scalar-tensor theories [143–145, 229–232] which are (in part) motivated by higher dimensional unification models, à la Kaluza-Klein [233, 234]. In this case the scalar field arises through the compactification of the higher dimensions and couples to the metric with gravitational strength. As such the gravitational interaction is mediated by both the metric and scalar fields so that scalar-tensor gravity models represent a departure from standard General Relativity (GR).

Importantly, the new long range interaction introduced by the coupling, $A(\varphi_*)$, between the scalar field, φ_* , and the metric, $g_{\mu\nu}$,¹ is subject to stringent experimental bounds from fifth force searches and solar system tests of gravity [235]. To evade detection in high density environments non-linear effects act to shield the scalar field through one of

¹Matter fields Ψ_{mat} couple directly to the so-called *Jordan frame* metric $g_{\mu\nu} = A^2(\varphi_*)g_{\mu\nu}^*$, where an asterisk is used to denote *Einstein frame* quantities which is the frame in which the gravitational field equations take their standard form (see later).

several screening mechanisms such as the Vainshtein or chameleon mechanisms [236].² In the chameleon case for example, the mass of the scalar field is background dependent so that in regions of high density (e.g. our solar system) the field mass is large and the interaction range is suppressed. Conversely, in low density backgrounds (i.e. on cosmological scales) the field can be extremely light, allowing the scalar interaction to drive the accelerated expansion of the universe.

In addition to the screening mechanisms that help shield the scalar field from astrophysical observations, many scalar-tensor gravity models exhibit an inherent attraction mechanism towards General Relativity [147, 148]: throughout its cosmological evolution, the scalar field is driven towards a state where the coupling $A(\varphi_*)$ remains constant so that the scalar-tensor theory is indistinguishable from GR (see section 4.4). This allows scalar-tensor gravity models to deviate from the standard cosmological scenario at early times whilst relaxing towards General Relativity prior to the onset of Big Bang Nucleosynthesis. Hence, these models could potentially disturb the timing of dark matter decoupling.

The effects of the modified early time expansion rate in the scalar-tensor scenario on the dark matter relic abundance were first studied by Catena *et al* in [156]. In their paper the authors determined the evolution of the scalar field for the coupling $A(\varphi_*) = 1 + Be^{-\beta\varphi_*}$ and found that, for T greater than some transition temperature T_{φ_*} , the early time expansion rate was enhanced by a factor of

$$\xi(T) = \frac{H_{ST}}{H_{GR}} \simeq 2.19 \times 10^{14} \left(\frac{T_0}{T} \right)^{0.82} \quad (\text{where } T_0 = 2.35 \times 10^{-13} \text{ GeV}) \quad (4.1)$$

before rapidly dropping to 1 at $T = T_{\varphi_*}$ (as a result of the attraction mechanism just mentioned). Interestingly, the authors discovered that the rapid relaxation of the scalar-tensor expansion rate, H_{ST} , towards the standard expansion rate, H_{GR} , at T_{φ_*} led to a phase of *reannihilation*: after the initial particle decoupling, the dark matter species experienced a subsidiary period of annihilation as the expansion rate of the universe dropped below the interaction rate. Despite this secondary annihilation phase, they showed that the relic abundance of dark matter in scalar-tensor gravity models can still be enhanced by up to three orders of magnitude (depending on the WIMP mass m_χ).

The approximate form (4.1) of the ratio H_{ST}/H_{GR} has since been adopted in several subsequent investigations including those by Gelmini *et al* [173], Rehagen and Gelmini [174] and, very recently, Wang *et al* [175] who studied the relic abundance of asymmetric dark matter species [173, 175] and sterile neutrinos [174], and naturally obtained similarly large enhancement factors for the dark matter relic abundance. Additionally, Catena *et*

²For a recent paper on laboratory searches for the chameleon (scalar) field see [237].

al released a follow up paper [159] where they considered the coupling $A(\varphi_*) = 1 + b\varphi_*^2$ as part of a more general study of dark matter relic abundances in non-standard cosmological scenarios and once again found that the relic abundance in scalar-tensor cosmology is enhanced by several orders of magnitude.

We should emphasize, however, that although the different couplings used by the Catena group allow for significant enhancements of the early time expansion rate, detailed studies of the BBN implications of scalar-tensor theories with these couplings are lacking. However, detailed BBN studies are available (see for instance [238, 239]) for the more popular choice of the scalar coupling

$$A(\varphi_*) = e^{\frac{1}{2}\beta\varphi_*^2}. \quad (4.2)$$

Thus it is important to determine if the relic abundance of dark matter can be similarly enhanced for these more widely investigated models.

The quadratic coupling (4.2) is the simplest generalization of the original Jordan—Fierz—Brans—Dicke model (see later). Besides being the prototypical coupling considered in numerous investigations of scalar-tensor gravity theories, including studies of slowly rotating anisotropic neutron stars [240] and pulsars in binary systems [241–243], the quadratic coupling was recently the subject of the rigorous investigation by Coc *et al* [176] in which BBN calculations were used to place stringent constraints on the various coupling parameters. These constraints are up to several orders of magnitude stronger than the solar system bounds (e.g. [244]) and, as we will show in the following, severely limit the possible deviations from the standard cosmological expansion history during the era of dark matter decoupling.

Finally, we mention the 2008 paper by Catena *et al* [172] where the authors introduced a new *hidden* matter sector that experienced a different coupling than the ordinary *visible* sector, thus allowing for slower pre-BBN expansion rates. This *non-universal* scalar-tensor theory was found to predict dark matter relic abundances that were reduced by up to a factor of ~ 0.05 .

In this chapter we revisit the calculation of dark matter relic abundances in scalar-tensor gravity from first principles. We assume that the coupling between the scalar field and matter (including dark matter) is universal; the case of non-universal scalar-tensor theories, in which the coupling between the scalar field and the visible and dark matter sectors is distinct, will be briefly considered at the end of the chapter. We explicitly determine the modified expansion rate by solving the equation of motion for the scalar field directly and use this result to numerically solve the Boltzmann rate equation. We find, for the coupling $A(\varphi_*) = e^{\frac{1}{2}\beta\varphi_*^2}$, that the efficiency of the attraction

mechanism towards GR combined with the strict BBN bounds on the input parameters only allow for modest enhancements of the dark matter relic abundance, particularly compared to those reported in Catena *et al* [156, 159] and found for the quintessential kination domination model considered in the previous chapter.

To begin, in section 4.2 we discuss the formulation of scalar-tensor theories in different conformal reference frames and comment on their physical interpretation. Then, after deriving the equations that govern the cosmological evolution in section 4.3, we explore in detail the dynamics of the coupled scalar field and the attraction mechanism towards General Relativity (section 4.4). We then investigate which regions of parameter space lead to the largest deviations from the standard expansion history (section 4.5) and, most importantly, which regions satisfy the bounds from Big Bang Nucleosynthesis and other astrophysical and dynamical constraints (section 4.6). In sections 4.7 and 4.8 we calculate the dark matter relic abundance for symmetric and asymmetric dark matter models respectively, and, for the first time, determine the annihilation cross section required to produce the observed dark matter density. Then, in section 4.9, we consider non-universal scalar-tensor theories and discuss the issues associated with determining the dark matter relic abundance when the scalar interaction with the standard matter (or visible) particle sector and dark matter particle sector is distinct. Finally in section 4.10 we summarize our results and comment on the potential for relic abundance calculations to discriminate between the scalar-tensor and standard cosmological scenarios.

4.2 Conformal transformations

4.2.1 Jordan and Einstein frames

Scalar-tensor gravity theories are often formulated in one of two conformal frames of reference, namely, the *Jordan* and *Einstein* frames.³ The advantage of using these different conformal frames is that the scalar coupling enters through either the gravitational sector (Jordan frame) or the matter sector (Einstein frame), leaving the other sector unaffected. For example, the general action integral for a scalar-tensor theory with a non-minimally coupled scalar field φ , formulated in the Jordan conformal frame, is given by

$$S_{\text{tot}} = \frac{1}{16\pi G_*} \int d^4x \sqrt{-g} [F(\varphi)R - g^{\mu\nu} Z(\varphi) \partial_\mu \varphi \partial_\nu \varphi - 2U(\varphi)] + S_{\text{mat}}[g_{\mu\nu}; \Psi_{\text{mat}}], \quad (4.4)$$

³Conformal reference frames are those connected by a conformal transformation, i.e. a local rescaling of the metric:

$$g_{\mu\nu} = \Omega^2(x) g_{\mu\nu}^*. \quad (4.3)$$

Here, $\Omega(x)$ is an arbitrary function of the spacetime coordinates x^μ , and we use the notation Ω^2 to preserve the sign of the line element $ds^2 = \Omega^2 ds_*^2$.

where $F(\varphi)$, $Z(\varphi)$ and $U(\varphi)$ are arbitrary functions of the field, G_* is the bare gravitational constant (i.e. the gravitational constant in the absence of the scalar interaction), and $R = g^{\mu\nu}R_{\mu\nu}$ is the Ricci scalar which has been constructed from the Jordan frame metric $g_{\mu\nu}$.⁴ The original Brans-Dicke model corresponds to $F(\varphi) = \phi$, $Z(\varphi) = \omega/\phi$ (where ω is a constant) and $U(\varphi) = 0$.

In this frame matter fields, Ψ_{mat} , are coupled directly to the metric, $g_{\mu\nu}$, so that the Weak Equivalence Principle is preserved by construction. This means that observables such as mass, length and time take their standard interpretation in the Jordan frame, making it the most convenient for particle physics considerations. However, since in this frame the scalar field couples to the gravitational sector, gravitational couplings pick up an additional φ dependence and the field equations take the cumbersome form (see Appendix E):

$$F(\varphi)G_{\mu\nu} - (\nabla_\mu \nabla_\nu - g_{\mu\nu} \square) F(\varphi) = 8\pi G_* (T_{\mu\nu} + T_{\mu\nu}^\varphi), \quad (4.5)$$

where the covariant derivative ∇_μ (see (A.7)) and Einstein's tensor, $G_{\mu\nu} = R_{\mu\nu} - \frac{1}{2}g_{\mu\nu}R$, are both defined using the Jordan frame metric $g_{\mu\nu}$, and the matter and scalar field energy-momentum tensors are given respectively by

$$T_{\mu\nu} = -\frac{2}{\sqrt{-g}} \frac{\delta S_{\text{mat}}}{\delta g^{\mu\nu}} \quad (4.6)$$

and

$$8\pi G_* T_{\mu\nu}^\varphi = Z(\varphi) \partial_\mu \varphi \partial_\nu \varphi - g_{\mu\nu} \left[\frac{1}{2} g^{\alpha\beta} Z(\varphi) \partial_\alpha \varphi \partial_\beta \varphi + U(\varphi) \right]. \quad (4.7)$$

To simplify the gravitational field equations we could formulate the scalar-tensor theory in the 'Einstein' frame, which is related to the Jordan frame by the conformal transformation

$$g_{\mu\nu}^* = F(\varphi) g_{\mu\nu}. \quad (4.8)$$

Here (and in the following) we use an asterisk to distinguish Einstein frame quantities from their Jordan frame counterparts. Applying the transformation (4.8), the action (4.4) becomes

$$S_{\text{tot}} = \frac{1}{16\pi G_*} \int d^4x \sqrt{-g_*} [R_* - 2g_*^{\mu\nu} \partial_\mu \varphi_* \partial_\nu \varphi_* - 4V(\varphi_*)] + S_{\text{mat}}[A^2(\varphi_*) g_{\mu\nu}^*; \Psi_{\text{mat}}] \quad (4.9)$$

⁴The quintessence type action with a minimally coupled scalar field ϕ given in the previous chapter can be recovered by taking $F(\varphi) = Z(\varphi) = 1$ and redefining $\varphi = \sqrt{8\pi G_*} \phi$ and $U(\varphi) = V(\phi)/8\pi G_*$.

where we have made the following redefinitions

$$\begin{aligned}\left(\frac{d\varphi_*}{d\varphi}\right)^2 &= \frac{3}{4} \left[\frac{d \ln F(\varphi)}{d\varphi} \right]^2 + \frac{Z(\varphi)}{2F(\varphi)}, \\ A(\varphi_*) &= F^{-1/2}(\varphi), \\ 2V(\varphi_*) &= \frac{U(\varphi)}{F^2(\varphi)}.\end{aligned}\tag{4.10}$$

The gravitational sector is now of the same form as the minimally coupled quintessence model (3.1) introduced in the previous chapter. Moreover, the field equations take the simplified form

$$G_{\mu\nu}^* = 8\pi G_* (T_{\mu\nu}^* + T_{\mu\nu}^{\varphi_*})\tag{4.11}$$

where the matter energy momentum tensor is now given by

$$T_{\mu\nu}^* = -\frac{2}{\sqrt{-g_*}} \frac{\delta S_{\text{mat}}}{\delta g_*^{\mu\nu}},\tag{4.12}$$

and the scalar field energy momentum tensor is

$$4\pi G_* T_{\mu\nu}^{\varphi_*} = \partial_\mu \varphi_* \partial_\nu \varphi_* - g_{\mu\nu}^* \left[\frac{1}{2} g_*^{\alpha\beta} \partial_\alpha \varphi_* \partial_\beta \varphi_* + V(\varphi_*) \right].\tag{4.13}$$

However, in the Einstein frame, the scalar coupling enters through the matter action $S_{\text{mat}} \equiv S_{\text{mat}}[A^2(\varphi_*)g_{\mu\nu}; \Psi_{\text{mat}}]$ so that the matter fields Ψ_{mat} couple to the φ_* -dependent metric $A^2(\varphi_*)g_{\mu\nu}^*$. This indicates that particle physics quantities (e.g. mass, length, time, energies, cross sections) measured in this frame are spacetime dependent.

We can characterize the departure of scalar-tensor theories from General Relativity by introducing the parameter

$$\alpha(\varphi_*) = \frac{d \ln A(\varphi_*)}{d\varphi_*}.\tag{4.14}$$

Large values of $\alpha(\varphi_*)$ correspond to large variations in the coupling $A(\varphi_*)$ whereas in the limit $\alpha(\varphi_*) \rightarrow 0$, corresponding to $A(\varphi_*) = \text{const.}$, the Einstein and Jordan frames coincide and the scalar-tensor theory reduces to standard General Relativity.

In the following our strategy will be to determine the cosmological evolution in the Einstein frame, where the cosmological equations take their simplest form, and then transform our results over to the Jordan frame, which is where we solve the Boltzmann equation for the dark matter number density.

4.2.2 Connection with $f(R)$ gravity

Before continuing, we would like to mention an interesting connection between scalar-tensor models and $f(R)$ theories of gravity [245, 246]. Nominally, $f(R)$ theories are presented as an extension of General Relativity where the standard Einstein-Hilbert Lagrangian, $L_{EH} = R/16\pi G$, is promoted to an arbitrary function of the Ricci scalar:⁵

$$S = \frac{1}{16\pi G} \int d^4x \sqrt{-g} f(R) + S_{\text{mat}}[g_{\mu\nu}; \Psi_{\text{mat}}]. \quad (4.15)$$

However, through a suitable redefinition of the fields, the $f(R)$ action (4.15) can be written as [248, 249]

$$S = \frac{1}{16\pi G} \int d^4x \sqrt{-g} [\phi R - V(\phi)] + S_{\text{mat}}[g_{\mu\nu}; \Psi_{\text{mat}}],$$

so that $f(R)$ theories can be considered as a subclass of scalar-tensor models with

$$\begin{aligned} \phi &= f'(R), \\ V(\phi) &= Rf'(R) - f \end{aligned} \quad (4.16)$$

where $f'(R) \equiv \partial f / \partial R$.

Applying the conformal transformation

$$g_{\mu\nu}^* = f'(R)g_{\mu\nu} = \phi g_{\mu\nu} \quad (4.17)$$

the action becomes

$$S = \frac{1}{16\pi G} \int d^4x \sqrt{-g_*} \left[R_* - \frac{1}{2} g_*^{\mu\nu} \partial_\mu \phi_* \partial_\nu \phi_* - U(\phi_*) \right] + S_{\text{mat}}[e^{2\phi_*/\sqrt{3}} g_{\mu\nu}^*; \Psi_{\text{mat}}], \quad (4.18)$$

where the new field ϕ_* and the potential $U(\phi_*)$ are given by

$$\begin{aligned} \phi_* &= \frac{\sqrt{3}}{2} \ln \phi, \\ U(\phi_*) &= \frac{Rf'(R) - f(R)}{f'(R)^2}. \end{aligned}$$

$f(R)$ theories have become increasingly popular in recent times due to their ability to explain both the accelerated expansion of the universe during the inflationary era, as in

⁵A powerful motivation for considering $f(R)$ theories of gravity is the observation that adding higher order curvature corrections to the Einstein-Hilbert Lagrangian ameliorates the ultraviolet divergences associated with standard General Relativity [247].

the Starobinsky model [250]

$$f(R) = R + \frac{R^2}{6M^2}, \quad (4.19)$$

and the late time accelerated expansion, as in the Hu-Sawicki model [251]

$$f(R) = R - m^2 \frac{c_1 (R/m^2)^n}{c_2 (R/m^2)^n + 1}. \quad (4.20)$$

We emphasize however, that although $f(R)$ models provide a prescriptive form for the coupling function and potential (in a scalar-tensor theory context), most models are specifically designed to account for the behaviour of the universe at either very early ($T \sim 10^{16}$ GeV) or very late ($T \sim 10^{-13}$ GeV) times. Therefore we expect that the $f(R)$ models considered in the literature will not provide significant modifications to the expansion rate of the universe during the era we are interested in, that is, during the era of dark matter decoupling ($T \sim \mathcal{O}(\text{GeV})$).

4.3 Cosmological equations

If we introduce the Einstein frame line element

$$ds_*^2 = g_{\mu\nu}^* dx_*^\mu dx_*^\nu = -dt_*^2 + a_*^2(t) \gamma_{ij}^* dx_*^i dx_*^j, \quad (4.21)$$

and assume that the matter fields are a perfect fluid described by the usual energy-momentum tensor (1.3), then the field equations (4.11) give

$$3H_*^2 = 8\pi G_* \rho_* + \dot{\varphi}_*^2 + 2V(\varphi_*), \quad (4.22)$$

$$3 \frac{\ddot{a}_*}{a_*} = -4\pi G_* (\rho_* + p_*) - 2\dot{\varphi}_*^2 + 2V(\varphi_*) \quad (4.23)$$

where ρ_* and p_* are the energy density and pressure of the fluid respectively. Here an overdot denotes differentiation with respect to t_* and we have introduced the Einstein frame Hubble factor $H_* \equiv d \ln a_* / dt_*$. Since the Friedmann equations (4.22) and (4.23) depend on the scalar field, we also need the equation of motion for φ_* to close the system and determine the evolution of the scale factor $a_*(t_*)$ (see Appendix E):⁶

$$\ddot{\varphi}_* + 3H_* \dot{\varphi}_* + \frac{\partial V}{\partial \varphi_*} = -4\pi G_* \alpha(\varphi_*) (\rho_* - 3p_*). \quad (4.24)$$

⁶To derive (4.24) we have simply varied the action (4.9) with respect to φ_* and substituted in the relation (E.16)

$$\frac{\delta S_{\text{mat}}[A^2(\varphi_*)g_{\mu\nu}^*, \Psi]}{\delta \varphi_*} = -\sqrt{-g_*} \alpha(\varphi_*) T_*.$$

Additionally, the Einstein frame energy density and pressure no longer satisfy the standard continuity equation. Instead there is an additional source term due to the scalar field interaction:

$$\frac{d\rho_{*i}}{dt_*} + 3H_*(\rho_{*i} + p_{*i}) = \alpha(\varphi_*) (\rho_{*i} - 3p_{*i}), \quad (4.25)$$

where i labels the various fluid components (e.g. radiation, baryonic matter, dark matter). Instead of solving this equation directly we can transform to the Jordan frame in which

$$\frac{d\rho_i}{dt} + 3H(\rho_i + p_i) = 0, \quad (4.26)$$

where the Jordan frame expansion rate, $H = d \ln a / dt$ is related to the Einstein frame one via

$$H = A^{-1}(\varphi_*) [H_* + \alpha(\varphi_*)\dot{\varphi}_*]. \quad (4.27)$$

Note that (4.26) can be derived from (4.25) by transforming to the Jordan frame coordinates

$$a = A(\varphi_*)a_*, \quad dt = A(\varphi_*)dt_*, \quad (4.28)$$

and substituting in the relation between the Einstein frame energy density, ρ_* , and pressure, p_* ,

$$\rho_* = A^4(\varphi_*)\rho, \quad p_* = A^4(\varphi_*)p. \quad (4.29)$$

Assuming the pressure and energy density of the i -th fluid component are related by $p_i = w_i \rho_i$, where w_i is the equation of state parameter, we get

$$\rho_i(t) = \rho_i(t_0) \exp \left[-3 \int_{t_0}^t H(1 + w_i) dt \right]. \quad (4.30)$$

Further, if we assume that w_i is constant,

$$\rho_i = \rho_i^0 \left(\frac{a}{a_0} \right)^{-3(1+w_i)} \quad (4.31)$$

where a (sub)superscript '0' denotes a quantity evaluated at the present epoch, i.e. $\rho_i^0 = \rho_i(t_0)$. Then, using (4.29), we finally have

$$\rho_{*i} = \rho_{*i}^0 \left[\frac{A(\varphi_*)}{A(\varphi_{*0})} \right]^{4-3(1+w_i)} \left(\frac{a_*}{a_{*0}} \right)^{-3(1+w_i)} \quad (4.32)$$

where $\rho_{*i}^0 = A^4 \rho_i^0$. Notice from the relationship (4.29) between the Einstein and Jordan frame energy densities and pressures that the equation of state parameter is a frame

invariant quantity:

$$w_i = \frac{p_i}{\rho_i} = \frac{p_{*i}}{\rho_{*i}}. \quad (4.33)$$

4.4 Scalar field dynamics

To determine the expansion rate of the universe in scalar-tensor gravity models we must solve the coupled system of equations (4.22)-(4.24). Fortunately, as pointed out by [147, 148], the equation of motion for the scalar field can be decoupled from the system by transforming the evolution parameter from the Einstein frame time t_* to $N \equiv \ln(a_*/a_{*0})$. In this case variables of the type \dot{Q} transform as $\dot{Q} = Q'H_*$ (where a $'$ denotes differentiation with respect to N), so that (4.22) becomes

$$(3 - \varphi_*'^2)H_*^2 = 8\pi G_*\rho_* + 2V(\varphi_*). \quad (4.34)$$

Setting the potential $V(\varphi_*) = 0$ ⁷ and substituting into (4.24) we get

$$\frac{2}{3 - \varphi_*'^2}\varphi_*'' + (1 - w)\varphi_*' = -\alpha(\varphi_*)(1 - 3w) \quad (4.35)$$

where w is the equation of state parameter of the total cosmic fluid:

$$w = \frac{p_{*\text{tot}}}{\rho_{*\text{tot}}} = \frac{p_{\text{tot}}}{\rho_{\text{tot}}}. \quad (4.36)$$

Following the analogy given in [148], the field φ_* can be thought of as a particle-like dynamical variable with a velocity dependent mass, $m(\varphi_*) = 2/(3 - \varphi_*'^2)$. In this instance the particle (φ_*) experiences simple damping and rolls down the potential $\propto \ln A(\varphi_*)$ towards the minimum, provided such a point exists. Hence, the late-time evolution of the field is reasonably straightforward given that the equation of state parameter during the matter dominated epoch is $w \approx 0$ so that the forcing term on the right hand side of (4.35) is simply given by $-\alpha(\varphi_*)$. Therefore, if the function $\alpha(\varphi_*)$ possesses a zero with a positive slope, the field will be dynamically attracted towards the point $\alpha = 0$, which is precisely the GR limit.⁸

At much earlier times, deep in the radiation era ($w \approx 1/3$), the forcing term in (4.35) is mostly ineffective and any initial velocity possessed by the field is rapidly damped away. This allows us to take as initial conditions

$$\varphi_{*\text{in}} = \text{const.} \quad \text{and} \quad \varphi_{*\text{in}}' = 0, \quad (4.37)$$

⁷The potential term only affects the cosmological evolution at late times and will not play a significant role during the early universe period we are interested in.

⁸For the choice of coupling $A(\varphi_*) = e^{\frac{1}{2}\beta\varphi_*^2}$ considered here, this condition implies that $\beta > 0$.

where $\varphi_{*\text{in}}$ and $\varphi'_{*\text{in}}$ are the values of the field and its N -derivative at some initial point N_{in} .

Although $1 - 3w \approx 0$ throughout most of the early universe, there is an important effect that arises when each of the particle species in the cosmic fluid becomes non-relativistic [148]. As the temperature of the universe drops below the rest mass of each of the particle types they provide a non-zero contribution to the quantity $1 - 3w$. This activates the forcing term in (4.35) and displaces, or 'kicks' the field along the potential $\propto \ln A(\varphi_*)$. In this way the attraction mechanism towards GR is initiated during the very early moments of the universe ($T \sim 10^2$ GeV), prior to the onset of Big Bang Nucleosynthesis.

To explore this effect in more detail we first write the quantity $1 - 3w$ as

$$\begin{aligned} 1 - 3w &= \frac{\rho_{\text{tot}} - 3p_{\text{tot}}}{\rho_{\text{tot}}} \\ &= \frac{1}{\rho_{\text{tot}}} \left\{ \sum_A [\rho_A - 3p_A] + \rho_m \right\} \end{aligned} \quad (4.38)$$

where we have separated out the contribution from the relativistic particle species A and the non-relativistic particle species m (for which $p_m = 0$). Assuming that the total energy density is dominated by relativistic matter and radiation during the crossing of each mass threshold, so that $\rho_{\text{tot}} \simeq \rho_r = \pi^2 g_{*\rho}(T) T^4 / 30$, the *kick function*

$$\Sigma(T) \equiv \sum_A \frac{\rho_A - 3p_A}{\rho_{\text{tot}}} \quad (4.39)$$

takes the form

$$\Sigma(T) = \sum_A \frac{15}{\pi^4} \frac{g_A}{g_{*\rho}(T)} z_A^2 \int_{z_A}^{\infty} dx \frac{\sqrt{x^2 - z_A^2}}{e^x \pm 1}, \quad (4.40)$$

where $z_A = m_A/T$, the $+$ ($-$) corresponds to fermions(bosons) and the expressions for the energy density ρ_A and pressure p_A of each of the particles of type A are given in appendix B.

It is important to note that the variable T in the expression for $\Sigma(T)$ is the Jordan frame temperature, which we can relate to the parameter N through

$$T[\varphi_*, N] = T_0 \frac{A(\varphi_{*0})}{A(\varphi_*)} \left[\frac{g_{*s}(T_0)}{g_{*s}(T)} \right]^{1/3} e^{-N}. \quad (4.41)$$

Here $T_0 = 2.35 \times 10^{-13}$ GeV is the current temperature of the universe and $\varphi_{*0} = \varphi_*(T_0)$. To derive this expression we have used the relationship between the scale factor a and temperature T (B.34) as well as the transformation (4.28).

Using the data contained in table B.1 for the properties of each of the Standard Model particles, we numerically evaluate (4.40) and plot the results in figure 4.1. In this figure we show the contribution from each of the individual particle species (dashed curves) as well as their combined sum (solid black).⁹

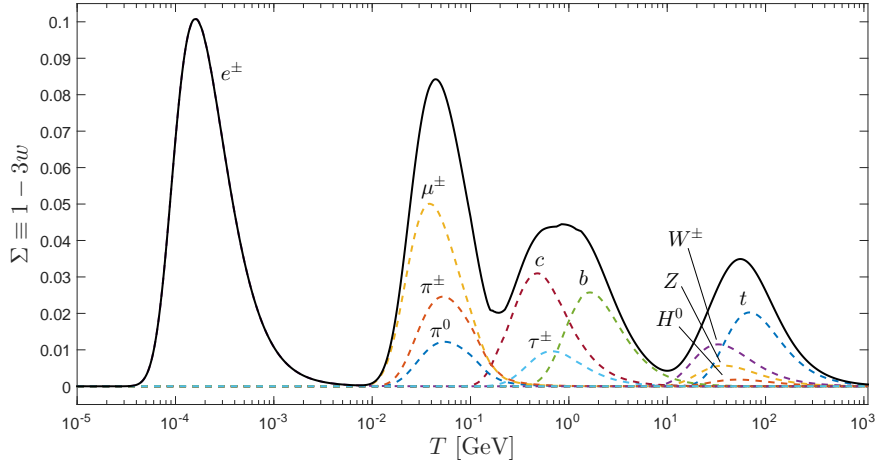


FIGURE 4.1: Evolution of the quantity $\Sigma(T) \equiv 1 - 3w$ (solid black curve) defined in (4.40) in the radiation era with the contribution from each particle species listed in table B.1 shown (colored dashed curves).

After the final e^\pm kick, the forcing term remains inactive until the universe transitions from the radiation dominated era to the matter dominated era. In this case we have

$$1 - 3w \simeq \frac{\rho_m}{\rho_m + \rho_r} \simeq \frac{1}{1 + T/T_{\text{eq}}} \quad (4.42)$$

where $T_{\text{eq}} \sim \mathcal{O}(10^{-9})$ GeV is the temperature of matter-radiation equality, i.e. $\rho_r(T_{\text{eq}}) = \rho_m(T_{\text{eq}})$. Combining the results in figure 4.1 with the late time behaviour described by equation (4.42), we plot the evolution of $1 - 3w$ from the radiation era up to the present in figure 4.2.

In the radiation era, $T \gtrsim T_{\text{eq}}$, $1 - 3w \approx 0$ except at the location of each of the kicks; then as T approaches T_{eq} , $1 - 3w$ smoothly rises to $1/2$; and in the limit $T \ll T_{\text{eq}}$, $1 - 3w \approx 1$.

Now that we have computed $1 - 3w$ we can finally determine the cosmological evolution of the scalar field φ_* . Substituting our particular choice of coupling $A(\varphi_*) = e^{\frac{1}{2}\beta\varphi_*^2}$ into (4.35) we numerically integrate the equation of motion for several sample values of β and $\varphi_{*\text{in}}$ (see figure 4.3).

⁹The quantity $\Sigma(T)$ has been evaluated in several other publications (e.g. [176, 252]) and in most cases the value of $g_{*\rho}(T)$ is assumed constant during the crossing of each particle threshold. However, since $g_{*\rho}(T)$ actually decreases during this interval, these calculations underestimate the height of $\Sigma(T)$, particularly for the final e^\pm 'kick'. In our work we have maintained the temperature dependence of $g_{*\rho}(T)$ and our results agree with those contained in the recent paper by Erickcek *et al* [253].

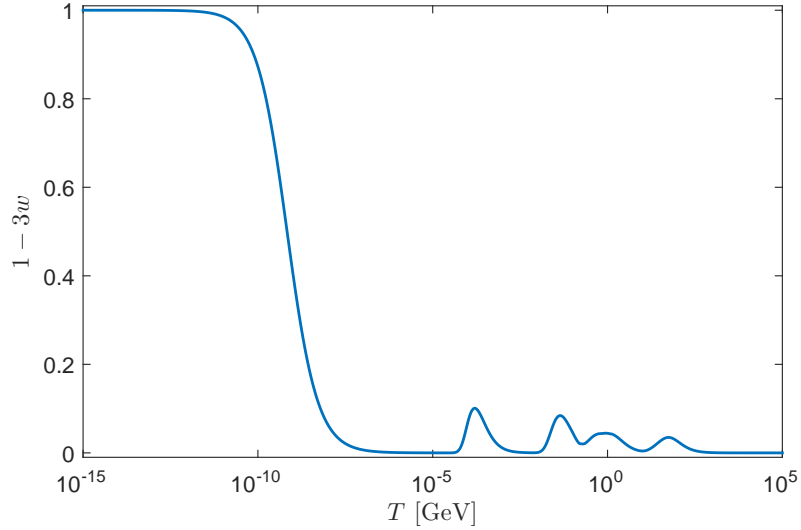


FIGURE 4.2: Evolution of the quantity $\Sigma(T) \equiv 1 - 3w$ defined in (4.40) from the radiation era through to the matter era.

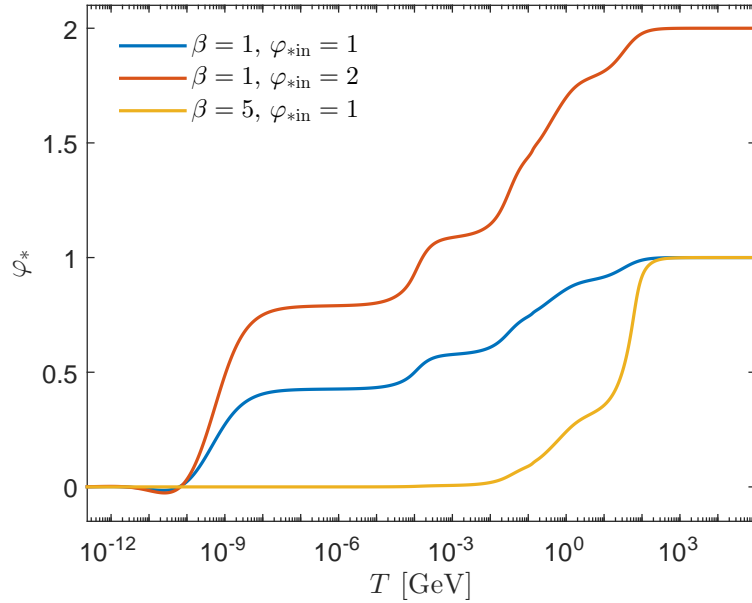


FIGURE 4.3: Evolution of φ_* for different values of the input parameters β and φ_{*in} .

In each case we see that the field is attracted towards $\varphi_* = 0$ which, for the quadratic coupling considered, corresponds to the GR limit. Importantly we notice that the attraction mechanism is initiated well before the radiation-matter transition at $T \sim 10^{-9}$ GeV due to the non-relativistic kicks mentioned above. In fact, for the $\beta = 1$ cases (blue and red curves) we can discern the four distinct kicks corresponding to the four peaks in figure 4.1. For the $(\beta, \varphi_{*in}) = (5, 1)$ case (yellow curve), the attraction mechanism is so efficient that the field approaches the GR limit at much earlier times, prior to BBN.

4.5 Modified expansion rate

Having calculated the cosmological evolution of φ_* we can now determine the modified expansion rate in the scalar-tensor scenario. For the purpose of calculating the dark matter relic abundance, we are particularly interested in the Jordan frame expansion rate $H = d \ln a / dt$ since the dark matter particles couple directly to the Jordan frame metric $g_{\mu\nu}$ and in this frame particle masses, number densities, etc. take their standard form. Therefore the expansion rate that governs the timing of particle decoupling and in turn the dark matter relic abundance is determined using (4.27),

$$H = A^{-1}(\varphi_*) H_* [1 + \alpha(\varphi_*) \varphi_*'] \quad (4.43)$$

where, using (4.34) and (4.29), we can write the Einstein frame expansion rate, H_* , in terms of

$$H_*^2 = \frac{8\pi G_*}{3 - \varphi_*'^2} \rho A^4(\varphi_*). \quad (4.44)$$

To compare the Jordan frame expansion rate, H , to the expansion rate in the standard cosmological scenario,

$$H_{GR}^2 = \frac{8\pi G}{3} \rho, \quad (4.45)$$

we note that the gravitational couplings used in each case are related via [230]

$$G = G_* A^2(\varphi_{*0}) [1 + \alpha^2(\varphi_{*0})], \quad (4.46)$$

where G is the gravitational coupling given in the standard General Relativity scenario and G_* is the bare gravitational coupling used here. Combining this expression with the connection between the Jordan and Einstein frame Hubble factors (4.27) we finally have

$$\xi \equiv \frac{H_{ST}}{H_{GR}} = \frac{A(\varphi_*)}{A(\varphi_{*0})} \frac{1 + \alpha(\varphi_*) \varphi_*'}{\sqrt{1 - \varphi_*'^2/3}} \frac{1}{\sqrt{1 + \alpha^2(\varphi_{*0})}} \quad (4.47)$$

where we now denote the Jordan frame expansion rate H , that will be used as input into the Boltzmann rate equation for the dark matter number density, by H_{ST} .

To estimate the possible enhancement of the dark matter relic abundance in the scalar-tensor gravity scenario, we first determine the magnitude of the ratio $\xi = H_{ST}/H_{GR}$ around the time of dark matter decoupling. Hence, in figure 4.4, we plot the magnitude of ξ evaluated at $T_f \sim m_\chi/20 \sim 5$ GeV, which is the typical freeze-out time for a 100 GeV WIMP. We have considered values of $\beta > 0$ to ensure that the model is dynamically attracted towards GR (see previous section).

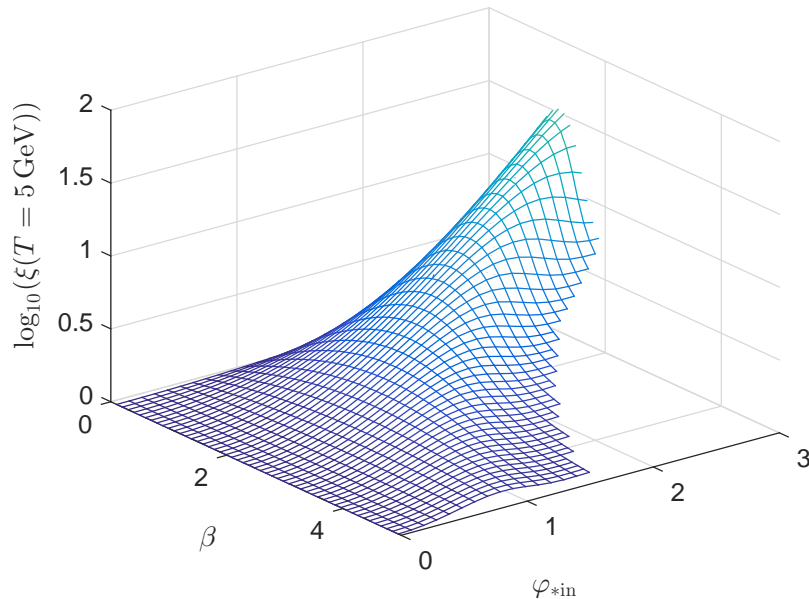


FIGURE 4.4: Magnitude of the ratio of the scalar-tensor and standard expansion rates, $\xi \equiv H_{ST}/H_{GR}$, evaluated at a temperature $T = 5$ GeV as a function of the input parameters β and φ_{*in} , which satisfy the dynamical constraints.

This figure shows that the scalar-tensor expansion rate at the time of dark matter decoupling can be more than an order of magnitude larger than the standard expansion rate. In particular, the largest enhancements are seen for small values of β and large φ_{*in} , specifically, for $\beta \lesssim 2$ and $\varphi_{*in} \gtrsim 2$. This parameter range leads to large initial values of $\xi_{in} \sim A(\varphi_{*in})$ (because of the large φ_{*in}) whilst exhibiting a less efficient attraction towards GR (small β) so that the expansion rate at the time of freeze-out still deviates significantly from the standard one.¹⁰ Note that the data points for larger β and φ_{*in} have been omitted because in this region the field violates the dynamical constraints, leading to unphysical results (see next section).

Although the early time expansion rate can certainly be much larger in the scalar-tensor scenario for certain regions of parameter space, we must be careful to ensure that such regions satisfy both the astrophysical and dynamical constraints placed on the scalar field and its evolution. In the next section we investigate in more detail these constraints and determine those points in parameter space which are viable.

4.6 Constraints

Solar system tests of gravity, including the perihelion shift of Mercury and Lunar Laser Ranging experiments, place strict constraints on deviations from General Relativity

¹⁰In general, although increasing both β and φ_{*in} increases the initial value ξ_{in} , because the displacement of the field towards $\varphi_* = 0$ due to each of the non-relativistic 'kicks' also increases with increasing β and φ_{*in} , the overall effect on $\xi(T_f)$ (and in turn on $\Omega_{DM}^{ST}/\Omega_{DM}^{GR}$) can be difficult to predict.

(see for example [235]). Most relevant for our purposes are the measurements of the Shapiro time delay performed by the Cassini spacecraft [244] which indicate that the present value of the scalar-tensor deviation parameter $\alpha_0^2 \equiv \alpha^2(\varphi_{*0}) < 10^{-5}$; so that if the gravitational interaction is truly described by a scalar-tensor theory, it must be extremely close to General Relativity in our local neighbourhood.¹¹

Although this constraint only applies to the present value $|\alpha_0|$, we can relate it to the input parameters β and $\varphi_{*\text{in}}$ by integrating the φ_* evolution equation up to the present epoch and calculating the predicted value of $|\alpha_0|$ directly. We can then determine which values of β and $\varphi_{*\text{in}}$ satisfy the Cassini bound $\alpha_0^2 \lesssim 10^{-5}$. The results are shown in figure 4.5 where we have indicated those points that violate the Cassini bound with a red cross and those that are acceptable with a green circle. We have also indicated with a blue cross those points that violate the various dynamical constraints on the evolution of the scalar field (see later).

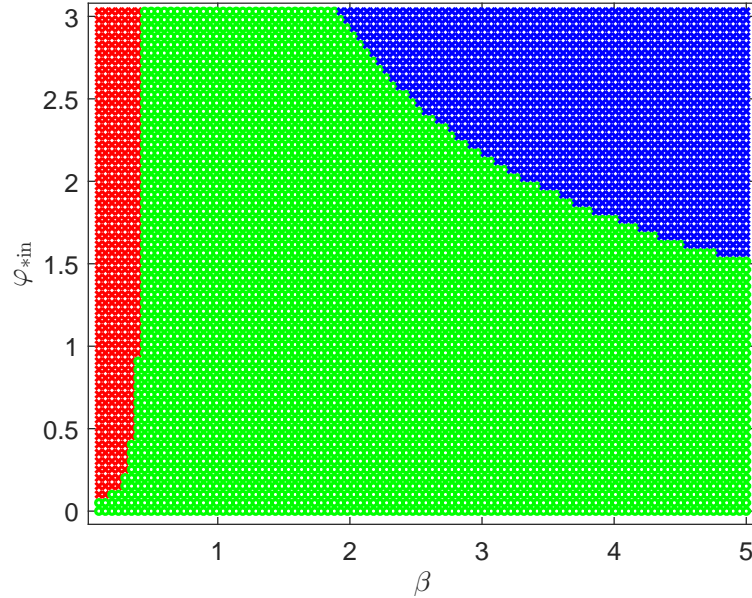


FIGURE 4.5: Exclusion plot following a scan of the input parameter space $(\beta, \varphi_{*\text{in}})$ and applying the Cassini bound $\alpha_0^2 < 10^{-5}$ [244]. The points excluded due to the Cassini (dynamical) constraints have been marked with a red (blue) cross and the allowed points are indicated by the green circles.

Interestingly, for the parameter range considered, the Cassini bound only excludes values of $\beta \lesssim 0.4$. Comparing this with the results in figure 4.4 for $\xi(T_f)$, we see that the regions of parameter space that lead to the fastest expansion rates at the time of dark matter decoupling ($0.4 \lesssim \beta \lesssim 2, \varphi_{*\text{in}} \gtrsim 2$) still satisfy the constraint $\alpha_0^2 < 10^{-5}$. Therefore, the Cassini bound alone (or, more generally, solar system tests of gravity) does not preclude large deviations from the standard cosmological history at early times. This is not so

¹¹Additionally, for the quadratic scalar coupling $A(\varphi_*) = e^{\frac{1}{2}\beta\varphi_*^2}$ considered here, the decay of the orbital period of pulsars in asymmetric binaries implies that the coupling parameter $\beta \gtrsim -4.5$ [243].

surprising given that solar system tests of gravity rely on data taken at late times — *long* after the attraction mechanism towards GR has been initiated.

To properly constrain the input parameters and the behaviour of the field in the early universe, we must also take into account the results presented in Coc *et al* [176] where they considered the Big Bang Nucleosynthesis implications of scalar-tensor theories with a quadratic coupling. In this work the authors perform a full numerical integration of the scalar field evolution equation and calculate the resulting light element abundances using an up-to-date BBN code. The results of these calculations are then compared to observed light element abundances to constrain the various scalar-tensor model parameters.¹²

Since these constraints are also given in terms of the present value $|\alpha_0|$, we must again integrate the φ_* evolution equation up to the present epoch for the different values of β and φ_{*in} and calculate $|\alpha_0|$ directly. As an example, in figure 4.6, we compare our results for $|\alpha_0|$ as a function of β for different starting values of φ_{*in} (solid curves) with both the Cassini (dot-dashed purple curve) and the Coc *et al* BBN bound (dot-dashed black curve).

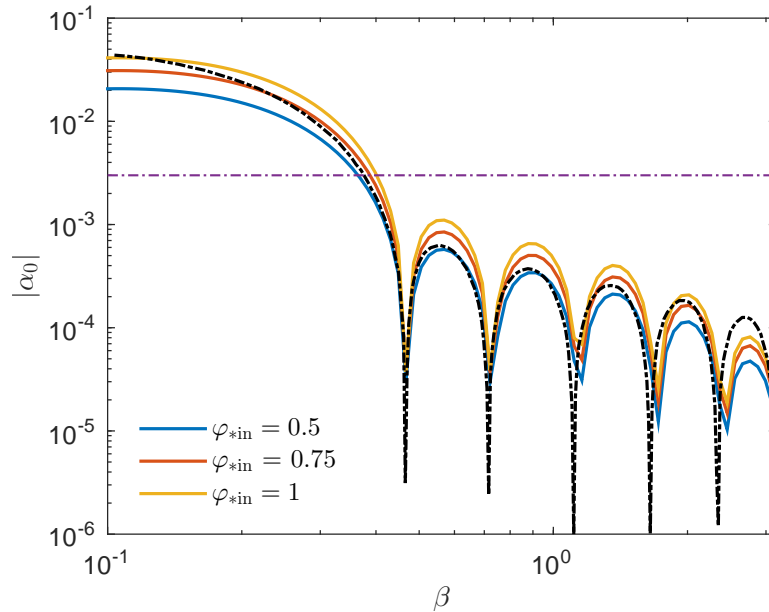


FIGURE 4.6: Magnitude of $|\alpha_0|$ as a function of the coupling parameter β for different initial values of the field (solid curves). The results are compared with the constraints derived using the solar system tests of gravity (dot-dashed purple) and the BBN constraints given in figure 19 of Coc *et al* [176] (dot-dashed black).

¹²Recall from the introductory chapter that a comparison of the observed light element abundances with the predictions of Big Bang Nucleosynthesis offers one of the most stringent available probes of non-standard cosmological models.

Ignoring any computational differences, (keep in mind that our computation of $\Sigma(T)$ differs from figure 5 of Coc *et al* [176] because we maintained the temperature dependence of $g_*(T)$) we notice that the blue, red and yellow curves for $|\alpha_0|$ do not drop below the BBN constraints (dot-dashed black curve) until after a particular oscillation. For example, for $\varphi_{*in} = 0.75$ (red curve), the calculated values of $|\alpha_0|$ do not drop below the BBN constraints until after the fourth oscillation at $\beta \simeq 1.65$. Similarly, for $\varphi_{*in} = 1$ (yellow curve), $|\alpha_0|$ does not drop below the BBN bound until after the fifth oscillation at $\beta = 2.35$. Therefore, once the BBN bounds become more stringent than the solar system bound, i.e. $\beta \gtrsim 0.4$, the values of β for which a particular φ_{*in} becomes acceptable are discrete. This is shown in figure 4.7 where we reproduce figure 4.5, this time applying the Coc *et al* BBN bound in addition to the Cassini bound. For $\beta \lesssim 0.4$, the boundary separating the allowed and rejected regions follows a smooth curve, whilst for $\beta \gtrsim 0.4$ the boundary increases in discrete steps.

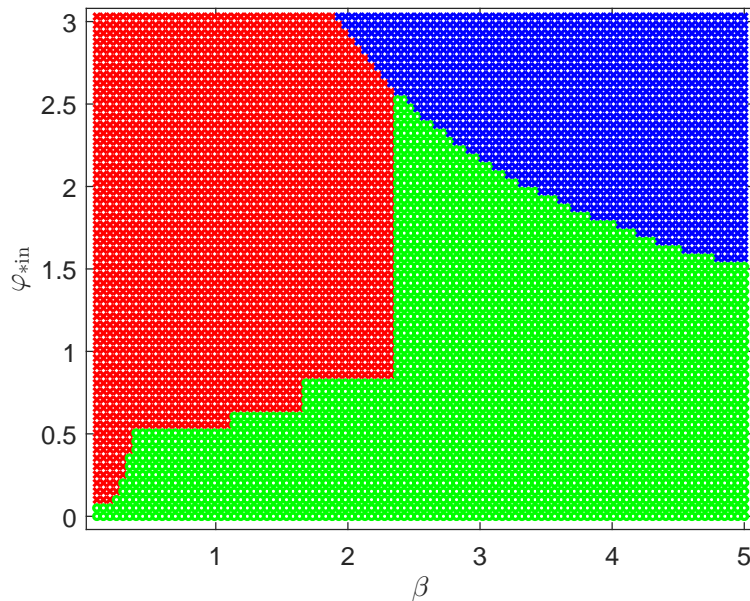


FIGURE 4.7: Scan of the input parameter space for the coupling $A(\varphi_*) = e^{\frac{1}{2}\beta\varphi_*^2}$. The points excluded due to astrophysical (dynamical) constraints have been marked with a red (blue) cross and the allowed points are indicated by the green circles.

Most importantly, a comparison of figures 4.5 and 4.7 shows that applying the Coc *et al* BBN constraints excludes most of the parameter space corresponding to large early time expansion rates (see figure 4.4). Also, because of the non-injective relationship between the input parameters and the present value of $|\alpha_0|$ (i.e. different initial conditions can lead to the same $|\alpha_0|$), the constraints in figure 19 of [176] can only be treated as a strict upper bound. This means that values of $|\alpha_0|$ lower than this upper bound are not necessarily acceptable so that the allowed region in the (β, φ_{*in}) parameter space is most likely smaller than what is shown in figure 4.7.

In addition to the astrophysical constraints, the dynamical evolution of the scalar field φ_* must also satisfy

$$1 + \alpha(\varphi_*)\varphi_*' > 0. \quad (4.48)$$

This ensures that the Jordan frame Hubble factor, derived from the Einstein frame Hubble factor through

$$H = A^{-1}(\varphi_*)H_* [1 + \alpha(\varphi_*)\varphi_*'], \quad (4.49)$$

is positive definite. Moreover, if this condition is violated, the Jordan frame temperature T becomes a multi-valued function of the evolution parameter N and the conformal transformation between the Jordan and Einstein frames breaks down.¹³ The points in the $(\beta, \varphi_{*\text{in}})$ plane that violate this dynamical constraint are indicated with blue crosses.

We can crudely estimate the general shape of the dynamical exclusion zone by approximating the maximum velocity reached by the field due to each 'kick' as $\varphi_{*\text{max}}' \sim \alpha(\varphi_*)$. The condition $1 + \alpha(\varphi_*)\varphi_*' > 0$ then becomes

$$\alpha(\varphi_*)^2 \lesssim \mathcal{D}^2, \quad (4.51)$$

where \mathcal{D} is some variable that depends on the magnitude of the kick. Substituting in the expression $\alpha(\varphi_*) = \beta\varphi_*$, we find that the values of φ_* in the region

$$\varphi_* \gtrsim \frac{\mathcal{D}}{\beta}, \quad (4.52)$$

are excluded.

Combining the astrophysical and dynamical constraints we see that a significant portion of the parameter space is excluded. In particular, the region corresponding to the greatest deviations from the standard expansion history at the time of dark matter decoupling (i.e. $\xi(T_f)$) is no longer allowed (compare figures 4.7 and 4.4). In fact the largest value of $\xi(T_f)$ permitted by the various constraints is only ~ 4 . Hence, although large early-time expansion rates can be achieved within scalar-tensor cosmological models with the coupling $A(\varphi_*) = e^{\frac{1}{2}\beta\varphi_*^2}$, those models that satisfy the various constraints mentioned above will not significantly deviate from the standard cosmological model at the time of dark matter decoupling. In turn, we expect that the relic abundance of dark matter to

¹³If we neglect the temperature dependence of $g_{*s}(T)$, the connection between the Jordan frame temperature and the evolution parameter N (4.41) gives

$$\frac{dT}{dN} = -T_0 \frac{A(\varphi_{*0})}{A(\varphi_*)} e^{-N} [1 + \alpha(\varphi_*)\varphi_*']. \quad (4.50)$$

If the quantity $1 + \alpha(\varphi_*)\varphi_*'$ changes sign, the relationship between T and N is not monotonic and T becomes a multi-valued function of N that cannot be inverted.

be relatively unaffected and that any enhancements with respect to the canonical result are modest.

4.7 Symmetric dark matter

To verify our assertion about the effects of scalar-tensor gravity models with a quadratic coupling on the relic abundance of dark matter we explicitly determine the present dark matter density using the Boltzmann rate equation

$$\frac{dY}{dx} = -\frac{s\langle\sigma v\rangle}{xH}\zeta(x)(Y^2 - Y_{\text{eq}}^2). \quad (4.53)$$

Drawing from our previous discussion we point out that each of the quantities in (4.53) such as the comoving number density, $Y = n/s$, and annihilation cross section, $\langle\sigma v\rangle$, is defined in the Jordan frame where particle physics quantities take their standard interpretation. Hence H is the Jordan frame expansion rate determined using (4.27).¹⁴

Taking the results from our scan over the input parameter space, we numerically integrate the φ_* evolution equation (4.35) and determine the Jordan frame expansion rate H from (4.43). In doing so we have chosen values of β and $\varphi_{*\text{in}}$ that are (i) permitted by the astrophysical and dynamical constraints (according to figure 4.7) and (ii) provide the greatest deviation from the standard expansion history (see figure 4.4).

Substituting this result into (4.53) we solve the Boltzmann equation to determine the present dark matter density. The results are shown in figure 4.8 where we plot the ratio of the dark matter relic abundance in the scalar-tensor gravity model to the corresponding value in the standard cosmological scenario as a function of $\varphi_{*\text{in}}$ for different values of β . In the left and right panels of figure 4.8 we have calculated the relic abundance enhancement ratio $\Omega_{\text{DM}}^{\text{ST}}/\Omega_{\text{DM}}^{\text{GR}}$ for $m_\chi = 10$ GeV and $m_\chi = 100$ GeV respectively with the solid (dashed) curves corresponding to $s(p)$ -wave annihilation. Note that for the values of β chosen, namely $\beta = (2.4, 3.0, 4.0)$, we have only calculated results up to $\varphi_{*\text{in}} = (2.5, 2.0, 1.5)$ respectively because larger values of $\varphi_{*\text{in}}$ are excluded due to dynamical constraints (see figure 4.7).

In each panel we see that the ratio $\Omega_{\text{DM}}^{\text{ST}}/\Omega_{\text{DM}}^{\text{GR}}$ increases for small $\varphi_{*\text{in}}$ reaching a β -dependent maximum value before falling as $\varphi_{*\text{in}}$ increases further. For the $m_\chi = 10$ GeV and $m_\chi = 100$ GeV cases the maximum enhancement for s -wave annihilation is only $\Omega_{\text{DM}}^{\text{ST}}/\Omega_{\text{DM}}^{\text{GR}} \sim 1.5$ and 2.6 respectively and is obtained for $(\beta, \varphi_{\text{in}}) = (2.4, 1.8)$ in both

¹⁴In the universal coupling case there is a unique Jordan frame in which both the Standard Model particles and the dark matter particles couple directly to the metric $g_{\mu\nu}$. This situation becomes more complicated in non-universal scalar-tensor theories where the coupling with the *visible* and *dark* sectors is distinct (see section 4.9).

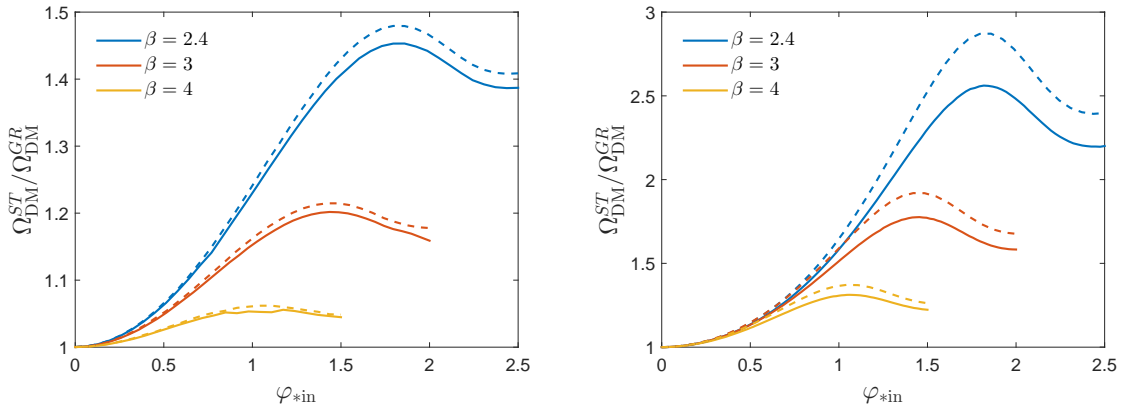


FIGURE 4.8: Ratio of the relic abundance of symmetric dark matter in the scalar-tensor and standard cosmological scenarios for $m_\chi = 10$ GeV (left panel) and $m_\chi = 100$ GeV (right panel) as a function of $\varphi_{*\text{in}}$ for different values of β . The solid (dashed) curves correspond to $s(p)$ -wave annihilation.

cases. For p -wave scattering and $m_\chi = 100$ GeV, this ratio increases to $\Omega_{\text{DM}}^{\text{ST}}/\Omega_{\text{DM}}^{\text{GR}} \sim 2.9$.

Because the lack of an algebraic expression for the Jordan frame expansion rate H (see (4.47)) inhibits our ability to derive an approximate analytical solution for the dark matter relic density, it is difficult to make any quantitative estimates for the ratio $\Omega_{\text{DM}}^{\text{ST}}/\Omega_{\text{DM}}^{\text{GR}}$ in terms of β and $\varphi_{*\text{in}}$. Although we expect that the relic density enhancement factor, $\Omega_{\text{DM}}^{\text{ST}}/\Omega_{\text{DM}}^{\text{GR}}$, is related to the magnitude of $\xi = H_{\text{ST}}/H_{\text{GR}}$ at dark matter decoupling, i.e. $\xi(T_f)$, the situation is still not straightforward given that the relationship between $\xi(T_f)$ and the input parameters β and $\varphi_{*\text{in}}$ is difficult to predict (see the discussion in section 4.5). We simply comment that the relic abundance curves displayed in figure 4.8 follow the same profile as the corresponding $\xi(T_f)$ curves evaluated at fixed $\varphi_{*\text{in}}$.

Most importantly, for the quadratic coupling $A(\varphi_*) = e^{\frac{1}{2}\beta\varphi_*^2}$ considered here, the maximum enhancement achieved is only ~ 2.9 which, for the equivalent WIMP mass, is much less than that observed in either the quintessential kination scenario considered in the previous chapter or the results reported by Catena *et al* [156, 159].

Moreover, we find no evidence for reannihilation. That is, during our scan over the input parameters we did not observe a secondary phase of dark matter annihilation following particle freeze-out. In the Catena *et al* 2004 paper [156], reannihilation was a consequence of the rapid relaxation of the scalar-tensor expansion rate towards the standard expansion rate, which they purport occurs *after* dark matter decoupling. However, we showed in section 4.4 that the attraction mechanism towards General Relativity is initiated when the temperature of the universe first drops below the rest masses of Standard Model particles at $T \gtrsim 10^2$ GeV. Even taking the most optimistic estimate that $x_f \sim 10$

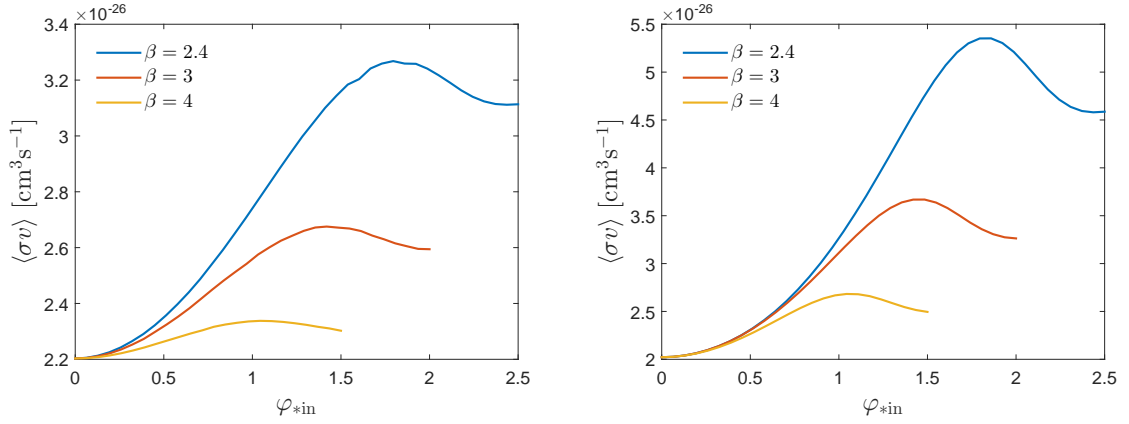


FIGURE 4.9: Required s -wave annihilation cross section $\langle\sigma v\rangle$ for symmetric dark matter for $m_\chi = 10$ GeV (left panel) and $m_\chi = 100$ GeV (right panel) as a function of φ_{*in} for different values of β .

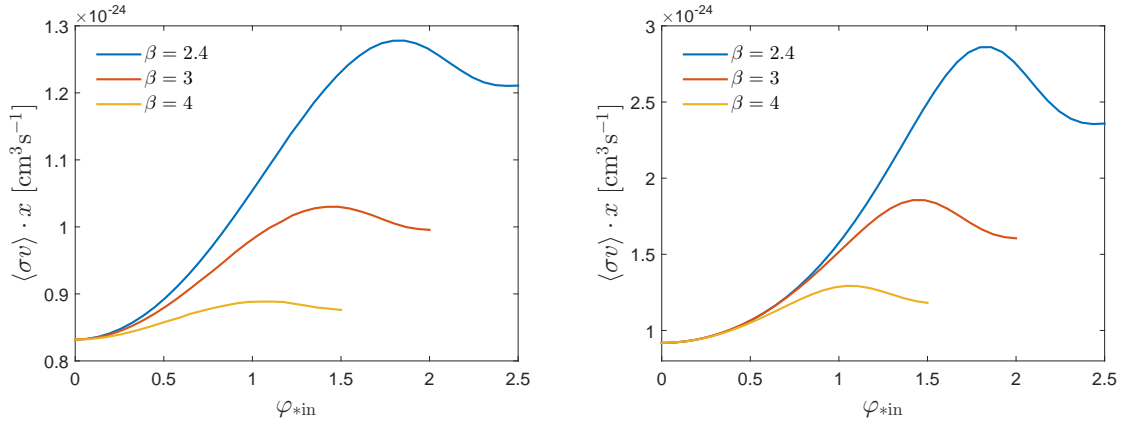


FIGURE 4.10: Same as figure 4.9 but for p -wave annihilation.

in the scalar-tensor scenario, a dark matter particle with $m_\chi = 50$ GeV (the same value used in figure 7 of [156]) would freeze out at $T_f = 5$ GeV. Therefore, by the time the dark matter particles decouple from the thermal background the attraction mechanism is typically well underway and the scalar-tensor expansion rate is already relatively close to the standard result.

As in the quintessence chapter we can invert our results for the relic density to determine the annihilation cross section required to produce the observed dark matter density. The results are plotted in figures 4.9 and 4.10 for the s - and p -wave annihilation cases respectively and show similar behaviour to the relic density curves given in figure 4.8.

In this case we find it unnecessary to compare our results with the Fermi-LAT data since the enhancement factors are so small the Fermi-LAT bounds would not be able to significantly constrain the allowed model parameters.

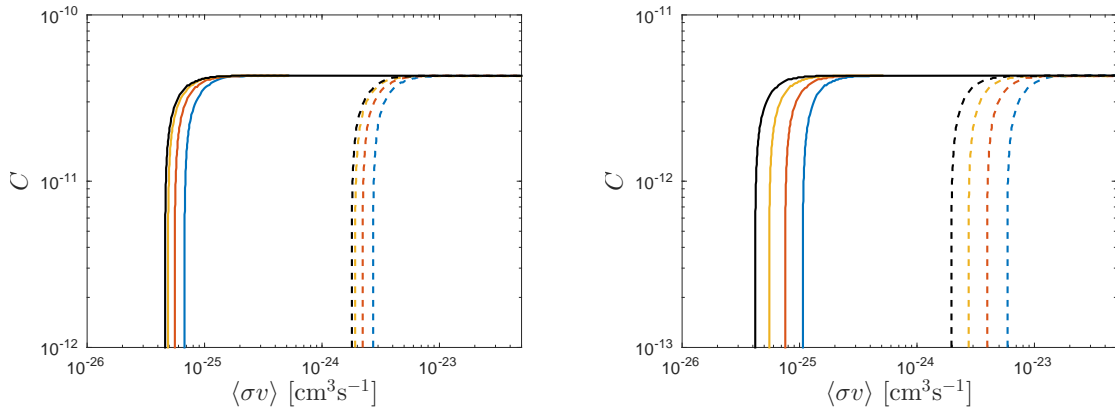


FIGURE 4.11: Iso-abundance contours in the $(\langle\sigma v\rangle, C)$ plane for asymmetric dark matter corresponding to the observed dark matter abundance $\Omega_{\text{DM}}h^2 = 0.1188$ for $m_\chi = 10$ GeV (left panel) and $m_\chi = 100$ GeV (right panel). The blue, red and yellow curves correspond to the input parameters $(\beta, \varphi_{*in}) = (2.4, 2.0)$, $(3.0, 2.0)$ and $(4.0, 1.5)$ respectively and the black curves correspond to the standard cosmology result. We have calculated the results for both s - (solid) and p - (dashed) wave annihilation.

4.8 Asymmetric dark matter

For completeness we also determine the relic abundance of asymmetric dark matter particles in scalar-tensor gravity. Since the symmetric annihilation cross section is only enhanced slightly, we expect a similarly small enhancement for the asymmetric annihilation cross section.

The relic abundance of asymmetric dark matter in scalar-tensor gravity has very recently been studied by Gelmini *et al* [173] and Wang *et al* [175]. However these studies are based upon the enhancement factor (4.1) and also neglect the temperature dependence of $g_*(T)$. This allowed the development of approximate analytic solutions for $Y_\chi(\infty)$ and $Y_{\bar{\chi}}(\infty)$ similar to (2.46) and (2.47). However, as we do not have an algebraic expression for the enhancement factor $\xi = H_{ST}/H_{GR}$ (see (4.47)), this is not possible here.

In figure 4.11 we plot the iso-abundance contours in the $(\langle\sigma v\rangle, C)$ plane corresponding to the observed dark matter density $\Omega_{\text{DM}}h^2 = 0.1188$. The results have been calculated for both $m_\chi = 10$ GeV (left panel) and $m_\chi = 100$ GeV (right panel) for both the s - (solid) and p - (dashed) wave cases.

Because the vertical asymptote is only slightly shifted from the standard cosmology result (black curve) we do not expect the asymmetric detection signal to differ appreciably in the scalar-tensor gravity scenario. However, because the curves are still shifted, it is possible to have a stronger asymmetric detection signal in the scalar-tensor scenario compared with the symmetric signal in the standard scenario.

Unsurprisingly, these results are much less dramatic than those given by Gelmini *et al* [173] and Wang *et al* [175] who found that the required annihilation cross section can be increased by several orders of magnitude.

4.9 Non-universal scalar-tensor theories

4.9.1 Visible and Dark Jordan frames

The formalism and results derived thus far only apply for the special class of scalar-tensor theories known as *universal* scalar-tensor theories in which each of the different matter fields experiences the same coupling $A(\varphi_*)$. Here we consider a more general arrangement where the coupling to each matter sector is distinct. Specifically, we will consider the case studied by Coc *et al* 2009 [254] where the coupling between the scalar field and the *visible* (or Standard Model) sector, denoted $A_V(\varphi_*)$, is distinct from that between the scalar field and the *dark* sector, $A_D(\varphi_*)$.¹⁵ After demonstrating how the cosmological equations given in section 4.3 are generalized to the non-universal case, we will discuss the implications for the derivation of the Boltzmann equation.

To begin, we introduce a generalized version of the Einstein frame action (4.9),

$$S_{\text{tot}} = \frac{1}{16\pi G_*} \int d^4x \sqrt{-g_*} [R_* - 2g_*^{\mu\nu} \partial_\mu \varphi_* \partial_\nu \varphi_* - 4V(\varphi_*)] \\ + S_V[A_V^2(\varphi_*)g_{\mu\nu}^*; \Psi_V] + S_D[A_D^2(\varphi_*)g_{\mu\nu}^*; \Psi_D], \quad (4.54)$$

where S_V and S_D are the action integrals for the visible, Ψ_V , and dark, Ψ_D , matter fields respectively. Following the prescription given in section 4.2, we can apply the conformal transformation

$$g_{\mu\nu}^V = A_V^2(\varphi_*)g_{\mu\nu}^* \quad (4.55)$$

to remove the coupling from the visible sector matter action so that the fields Ψ_V couple to the metric $g_{\mu\nu}^V$ directly. The action integral (4.54) then becomes

$$S_{\text{tot}} = \frac{1}{16\pi G_*} \int d^4x \sqrt{-g_V} [F(\varphi)R_V - g_V^{\mu\nu} Z(\varphi) \partial_\mu \varphi \partial_\nu \varphi - 2U(\varphi)] \\ + S_V[g_{\mu\nu}^V; \Psi_V] + S_D[B^2(\varphi_*)g_{\mu\nu}^V; \Psi_D]; \quad (4.56)$$

¹⁵This set-up is different from that considered by Catena *et al* in [172] in which they introduced a new *hidden* matter sector and included dark matter within the visible sector.

where the connection between φ and φ_* , and the definitions of the functions $F(\varphi)$, $Z(\varphi)$ and $U(\varphi)$, are given in (4.10) with $A(\varphi_*)$ replaced by $A_V(\varphi_*)$. Also, we have defined

$$B(\varphi_*) = \frac{A_D(\varphi_*)}{A_V(\varphi_*)}. \quad (4.57)$$

Although the visible sector action $S_V[g_{\mu\nu}^V; \Psi_V]$ is independent of the scalar field in this new frame, the term $S_D[B^2(\varphi_*)g_{\mu\nu}^V; \Psi_D]$ still contains a scalar coupling. In fact, in the general case $A_V \neq A_D$ it is not possible to transform to a conformal frame in which both the visible and dark sectors couple directly to the same metric, that is, there is no unique definition of the Jordan frame. Therefore we must distinguish between two separate Jordan frames: the Visible Jordan Frame (VJF) defined by the metric $g_{\mu\nu}^V$; and the Dark Jordan Frame (DJF) defined by

$$g_{\mu\nu}^D = A_D(\varphi_*)g_{\mu\nu}^* = B(\varphi_*)g_{\mu\nu}^V. \quad (4.58)$$

In the VJF and DJF respectively, the visible and dark sector matter fields do not experience the scalar coupling and particle properties (e.g. mass, energy, cross sections) and their interactions take their standard form.

Similar to (4.14), we can define the parameters that characterize the deviation from General Relativity as

$$\alpha_j(\varphi_*) = \frac{d \ln A_j(\varphi_*)}{d\varphi_*}, \quad (4.59)$$

where $j = V, D$ labels the different matter sectors.

In the non-universal case the cosmological equations (4.22) and (4.23) for the evolution of the Einstein frame scale factor a_* remain unaltered. However, the matter fields of each sector obey separate continuity equations

$$\frac{d\rho_{*j}}{dt_*} + 3H_* (\rho_{*j} + p_{*j}) = \alpha_j(\varphi_*) (\rho_{*j} - 3p_{*j}) \dot{\varphi}_*. \quad (4.60)$$

This implies (following our discussion above) that the visible (dark) sector matter fields are no longer conserved in the DJF (VJF) so that, for example, in the VJF we have

$$\begin{aligned} \rho_{Vi} &= \rho_{Vi}^0 \left(\frac{a_V}{a_{V0}} \right)^{-3(1+w_i)}, \\ \rho_D &= \rho_D^0 \left[\frac{B(\varphi_*)}{B(\varphi_{*0})} \right]^{4-3(1+w_D)} \left(\frac{a_V}{a_{V0}} \right)^{3(1+w_D)}, \end{aligned} \quad (4.61)$$

where i labels the different visible fluid components and ρ_D is the dark matter energy density as measured in the VJF.

Moreover, the equation of motion (4.24) for the scalar field is generalized to

$$\ddot{\varphi}_* + 3H_*\dot{\varphi}_* + \frac{\partial V}{\partial \varphi_*} = -4\pi G_* \sum_{j=V,D} \alpha_j (\rho_{*j} - 3p_{*j}). \quad (4.62)$$

Finally, the connection between the Einstein frame expansion rate and the VJF and DJF expansion rates is given by

$$H_j = A_j^{-1}(\varphi_*) [H_* + \alpha_j(\varphi_*)\dot{\varphi}_*]. \quad (4.63)$$

Coc *et al* 2009 [254] have studied the BBN constraints on models with quadratic couplings

$$A_j(\varphi_*) = e^{\frac{1}{2}\beta_j\varphi_*^2} \quad (j = V, D). \quad (4.64)$$

In particular, they studied regions in the (β_V, β_D) parameter space for which there is late time attraction towards GR and then derived additional constraints on the parameter space from BBN and precision gravitational tests.

4.9.2 Boltzmann equation

Before attempting to calculate the dark matter relic abundance, we should first pause to contemplate whether, in the non-universal coupling case, the assumptions made in deriving the Boltzmann rate equation (2.6) (see Appendix C) remain valid.

Starting with the fundamental form of the Boltzmann equation,

$$\hat{L}[f(x^\mu, p^\mu)] = \hat{C}[f(x^\mu, p^\mu)] \quad (4.65)$$

where $f(x^\mu, p^\mu)$ is the dark matter distribution function, \hat{L} is the relativistic Liouville operator and \hat{C} is the collision operator, the first question to address is in which frame should we formulate the problem? Given that the subject of the calculation, the dark matter particles, couple directly to the metric $g_{\mu\nu}^D$, the obvious answer is the DJF. Then, proceeding as in Appendix C we can determine the zeroth moment of (4.65) by integrating both sides of the equation over momentum space.

To evaluate the integral of the Liouville operator, we note that the conformal transformation (4.58) conserves both the isotropy and homogeneity of the VJF metric $g_{\mu\nu}^V$ so that the dark matter distribution function, which is defined in the DJF, reduces to

$f(x^\mu, p^\mu) = f(E, t)$.^{16,17} Therefore, we recover the standard expression (see Appendix C)

$$\frac{g}{(2\pi)^3} \int \hat{L}[f(E, t)] \frac{d\vec{p}}{E} = \frac{dn_D}{dt_D} + 3H_D n_D \quad (4.67)$$

where $n_D \equiv n_D(t_D)$ and t_D are the dark matter number density and time as defined in the DJF.

However, the evaluation of the collision term in (4.65) is not so straightforward. The change in the dark matter particle number is governed by reactions of the type

$$\chi\bar{\chi} \leftrightarrow X\bar{X} \quad (4.68)$$

where the χ 's are the dark matter particles and the X 's are particles belonging to the visible sector. In the non-universal case the particles on either the left or right hand side of the reaction (4.68) will either be susceptible or immune to the scalar interaction depending on the choice of conformal frame of reference; there is no conformal frame in which the scalar coupling vanishes for both sides of the reaction. Therefore, if we decide to formulate the Boltzmann equation in the DJF we must account for the varying φ_* dependent masses, energies, cross sections, etc. of the visible particles. Of course, transforming to the VJF does not alleviate the problem because then dark matter particles would be φ_* -dependent.

A proper analysis of the problem would require a thorough reexamination of the derivation of the Boltzmann equation and in particular the evaluation of the collision integral. Since this is beyond the scope of the present study we leave it as a suggestion for future work.

4.10 Summary

The inherent attraction mechanism exhibited by many scalar-tensor gravity models towards General Relativity allows for deviations from the standard cosmological scenario in the early universe that may not show up in present observational data. In fact, we originally conjectured that relic abundance calculations may be one of the few probes

¹⁶Observations of the isotropy and homogeneity of the universe are made with Standard Model particles and therefore apply to the VJF.

¹⁷In general, a conformal transformation is a *local* rescaling of the metric,

$$\tilde{g}_{\mu\nu} = \Omega^2(x)g_{\mu\nu}, \quad (4.66)$$

that only preserves the isotropy of spacetime and not homogeneity. But, if the conformal factor is a function of time only, i.e. $\Omega(x^\mu) \equiv \Omega(t)$, as in (4.58), then homogeneity is conserved also.

capable of discriminating the predictions of scalar-tensor scenarios from standard General Relativity. To find out, we determined the evolution of the coupled scalar field from first principles, allowing us to calculate the modified expansion rate in the scalar-tensor gravity scenario, which we then used to calculate the dark matter relic abundance.

As a specific example we considered the prototypical quadratic coupling $A(\varphi_*) = e^{\frac{1}{2}\beta\varphi_*^2}$ and found that the maximum enhancement for a $m_\chi = 100$ GeV WIMP was $\Omega_{\text{DM}}^{ST}/\Omega_{\text{DM}}^{GR} \sim 3$. Although this ratio would increase with increasing WIMP mass, the level of enhancement is still far below that observed in both the previous chapter for the quintessential kination model and in previous relic abundance investigations in scalar-tensor cosmology [156, 159].

Interestingly, we showed in figure 4.4 that the expansion rate at the time of dark matter decoupling in the scalar-tensor scenario can be up to several orders of magnitude larger than the expansion rate in the standard scenario. However, these points were excluded by BBN constraints [176]; had these points been acceptable, we would have found much larger relic density enhancement factors, possibly in line with those reported in [156] and [159]. Given that detailed BBN constraints for the couplings $A(\varphi_*) = 1 + Be^{-\beta\varphi_*}$ and $A(\varphi_*) = 1 + b\varphi_*^2$, considered in [156] and [159] respectively, were not applied in their investigations because a study equivalent to [176] was not available, we suggest that the allowed expansion rate in those models may be much smaller than previously reported, and that the level of enhancement of the dark matter relic abundance might actually be much closer to the levels found here.

To complete our study we also investigated the relic abundance of asymmetric dark matter species in scalar-tensor gravity models and found that the required annihilation cross section was enhanced only slightly, in contrast to the several order of magnitude estimates given in Gelmini *et al* [173] and Wang *et al* [175] who both used the parameterization (4.1) given in Catena *et al* [156].

Finally, since the attraction mechanism towards GR is typically initiated prior to dark matter freeze-out so that the effect on the dark matter relic abundance is only modest, the scalar-tensor scenario with a quadratic coupling to matter does not provide a significantly different picture from the standard cosmological scenario. Hence, we conclude that unless reasonably precise details about the nature of the dark matter particle and its interactions are known, relic abundance calculations are most likely unable to discriminate scalar-tensor gravity from General Relativity.

Chapter 5

Randall-Sundrum Braneworlds

5.1 Introduction

In the braneworld scenario, our universe is modelled as a 3(+1) dimensional surface (the *brane*) embedded in a higher dimensional spacetime known as the *bulk* [255, 256].¹ Standard Model particles are confined to the surface of the brane whilst gravity is free to propagate in the bulk. In several models with compact extra dimensions this offers an explanation for the apparent weakness of gravity with respect to the other fundamental forces [151, 261].

In this chapter we focus on the Randall-Sundrum type II (RSII) (1-brane) model [150] which is generally considered the simplest and most appealing of the braneworld scenarios. In this model, General Relativity (GR) is recovered on the surface of a 3(+1) Minkowski brane located at the ultraviolet boundary of a five dimensional Anti-de Sitter bulk.² The warped geometry of the bulk spacetime ensures the fifth dimension is only accessible in the ultraviolet regime and that Λ CDM is reproduced in the low energy limit.

Interestingly, the Friedmann equation in the RSII braneworld cosmology is modified from the standard expression and predicts an enhanced early time expansion rate. This has significant implications for several early universe phenomena (including providing a

¹For introductory reviews on the braneworld scenario see [257–260].

²Minkowski space is the four dimensional generalization of flat Euclidean space whilst Anti-de Sitter space is a maximally symmetric space with a negative curvature constant.

possible resolution to the gravitino problem³ [262–265]), the most pertinent of which is dark matter decoupling.⁴

In [155], Okada and Seto (see also [262]) showed that the dark matter relic abundance can be enhanced by several orders of magnitude if the ‘transition temperature’, at which the modified expansion law in the brane world cosmology reduces to the standard one, is low enough and derived approximate analytical expressions for the level of enhancement. Then, in a series of follow-up papers, they [263, 265, 270, 271] and others [264, 272–274] (see also [169, 221]), applied these results to specific supersymmetric particle models and, by assuming a particular dark matter particle candidate, were able to derive constraints on the five dimensional Planck mass, M_5 , which is often used to parameterize the deviation from the standard expansion law (see section 5.3).

In [224] the authors adopted a model-independent approach and assumed that the dark matter annihilation cross section is dominated by s -wave processes, taking $\langle\sigma v\rangle = \sigma_0$. As such, they were able to use the observed dark matter density to constrain the annihilation cross section as a function of the WIMP mass for varying M_5 . However, in their calculation, the authors chose to fix the number of degrees of freedom at $g_*(T) = 106.75$, which, as we will show, can lead to considerable errors.

Lastly, it was shown in [165, 224, 271] that the enhanced annihilation cross section required in the Randall-Sundrum braneworld model allows for a dark matter interpretation of the positron excess originally observed by the HEAT experiment and recently confirmed by PAMELA [95, 112] and AMS-02 [113].

In this chapter we study the modified evolution of the dark matter density in the braneworld scenario for both s - and p -wave dominated annihilation cross sections and numerically verify the approximate analytical expressions derived in [155] (which are extensively quoted in the literature). In doing so, we dispute the claim made by [273] that, for some values of M_5 , the relic abundance in the braneworld scenario is suppressed. Next, we constrain the dark matter annihilation cross section for both the s - and p -wave cases using the observed dark matter density and compare our results with those presented in [224] (s -wave only) to highlight the importance of maintaining the full temperature dependence of $g_*(T)$, particularly for the s -wave case. We then compare the required annihilation cross section to the latest Fermi-LAT data, allowing us to

³In the standard cosmological scenario, gravitinos (the supersymmetric partner of the graviton) are overproduced and their energetic decay products disrupt the standard Big Bang Nucleosynthesis picture. In the braneworld scenario, the enhanced expansion rate dilutes the gravitino abundance and the problem is resolved.

⁴The braneworld cosmological effect also modifies both scalar and tensor primordial perturbations and the consistency relation between them [266, 267]. This results in larger tensor-to-scalar ratios r which were favoured by the recent BICEP2 measurement [139] with a simple quadratic inflation potential $V(\phi) = m^2\phi^2$ capable of reproducing the reported value $r \simeq 0.2$ [268]. However, with the withdrawal of the BICEP2 result (see [140]) the situation is unclear [269].

constrain the five dimensional Planck mass M_5 in a model-independent fashion. Finally, we generalize our discussion to the case of asymmetric dark matter, which, prior to our publication [178], had not been considered in a braneworld context, and show that the enhanced expansion rate in the RSII braneworld model implies an amplified asymmetric detection signal.

5.2 Randall-Sundrum II model

The field equations are derived from a total action of the form [149, 150, 275]

$$S_{\text{tot}} = S_{\mathcal{M}} + S_{\text{mat}} + S_{\Sigma}, \quad (5.1)$$

where $S_{\mathcal{M}}$ and S_{mat} are the bulk and brane action integrals and S_{Σ} is a boundary term required to cancel the extra contributions to the field equations induced by the presence of the brane. The bulk action integral taken over the five dimensional manifold \mathcal{M} is given by

$$S_{\mathcal{M}} = \frac{1}{2\kappa_5^2} \int_{\mathcal{M}} d^5x \sqrt{-g} (R - 2\Lambda_5) \quad (5.2)$$

where g is the determinant of the bulk metric g_{ab} ⁵, R is the five dimensional Ricci scalar (constructed from g_{ab}) and Λ_5 is the bulk cosmological constant. We define the constant κ_5 so that

$$\kappa_5^2 = 8\pi G_5 = M_5^{-3}, \quad (5.3)$$

where G_5 and M_5 are the five dimensional Newton's constant and Planck mass respectively.⁶ The matter fields, which are localized on the brane surface $\partial\mathcal{M}$, are included via

$$S_{\text{mat}} = - \int_{\partial\mathcal{M}} d^4x \sqrt{-h} L_{\text{mat}} \quad (5.4)$$

where h is the determinant of the induced metric $h_{\mu\nu}$ on the brane surface and L_{mat} is the matter field Lagrangian. Varying the total action S_{tot} with respect to the bulk metric field and solving the (0,0) component of the resulting equations, we obtain the modified Friedmann equation in the braneworld scenario [275] (see Appendix F)

$$H^2 = \frac{\kappa_5^4}{36} \rho_b^2 + \frac{\Lambda_5}{6} - \frac{k}{a^2} + \frac{\mathcal{C}}{a^4}, \quad (5.5)$$

where ρ_b is the total brane energy density, which is the sum of the brane tension $\sigma = 48\pi M_5^6/M_{\text{Pl}}^2$ and the energy density of brane matter fields ρ . Substituting $\rho_b = \rho + \sigma$

⁵Here, lower case indices run over the five dimensions of the bulk spacetime.

⁶Note that this definition of M_5 includes a factor of 8π and can therefore be considered as the *reduced* five dimensional Planck mass. This should be compared with our definition of the four dimensional Planck mass which does not include this factor and is defined as $M_{\text{Pl}} = G^{-1/2} = 1.22 \times 10^{19}$ GeV.

into (5.5) gives

$$H^2 = \left(\frac{\kappa_5^4}{36} \sigma^2 + \frac{\Lambda_5}{6} \right) + \frac{\kappa_5^4}{18} \sigma \rho + \frac{\kappa_5^4}{36} \rho^2 - \frac{k}{a^2} + \frac{C}{a^4}. \quad (5.6)$$

In the widely studied Randall-Sundrum type II (RSII) model [150], the brane tension is fine-tuned so that General Relativity is recovered on the brane surface. Choosing

$$\kappa_5^2 \sigma = \sqrt{-6\Lambda_5} \quad (5.7)$$

and introducing the Anti-de Sitter length scale, ℓ , via $\Lambda_5 = -6/\ell^2$, then the terms in the brackets cancel and the $\sigma\rho$ term in (5.6) becomes the canonical term $8\pi\rho/(3M_{\text{Pl}}^2)$ if we identify

$$\frac{8\pi}{M_{\text{Pl}}^2} = \frac{\kappa_5^2}{\ell}. \quad (5.8)$$

The expansion rate in the Randall-Sundrum model is then

$$H_{RS}^2 = \frac{8\pi}{3M_{\text{Pl}}^2} \rho \left(1 + \frac{\rho}{2\sigma} \right), \quad (5.9)$$

where the dark radiation term $\propto a^{-4}$, which is severely constrained by BBN considerations [276], has been omitted. Besides, the contribution from this term during the era of dark matter decoupling is negligible compared to that from the ρ^2 term.

A novel feature of (5.9) is the presence of the term quadratic in ρ . At high energies ($\rho \gg 2\sigma$) this term dominates the expansion and $H_{RS} \propto \rho$. Comparing this to the standard scenario where $H_{GR} \propto \rho^{1/2}$ we see that the early time expansion rate is enhanced in the RSII braneworld model. As the energy density drops ($\rho \ll 2\sigma$) the quadratic term becomes negligible and the standard expansion law is recovered.

Writing the modified Friedmann equation (5.9) in terms of the standard cosmology expression, we have

$$H_{RS}^2 = H_{GR}^2 [1 + Z_{RS}(T)] \quad (5.10)$$

where

$$Z_{RS}(T) \equiv \frac{\rho}{2\sigma} = g_{*\rho}(T) \frac{\pi}{2880} \frac{M_{\text{Pl}}^2}{M_5^6} T^4 \quad (5.11)$$

and we have used the Randall-Sundrum tuning to get $\sigma = 48\pi M_5^6/M_{\text{Pl}}^2$ and have assumed that $\rho \simeq \rho_r = \pi^2 g_{*\rho}(T) T^4/30$. In the following, we choose to use the five dimensional Planck mass, M_5 , as the free parameter that characterizes the departure from the standard expansion law.

In the RSII braneworld scenario, the modification to the Hubble factor, $Z_{RS}(T)$, grows as T^4 . Therefore, we expect larger deviations from the standard expansion history at early times in this model compared to the quintessence and scalar-tensor models considered

so far. To ensure the modified expansion rate in the RSII braneworld scenario does not disturb the successful predictions of Big Bang Nucleosynthesis we require $Z_{RS}(T_B) \lesssim 1$, which corresponds to $M_5 \gtrsim 1.1 \times 10^4$ GeV.⁷

We can also find the relevant upper limit to the five dimensional Planck mass required to modify particle decoupling which we will denote here as M_5^{\max} . Assuming freeze-out occurs at roughly $T_f \approx m_\chi/23$, the condition $Z_{RS}(T_f) \gtrsim 1$ implies $M_5 \lesssim M_5^{\max} = 2 \times 10^5 m_\chi^{2/3}$. Again we see that the modification will be amplified for heavier dark matter particles, since these particles freeze-out at higher temperatures, when the deviation from the standard expansion history is greater.

5.3 Symmetric dark matter

To begin, we compare the evolution of the comoving dark matter density $Y \equiv n_\chi/s$ in the RSII braneworld scenario to the corresponding result in the standard cosmology for both s - (figure 5.1) and p - (figure 5.2) wave domination and varying M_5 .⁸

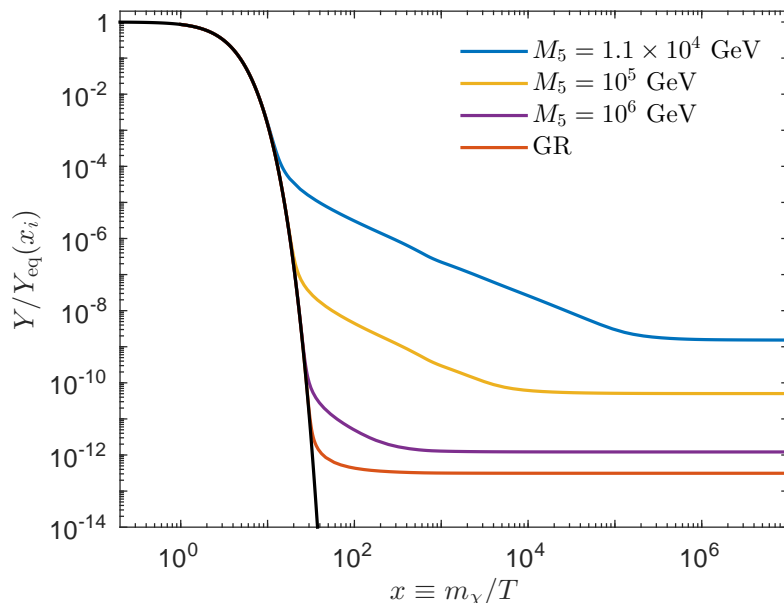


FIGURE 5.1: Evolution of the comoving density Y for varying M_5 as a function of $x \equiv m_\chi/T$ in the s -wave case. The results have been calculated for a dark matter particle with $m_\chi = 100$ GeV, $g_\chi = 2$ and $\langle\sigma v\rangle = 10^{-22}$ cm³s⁻¹. We have also plotted the density evolution in the standard GR scenario (red) for comparison as well as the equilibrium density (black).

⁷More stringent constraints have been placed on M_5 from sub-millimeter measurements of the gravitational force [277, 278] and the requirement of a vanishing cosmological constant, however these constraints are sensitive to the presence of a bulk scalar field [279] and will not be considered here.

⁸We have chosen a considerably larger dark matter annihilation cross section (compared to the quintessence case) in figures 5.1 and 5.2 to compensate for the much faster expansion rate in the RSII model.

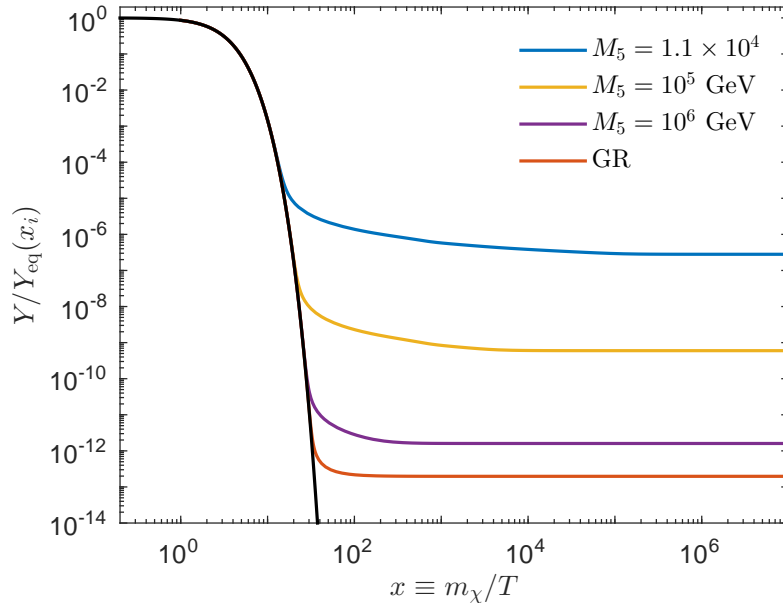


FIGURE 5.2: Same as figure 5.1 but for a p -wave dominated annihilation cross section, $\langle\sigma v\rangle = 10^{-20}/x \text{ cm}^3\text{s}^{-1}$.

Immediately we notice that the enhanced expansion rate in the Randall-Sundrum braneworld scenario leads to earlier particle freeze-out and an enhanced relic abundance, as expected. Interestingly, however, the post freeze-out evolution of the comoving density in the braneworld scenario is drastically modified compared to the standard behaviour (red curve) when the dark matter annihilation cross section is predominantly s -wave (figure 5.1). In this case, the comoving density, $Y(x)$, decays without saturation between particle freeze-out and freeze-in. This is because the dark matter annihilation rate $\Gamma = n_\chi\langle\sigma v\rangle$, which, when the dark matter particles have decoupled, usually scales as $\Gamma \sim T^3$, struggles to 'overtake' the enhanced expansion rate in the braneworld scenario, $H_{RS} \sim T^4$. As such, particle annihilations persist and the comoving density can decay by up to five orders of magnitude (depending on the value of M_5) before the standard expansion rate is restored and freeze-in occurs. This effect is absent for the p -wave case because, in this instance, the annihilation rate scales as $\Gamma \sim T^4$ and post freeze-out annihilations are damped.⁹ Consequently, for fixed M_5 , the relic abundance increases by a larger factor in the p -wave case than for the s -wave case. This behaviour is illustrated in figure 5.3 where we compare Γ (solid and dashed curves) with the expansion rate H (dot-dashed curves).

The trends observed in figures 5.1 and 5.2 can be predicted using the approximate solution (2.26),

$$Y(x) \simeq \left[\int_{x_f}^x \frac{s\langle\sigma v\rangle}{xH} dx \right]^{-1}, \quad (5.12)$$

⁹Similarly, this effect was not observed in the kination scenario considered in chapter 3 for either the s - or p -wave cases because the scaling of the kination expansion rate, $H_Q \sim T^3$, was not fast enough.

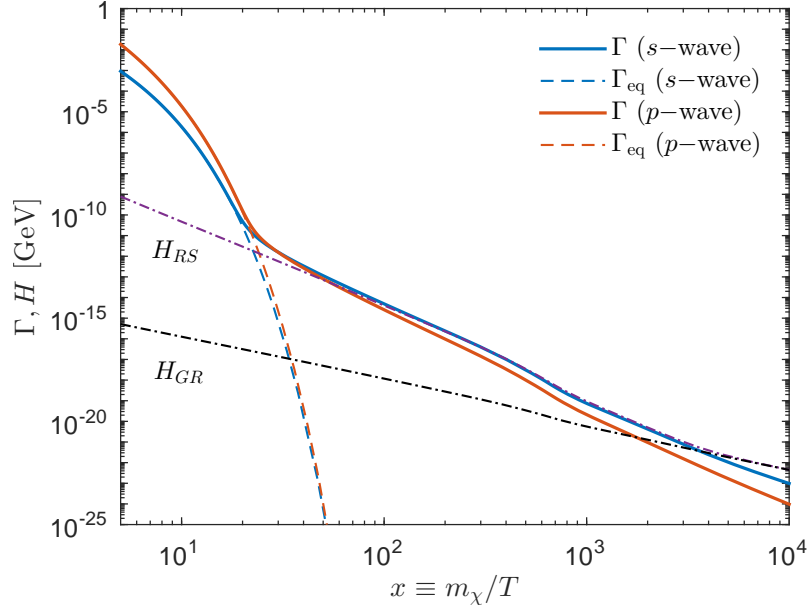


FIGURE 5.3: Comparison of the dark matter annihilation rate $\Gamma = n\langle\sigma v\rangle$ for both the s - (blue curve) and p -wave (red curve) annihilation cases compared to the braneworld expansion rate H_{RS} (dashed-dot purple curve). The results have been calculated assuming that $\langle\sigma v\rangle = 10^{-22} \text{ cm}^3\text{s}^{-1}$ for the s -wave case and $\langle\sigma v\rangle = 10^{-20} \text{ cm}^3\text{s}^{-1}$ p -wave case. We have also shown the equilibrium annihilation rates $\Gamma_{\text{eq}} = n_{\text{eq}}\langle\sigma v\rangle$ (dashed curves) and the standard cosmology expansion rate H_{GR} (dot-dashed black).

where, for now, we have replaced the upper limit in the integral by the variable x to study the post freeze-out behaviour in the RSII cosmology, leaving our discussion of the asymptotic solution for later. To evaluate (5.12) we first rewrite the RSII Hubble factor in terms of x :

$$H_{RS}^2 = H_{GR}^2 \left[1 + \left(\frac{x_t}{x} \right)^4 \right]. \quad (5.13)$$

Here, $x_t \equiv m_\chi/T_t$ denotes the transition point from the brane expansion era ($\rho \gg 2\sigma$) to the standard expansion era ($\rho \ll 2\sigma$) and is defined as

$$x_t^4 = g_{*\rho} \frac{\pi}{2880} \frac{m_\chi^4}{M_5^6} M_{\text{Pl}}^2. \quad (5.14)$$

We note that smaller values of M_5 give a larger x_t and a greater departure from the standard expansion history as mentioned in section 5.2. Substituting the expression (5.14) into (5.12) along with $s \simeq 0.439g_{*s}m_\chi^3/x^3$, and taking $\langle\sigma v\rangle = \sigma_n x^{-n}$, the integral becomes [155]

$$Y(x) \simeq \left[\lambda \sigma_n \int_{x_f}^x \frac{x^{-n}}{\sqrt{x^4 + x_t^4}} dx \right]^{-1}, \quad (5.15)$$

where $\lambda \simeq 0.264(g_{*s}/\sqrt{g_{*\rho}})m_\chi M_{\text{Pl}}$. In the limit $x \ll x_t$, this yields [155]

$$Y(x) \simeq \frac{x_t^2}{\lambda \sigma_0} (x - x_f)^{-1}; \quad n = 0 \text{ (s-wave)}, \quad (5.16)$$

and

$$Y(x) \simeq \frac{x_t^2}{\lambda \sigma_1} \left[\ln \left(\frac{x}{x_f} \right) \right]^{-1}; \quad n = 1 \text{ (} p\text{-wave)}. \quad (5.17)$$

The expressions (5.16) and (5.17) show that the comoving density $Y(x)$ continues to decay without saturation for $x_f < x < x_t$. This behaviour was originally observed in [155] and is a characteristic feature of braneworld cosmology.

Given the post freeze-out evolution in the braneworld scenario, we stress the importance of maintaining the full temperature dependence of $g_*(T)$ when integrating the Boltzmann equation (2.6). This term varies by more than an order of magnitude between $T \sim 10^3$ GeV and $T \sim 10^{-5}$ GeV (see figure B.1) and neglecting this effect can lead to significant errors (see figure 5.7).

Next, we show the enhancement factor $\Omega_{\text{DM}}^{\text{RS}}/\Omega_{\text{DM}}^{\text{GR}}$ for the relic density in the braneworld scenario, $\Omega_{\text{DM}}^{\text{RS}}$, compared to the corresponding standard cosmology result, $\Omega_{\text{DM}}^{\text{GR}}$, for both the s - and p -wave cases in figure 5.4. These results match (despite one key conclusion, see below) those contained in figure 1 of [280], which considers the p -wave case only.

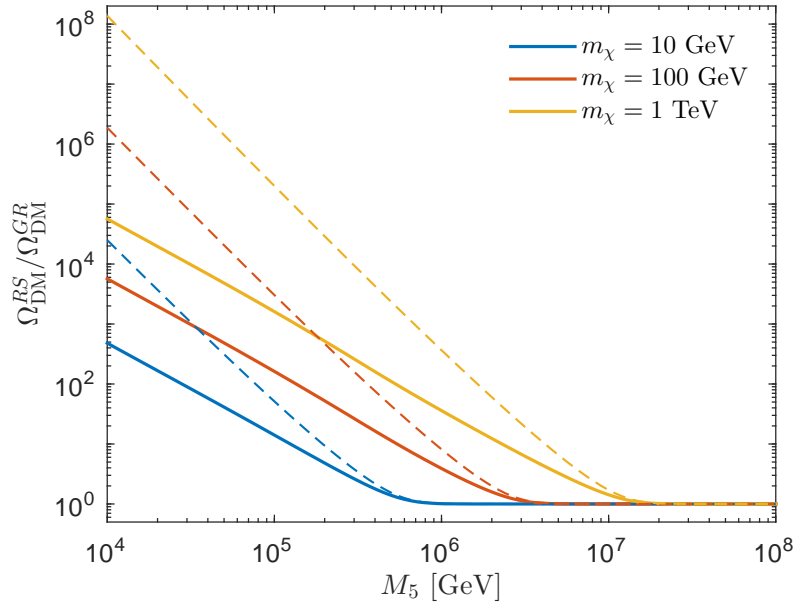


FIGURE 5.4: Ratio of the relic abundance in the braneworld scenario and the corresponding abundance in the standard scenario as a function of M_5 for varying WIMP mass. The results have been calculated for both s - (solid) and p -wave (dashed) cases with $\langle\sigma v\rangle = 10^{-22} \text{ cm}^3\text{s}^{-1}$ and $\langle\sigma v\rangle = 10^{-20}/x \text{ cm}^3\text{s}^{-1}$, respectively for the two cases.

At large M_5 the deviation from the standard expansion history at the time of dark matter decoupling is negligible and the brane world relic abundance saturates to the standard result. However, for smaller M_5 , dark matter decoupling is modified and the relic density can be enhanced by more than several orders of magnitude. In fact, for the smallest value of M_5 permitted by BBN constraints (namely, $M_5 \approx 1.1 \times 10^4$ GeV) we

find that in the s -wave case, the ratio $\Omega_{\text{DM}}^{\text{RS}}/\Omega_{\text{DM}}^{\text{GR}}$ can be as large as 400, 5000 and 5×10^4 for WIMP masses of $m_\chi = 10$ GeV, 100 GeV and 1 TeV respectively. The amplification is even larger in the p -wave case, with $\Omega_{\text{DM}}^{\text{RS}}/\Omega_{\text{DM}}^{\text{GR}}$ greater than 2×10^4 , 1.5×10^6 and 10^8 for $m_\chi = 10$, 100 and 1000 GeV respectively. The difference in amplification between the two cases follows from the different post freeze-out evolution in the s - and p -wave cases.

Lastly, we note that the scale at which the modification parameter M_5 becomes effective matches well the estimate given in the previous section, $M_5^{\text{max}} \sim 2 \times 10^5 m_\chi^{2/3}$, and is the same for both the s - and p -wave cases.

The authors [280] reported a slight suppression in the braneworld relic abundance for $M_5 \gtrsim 5 \times 10^6$ GeV when the annihilation cross section is dominated by p -wave processes. However, we find that the ratio $\Omega_{\text{DM}}^{\text{RS}}/\Omega_{\text{DM}}^{\text{GR}}$ is strictly greater than or equal to 1 for all values of M_5 , in contradiction to this claim.

We have also checked the sensitivity of $\Omega_{\text{DM}}^{\text{RS}}/\Omega_{\text{DM}}^{\text{GR}}$ to the dark matter annihilation cross section and found that when $\langle\sigma v\rangle$ is changed by an order of magnitude, this ratio changes by only 10 – 15%, indicating that the results in figure 5.4 are relatively insensitive to $\langle\sigma v\rangle$.

The asymptotic density can be estimated using (5.15) by taking the limit $x \rightarrow \infty$, in which case we get [155]

$$Y(\infty) \simeq 0.54 \frac{x_t}{\lambda \sigma_0}; \quad n = 0 \text{ (} s \text{- wave)}, \quad (5.18)$$

and

$$Y(\infty) \simeq \frac{x_t^2}{\lambda \sigma_1 \ln(x_t)}; \quad n = 1 \text{ (} p \text{- wave)}. \quad (5.19)$$

In deriving (5.18) and (5.19) we have also assumed that $x_t \gg x_f^{\text{RS}}$ where x_f^{RS} is the freeze-out point in the Randall-Sundrum scenario given by

$$x_f^{\text{RS}} \simeq \ln [(2+c)\lambda\sigma_n ac/x_t^2] - \left(n - \frac{3}{2}\right) \ln \{ \ln [(2+c)\lambda\sigma_n ac/x_t^2] \}. \quad (5.20)$$

Therefore, these expressions are only valid if particle decoupling occurs deep in the braneworld expansion era. Interestingly, the asymptotic densities in both the s - and p - wave cases depend on the transition point, x_t , between the braneworld and standard expansion eras instead of the freeze-out point x_f . Inserting the expression for the transition point (5.14), we see that the asymptotic density scales as $Y(\infty) \sim M_5^{-3/2}$ and $Y(\infty) \sim M_5^{-3}/\ln M_5$ in the s - and p -wave cases respectively.

Comparing these results with the standard approximation (2.28), we see that for the s -wave ($n = 0$) case, the relic density in the Randall-Sundrum braneworld model is boosted by a factor of [155]

$$\frac{\Omega_{\text{DM}}^{\text{RS}}}{\Omega_{\text{DM}}^{\text{GR}}} \simeq 0.54 \frac{x_t}{x_f^{\text{GR}}} \quad (5.21)$$

and for the p -wave ($n = 1$) case, by a factor of

$$\frac{\Omega_{\text{DM}}^{\text{RS}}}{\Omega_{\text{DM}}^{\text{GR}}} \simeq \frac{x_t^2}{2 \left(x_f^{\text{GR}}\right)^2 \ln x_t}. \quad (5.22)$$

These two approximate expressions, which are frequently quoted in the literature (in particular the s -wave result), are compared to the numerical results in figures 5.5 and 5.6 for the s - and p -wave cases respectively.

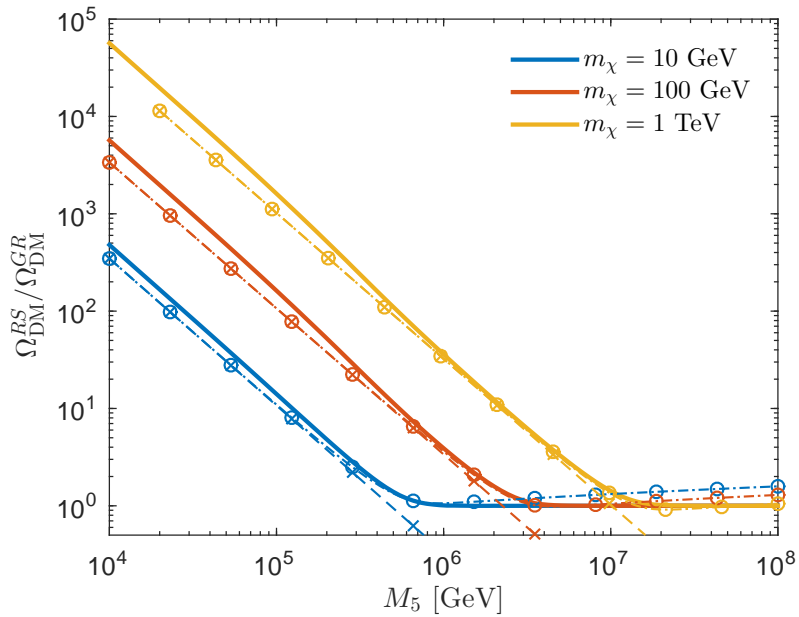


FIGURE 5.5: Comparison of the numerical results (solid) and the approximate expression (5.21) (dashed with crosses) and (5.23) (dot-dashed with open circles) for the braneworld enhancement ratio $\Omega_{\text{DM}}^{\text{RS}}/\Omega_{\text{DM}}^{\text{GR}}$ for the s -wave case using the same parameter values as figure 5.4.

In general, we find that both approximations give predictions below the numerical result. Even in the limit $x_t \gg x_f^{\text{RS}}$ the difference can be as large as 70%, indicating that the expressions (5.21) and (5.22) should only be used as a rough estimate.

However, we can improve our approximate results by abandoning the assumption $x_t \gg x_f^{\text{RS}}$, and by evaluating the integral (5.15) for the general case. This gives [155]

$$Y(\infty) \simeq \frac{x_f^{\text{RS}}}{\lambda \sigma_0} \left\{ {}_2F_1 \left[\frac{1}{4}, \frac{1}{2}; \frac{5}{4}; - \left(\frac{x_t}{x_f^{\text{RS}}} \right)^4 \right] \right\}^{-1}; \quad s\text{-wave} \quad (5.23)$$

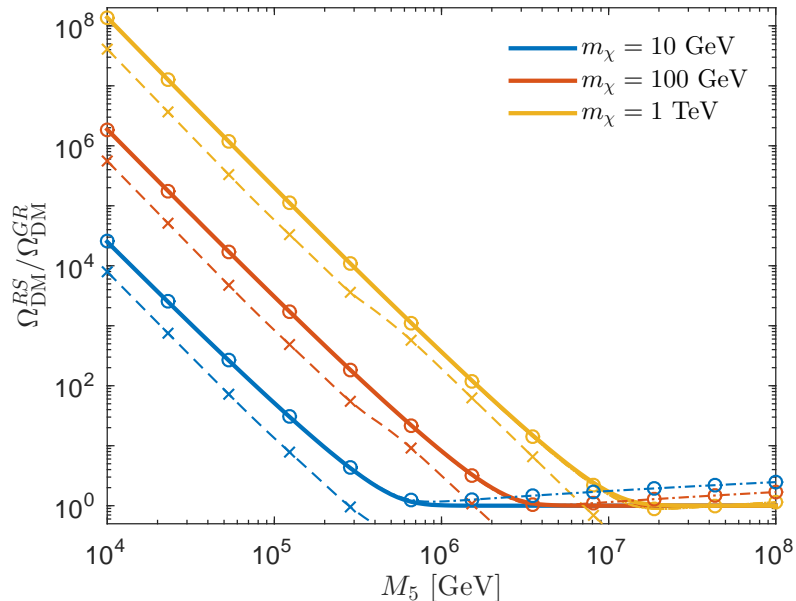


FIGURE 5.6: Comparison of the numerical results (solid) and the approximate expression (5.22) (dashed with crosses) and (5.24) (dot-dashed with open circles) for the braneworld enhancement ratio $\Omega_{\text{DM}}^{\text{RS}}/\Omega_{\text{DM}}^{\text{GR}}$ for the p -wave case using the same parameter values as figure 5.4.

and

$$Y(\infty) \simeq \frac{2x_t^2}{\sinh^{-1}\left(x_t/x_f^{\text{RS}}\right)^2 \sigma_1}; \quad p\text{-wave}, \quad (5.24)$$

where ${}_2F_1[a, b; c; x]$ is the hypergeometric function.

In figures 5.5 and 5.6 we have also shown the approximations (5.23) and (5.24) (dot-dashed curves with open circles). In the s -wave case, the generalized approximation (5.23) performs almost as poorly as the simplified approximation (5.21). The reason neither expression can accurately reproduce the numerical results is because in the s -wave case, the comoving density continues to decay without saturation following particle freeze-out and the variation in $g_*(T)$, which we have assumed is fixed when evaluating the integral (5.15) for $Y(\infty)$, can modify the asymptotic value (see figure 5.7).

In contrast, for the p -wave case there is excellent agreement between the approximate solution (5.24) and the numerical results for $M_5 \lesssim 2 \times 10^5 m_\chi^{2/3}$, or, equivalently, $x_t \gtrsim x_f^{\text{RS}}$. This is because in the p -wave case the comoving density $Y(x)$ varies much less after particle freeze-out and the variation in $g_*(T)$ is less significant (see figure 5.8).

Following [224], we use the observed dark matter relic density, $\Omega_{\text{DM}} h^2 = 0.1188$, to constrain the dark matter annihilation cross section $\langle \sigma v \rangle$ as a function of the WIMP mass m_χ for varying M_5 . The results are shown in figures 5.7 and 5.8 for the s - and p -wave cases respectively. In each figure we have calculated the required annihilation cross section by first assuming that the number of relativistic degrees of freedom $g_*(T)$

is fixed (dashed curves), as in [224] where the authors set $g_*(T) = 106.75$ (and hence $\zeta(x) = 1$), and, then, by maintaining the full temperature dependence of $g_*(T)$ (solid curves).

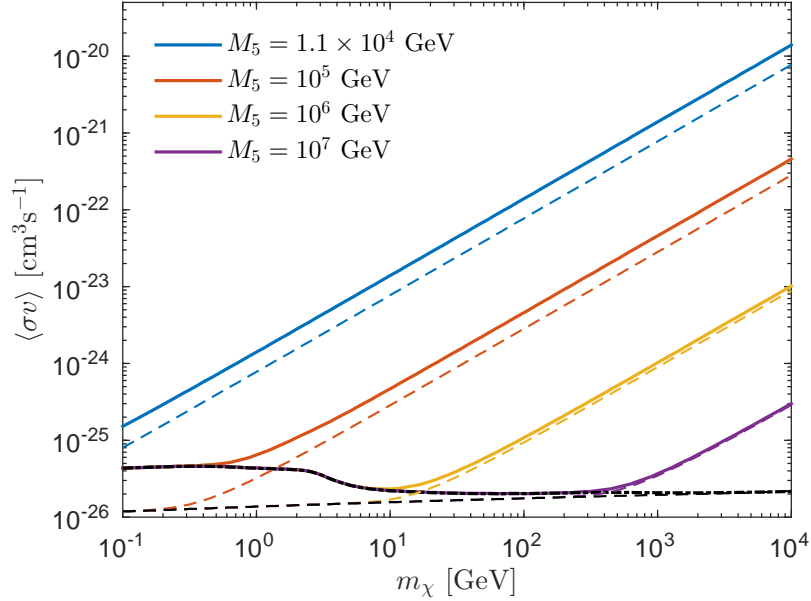


FIGURE 5.7: Required annihilation cross section (s -wave) in the braneworld scenario as a function WIMP mass for varying M_5 . The solid curves correspond to the varying $g_* = g_*(T)$ results, whereas the dashed curves have been calculated for fixed $g_* = 106.75$. The black curves correspond to the standard cosmology result.

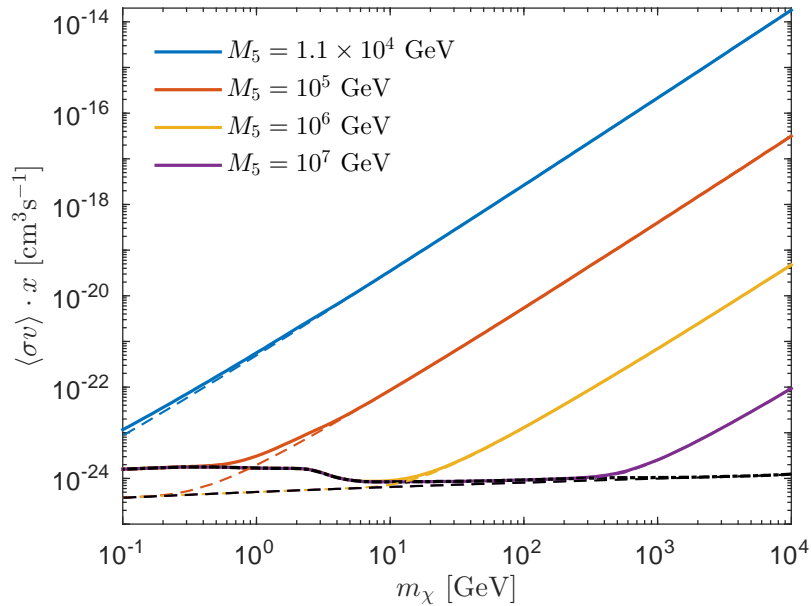


FIGURE 5.8: Same as figure 5.7 but for p -wave annihilation.

In the s -wave case (figure 5.7), the results show that neglecting the temperature dependence of $g_*(T)$ can produce large errors, reaching up to a factor of nearly two for small values of M_5 ; the error increases with decreasing M_5 because reducing M_5 extends the

gap between freeze-out and freeze-in and the change in $g_*(T)$ becomes more important. The p -wave results are much less sensitive to the variation in $g_*(T)$ and only differ for small WIMP masses, $m_\chi \lesssim 10$ GeV. Therefore, the results in [224], where they consider s -wave processes for fixed g_* , are inaccurate.

Variation in $g_*(T)$ aside, figures 5.7 and 5.8 show that the required annihilation cross section $\langle\sigma v\rangle$, much like the dark matter relic abundance, can be amplified by many orders of magnitude. For s -wave annihilation, $\langle\sigma v\rangle$ can be as large as $\sim 10^{-20}$ cm³s⁻¹ when the five dimensional Planck mass assumes its minimum allowed value $M_5 = 1.1 \times 10^4$ GeV and $m_\chi = 10$ TeV; and for p -wave annihilation, the cross section can be as large as $\sim 10^{-14}$ cm³s⁻¹. These two values are some four and ten orders of magnitude larger than their respective canonical values.

To estimate the required annihilation cross section, we can invert the approximate solutions (5.18) and (5.19), in which case we find that, for s -wave,

$$\sigma_0 \simeq 1.5 \times 10^8 \frac{m_\chi x_t}{\lambda \Omega_{\text{DM}} h^2} \text{ GeV}^{-2}, \quad (5.25)$$

and, for p -wave

$$\sigma_1 \simeq 2.75 \times 10^8 \frac{m_\chi x_t}{\lambda \Omega_{\text{DM}} h^2 \ln(x_t)} \text{ GeV}^{-2}. \quad (5.26)$$

Finally, in figure 5.9, we compare the s -wave results from figure 5.7 with the latest data from the Fermi-LAT satellite to constrain the five dimensional Planck mass, M_5 . This figure shows that values of $M_5 \lesssim 10^5$ GeV are mostly excluded (except in the low WIMP mass region where Fermi-LAT data is unavailable) for all annihilation channels studied. That said, values of the five dimensional Planck mass as small as $M_5 \simeq 10^6$ GeV are certainly permitted and even satisfy the most stringent constraints arising from the $u\bar{u}$ and $b\bar{b}$ annihilation channels.

5.4 Asymmetric dark matter

To complete our discussion, we extend the findings from the previous section to asymmetric dark matter models and use the observed dark matter abundance to constrain M_5 and the asymmetry parameter $C \equiv Y_\chi - Y_{\bar{\chi}}$. The results, which are presented in figures 5.10 and 5.11, have been extracted from our publication [178].

In figures 5.10 (s -wave) and 5.11 (p -wave) we plot the contours in the $(\langle\sigma v\rangle, C)$ plane that give the correct relic abundance for varying M_5 for $m_\chi = 10$ GeV (left) and $m_\chi = 100$ GeV (right). The red and yellow curves correspond to $M_5 = 10^6$ GeV and $M_5 = 10^5$ GeV respectively and the blue curve gives the standard cosmology result.

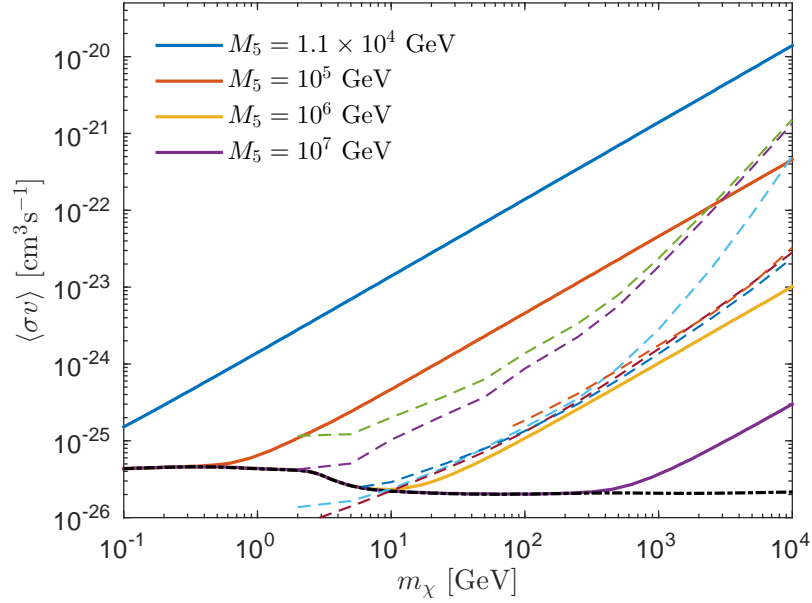


FIGURE 5.9: Required s -wave annihilation cross section in the braneworld scenario as a function WIMP mass for varying M_5 . We have also included the standard cosmology result (dashed black) for reference as well as the Fermi-LAT constraints for the e^+e^- (dashed purple), $\mu^+\mu^-$ (dashed green), $\tau^+\tau^-$ (dashed light blue), $u\bar{u}$ (dashed maroon), $b\bar{b}$ (dashed blue) and W^+W^- (dashed red) annihilation channels.

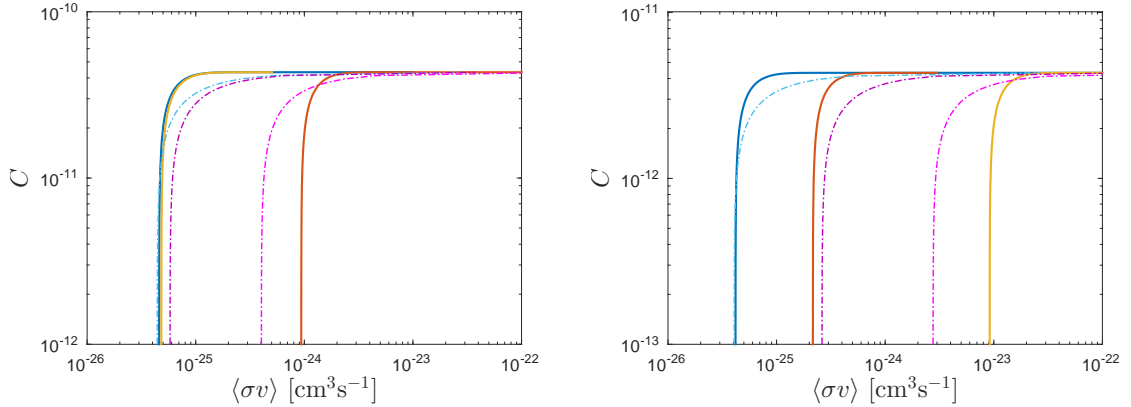
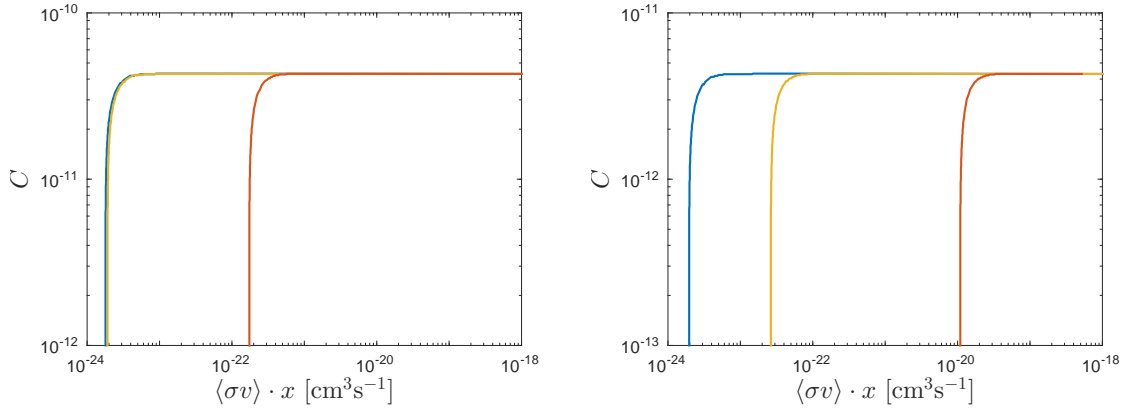


FIGURE 5.10: Iso-abundance contours in the $(\langle\sigma v\rangle, C)$ plane for s -wave annihilation corresponding to the observed dark matter abundance $\Omega_{DM}h^2 = 0.1188$ for $m_\chi = 10$ GeV (left) and $m_\chi = 100$ GeV (right). The contours shown are for $M_5 = 10^6$ GeV (solid red curve) and $M_5 = 10^5$ GeV (solid yellow curve). Also shown is the standard cosmology result (solid blue curve). We have superimposed the constraints derived from the Fermi-LAT gamma ray data [125] with the regions below the dark purple and magenta (dot-dashed) curves excluded for the $\mu^+\mu^-$ and $b\bar{b}$ annihilation channels respectively. We have also indicated the region (below the dot-dashed blue curve) for which the asymmetric detection signal in the Randall-Sundrum scenario exceeds the symmetric signal in the standard scenario.

FIGURE 5.11: Same as figure 5.10 but for p -wave annihilation.

The faster expansion rate in the braneworld scenario shifts the required annihilation cross section towards higher values (to the right in figures 5.10 and 5.11), and in the limit $x_t \gg x_f$, the relationship between the annihilation cross section and the asymmetry can be derived using (2.53) and (5.18),

$$\sigma_0 \simeq \frac{1.08 x_t}{\lambda C} \coth^{-1} \left(\frac{\omega}{C} \right); \quad s - \text{wave} \quad (5.27)$$

and (5.19)

$$\sigma_1 \simeq \frac{2 x_t^2}{\lambda C \ln x_t} \coth^{-1} \left(\frac{\omega}{C} \right); \quad p - \text{wave} \quad (5.28)$$

where $\omega = \Omega_{\text{DM}} h^2 / (2.75 \times 10^8 m_\chi)$.

Just as we saw in the quintessence model (chapter 3), the enhanced annihilation cross section in the braneworld scenario indicates that the asymmetric annihilation rate can produce a detectable signal that is even stronger than the symmetric signal predicted in the standard scenario. From section 2.4.6 this situation is realized if,

$$\langle\sigma v\rangle_{GR} < \gamma \langle\sigma v\rangle_{RS} \quad (5.29)$$

where $\langle\sigma v\rangle_{GR}$ and $\langle\sigma v\rangle_{RS}$ are the symmetric and asymmetric annihilation cross sections in the standard and braneworld cosmological scenarios respectively, and $\gamma \equiv 2Y_\chi Y_{\bar{\chi}} / (Y_\chi + Y_{\bar{\chi}})^2$ is a damping factor induced by the asymmetry between the particles, χ , and antiparticles, $\bar{\chi}$. The dashed-dot blue line in figure 5.10 indicates the boundary $\langle\sigma v\rangle_{GR} = \gamma \langle\sigma v\rangle_{RS}$ with the region below this curve satisfying the condition (5.29).

In figure 5.10 we have also indicated the upper limit to the annihilation cross section derived from the Fermi-LAT data for the $\mu^+ \mu^-$ (dot-dashed magenta) and $b\bar{b}$ (dot dashed purple) for illustration only, with the allowed region lying to the left of these curves. Combining the Fermi-LAT constraints with the condition (5.29), we see that the allowed

region capable of producing an enhanced asymmetric detection signal is given by

$$\langle\sigma v\rangle_{GR} < \gamma\langle\sigma v\rangle_{RS} < \langle\sigma v\rangle_{\text{Fermi}}, \quad (5.30)$$

where $\langle\sigma v\rangle_{\text{Fermi}}$ is the annihilation cross section derived from the Fermi-LAT data, and lies between the dot-dashed blue and dot-dashed magenta(purple) curves in figure 5.10. Although this region is smaller for the $m_\chi = 10$ GeV case, owing to the more stringent Fermi-LAT constraints, figure 5.10 shows that an enhanced asymmetric annihilation signal is certainly possible.

5.5 Summary

In this chapter we have investigated the relic abundance of dark matter in the Randall-Sundrum type II braneworld model and numerically verified the analytical results derived in [155]. Specifically, we have shown that the dark matter relic abundance can be enhanced by up to a factor of $\sim 40m_\chi$ and $\sim 100m_\chi^2$ for the s - and p -wave cases respectively when the five dimensional Planck mass assumes the minimum value permitted by BBN constraints, namely $M_5 = 1.1 \times 10^4$ GeV. These results should be compared with the corresponding enhancement factors found in the kination scenario (see chapter 3) where the maximum enhancement only reached $\mathcal{O}(10m_\chi)$ for both the s - and p -wave cases. The larger enhancement factors produced here derive from the faster expansion rate in the braneworld scenario which scales as $H_{RS} \sim T^4$ compared with the kination scenario where $H_Q \sim T^3$.

Notably, we have disputed the claim made by [273] that for $M_5 \gtrsim 5 \times 10^6$ GeV the relic abundance in the braneworld scenario is suppressed. Instead, we find that the ratio $\Omega_{\text{DM}}^{RS}/\Omega_{\text{DM}}^{GR}$ is strictly greater than or equal to 1 for all values of M_5 . This result follows naturally from the fact that the braneworld expansion rate H_{RS} is greater than (or equal to) the standard expansion rate H_{GR} at all times.

We also used the observed dark matter density to constrain the annihilation cross section as a function of WIMP mass for varying M_5 in both the s - and p -wave dominated cases. We found that neglecting the temperature dependence of the number of degrees of freedom $g_*(T)$, as done in [224], can incur errors by up to a factor of two. Then, comparing these results to Fermi-LAT data we were able to place model-independent constraints on the five dimensional Planck mass M_5 and found that values of $M_5 \lesssim 10^5$ GeV are excluded for all annihilation channels considered, however, values as small as $M_5 \gtrsim 10^6$ GeV are still permitted.

Finally, within the context of asymmetric dark matter models, we found that the enhanced annihilation cross section required by the faster braneworld expansion rate leads to an enhanced asymmetric detection signal. In particular, we showed that the asymmetric detection signal in the RSII braneworld model can be even larger than the symmetric signal in the standard cosmological scenario, whilst still respecting the Fermi-LAT observations.

The Randall-Sundrum type II model represents a first attempt to phenomenologically realize some of the complex ideas arising from string theory and M-theory. In the next chapter we consider a more complete example in this direction; an extended version of the RSII model that incorporates a higher order curvature correction in the bulk action integral, known as the Gauss-Bonnet term.

Chapter 6

Gauss-Bonnet Braneworlds

6.1 Introduction

In this chapter we consider an extension of the RSII model which incorporates a Gauss-Bonnet (GB) higher order curvature term in the bulk action integral, thus modifying the braneworld dynamics at high energies.¹ The relic density of dark matter in the Gauss-Bonnet braneworld scenario has been studied by Okada and Okada in [158] for the case of symmetric dark matter. The GB braneworld effect is treated approximately through the use of a simple multiplicatively modified Hubble expansion which can be interpreted as a multiplicatively modified annihilation cross section in the Boltzmann rate equation and allows the development of an approximate analytic expression for the asymptotic relic abundance. They found that the expansion rate was reduced in the GB model, delaying particle freeze-out and leading to a suppressed relic abundance. This is in direct contrast to the behaviour observed in the RSII braneworld model. This finding, however, is based upon a highly contrived situation in which the Gauss-Bonnet expansion era evolves directly into a standard General Relativity expansion era, rather than passing through a Randall-Sundrum expansion era as is the general case. This collapse of the RS era requires equating the mass scale m_α of the GB modification and the mass scale m_σ of the brane tension. However, if the GB contribution is to be considered as the lowest order correction from string theory to the RS action, we would expect $m_\alpha > m_\sigma$. It is therefore important to investigate the effect upon the relic abundance of choosing more realistic values for the ratio $\mathcal{R}_m \equiv m_\alpha/m_\sigma$ of these two mass scales.

¹The inclusion of a GB term also affects early universe inflation and the magnitude of scalar and tensor primordial perturbations. For recent studies see [267, 281–285].

In this chapter we revisit the calculation of the relic abundance of dark matter in the GB scenario and study the effects of breaking the assumption $\mathcal{R}_m = 1$ made by [158], replacing it by more realistic values. We also extend the investigation to consider both symmetric and asymmetric dark matter species and discuss the implications for dark matter detection experiments and dark matter particle models.

In the next section we introduce the action integral for the braneworld bulk which includes the Gauss-Bonnet higher order curvature term and discuss the modified Friedmann equation in this model. Then, in section 6.3, we calculate the dark matter relic abundance in the Gauss-Bonnet braneworld scenario before deriving constraints on the GB model parameters using the observed relic density. This is repeated for the case of asymmetric dark matter in section 6.4 and, finally, in section 6.5 we summarize our results.

6.2 Gauss-Bonnet Braneworlds

The Randall-Sundrum braneworld model derived from the five dimensional Einstein-Hilbert action can be considered as a low energy effective model of some higher order field theory such as string theory or M-theory [286]. Since our interest in the model lies in the high energy regime where additional quantum corrections in the bulk action may contribute to the braneworld dynamics, we include the leading order correction from heterotic string theory, known as the Gauss-Bonnet term L_{GB} [287], which is given by²

$$L_{GB} = R^2 - 4R_{ab}R^{ab} + R^{abcd}R_{abcd}. \quad (6.1)$$

Inclusion of higher order curvature terms generally leads to fourth order equations of motion. However, in five dimensions, the GB combination of invariants constructed from the Riemann tensor R_{abcd} is of particular significance since it is the unique combination that leads to second order gravitational field equations in the bulk metric which are symmetric, divergenceless and ghost free [288].³

Inclusion of the Gauss-Bonnet term modifies the Randall-Sundrum action so that the action integral for the GB braneworld model, taken over the five dimensional bulk space-time \mathcal{M} , is

$$S_{\mathcal{M}} = \frac{1}{2\kappa_5^2} \int_{\mathcal{M}} d^5x \sqrt{-g} [R - 2\Lambda_5 + \alpha L_{GB}], \quad (6.2)$$

²Here, lower case indices run over the five dimensions of the bulk spacetime.

³By ghosts we mean negative-norm 'tachyonic' states that violate unitarity.

where g is the determinant of the bulk metric g_{ab} , R is the five dimensional Ricci scalar and $\Lambda_5 (< 0)$ is the bulk cosmological constant. We have parameterized the GB contribution through the coupling α which, if this contribution is to be considered as the lowest order correction from string theory to the Randall-Sundrum action, must satisfy [281, 282] $|\alpha R^2| \ll |R|$. Consequently, $\alpha \ll \ell^2$ where ℓ is the bulk curvature scale $|R| \propto \ell^{-2}$. Introducing the associated energy scale $\mu \equiv \ell^{-1}$, we then require

$$\beta \equiv 4\alpha\mu^2 \ll 1. \quad (6.3)$$

The matter fields, which are localized on the brane surface $\partial\mathcal{M}$, are included via

$$S_{\text{mat}} = - \int_{\partial\mathcal{M}} d^4x \sqrt{-h} [L_{\text{mat}} + \sigma], \quad (6.4)$$

where h is the determinant of the induced metric $h_{\mu\nu}$ on the brane surface, L_{mat} is the matter field Lagrangian and $\sigma (> 0)$ is the brane tension. Varying the total action $S_{\text{tot}} = S_{\mathcal{M}} + S_{\text{mat}}$ (+ boundary terms) with respect to the metric field, and solving the resulting field equations, yields the modified Friedmann equation for the GB braneworld scenario [289, 290]

$$\kappa_5^2 (\rho + \sigma) = 2\mu \sqrt{1 + \frac{H^2}{\mu^2}} \left(3 - \beta + 2\beta \frac{H^2}{\mu^2} \right), \quad (6.5)$$

where ρ is the energy density of matter fields on the brane and $\beta = 1 - \sqrt{1 + 4\alpha\Lambda_5/3}$.

The modified Friedmann equation (6.5) clearly predicts non-standard behaviour for the expansion of the universe. However, in the low energy limit, equation (6.5) reduces to the standard expansion law for a flat universe

$$H^2 = \frac{8\pi}{3M_{\text{Pl}}^2} \rho + \frac{\Lambda_4}{3}, \quad (6.6)$$

provided we identify [284]⁴

$$\kappa_4^2 \equiv \frac{8\pi}{M_{\text{Pl}}^2} = \frac{\mu}{1 + \beta} \kappa_5^2. \quad (6.7)$$

Additionally, requiring that the four dimensional cosmological constant Λ_4 vanishes gives

$$\kappa_5^2 \sigma = 2\mu (3 - \beta), \quad (6.8)$$

which is equivalent to the familiar Randall-Sundrum tuning (5.7) in the limit $\alpha \rightarrow 0$.

⁴For comparison with the previous chapter, we note that μ and β are related to the five dimensional Planck mass M_5 via

$$M_5^3 = \frac{\mu}{1 + \beta} \frac{M_{\text{Pl}}^2}{8\pi}.$$

As shown in [291], it is possible to solve equation (6.5) to get an explicit expression for the Hubble factor H ;

$$H^2 = \frac{\mu^2}{\beta} \left[(1 - \beta) \cosh \left(\frac{2\chi}{3} \right) - 1 \right], \quad (6.9)$$

where χ is related to the energy density ρ via

$$\rho + m_\sigma^4 = m_\alpha^4 \sinh \chi, \quad (6.10)$$

and the two mass scales m_α and m_σ , which correspond to the GB correction and the brane tension respectively, are given by

$$m_\alpha^4 = \sqrt{\frac{8\mu^2(1-\beta)^3}{\beta\kappa_5^4}}, \quad m_\sigma^4 = \sigma. \quad (6.11)$$

Substituting in the constraints (6.7) and (6.8), m_α and m_σ can be written in terms of the two remaining free parameters μ and β as

$$m_\alpha^4 = 2 \frac{\mu^2}{\kappa_4^2} \sqrt{\frac{2(1-\beta)^3}{\beta(1+\beta)^2}}, \quad m_\sigma^4 = 2 \frac{\mu^2}{\kappa_4^2} \left(\frac{3-\beta}{1+\beta} \right). \quad (6.12)$$

Since the Gauss-Bonnet term is a high energy correction to the regular Randall-Sundrum action, we expect $\beta \ll 1$. This motivates us to introduce the quantity

$$\mathcal{R}_m \equiv \frac{m_\alpha}{m_\sigma} = \left[\frac{2(1-\beta)^3}{\beta(3-\beta)^2} \right]^{1/8}, \quad (6.13)$$

which measures the ratio of the two mass scales and depends only on β . The two mass scales are equal for $\beta = 0.1509$ but, as we expect $\beta \ll 1$, the general situation will be $\mathcal{R}_m > 1$.

Before choosing specific values of β , we first discuss the evolution of the modified expansion rate in the generalized Gauss-Bonnet scenario. By expanding (6.5) in the high, intermediate, and low energy limits, we see that the Hubble factor evolves through three distinct expansion regimes, characterized by the mass scales m_α and m_σ [158, 281]:

1. the GB regime: $\rho \gg m_\alpha^4$

$$H^2 \simeq \left(\frac{1+\beta}{4\beta} \mu \kappa_4^2 \rho \right)^{2/3}, \quad (6.14)$$

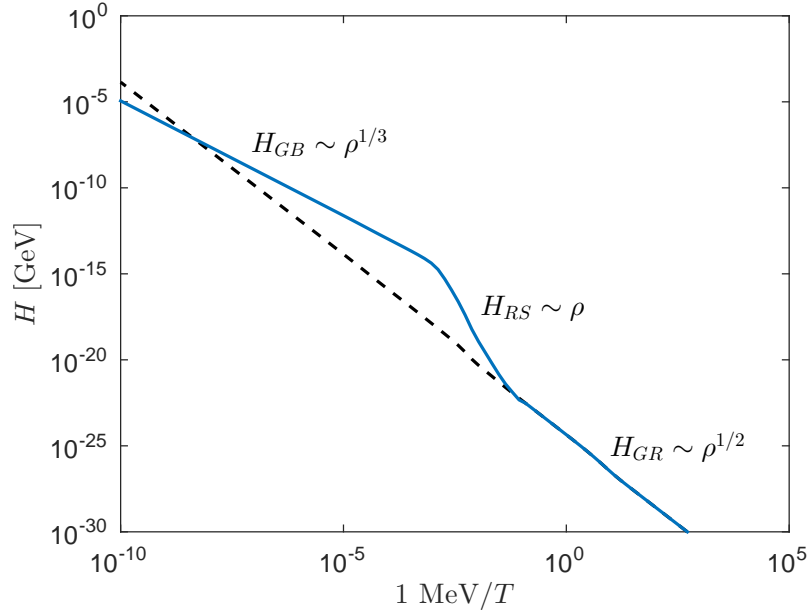


FIGURE 6.1: Modified expansion rate in the Gauss-Bonnet scenario (solid blue curve) for $\mu = 10^{-22}$ GeV and $\beta = 10^{-15}$. We have assumed that the energy density is radiation dominated for the period shown, taking $\rho = \rho_r = \pi^2 g_*(T)T^4/30$. The various expansion regimes through which the Hubble parameter evolves are indicated, together with the standard expansion rate (dashed black curve) for reference.

2. the RS regime: $m_\alpha^4 \gg \rho \gg m_\sigma^4$

$$H^2 \simeq \frac{\kappa_4^2}{6m_\sigma^4} \rho^2, \quad (6.15)$$

3. the standard regime: $m_\sigma^4 \gg \rho$

$$H^2 \simeq \frac{\kappa_4^2}{3} \rho. \quad (6.16)$$

At early times, during the Gauss-Bonnet regime, the expansion rate of the universe $H \sim \rho^{1/3}$ falls more slowly than the standard expansion law $H \sim \rho^{1/2}$. Later, the universe evolves into a Randall-Sundrum type era with an enhanced expansion $H \sim \rho$, before finally reducing to the standard expansion law in the low energy limit (see figure 6.1). The duration of the Randall-Sundrum regime is determined by the magnitude of $\mathcal{R}_m \equiv m_\alpha/m_\sigma$: when \mathcal{R}_m is small, the RS era is short and the expansion rate passes quickly from the Gauss-Bonnet era to the standard era; when \mathcal{R}_m is large, the duration of the Randall-Sundrum era is extended. Using the expression for \mathcal{R}_m (equation (6.13)) we see that these two cases correspond to $\beta \lesssim 0.1509$ and $\beta \rightarrow 0$, respectively.

The investigation by [158] chose to collapse the Randall-Sundrum era by equating $m_\alpha = m_\sigma$, setting $\beta = 0.1509$. In this case, the early time expansion rate is always slower than (or equal to) the standard expansion rate. The slower expansion rate delays dark matter particle freeze-out and suppresses the relic abundance. This is obviously a contrived

scenario considering the Gauss-Bonnet term is a high energy correction to the Randall-Sundrum action and we expect $m_\alpha > m_\sigma$, corresponding to $\beta \ll 1$. In the next section we will show that the unnatural choice of $\beta = 0.1509$ and the conclusions drawn in [158] misrepresent the typical behaviour of the relic density in the Gauss-Bonnet braneworld model and that, in fact, the dark matter abundance tends to be enhanced rather than suppressed when realistic values of β are used.

To determine which parameter values sufficiently modify the early time expansion rate so as to affect dark matter decoupling, we first rewrite equations (6.14) and (6.15) in terms of the dimensionless parameter $x \equiv m_\chi/T$,

$$H_{GB} = H_{GR} \left(\frac{x}{x_t^{GB}} \right)^{2/3}, \quad (6.17)$$

$$H_{RS} = H_{GR} \left(\frac{x_t^{RS}}{x} \right)^2, \quad (6.18)$$

where

$$(x_t^{GB})^4 \simeq 0.195 g_*(T_t) m_\chi^4 \left(\frac{\beta}{1+\beta} \right)^2 \frac{\kappa_4^2}{\mu^2}, \quad (6.19)$$

$$(x_t^{RS})^4 \simeq 0.082 g_*(T_t) m_\chi^4 \left(\frac{1+\beta}{3-\beta} \right) \frac{\kappa_4^2}{\mu^2}, \quad (6.20)$$

and we have assumed that the energy density at the time of decoupling is radiation dominated with $\rho_r = \pi^2 g_{*\rho}(T) T^4/30$. The quantity x_t^{RS} effectively denotes the transition point between the Randall-Sundrum expansion era and the standard expansion era. Anticipating that particle freeze-out occurs at $x_f \gtrsim 10$, we can derive an upper limit $\mu \lesssim 3 \times 10^{-21} m_\chi^2$ GeV on the relevant range of μ ; for larger values, the standard expansion rate is restored prior to particle freeze-out and decoupling is unaffected.

Finally, in order to preserve the successful predictions of BBN, the standard expansion law H_{GR} must be restored prior to $T = 1$ MeV. Thus we require $x_t^{RS} \lesssim 10^3 m_\chi$, which, using (6.20), gives the conservative bound

$$\mu \gtrsim 1 \times 10^{-25} \text{ GeV}. \quad (6.21)$$

6.3 Symmetric Dark Matter

Before solving the Boltzmann equation (2.6) numerically, we first derive approximate analytic formulae for the asymptotic comoving density using the general expression (2.26)

derived in chapter 2,

$$Y(\infty) \simeq \left[\int_{x_f}^{\infty} \frac{s\langle\sigma v\rangle}{xH} dx \right]^{-1} \quad (6.22)$$

remembering that, in the Gauss-Bonnet braneworld scenario, the universe first passes through a Gauss-Bonnet and then a Randall-Sundrum type expansion era before relaxing to the standard expansion law (see previous section). Then, taking $H = H_{GB}$ (equation (6.17)), we find that if decoupling occurs during a Gauss-Bonnet type expansion regime [158],

$$Y_{\infty}^{GB} \simeq \frac{5}{3} \frac{(x_f^{GB})^{5/3}}{\lambda_{GB}\langle\sigma v\rangle}, \quad (6.23)$$

where, in terms of $\lambda_{GR} \simeq 0.264(g_{*s}/\sqrt{g_{*\rho}})m_{\chi}M_{\text{Pl}}$,

$$\begin{aligned} \lambda_{GB} &= \lambda_{GR} (x_t^{GB})^{2/3} \\ &\simeq \left[\left(\frac{\beta}{1+\beta} \right) g_*^2 \frac{m_{\chi}^5}{\mu\kappa_4^2} \right]^{1/3}. \end{aligned} \quad (6.24)$$

The GB freeze-out point is

$$x_f^{GB} \simeq \ln [(2+c)\lambda_{GB}\langle\sigma v\rangle ac] - \frac{7}{6} \ln \{ \ln [(2+c)\lambda_{GB}\langle\sigma v\rangle ac] \} \quad (6.25)$$

where $a \simeq 0.145(g_{\chi}/g_{*s})$ and $c \approx 0.6$ is a numerical constant. Similarly, if decoupling occurs during the Randall-Sundrum era, we get [155]

$$Y_{\infty}^{RS} \simeq \frac{0.54 x_t^{RS}}{\lambda_{GR}\langle\sigma v\rangle}, \quad (6.26)$$

which we note is independent of the freeze-out point x_f (provided $x_t^{RS} \gg x_f$).

Comparing equations (6.23) and (6.26) with the standard expression (2.28)

$$Y_{\infty}^{GR} \simeq \frac{x_f}{\lambda_{GR}\langle\sigma v\rangle}, \quad (6.27)$$

we see that the asymptotic comoving density can be either suppressed or enhanced depending on the relative magnitude of μ and β and the timing of particle decoupling. More specifically, if decoupling occurs during the Gauss-Bonnet era, the comoving density may be either enhanced or suppressed, whereas, if decoupling occurs during the Randall-Sundrum era, the comoving density is always enhanced.

In this chapter we consider only the s -wave annihilation case since our general conclusions relating to whether (rather than by how much) the relic density is enhanced or suppressed will be independent of whether $\langle\sigma v\rangle$ is s -wave or p -wave.

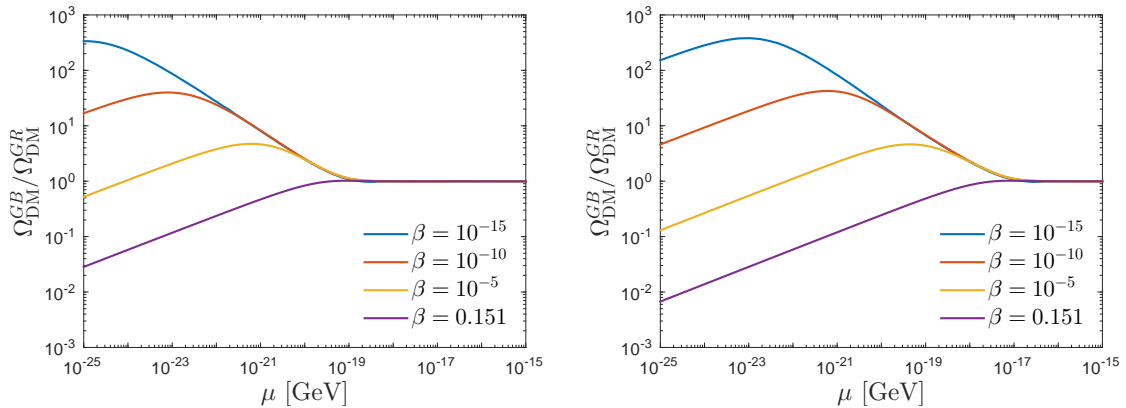


FIGURE 6.2: Ratio of the relic abundance in the GB scenario to the standard result for $\langle\sigma v\rangle = 2 \times 10^{-26} \text{ cm}^3\text{s}^{-1}$ as a function of μ for $\beta = 10^{-15}$ (blue curve), $\beta = 10^{-10}$ (red curve), $\beta = 10^{-5}$ (yellow curve) and $\beta = 0.151$ (purple curve). The left and right panels correspond to WIMP masses $m_\chi = 10 \text{ GeV}$ and 100 GeV respectively.

To determine which parameter combinations lead to suppression, and which lead to enhancement, we can equate equations (6.23) and (6.26) with the standard cosmology result (6.27). Rearranging for μ , we find that the relic abundance is enhanced for the interval⁵

$$7 \times 10^{-22} m_\chi^2 \left(\frac{\beta}{1 + \beta} \right) \lesssim \mu \lesssim 3 \times 10^{-21} m_\chi^2, \quad (6.28)$$

and suppressed for

$$\mu \lesssim 7 \times 10^{-22} m_\chi^2 \left(\frac{\beta}{1 + \beta} \right). \quad (6.29)$$

For $\mu \gtrsim 3 \times 10^{-21} m_\chi^2$, the standard expansion rate is restored prior to particle decoupling and the predicted value of $\Omega_{\text{DM}} h^2$ reduces to the canonical result.

In figure 6.2 we plot the ratio of the predicted relic abundance in the general Gauss-Bonnet scenario to the standard cosmology result as a function of μ for varying β . Immediately we see that the ratio $\Omega_{\text{DM}}^{\text{GB}}/\Omega_{\text{DM}}^{\text{GR}}$ (much like the expansion rate H) can be split up into three distinct regions: for small μ (and large β), the relic density increases with increasing μ (and decreasing β), reaching a maximum that is approximately given by⁶

$$\Omega_{\text{DM}}^{\text{max}} h^2 \sim 9 \times 10^{-11} \left(\beta^{1/5} \langle\sigma v\rangle \right)^{-1}; \quad \mu_{\text{max}} \sim 5 \times 10^{-22} (m_\chi \beta^{1/5})^2 \text{ GeV}. \quad (6.30)$$

In this region, decoupling occurs during the Gauss-Bonnet expansion era and the relic density can be estimated using (6.23). Next, for $\mu \gtrsim \mu_{\text{max}}$, the relic density decreases with increasing μ and is relatively independent of β . Here, decoupling occurs during

⁵To derive (6.28) and (6.29) we have assumed that the freeze-out point is roughly constant. In doing so we have neglected a logarithmic dependence on the annihilation cross section $\langle\sigma v\rangle$.

⁶The parameter dependence of the maximum can be derived by equating (6.23) with (6.26). Note, however, that the numerical constants are only approximate because we have not taken into account the variation in x_f .

the Randall-Sundrum era and each curve approaches the Randall-Sundrum result [155]. Finally, when $\mu \gtrsim 3 \times 10^{-21} m_\chi^2$, each curve reduces to the standard cosmology result. Hence, for the purpose of estimating the relic density, three approximate regimes can be identified:

$$\mu \lesssim 5 \times 10^{-22} m_\chi^2 \beta^{2/5} \quad : \quad \text{GB regime} \quad (6.31)$$

$$5 \times 10^{-22} m_\chi^2 \beta^{2/5} \lesssim \mu \lesssim 3 \times 10^{-21} m_\chi^2 \quad : \quad \text{RS regime} \quad (6.32)$$

$$\mu \gtrsim 3 \times 10^{-21} m_\chi^2 \quad : \quad \text{GR regime} \quad (6.33)$$

within which equations (6.23), (6.26) and (6.27) for Y_∞ would be appropriately used.

Figure 6.2 shows that the dark matter relic abundance may be either enhanced or suppressed by up to two or more orders of magnitude, depending on the values of μ and β . We must stress, however, that as the value of β is reduced, the predicted relic density tends towards the Randall-Sundrum result, and is therefore enhanced. Also, since $\mu \gtrsim 10^{-25}$ GeV is bounded from below by BBN constraints, suppression is only possible if $\beta \gtrsim 1.4 \times 10^{-4} / m_\chi^2$, corresponding to the condition $\mathcal{R}_m \lesssim 3.3 m_\chi^{1/4}$. Furthermore, it is only for the particular case considered in [158], that is $\beta = 0.1509$ ($\mathcal{R}_m = 1$) (purple curve), that $\Omega_{\text{DM}} h^2$ is exclusively suppressed. In fact, for the parameter values considered in [158], we find that the authors underestimate the value of $\Omega_{\text{DM}} h^2$ by 15%. In any case, for reasonable values of β (and \mathcal{R}_m) the relic density is typically enhanced.

We can invert these results to find the annihilation cross section required to produce the observed relic density $\Omega_{\text{DM}} h^2 = 0.1188$. In figure 6.3 we plot this cross section as a function of μ for varying β along with the Fermi-LAT constraints [125]. The cross section, which is inversely proportional to $\Omega_{\text{DM}} h^2$, exhibits similar behaviour to the relic density curves presented in figure 6.2 in that the three regimes — Gauss-Bonnet, Randall-Sundrum and standard — are immediately apparent.

The required cross section in each regime can be estimated by rearranging the approximate expressions (6.23), (6.26) and (6.27) and substituting in the observed relic density $\Omega_{\text{DM}} h^2$. Thus, if decoupling occurs deep in the Gauss-Bonnet era, the required annihilation cross section is given by

$$\langle \sigma v \rangle \simeq 2.0 \times 10^{-22} \left(\frac{1 + \beta}{\beta} \frac{\mu}{m_\chi^2} \right)^{1/3} \frac{(x_f^{GB})^{5/3}}{\Omega_{\text{DM}} h^2} \text{ cm}^3 \text{ s}^{-1}. \quad (6.34)$$

Similarly, if decoupling occurs during the Randall-Sundrum era,

$$\langle \sigma v \rangle \simeq 9.4 \times 10^{-38} \left[\left(\frac{1 + \beta}{3 - \beta} \right) \frac{1}{\mu^2} \right]^{1/4} \frac{m_\chi}{\Omega_{\text{DM}} h^2} \text{ cm}^3 \text{ s}^{-1}, \quad (6.35)$$

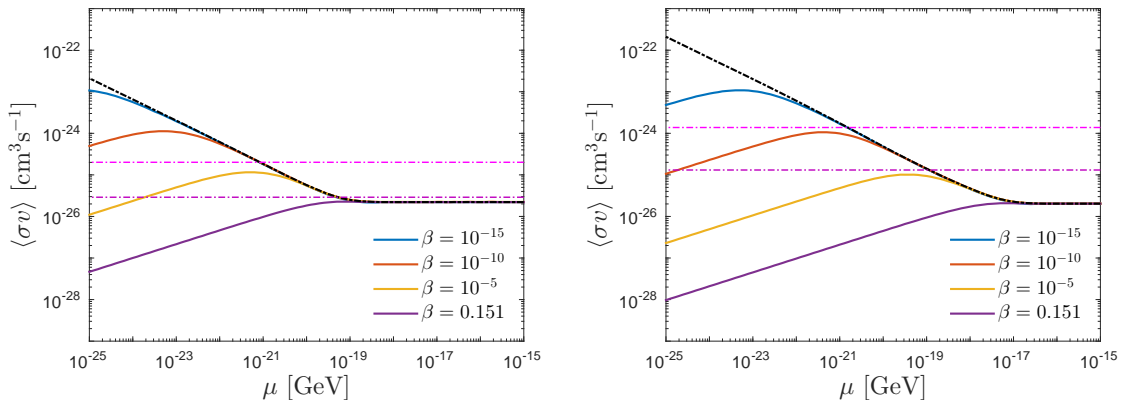


FIGURE 6.3: Required annihilation cross section $\langle\sigma v\rangle$ for a symmetric WIMP as a function of μ for $\beta = 10^{-15}$ (blue curve), $\beta = 10^{-10}$ (red curve), $\beta = 10^{-5}$ (yellow curve) and $\beta = 0.151$ (purple curve). Also shown is the corresponding result for a pure Randall-Sundrum scenario (dot-dashed black curve) as well as the Fermi-LAT constraints [125] for the $b\bar{b}$ (dot-dashed purple) and $\mu^-\mu^+$ (dot-dashed magenta) channels. The left and right panels correspond to WIMP masses $m_\chi = 10$ GeV and 100 GeV respectively.

which is relatively independent of β . For $\mu \gtrsim 3 \times 10^{-21} m_\chi^2$, the transition point x_t^{RS} precedes the freeze-out point and we recover the canonical result $\langle\sigma v\rangle \simeq \langle\sigma v\rangle_{GR} \simeq 2.03 \times 10^{-26} \text{ cm}^3\text{s}^{-1}$ and $\langle\sigma v\rangle \simeq \langle\sigma v\rangle_{GR} \simeq 2.21 \times 10^{-26} \text{ cm}^3\text{s}^{-1}$ for $m_\chi = 100$ GeV and $m_\chi = 10$ GeV respectively.

6.4 Asymmetric Dark Matter

Since both suppression and enhancement of the dark matter relic density are possible in the Gauss-Bonnet braneworld scenario, these models are capable of driving an asymmetric dark matter model towards both the weakly and strongly asymmetric regimes discussed in section 2.4. To determine which parameter values correspond to each, we use the results derived in the previous section for symmetric dark matter where we saw that the relic density was enhanced for the interval (6.28),

$$7 \times 10^{-22} m_\chi^2 \left(\frac{\beta}{1 + \beta} \right) \lesssim \mu \lesssim 3 \times 10^{-21} m_\chi^2, \quad (6.36)$$

and suppressed for the interval (6.29)

$$\mu \lesssim 7 \times 10^{-22} m_\chi^2 \left(\frac{\beta}{1 + \beta} \right). \quad (6.37)$$

Therefore, for a fixed value of the asymmetry C , these two cases would drive the dark matter species towards the weakly or strongly asymmetric regimes respectively.

Then, depending on the timing of freeze-out (see equations (6.31)-(6.33)), the cross section and asymmetry can be related by substituting (6.23), (6.26) and (6.27) into (2.53),

$$\langle\sigma v\rangle \simeq \frac{A}{C} \coth^{-1}\left(\frac{\omega}{C}\right) \times \begin{cases} 10 \left(x_f^{GB}\right)^{5/3} / (3\lambda_{GB}) & ; \text{ (GB regime)} \\ 1.1 x_t^{RS} / \lambda_{GR} & ; \text{ (RS regime)} \\ 2 \left(x_f^{GB}\right) / \lambda_{GR} & ; \text{ (GR regime)} \end{cases} \quad (6.38)$$

where $\omega = \Omega_{\text{DM}} h^2 / (2.75 \times 10^8 m_\chi)$ and $A = 1.167 \times 10^{-17} \text{cm}^3 \text{s}^{-1}$.

The numerical results for the required annihilation cross section are plotted in figures 6.4 and 6.5 (solid curves) for $m_\chi = 100 \text{ GeV}$ and $m_\chi = 10 \text{ GeV}$ respectively. The different curves within each panel correspond to different values of μ and we have reduced the magnitude of β in the successive panels. In each figure we plot the standard cosmology result (black curve) for reference.

Since the vertical section of each curve corresponds to the weakly asymmetric regime, the position of the vertical asymptotes can be deduced from figure 6.3 (with allowance for the additional factor of two due to the χ and $\bar{\chi}$ contributions). When the annihilation cross section is enhanced in figure 6.3, the curves in figures 6.4 and 6.5 will be shifted to the right of the standard cosmology result. Similarly, when the symmetric cross section is suppressed, the asymmetric curves will be shifted towards the left. Thus the symmetric cross section determines the vertical asymptote of the required asymmetric cross section.

Consequently, just like the symmetric case, the required annihilation cross section is reduced for all values of μ when $\beta = 0.1509$ (panel 1), getting smaller with decreasing μ . Then, as the magnitude of β is decreased (in successive panels), the curves are shifted towards larger cross sections. There is a limit however, to how much each curve is shifted for a fixed value of μ . For example, in figure 6.4, the $\mu = 10^{-19} \text{ GeV}$ case (solid blue curve) is shifted to higher cross sections when β is reduced from $\beta = 0.1509$ to $\beta = 10^{-5}$ (i.e. going from panel 1 to panel 2). But, as the value of β is reduced further in the successive panels, the curve does not move. The same thing happens for the $\mu = 10^{-22} \text{ GeV}$ case (solid red curve) once $\beta \lesssim 10^{-10}$ (panels 3 and 4). We understand this by noting that once the value of β has dropped below the threshold given in (6.32), the behaviour of each curve is given by the Randall-Sundrum result (see (6.38)), and is therefore independent of β .

Finally, using the formalism developed in chapter 2, we indicate in figures 6.4 and 6.5 the regions in the $(\langle\sigma v\rangle, C)$ plane that produce an amplified asymmetric dark matter detection signal (dot-dashed blue curve) whilst still respecting the Fermi-LAT bounds,

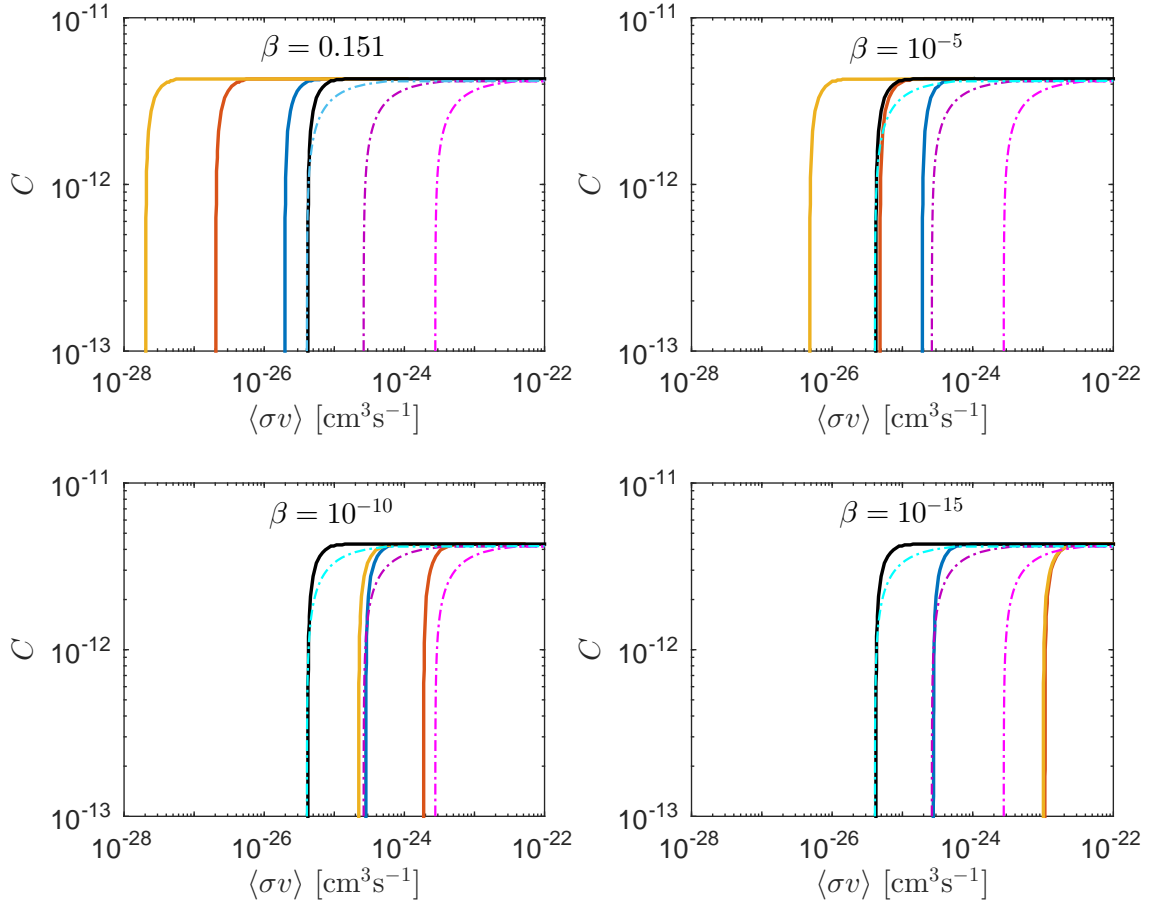


FIGURE 6.4: Iso-abundance contours in the $(\langle\sigma v\rangle, C)$ plane corresponding to the observed dark matter abundance $\Omega_{\text{DM}}h^2 = 0.1188$ for a 100 GeV WIMP. The contours shown are for $\mu = 10^{-19}$ GeV (solid blue curve), $\mu = 10^{-22}$ GeV (solid red curve) and $\mu = 10^{-25}$ GeV (solid yellow curve). Also shown is the standard cosmology result (solid black curve). The panels correspond to $\beta = 0.1509$ (top left), $\beta = 10^{-5}$ (top right), $\beta = 10^{-10}$ (bottom left) and $\beta = 10^{-15}$ (bottom right). Note that, for $\beta = 10^{-15}$, the contours for $\mu = 10^{-22}$ GeV and $\mu = 10^{-25}$ GeV (almost) coincide. In each panel we have superimposed the constraints derived from the Fermi-LAT gamma ray data [125] with the regions below the dark purple and magenta (dot-dashed) curves excluded for the $\mu^+\mu^-$ and $b\bar{b}$ annihilation channels respectively. We have also indicated the region (below the dot-dashed blue curve) for which the asymmetric detection signal in the Gauss-Bonnet scenario exceeds the symmetric signal in the standard scenario.

namely

$$\langle\sigma v\rangle_{GR} < \langle\sigma v\rangle\gamma < \langle\sigma v\rangle_{\text{Fermi}}, \quad (6.39)$$

where $\langle\sigma v\rangle_{GR}$ is the required annihilation cross section for symmetric dark matter in the standard cosmological scenario, $\langle\sigma v\rangle_{\text{Fermi}}$ is the upper limit on $\langle\sigma v\rangle$ derived from the Fermi-LAT data and the damping factor γ is given by

$$\gamma \equiv \frac{2Y_\chi Y_{\bar{\chi}}}{(Y_\chi + Y_{\bar{\chi}})^2} = \frac{\omega^2 - C^2}{2\omega^2}. \quad (6.40)$$

Figures 6.4 and 6.5 show that it is possible to produce an amplified asymmetric detection

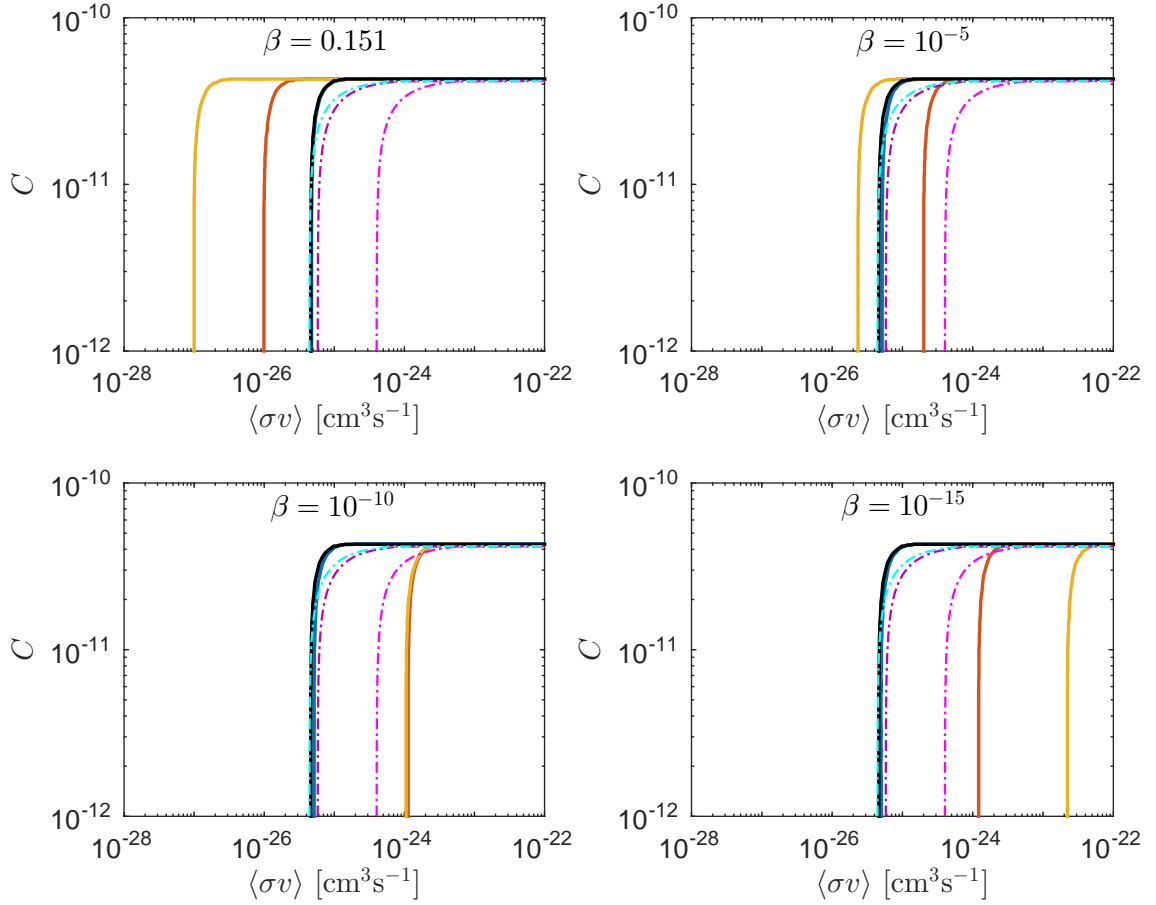


FIGURE 6.5: Same as figure 6.4 but for $m_\chi = 10$ GeV. In each panel the contour for $\mu = 10^{-19}$ GeV (almost) overlaps the standard cosmology result.

signal in the Gauss-Bonnet braneworld model, however, the allowed region decreases as the dark matter particle mass drops from $m_\chi = 100$ GeV to $m_\chi = 10$ GeV due to the more stringent Fermi-LAT constraints.

6.5 Summary

In this chapter we have investigated the relic abundance in the Gauss-Bonnet braneworld scenario in which a Gauss-Bonnet curvature invariant is added to the Randall-Sundrum braneworld action. A previous investigation by [158] found that the dark matter density is suppressed in the GB braneworld model, however, this conclusion is based on a highly contrived assumption that collapses the Randall-Sundrum expansion era, leading to a slower early time expansion law. We find that when this assumption is relaxed, the early time expansion rate can be either faster or slower than the standard expansion law, depending on the model parameters. In turn, the dark matter relic abundance is either enhanced or suppressed by up to several orders of magnitude with respect

to the standard cosmology result, respectively. Importantly, when realistic parameter values are chosen, the early time expansion rate is typically faster than the standard expansion law during the era of dark matter decoupling and the resulting relic abundance is enhanced. Moreover, in the limit $\beta \lll 1$ (corresponding to $\mathcal{R}_m \gg 1$) the usual Randall-Sundrum type behaviour is recovered [155, 224].

Note that we have not considered the p -wave annihilation case since this would not alter our conclusions about whether the dark matter relic density is enhanced or suppressed, it would simply modify the magnitude of the deviation (which has already been investigated in the previous chapter).

We have also investigated the GB braneworld effect on asymmetric dark matter species and found that the enhanced annihilation cross section required to provide the observed relic density is capable of producing an amplified annihilation signal with respect to the symmetric signal in the standard cosmological scenario. This effect has also been demonstrated in quintessence, scalar-tensor [173] and Randall-Sundrum braneworld models [178].

The implications of the latest Fermi-LAT constraints on the dark matter annihilation cross section have been considered for both the symmetric and asymmetric models. For small β , corresponding to realistic values for the mass ratio \mathcal{R}_m , larger values of μ are favoured, suggesting that the Gauss-Bonnet braneworld expansion rate has reduced to the standard expansion law before dark matter decoupling.

Chapter 7

Discussion and Outlook

7.1 Context of project and investigations undertaken

Despite the overwhelming observational evidence for the existence of dark matter [67], very little is known about its particle nature. Many theoretical candidates capable of explaining the observational data have been proposed, however, in the absence of a positive detection signal, the experimental status of each candidate remains far from conclusive.

The present dark matter density, $\Omega_{\text{DM}}h^2 = 0.1188 \pm 0.0010$ [2], can be well explained by the thermal relic scenario in which the dark matter particles are initially in thermodynamic equilibrium with the background cosmic bath. Here, the dark matter particles are created and annihilated in ample numbers so that their number density is comparable to that of photons. However, as the universe expands and cools, the dark matter interaction rate drops below the expansion rate of the universe and the particles fall out of equilibrium. At this point, known as particle freeze-out, both creation and annihilation processes cease and the number density redshifts with expansion. The remaining 'relic' particles constitute the dark matter density we observe today.

Since, for $T \lesssim m_\chi$ (where T is the temperature of the universe and m_χ is the dark matter particle mass), the number density in equilibrium is decaying exponentially, the present dark matter density depends sensitively on the timing of particle freeze-out. Indeed, species with larger interaction cross sections that maintain thermal contact longer, freeze-out with diminished abundances. In a radiation dominated universe with Hubble expansion rate $H \sim T^2$, a dark matter species with a weak scale annihilation cross section, $\langle\sigma v\rangle \sim 10^{-26} \text{ cm}^3\text{s}^{-1}$, freezes out with an abundance that matches the

observed value. This result provides strong motivation for thermal WIMP¹ dark matter and is routinely used to guide dark matter theory and experiments.

That said, it is important to realize that the conditions in the universe at the time of dark matter decoupling ($T \sim \mathcal{O}(\text{GeV})$) are relatively unconstrained with current observational datasets only advocating the standard cosmological model back to the time of Big Bang Nucleosynthesis (BBN) ($T \sim \mathcal{O}(\text{MeV})$). Indeed, several alternative cosmological scenarios that predict modified behaviour in the pre-BBN era are perfectly compatible with the various observational bounds. Therefore, the customary assumptions used in generic relic abundance calculations may not be valid, making it important to consider how variations in the cosmological conditions in the early universe affect dark matter decoupling and the inferred properties of the dark matter particles.

The aim of the present investigation was to calculate the relic abundance of both symmetric (where the particle χ and antiparticle $\bar{\chi}$ are identical and therefore self-annihilating) and asymmetric (where $\chi \neq \bar{\chi}$) dark matter particles in non-standard cosmological scenarios that predict a modified expansion rate in the pre-BBN era. Specifically, using the precise numerical considerations outlined in the recent paper by Steigman *et al* [170], in conjunction with the analytical scheme introduced in [123] (see also [80]), we set out to accurately quantify the level of enhancement (or suppression) of the dark matter relic abundance in each of these models with respect to the standard cosmology result.

Furthermore, knowing the present dark matter density is a precisely measured quantity, another goal was to invert the relic abundance calculations to determine the annihilation cross section, $\langle\sigma v\rangle$, required to provide the observed density in each of the scenarios considered. Comparing these results with observational bounds on $\langle\sigma v\rangle$ (e.g. Fermi-LAT [125]) we would then be able to constrain any deviations from the standard expansion history in the pre-BBN era. Finally, where possible, we wanted to compare and contrast our findings with existing results in the literature.

For the purposes of this investigation we considered several prominent classes of non-standard cosmological scenarios that are known to predict modified behaviour in the early universe. These classes fall within two categories: gravity supplemented with a scalar field; and gravity in higher dimensional universes. We began, in chapter 3, with quintessential kination scenarios in which the energy density of the universe in the pre-BBN era is dominated by the kinetic energy of a non-interacting quintessence-type scalar field [213–215] such as that introduced to describe dark energy. This simple model, which had been the subject of several previous relic abundance investigations [142, 157, 167, 168], was used as an illustrative example of how modifying the early time expansion rate can influence dark matter decoupling and the present dark matter density.

¹Weakly Interacting Massive Particle.

We then considered in chapter 4 an extension of the quintessence scenario known as scalar-tensor gravity [143–145, 229–232] in which the scalar field couples directly to the gravitational metric. These extensively studied alternative theories of gravity are a well motivated extension of General Relativity and are capable of producing large deviations from the standard expansion law at early times. Several previous investigations of dark matter relic abundances in scalar-tensor cosmology [173–175] relied on a simple parametric form for the modified expansion rate suggested by the seminal paper by Catena *et al* [156]. However, this form for the modified expansion rate is derived from a specific coupling, $A(\varphi_*) = 1 + Be^{-\beta\varphi_*}$, for the scalar field φ_* which is seldom encountered elsewhere in the literature and for which detailed BBN constraints are unavailable.

In our study we considered the prototypical coupling $A(\varphi_*) = e^{\frac{1}{2}\beta\varphi_*^2}$ which appears in numerous investigations of scalar-tensor gravity and was recently the subject of the detailed study by Coc *et al* [176] who used BBN calculations to place stringent constraints on the various model parameters. By solving the modified expansion rate explicitly, we calculated the dark matter relic abundance for this more widely investigated coupling and determined if the results reported in Catena *et al* [156] (and its descendants) are representative of scalar-tensor models in general.

As a contrast to the scalar field models just mentioned, we also studied extra-dimensional braneworld scenarios in which our universe is modeled as a 3(+1) dimensional surface (i.e. the *brane*) embedded in a higher dimensional spacetime known as the *bulk*. In particular we considered in chapter 5 the Randall-Sundrum type II (RSII) model [150] in which standard General Relativity is recovered on the surface of a four dimensional Minkowski brane located at the ultraviolet boundary of a five dimensional anti-de Sitter bulk. The modified gravitational effects induced by the presence of the extra dimension manifest at high energies so that these models predict a non-standard expansion law in the pre-BBN era. We extended previous investigations by also calculating the relic abundance of asymmetric dark matter in these models [178].

We then considered in chapter 6 the Gauss-Bonnet (GB) braneworld model [289] that incorporates a Gauss-Bonnet curvature invariant in the standard Randall-Sundrum bulk action integral [287]. This correction term modifies the braneworld dynamics at high energies leading to three distinct expansion regimes: the GB expansion era, the RS expansion era and the standard expansion era. The existing investigation of symmetric dark matter in GB braneworld models by Okada and Okada [158] chose to collapse the RS expansion era by equating the energy scales associated with the GB correction, m_α , and the brane tension, m_σ . This ensures that the early time expansion rate is always slower than that predicted by the standard model so that the dark matter relic abundance is suppressed by up to $\mathcal{O}(10^{-2})$. However, if the GB contribution is to be

considered as the lowest order correction from string theory to the RS action, we would expect $m_\alpha > m_\sigma$. Therefore, in our work [179] we relaxed the assumption made by Okada and Okada [158] and considered more realistic values of the ratio $\mathcal{R}_m \equiv m_\alpha/m_\sigma$.

7.2 Overview of methods used

The relic abundance in each of the non-standard cosmological scenarios was calculated from the Boltzmann rate equation,

$$\frac{dY}{dx} = -\frac{s\langle\sigma v\rangle}{xH}\zeta(x)[Y^2 - Y_{\text{eq}}^2], \quad (7.1)$$

that describes the evolution of the (symmetric) *comoving* number density $Y \equiv n/s$ (where n and s are the dark matter number density and the entropy density of the universe respectively) as a function of $x \equiv m_\chi/T$. This equation assumes that at sufficiently high temperatures the dark matter particles are in thermodynamic equilibrium with the background cosmic bath and that particle-antiparticle pairs are produced through thermal interactions. Additionally, the dark matter particles are assumed to maintain kinetic equilibrium throughout chemical decoupling and have negligible chemical potentials, and the annihilation products are expected to rapidly reach thermal equilibrium with the cosmic background. Further information on the underlying assumptions used to derive the Boltzmann rate equation including the form of the dark matter distribution function can be found in Chapter 2 and Appendices C and B.

The calculations required as input the thermally averaged annihilation cross section (times relative velocity), $\langle\sigma v\rangle$, the expansion rate of the universe H , and the temperature dependent function, $\zeta(x)$, related to the change in the number of entropic degrees of freedom $g_{*s}(T)$,

$$\zeta(x) = 1 - \frac{1}{3} \frac{d \ln g_{*s}}{d \ln x}. \quad (7.2)$$

The dark matter particles were assumed non-relativistic at decoupling so that the equilibrium comoving density, $Y_{\text{eq}} \equiv n_{\text{eq}}/s$, is given by $Y_{\text{eq}} \simeq 0.145 (g_\chi/g_{*s}) x^{3/2} e^{-x}$ where g_χ is the number of degrees of freedom of the dark matter particle.

The present dark matter density (or relic abundance) was determined from the asymptotic solution $Y(\infty)$ of the Boltzmann equation using

$$\Omega_{\text{DM}} h^2 = 2.75 \times 10^8 m_\chi Y(\infty). \quad (7.3)$$

For asymmetric dark matter species ($\chi \neq \bar{\chi}$) the Boltzmann rate equation is generalized to the coupled system

$$\begin{aligned}\frac{dY_\chi}{dx} &= -\frac{s\langle\sigma v\rangle}{xH}\zeta(x)[Y_\chi^2 - CY_\chi - P], \\ \frac{dY_{\bar{\chi}}}{dx} &= -\frac{s\langle\sigma v\rangle}{xH}\zeta(x)[Y_{\bar{\chi}}^2 + CY_{\bar{\chi}} - P],\end{aligned}\quad (7.4)$$

where $P \equiv Y_\chi^{\text{eq}}Y_{\bar{\chi}}^{\text{eq}} \simeq (0.145g_\chi/g_{*s})^2x^3e^{-2x}$ and the constant $C \equiv Y_\chi - Y_{\bar{\chi}}$ defines the asymmetry between the particles and antiparticles. In this case the total dark matter density is given by the sum of the particle and antiparticle contributions, i.e. $\Omega_{\text{DM}}h^2 = \Omega_\chi h^2 + \Omega_{\bar{\chi}} h^2$.

The two major inputs in the Boltzmann equation are the expansion rate of the universe H , which we derived directly from the action integral defining each of the cosmological models, and the annihilation cross section $\langle\sigma v\rangle$. In general, the form of the annihilation cross section depends on the particular dark matter particle model and the nature and strength of its interactions. However, given the lack of observational data and the nebulous state of dark matter particle theory (in particular Supersymmetry and its status in light of recent and upcoming collider experiments), we decided to use a generic form for the annihilation cross section,

$$\langle\sigma v\rangle = \sigma_n x^{-n}, \quad (7.5)$$

where n labels the different powers in the partial wave expansion so that $n = 0$ corresponds to s -wave, $n = 1$ corresponds to p -wave, etc. This form allowed us to draw model-independent conclusions about how the early time expansion rate affects the dark matter relic abundance, which, after all, was the primary focus of the investigation.

The Boltzmann equation was solved using the numerical techniques outlined in Steigman *et al* [170] where, in addition to emphasizing the importance of maintaining the temperature dependence of the number of (entropic) degrees of freedom $g_{*s}(T)$, they provide useful recommendations for handling the 'stiffness' of the differential equation (7.1). Moreover, the precise calculations presented in their paper were used to benchmark our numerical scheme.

Additionally, to gain insight into our numerical results, we have also adopted the semi-analytical scheme outlined in [80, 123] which allows the development of a general approximate solution for the asymptotic comoving density applicable to various non-standard cosmological scenarios (2.26):

$$Y(\infty) \simeq \left[\int_{x_f}^{\infty} \frac{s\langle\sigma v\rangle}{xH} dx \right]^{-1} \quad (7.6)$$

where $x_f = m_\chi/T_f$ is the freeze-out point introduced in section 2.2.2. This result can be derived from (7.1) by noting that the contribution from the creation term $\propto Y_{\text{eq}}^2$ is negligible following particle freeze-out, i.e. $Y_{\text{eq}}(x) \ll Y(x)$ for $x > x_f$, allowing the Boltzmann equation to be integrated directly. Further, to derive (7.6) we have assumed that $\zeta(x) \simeq 1$ and $Y(x_f) \gg Y(\infty)$. Note that the full temperature dependence of $g_*(T)$ was maintained in the numerical solution in accordance with the recommendations made by Steigman *et al* [170].

The generalization of this approximate solution to asymmetric dark matter models is given by (2.46) and (2.47) [207],

$$Y_\chi(\infty) \simeq \frac{C}{1 - \exp\{-C/Y_{(s)}(\infty)\}}, \quad (7.7)$$

$$Y_{\bar{\chi}}(\infty) \simeq \frac{C}{\exp\{C/Y_{(s)}(\infty)\} - 1}, \quad (7.8)$$

where $Y_{(s)}(\infty)$ is the asymptotic solution for the symmetric case (7.6).

7.3 Results of investigation

The investigations of non-standard cosmological scenarios have shown that those models that predicted a faster expansion rate in the early universe led to earlier dark matter decoupling and an enhanced dark matter relic abundance. Conversely, if the expansion rate during this era was slower than that predicted by the standard cosmological model, freeze-out was delayed and the relic abundance was suppressed. Of the four models considered, three predicted faster expansion rates at early times with only the Gauss-Bonnet braneworld model admitting both faster and slower pre-BBN expansion rates. Hence, the quintessential kination, scalar-tensor gravity and Randall-Sundrum type II braneworld models all predicted an enhanced dark matter relic abundance whilst the Gauss-Bonnet braneworld model allowed for either enhanced or suppressed relic abundances.

The level of enhancement (or suppression) for scenario i , as measured by the ratio $\Omega_{\text{DM}}^i/\Omega_{\text{DM}}^{\text{GR}}$, depended on the level of deviation from the standard expansion law at the time of dark matter decoupling. Since the braneworld scenarios predicted the greatest deviation, these models provided the greatest enhancements of the relic abundance. Conversely, scalar-tensor gravity models, when constrained by detailed BBN studies [176], are relatively degenerate with the standard cosmological scenario at the time of dark

matter decoupling and only lead to modest enhancements (of the order of a few). Importantly, if the standard expansion law was restored prior to dark matter decoupling, freeze-out was unaffected and the canonical relic abundance was recovered.

Moreover, since the freeze-out temperature $T_f = m_\chi/x_f$ (where $x_f \sim 10 - 30$ for the non-standard scenarios considered) is mass dependent, the level of enhancement or suppression also increases with increasing WIMP mass. This is because, for each of the non-standard cosmological scenarios considered, the deviation from the standard expansion rate increases with increasing temperature. Therefore, heavier mass particles, that freeze-out at higher temperatures, will experience greater deviations during the decoupling process. This should be compared with the standard cosmology result where the relic abundance is roughly independent of the particle mass (varying by only a factor of 2 as m_χ varies from 100 MeV up to 1 TeV). The maximum level of enhancement/suppression for each of the cosmological models is illustrated in figure 7.1 as a function of WIMP mass.

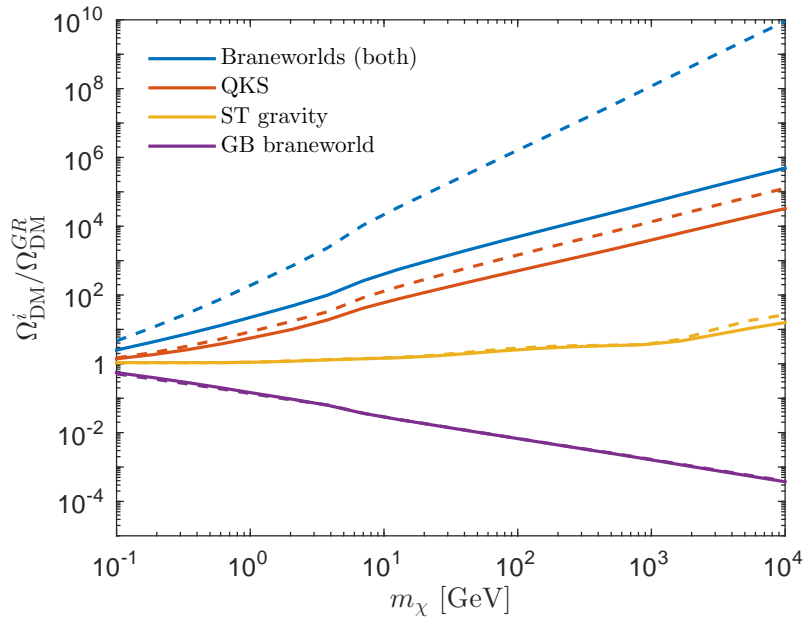


FIGURE 7.1: Ratio of the relic density in non-standard cosmological scenarios to that in the standard cosmological model, $\Omega_{\text{DM}}^i/\Omega_{\text{DM}}^{GR}$, as a function of WIMP mass m_χ . The results are shown for the Quintessential Kination Scenario (QKS) (red), Scalar-Tensor gravity models (ST gravity) (yellow), the Randall-Sundrum type II braneworld model (RSII braneworld) (blue) and the Gauss-Bonnet braneworld model (GB braneworld) (blue and purple) for both the s - (solid) and p -wave (dashed) annihilation cases. Since the Randall-Sundrum type II model is a sub-class of the more general Gauss-Bonnet braneworld model, the upper blue curves are obtained in both of these models.

In table 7.1 we summarize the maximum and minimum values of the ratio $\Omega_{\text{DM}}^i/\Omega_{\text{DM}}^{GR}$ for each of the cosmological scenarios considered for both the s - and p -wave annihilation cases. As the level of enhancement is mass dependent, the values given in table 7.1

Dark matter relic density

Model	s -wave		p -wave	
	$\min(\Omega_{\text{DM}}^i/\Omega_{\text{DM}}^{\text{GR}})$	$\max(\Omega_{\text{DM}}^i/\Omega_{\text{DM}}^{\text{GR}})$	$\min(\Omega_{\text{DM}}^i/\Omega_{\text{DM}}^{\text{GR}})$	$\max(\Omega_{\text{DM}}^i/\Omega_{\text{DM}}^{\text{GR}})$
QKS	1	10^2	1	10^3
ST gravity	1	2 – 3	1	2 – 3
RSII braneworld	1	10^3	1	10^6
GB braneworld	10^{-3}	10^3	10^{-3}	10^6

TABLE 7.1: Ratio of the dark matter relic abundance in each of the non-standard cosmological scenarios, Ω_{DM}^i , compared to the standard cosmology result, $\Omega_{\text{DM}}^{\text{GR}}$, for a $m_\chi = 100$ GeV WIMP. The results are shown for the Quintessential Kination Scenario (QKS), Scalar-Tensor gravity models (ST gravity), the Randall-Sundrum type II braneworld model (RSII braneworld) and the Gauss-Bonnet braneworld model (GB braneworld).

have all been calculated for a fixed WIMP mass of $m_\chi = 100$ GeV. Additionally, since the ratio $\Omega_{\text{DM}}^i/\Omega_{\text{DM}}^{\text{GR}}$ depends slightly on the magnitude of $\langle\sigma v\rangle$, we only report order of magnitude estimates for the enhancement/suppression factors. The detailed numerical results for each scenario are given in the respective chapters of this thesis.

Aside from the level of enhancement/suppression found for each of the non-standard cosmological scenarios, an interesting feature of figure 7.1 (and table 7.1) is the difference in the maximum value of $\Omega_{\text{DM}}^i/\Omega_{\text{DM}}^{\text{GR}}$ between the s - and p -wave annihilation cases. Since the freeze-out process occurs more rapidly in the p -wave annihilation case, the comoving density is allowed less time to decay following particle freeze-out, which therefore results in greater enhancements of the dark matter relic abundance.² We have not considered the cases of mixed s - and p -wave annihilation but the results of such cases are expected to be similar to those presented here.

In general, our results for the quintessential kination and the symmetric RSII braneworld scenario were in agreement with existing results in the literature. However, we did find that previous calculations that failed to properly account for the variation in the number of degrees of freedom $g_*(T)$ incurred errors of up to a factor of two, with the larger errors arising for smaller WIMP masses $m_\chi \lesssim 10$ GeV and for those models in which the freeze-out process took longer to occur (e.g. braneworld models).

Conversely, for the scalar-tensor gravity and Gauss-Bonnet models, our findings differed significantly from those presented in previous investigations. In scalar-tensor models we

²See section 2.2.1 for a discussion on the distinction between *freeze-out*, the time at which the comoving density initially deviates from its equilibrium value, and *freeze-in*, the time at which the comoving density is conserved.

found that, although large deviations from the standard expansion history at the time of dark matter decoupling were possible, the stringent constraints imposed by BBN calculations excluded these regions of parameter space, ensuring the modified expansion rate was nearly coincident with the standard expansion law. Accordingly, the relic abundance in these models only increased by a factor of 2–3 which is in stark contrast to the several orders of magnitude enhancement factors reported in Catena *et al* [156, 159].

Moreover, in the Gauss-Bonnet braneworld model we found that, for values of the ratio $\mathcal{R}_m = m_\alpha/m_\sigma > 1$, the dark matter relic density was typically enhanced with respect to the standard cosmology result. In particular, in the limit $\mathcal{R}_m \gg 1$ the familiar RSII (enhancement) type behaviour was recovered. The finding by Okada and Okada [158] for $\mathcal{R}_m = 1$ that the relic abundances are suppressed in the GB braneworld model only applies for a small subset of possible parameter values and is atypical of the general behaviour.

In addition to calculating the relic density in each of the non-standard cosmological scenarios we also determined the annihilation cross section required to provide the observed dark matter density. Since the relic density is inversely proportional to the annihilation cross section, the enhanced (suppressed) relic density induced by a faster (slower) pre-BBN expansion rate must be compensated by an enhanced (suppressed) annihilation cross section in order to recover the observed dark matter density. In particular, we found that the levels of enhancement (suppression) of the required annihilation cross section with respect to the canonical result $\langle\sigma v\rangle_{GR} \sim 10^{-26} \text{ cm}^3\text{s}^{-1}$ roughly matched the levels of enhancement (suppression) of the relic density.

As an illustration of how dark matter observations can constrain non-standard cosmological models we also compared our results for the required annihilation cross section with the latest bounds derived from the Fermi-LAT gamma ray data [125]. These bounds already probe the weak scale annihilation region predicted by generic relic abundance calculations and are comparable to those from other indirect detection experiments (e.g. [126]). We found that the Fermi-LAT bounds on $\langle\sigma v\rangle$ can already exclude large regions of parameter space, particularly for the quintessential kination and braneworld models. However, we must emphasize that this interpretation relies on the assumption that the dark matter particle annihilates primarily through one of the (Standard Model) annihilation channels considered. In the general case, the dark matter particle will annihilate through multiple (possibly non-Standard Model) annihilation channels and the upper bound imposed by the Fermi-LAT gamma ray data can be evaded.

Finally, we calculated for each of cosmological scenario the relic abundance of asymmetric dark matter for which the particle χ and anti-particle $\bar{\chi}$ are distinct. These models are a natural extension of symmetric, or self-conjugate ($\chi = \bar{\chi}$) dark matter models and are

motivated by the fact that most of the known particles are not self-conjugate. Moreover, since the relic abundance in asymmetric models is typically fixed by the asymmetry $C \equiv Y_{\chi} - Y_{\bar{\chi}}$, with the density of the minority component exponentially suppressed, a shared asymmetry between the dark and baryonic sectors could explain the relative proximity of their respective densities, $\Omega_{\text{DM}}/\Omega_{\text{b}} \sim 5$. If the asymmetry in the dark sector is related to the baryonic asymmetry,

$$\eta_{\text{b}} = \frac{n_{\text{B}}}{n_{\gamma}} = \frac{n_{\text{b}} - n_{\bar{\text{b}}}}{n_{\gamma}} \approx 6 \times 10^{-10}, \quad (7.9)$$

where n_{b} and n_{γ} are the present baryon and photon number densities respectively, then the parameter $C \sim \mathcal{O}(10^{-11})$.

We found that the modified decoupling predicted in non-standard cosmological models can either 'wash out' or amplify the asymmetry between the majority and minority dark matter components depending on whether the early time expansion rate is faster or slower than the standard expansion law respectively. Interestingly, in the former case, the relic density of the asymmetric dark matter species depends on the annihilation cross section, $\langle\sigma v\rangle$, rather than the asymmetry parameter, C , so that it behaves like symmetric dark matter in this sense. This leads to the intriguing prospect [173] that the enhanced annihilation cross section required to provide the observed dark matter density can compensate for the suppressed abundance of the minority dark matter component and produce an observable detection signal. This result, which is contrary to the usual expectation that the asymmetric annihilation rate is negligible due to the exponentially suppressed abundance of the minority component, can be achieved for a wide range of parameter values within the quintessential kination and braneworld scenarios (and even for particular parameter values within the scalar-tensor gravity scenario).

7.4 Outlook

This is an exciting time for dark matter research as both present and near future astronomical and laboratory detection experiments are beginning to probe the weak scale interaction region expected from generic dark matter calculations. Therefore, it is important to contemplate the possible outcomes of these experiments and their interpretation in light of the findings presented in the previous section.

Broadly speaking, there are two possible outcomes: either a dark matter signal *is* detected, thus allowing a *lower* bound to be placed on the dark matter interaction cross section; or, no such signal is found. The latter case, which is a continuation of the present situation, would instead impose an *upper* bound on the strength of dark matter

interactions. Assuming that these bounds can be related to a bound on the annihilation cross section, which we will denote respectively as $\langle\sigma v\rangle_{\text{lower}}$ and $\langle\sigma v\rangle_{\text{upper}}$,³ we can then use these results to gain insight into the conditions in the early universe.

For instance, if the lower bound on the annihilation cross section inferred from a positive dark matter signal, $\langle\sigma v\rangle_{\text{lower}}$, was greater than the annihilation cross section required to produce the observed dark matter density in the standard cosmological model, $\langle\sigma v\rangle_{\text{GR}} \sim 10^{-26} \text{ cm}^3\text{s}^{-1}$, this would imply that the dark matter particles are under-produced in the standard model, i.e. $\langle\sigma v\rangle_{\text{lower}} > \langle\sigma v\rangle_{\text{GR}} \Rightarrow \Omega_{\text{DM}}^{\text{GR}} < \Omega_{\text{DM}}^{\text{obs}}$ since the relic abundance of a particular species χ is inversely related to its annihilation cross section $\langle\sigma v\rangle$ so that an upper (lower) bound on $\langle\sigma v\rangle$ corresponds to a lower (upper) bound on its contribution to Ω_{DM} . To resolve this discrepancy we would either need to introduce additional dark matter species to make up the balance of the observed dark matter density, or the relic density must be enhanced due to a faster pre-BBN expansion rate.

Alternatively, null results from detection experiments could place an upper bound on the annihilation cross section that is less than $\langle\sigma v\rangle_{\text{GR}}$. In this case the dark matter particles are overproduced in the standard cosmological model, i.e. $\langle\sigma v\rangle_{\text{upper}} < \langle\sigma v\rangle_{\text{GR}} \Rightarrow \Omega_{\text{DM}}^{\text{GR}} > \Omega_{\text{DM}}^{\text{obs}}$, and some mechanism is required to suppress the dark matter density. This scenario is more conclusive and indicates either a slower pre-BBN expansion rate or some dilution mechanism such as entropy production. The other two scenarios, $\langle\sigma v\rangle_{\text{lower}} > \langle\sigma v\rangle_{\text{GR}}$ and $\langle\sigma v\rangle_{\text{upper}} < \langle\sigma v\rangle_{\text{GR}}$, can be accommodated within the standard cosmological model and do not require the introduction of any new physics.^{4,5}

Although dark matter experiments can indicate whether the expansion rate in the pre-BBN era is different from that predicted by the standard cosmological scenario, the results from relic abundance calculations alone are not enough to discriminate amongst the various non-standard alternatives. This is because there is a large degeneracy between each of the models with the same level of enhancement or suppression achievable within several different cosmological scenarios. Of course, if the annihilation cross section inferred from detection experiments is such that the dark matter particles are overproduced in the standard cosmological scenario, then this would indicate a cosmology with a slower pre-BBN expansion rate (e.g. Gauss-Bonnet braneworlds, non-universal scalar-tensor theories [172]). However, we would still require further information to determine

³It is important to remember that different detection experiments probe different types of dark matter interactions so that if, for example, a dark matter particle is detected scattering off the nucleus of a particle inside a laboratory (i.e. direct detection), this only places a lower bound on the scattering cross section $\sigma_{\chi N \leftrightarrow \chi N}$ which can be related to the annihilation cross section via a crossing symmetry.

⁴As discussed in [219], there are several caveats to each of the interpretations just mentioned. For instance, if the dark matter candidate annihilates into non-Standard Model final states this would invalidate the upper bound $\langle\sigma v\rangle_{\text{upper}}$ because such states cannot be probed by Standard Model detectors.

⁵For further discussion on how dark matter experiments can be used to probe the physics of the pre-BBN era see [160].

which of the alternative cosmologies is responsible. Similarly, if the annihilation cross section was such that the dark matter particles are under-produced in the standard cosmological scenario, there are most likely many non-standard models capable of providing the appropriate level of enhancement (e.g. Quintessential kination, braneworld models). Even in this case, cosmological models with a slower early time expansion rate cannot be ruled out — they would simply require the introduction of additional dark matter species. Therefore, unless some additional information is provided, such as the temperature at which the modified expansion rate reduces to the standard expansion law (often referred to as the transition temperature, see for example [173]), the underlying cosmological scenario cannot be ascertained.

7.5 Future work

One possible approach to breaking the degeneracy amongst the various cosmological scenarios considered here would be to consider higher order moments of the Boltzmann equation. Indeed, a straightforward extension of the present work would be to consider the *kinetic decoupling* of dark matter in non-standard cosmological scenarios. Kinetic decoupling, as opposed to chemical decoupling (which has been the sole focus of the present investigation), occurs when the dark matter particles cease to efficiently exchange momentum with the other background particles in the cosmic bath (see e.g. [180]). Subsequently the temperature (or velocity distribution) of the dark matter particles, defined as the second moment of the dark matter distribution function $f(\vec{p})$

$$T_\chi \equiv \frac{2}{3} \int \frac{|\vec{p}|^2}{2m_\chi} f(\vec{p}) d\vec{p}, \quad (7.10)$$

evolves separately from the cosmic background. Significantly, the decoupling temperature sets the size of the smallest dark matter protohalos and therefore has important implications for the evolution of primordial structures [292, 293].

In a general cosmological scenario the decoupling temperature can be determined by solving the Boltzmann equation [294, 295]

$$a \frac{dT_\chi}{da} + 2T_\chi = -\frac{2\gamma(a)}{H} (T_\chi - T) \quad (7.11)$$

where a is the cosmic scale factor, T is the temperature of the background and γ is the momentum relaxation rate defined in terms of the scattering cross section $\sigma_{\chi X \leftrightarrow \chi X}$. Although kinetic decoupling in quintessential kination models has been considered [295, 296], similar studies for scalar-tensor and braneworld models are lacking.

It's possible that a combined analysis of kinetic and chemical decoupling in non-standard cosmological scenarios could help break the degeneracy between these models.

Additionally, during the course of our investigation, several interesting issues were raised that have not been fully explored. This is because they were either beyond the scope of the present study or because they could not be properly addressed within the allotted time period.

Firstly, it would be interesting to apply our results for the enhancement (suppression) of the dark matter relic abundance in non-standard cosmological scenarios to specific dark matter particle models (see e.g. [168, 219, 223, 270, 271]). In the present investigation we have remained agnostic about the identity of the dark matter particle and worked with a generic form for the annihilation cross section $\langle\sigma v\rangle = \sigma_n x^{-n}$. This allowed us to draw model independent conclusions about the effects of a modified early time expansion rate on the dark matter relic abundance from which we simply inferred the implications for the different dark matter particle candidates. However, if we were to repeat our calculations using detailed forms for the annihilation cross section derived from a particular particle physics model, we would be able to draw specific conclusions about the viability of different dark matter candidates, and, possibly particle physics models (e.g. Supersymmetry) more generally.

We also mention the topic of dark matter decoupling in non-universal scalar-tensor models, i.e. scalar-tensor models in which the coupling of the scalar field φ_* with the visible and dark matter sectors is distinct (see section 4.9). In these models interactions of the type $\chi\bar{\chi} \leftrightarrow X\bar{X}$ (where the X 's are Standard Model particles) occur between particles that experience different couplings with the scalar field. Consequently, there is no (Jordan) frame in which all particles have their normal φ_* -independent properties and for which the standard Boltzmann equation is applicable. In this case the appropriate form of the Boltzmann equation collision term is not immediately clear, indicating that the relic abundance of dark matter in non-universal scalar-tensor models could represent a substantial research investigation in its own right.

Finally, we point out that the formalism and techniques developed in this thesis can be readily applied to general cosmological scenarios. It would be interesting then to consider other prominent non-standard cosmological models (e.g. decaying vacuum energy models [297, 298]) and determine if similar levels of enhancement or suppression of the dark matter relic abundance can be realized in these scenarios as well.

Bibliography

- [1] PLANCK COLLABORATION, R. Adam et al., *Planck 2015 results. I. Overview of products and scientific results* (2015), arXiv:1502.01582.
- [2] PLANCK COLLABORATION, P. Ade et al., *Planck 2015 results. XIII. Cosmological parameters* (2015), arXiv:1502.01589.
- [3] S. Capozziello and G. Lambiase, *A comprehensive view of cosmological dark side* (2013), arXiv:1304.5640.
- [4] S. Weinberg, *Ultraviolet divergences in quantum theories of gravitation*, in *General Relativity: an Einstein centenary survey*, edited by S. W. Hawking and W. Israel (Cambridge University Press, Cambridge, 1979), pp. 790–831.
- [5] R. P. Woodard, *How far are we from the quantum theory of gravity?*, Rep. Prog. Phys. **72** (2009), 126002.
- [6] J. Polchinski, *String Theory: Volume 1, An introduction to the bosonic string* (Cambridge University Press, Cambridge, 1998).
- [7] J. Polchinski, *String theory: Volume 2, Superstring theory and beyond* (Cambridge University Press, Cambridge, 1998).
- [8] N. Arkani-Hamed and J. Maldacena, *Cosmological collider physics* (2015), arXiv:1503.08043.
- [9] A. H. Guth, *Inflationary universe: a possible solution to the horizon and flatness problems*, Phys. Rev. D **23** (1981), 347.
- [10] A. Linde, *A new inflationary universe scenario: a possible solution of the horizon, flatness, homogeneity, isotropy and primordial monopole problems*, Phys. Lett. B **108** (1982), 389.
- [11] A. Linde, *Chaotic inflation*, Phys. Lett. B **129** (1983), 177.
- [12] D. Baumann, *TASI Lectures on inflation* (2009), arXiv:0907.5424.

-
- [13] A. Linde, *Inflationary cosmology after Planck 2013* (2014), arXiv:1402.0526.
- [14] B. D. Fields and K. A. Olive, *Big bang nucleosynthesis*, Nucl. Phys. A **777** (2006), 208.
- [15] A. Einstein, *Die Grundlage der allgemeinen Relativitätstheorie*, Ann. Phys. **354** (1916), 769.
- [16] A. Friedmann, *Über die Krümmung des Raumes*, Z. Phys. **10** (1922), 377.
- [17] G. Lemaître, *Un Univers homogène de masse constante et de rayon croissant rendant compte de la vitesse radiale des nébuleuses extra-galactiques*, Ann. Soc. Sci. Brux. **47** (1927), 49.
- [18] PARTICLE DATA GROUP, J. Beringer et al., *The review of particle physics*, Phys. Rev. D **86** (2012), 010001.
- [19] PLANCK COLLABORATION, P. Ade et al., *Planck 2015 results. XIV. Dark energy and modified gravity* (2015), arXiv:1502.01590.
- [20] A. G. Riess et al., *Observational evidence from supernovae for an accelerating universe and a cosmological constant*, Astrophys. J. **116** (1998), 1009.
- [21] S. Perlmutter et al., *Measurements of Ω and Λ from 42 high-redshift supernovae*, Astrophys. J. **517** (1999), 565.
- [22] G. Efstathiou, W. Sutherland, and S. Maddox, *The cosmological constant and cold dark matter*, Nature **348** (1990), 705.
- [23] J. Ostriker and P. J. Steinhardt, *The observational case for a low density universe with a nonzero cosmological constant*, Nature **377** (1995), 600.
- [24] L. M. Krauss and M. S. Turner, *The cosmological constant is back*, Gen. Relat. Gravit. **27** (1995), 1137.
- [25] D. H. Weinberg et al., *Observational probes of cosmic acceleration*, Phys. Rep. **530** (2013), 87.
- [26] T. M. Davis, *Cosmological constraints on dark energy*, Gen. Relat. Gravit. **46** (2014), 1731.
- [27] A. Einstein, *Kosmologische betrachtungen zur allgemeinen Relativitätstheorie*, Sitzungsber. Preuß. Akad. Wiss. (Berlin) (1917), 142.
- [28] E. Hubble, *A relation between distance and radial velocity among extra-galactic nebulae*, Proc. Nat. Acad. Sci. **15** (1929), 168.

- [29] Y. B. Zel'dovich, *The cosmological constant and the theory of elementary particles*, Sov. Phys. Uspekhi **11** (1968), 381.
- [30] A. Padilla, *Lectures on the cosmological constant problem* (2015), arXiv:1502.05296.
- [31] S. M. Carroll, *The cosmological constant*, Living Rev. Relativ. **4** (2001), 1.
- [32] P. J. E. Peebles and B. Ratra, *The cosmological constant and dark energy*, Rev. Mod. Phys. **75** (2003), 559.
- [33] T. Padmanabhan, *Cosmological constant: the weight of the vacuum*, Phys. Rept. **380** (2003), 235.
- [34] O. Bertolami, *Time-dependent cosmological term*, Nuovo Ciment. B **93** (1986), 36.
- [35] C. Wetterich, *Cosmologies with variable Newton's 'constant'*, Nucl. Phys. B **302** (1988), 645.
- [36] P. J. E. Peebles and B. Ratra, *Cosmology with a time-variable cosmological 'constant'*, Astrophys. J. **325** (1988), L17.
- [37] S. Tsujikawa, *Quintessence: a review*, Classical Quant. Grav. **30** (2013), 214003.
- [38] E. Copeland, A. Liddle, and D. Wands, *Exponential potentials and cosmological scaling solutions*, Phys. Rev. D **57** (1998), 4686.
- [39] P. Steinhardt, L. Wang, and I. Zlatev, *Cosmological tracking solutions*, Phys. Rev. D **59** (1999), 123504.
- [40] J. H. Oort, *The force exerted by the stellar system in the direction perpendicular to the galactic plane and some related problems*, B. Astron. I. Netherlands **6** (1932), 249.
- [41] F. Zwicky, *Spectral displacement of extra galactic nebulae*, Helv. Phys. Acta **6** (1933), 110.
- [42] V. C. Rubin and W. K. J. Ford, *Rotation of the Andromeda Nebula from a spectroscopic survey of emission regions*, Astrophys. J. **159** (1970), 379.
- [43] G. Bertone, *Particle dark matter: observations, models and searches* (Cambridge University Press, Cambridge, 2010).
- [44] J. Einasto, *Dark matter* (2009), arXiv:0901.0632.
- [45] L. Bergström, *Dark matter evidence, particle physics candidates and detection methods*, Ann. Phys.-Berlin **524** (2012), 479.

- [46] M. Milgrom, *A modification of the Newtonian dynamics as a possible alternative to the hidden mass hypothesis*, *Astrophys. J.* **270** (1983), 365.
- [47] M. Taoso, G. Bertone, and A. Masiero, *Dark matter candidates: a ten-point test*, *JCAP* **0803** (2008), 022.
- [48] MACHO COLLABORATION, C. Alcock et al., *The MACHO project: microlensing results from 5.7 years of LMC observations*, *Astrophys. J.* **542** (2000), 281.
- [49] J. Wess and B. Zumino, *Supergauge transformations in four dimensions*, *Nucl. Phys. B* **70** (1974), 39.
- [50] H. Nilles, *Supersymmetry, supergravity and particle physics*, *Phys. Rep.* **110** (1984), 1.
- [51] H. Haber and G. Kane, *The search for supersymmetry: probing physics beyond the standard model*, *Phys. Rep.* **117** (1985), 75.
- [52] J. R. Ellis, J. Hagelin, D. V. Nanopoulos, K. A. Olive, and M. Srednicki, *Supersymmetric relics from the big bang*, *Nucl. Phys. B* **238** (1984), 453.
- [53] H. Goldberg, *Constraint on the photino mass from cosmology*, *Phys. Rev. Lett.* **50** (1983), 1419.
- [54] P. Gondolo et al., *DarkSUSY: computing supersymmetric dark matter properties numerically*, *JCAP* **0407** (2004), 008.
- [55] A. Arbey and F. Mahmoudi, *SuperIso Relic: a program for calculating relic density and flavor physics observables in supersymmetry*, *Comput. Phys. Commun.* **181** (2010), 1277.
- [56] G. Berlanger, F. Boudjema, A. Pukhov, and A. Semenov, *micrOMEGAs2.0: a program to calculate the relic density of dark matter in a generic model*, *Comput. Phys. Commun.* **176** (2007), 367.
- [57] G. Jungman, M. Kamionkowski, and K. Griest, *Supersymmetric dark matter*, *Phys. Rep.* **267** (1996), 195.
- [58] R. Catena and L. Covi, *SUSY dark matter(s)*, *Eur. Phys. J. C* **74** (2014), 2703.
- [59] H. Baer, V. Barger, D. Mickelson, and M. Padeffke-Kirkland, *SUSY models under siege: LHC constraints and electroweak fine-tuning*, *Phys. Rev. D* **89** (2014), 115019.
- [60] J. L. Feng, *Naturalness and the status of supersymmetry*, *Ann. Rev. Nucl. Part. Sci.* **63** (2013), 351.

-
- [61] N. Craig, *The state of supersymmetry after run I of the LHC* (2013), arXiv:1309.0528.
- [62] O. Buchmueller et al., *The CMSSM and NUHM1 after LHC Run 1*, Eur. Phys. J. C **74** (2014), 2922.
- [63] K. J. de Vries et al., *The pMSSM10 after LHC Run 1* (2015), arXiv:1504.03260.
- [64] R. D. Peccei and H. R. Quinn, *Constraints imposed by CP conservation in the presence of pseudoparticles*, Phys. Rev. D **16** (1977), 1791.
- [65] J. E. Kim and G. Carosi, *Axions and the strong CP problem*, Rev. Mod. Phys. **82** (2010), 557.
- [66] S. Dodelson and L. M. Widrow, *Sterile neutrinos as dark matter*, Phys. Rev. Lett. **72** (1994), 17.
- [67] G. Bertone, D. Hooper, and J. Silk, *Particle dark matter: evidence, candidates and constraints*, Phys. Rept. **405** (2005), 279.
- [68] J. L. Feng, *Dark matter candidates from particle physics and methods of detection*, Annu. Rev. Astron. Astr. **48** (2010), 495.
- [69] K. Petraki and R. R. Volkas, *Review of asymmetric dark matter*, Int. J. Mod. Phys. A **28** (2013), 1330028.
- [70] J. Kumar, *Asymmetric dark matter*, AIP Conf. Proc. **1604** (2014), 389.
- [71] K. M. Zurek, *Asymmetric dark matter: theories, signatures, and constraints*, Phys. Rep. **537** (2014), 91.
- [72] M. L. Graesser, I. M. Shoemaker, and L. Vecchi, *Asymmetric WIMP dark matter*, J. High Energy Phys. **1110** (2011), 110.
- [73] D. E. Kaplan, M. A. Luty, and K. M. Zurek, *Asymmetric dark matter*, Phys. Rev. D **79** (2009), 115016.
- [74] M. Y. Khlopov and C. Kouvaris, *Strong interactive massive particles from a strong coupled theory*, Phys. Rev. D **77** (2008), 065002.
- [75] DAMA COLLABORATION, R. Bernabei et al., *First results from DAMA/LIBRA and the combined results with DAMA/NaI*, Eur. Phys. J. C **56** (2008), 333.
- [76] CoGeNT COLLABORATION, C. Aalseth et al., *CoGeNT: a search for low-mass dark matter using p-type point contact germanium detectors*, Phys. Rev. D **88** (2013), 012002.

- [77] D. Hooper, *The empirical case for 10 GeV dark matter*, Phys. Dark Univ. **1** (2012), 1.
- [78] T. Lin, H.-B. Yu, and K. M. Zurek, *Symmetric and asymmetric light dark matter*, Phys. Rev. D **85** (2012), 063503.
- [79] I.-W. Kim and K. M. Zurek, *Flavor and collider signatures of asymmetric dark matter*, Phys. Rev. D **89** (2014), 035008.
- [80] E. W. Kolb and M. S. Turner, *The early universe* (Addison-Wesley, Reading, MA, 1990).
- [81] J. L. Feng and J. Kumar, *Dark matter particles without weak scale masses or weak interactions*, Phys. Rev. Lett. **101** (2008), 231301.
- [82] S. Watson, *Reevaluating the cosmological origin of dark matter*, Adv. Ser. Direct. High Energy Phys. **21** (2010), 305.
- [83] G. Gelmini and P. Gondolo, *DM production mechanisms* (2010), arXiv:1009.3690.
- [84] H. Baer, K.-Y. Choi, J. E. Kim, and L. Roszkowski, *Dark matter production in the early universe: beyond the thermal WIMP paradigm*, Phys. Rept. **555** (2015), 1.
- [85] G. B. Gelmini, *TASI 2014 lectures: the hunt for dark matter* (2015), arXiv:1502.01320.
- [86] R. Bernabei et al., *Final model independent result of DAMA/LIBRA-phase1*, Eur. Phys. J. C **73** (2013), 2648.
- [87] CDMS COLLABORATION, R. Agnese et al., *Silicon detector dark matter results from the final exposure of CDMS II*, Phys. Rev. Lett. **111** (2013), 251301.
- [88] LUX COLLABORATION, D. S. Akerib et al., *First results from the LUX dark matter experiment at the Sanford Underground Research Facility*, Phys. Rev. Lett. **112** (2014), 091303.
- [89] SUPERCDMS COLLABORATION, R. Agnese et al., *Search for low-mass Weakly Interacting Massive Particles with SuperCDMS*, Phys. Rev. Lett. **112** (2014), 241302.
- [90] Angloher, G. et al., *Results on low mass WIMPs using an upgraded CRESST-II detector*, Eur. Phys. J. C **74** (2014), 3184.
- [91] C. Amole et al., *Dark matter search results from the PICO-2L C₃F₈ bubble chamber* (2015), arXiv:1503.00008.

- [92] M. Schumann, *Dark matter 2014* (2015), arXiv:1501.01200.
- [93] S. Profumo, W. Shepherd, and T. M. P. Tait, *Pitfalls of dark matter crossing symmetries*, Phys. Rev. D **88** (2013), 056018.
- [94] W. B. Atwood et al., *The Large Area Telescope on the Fermi Gamma-Ray Space Telescope Mission*, Astrophys. J. **697** (2009), 1071.
- [95] O. Adriani et al., *The PAMELA mission: heralding a new era in precision cosmic ray physics*, Phys. Rep. **544** (2014), 323 .
- [96] M. Aguilar et al., *The Alpha Magnetic Spectrometer (AMS) on the International Space Station: Part I. Results from the test flight on the space shuttle*, Phys. Rep. **366** (2002), 331.
- [97] T. Gaisser and F. Halzen, *IceCube*, Ann. Rev. Nucl. Part. S. **64** (2014), 101.
- [98] T. Tanaka et al., *An indirect search for Weakly Interacting Massive Particles in the Sun using 3109.6 days of upward-going muons in Super-Kamiokande*, Astrophys. J. **742** (2011), 78.
- [99] L. M. Krauss, M. Srednicki, and F. Wilczek, *Solar System constraints and signatures for dark-matter candidates*, Phys. Rev. D **33** (1986), 2079.
- [100] C. Weniger, *A tentative gamma-ray line from dark matter annihilation at the Fermi Large Area Telescope*, JCAP **1208** (2012), 007.
- [101] M. Ackermann et al., *Search for gamma-ray spectral lines with the Fermi Large Area Telescope and dark matter implications*, Phys. Rev. D **88** (2013), 082002.
- [102] D. Hooper and L. Goodenough, *Dark matter annihilation in the Galactic Center as seen by the Fermi Gamma Ray Space Telescope*, Phys. Lett. B **697** (2011), 412.
- [103] L. Bergström, J. Edsjö, and G. Zaharijas, *Dark matter interpretation of recent electron and positron data*, Phys. Rev. Lett. **103** (2009), 031103.
- [104] P. Meade, M. Papucci, A. Strumia, and T. Volansky, *Dark matter interpretations of the excesses after FERMI*, Nucl. Phys. B **831** (2010), 178.
- [105] L. Bergström, T. Bringmann, and J. Edsjö, *New positron spectral features from supersymmetric dark matter: a way to explain the PAMELA data?*, Phys. Rev. D **78** (2008), 103520.
- [106] L. Bergström, *Dark matter candidates*, New J. Phys. **11** (2009), 105006.
- [107] D. Hooper and T. Linden, *Origin of the gamma rays from the Galactic Center*, Phys. Rev. D **84** (2011), 123005.

- [108] T. Lacroix, *Fitting the Fermi-LAT GeV excess: on the importance of the propagation of electrons from dark matter* (2015), arXiv:1501.07485.
- [109] S. Caron, A. Achterberg, L. Hendriks, R. R. de Austri, and C. Weniger, *A description of the Galactic Center excess in the Minimal Supersymmetric Standard Model and the dark matter signatures for the LHC and direct and indirect detection experiments* (2015), arXiv:1502.05703.
- [110] T. Gherghetta, B. von Harling, A. D. Medina, M. A. Schmidt, and T. Trott, *SUSY implications from WIMP annihilation into scalars at the Galactic Centre* (2015), arXiv:1502.07173.
- [111] PAMELA COLLABORATION, O. Adriani et al., *An anomalous positron abundance in cosmic rays with energies 1.5-100 GeV*, Nature **458** (2009), 607.
- [112] O. Adriani et al., *Cosmic-ray positron energy spectrum measured by PAMELA*, Phys. Rev. Lett. **111** (2013), 081102.
- [113] AMS COLLABORATION, M. Aguilar et al., *First result from the Alpha Magnetic Spectrometer on the International Space Station: precision measurement of the positron fraction in primary cosmic rays of 0.5-350 GeV*, Phys. Rev. Lett. **110** (2013), 141102.
- [114] AMS COLLABORATION, L. Accardo et al., *High statistics measurement of the positron fraction in primary cosmic rays of 0.5-500 GeV with the Alpha Magnetic Spectrometer on the International Space Station*, Phys. Rev. Lett. **113** (2014), 121101.
- [115] P.-F. Yin, Z.-H. Yu, Q. Yuan, and X.-J. Bi, *Pulsar interpretation for the AMS-02 result*, Phys. Rev. D **88** (2013), 023001.
- [116] M. Cirelli, M. Kadastik, M. Raidal, and A. Strumia, *Model-independent implications of the e^\pm , \bar{p} cosmic ray spectra on properties of dark matter*, Nucl. Phys. B **813** (2009), 1.
- [117] L. Feng et al., *AMS-02 positron excess: new bounds on dark matter models and hint for primary electron spectrum hardening*, Phys. Lett. B **728** (2014), 250.
- [118] N. Arkani-Hamed, D. P. Finkbeiner, T. R. Slatyer, and N. Weiner, *A theory of dark matter*, Phys. Rev. D **79** (2009), 015014.
- [119] M. Cirelli, *Indirect searches for dark matter*, Pramana **79** (2012), 1021.
- [120] F. Donato, *Indirect searches for dark matter*, Phys. Dark Univ. **4** (2014), 41.

-
- [121] D. Bauer et al., *Dark matter in the coming decade: complementary paths to discovery and beyond* (2013), arXiv:1305.1605.
- [122] S. Colafrancesco et al., *Probing the nature of dark matter with the SKA* (2015), arXiv:1502.03738.
- [123] R. J. Scherrer and M. S. Turner, *On the relic, cosmic abundance of stable, weakly interacting massive particles*, Phys. Rev. D **33** (1986), 1585.
- [124] K. Griest and M. Kamionkowski, *Unitarity limits on the mass and radius of dark-matter particles*, Phys. Rev. Lett. **64** (1990), 615.
- [125] FERMI-LAT COLLABORATION, M. Ackermann et al., *Dark matter constraints from observations of 25 Milky Way satellite galaxies with the Fermi Large Area Telescope*, Phys. Rev. D **89** (2014), 042001.
- [126] L. Bergström, T. Bringmann, I. Cholis, D. Hooper, and C. Weniger, *New limits on dark matter annihilation from Alpha Magnetic Spectrometer cosmic ray positron data*, Phys. Rev. Lett. **111** (2013), 171101.
- [127] FERMI-LAT COLLABORATION, M. Ackermann et al., *Limits on dark matter annihilation signals from the Fermi-LAT 4-year measurement of the isotropic gamma-ray background* (2015), arXiv:1501.05464.
- [128] T. Bringmann, F. Calore, M. Di Mauro, and F. Donato, *Constraining dark matter annihilation with the isotropic γ -ray background: updated limits and future potential*, Phys. Rev. D **89** (2014), 023012.
- [129] T. R. Slatyer, N. Padmanabhan, and D. P. Finkbeiner, *CMB constraints on WIMP annihilation: energy absorption during the recombination epoch*, Phys. Rev. D **80** (2009), 043526.
- [130] M. S. Madhavacheril, N. Sehgal, and T. R. Slatyer, *Current dark matter annihilation constraints from CMB and low-redshift data*, Phys. Rev. D **89** (2014), 103508.
- [131] S. Galli, F. Iocco, G. Bertone, and A. Melchiorri, *CMB constraints on dark matter models with large annihilation cross section*, Phys. Rev. D **80** (2009), 023505.
- [132] J. M. Cline and P. Scott, *Dark matter CMB constraints and likelihoods for poor particle physicists*, JCAP **2013** (2013), 044.
- [133] S. Galli, F. Iocco, G. Bertone, and A. Melchiorri, *Updated CMB constraints on dark matter annihilation cross sections*, Phys. Rev. D **84** (2011), 027302.

- [134] G. Steigman, *CMB constraints on the thermal WIMP annihilation cross section* (2015), arXiv:1502.01884.
- [135] M. Ackermann et al., *Constraints on the galactic halo dark matter from Fermi-LAT diffuse measurements*, *Astrophys. J.* **761** (2012), 91.
- [136] T. Bringmann, M. Vollmann, and C. Weniger, *Updated cosmic-ray and radio constraints on light dark matter: implications for the GeV gamma-ray excess at the Galactic Center*, *Phys. Rev. D* **90** (2014), 123001.
- [137] A. Abramowski et al., *Search for a dark matter annihilation signal from the Galactic Center Halo with H.E.S.S.*, *Phys. Rev. Lett.* **106** (2011), 161301.
- [138] F. Donato, D. Maurin, P. Brun, T. Delahaye, and P. Salati, *Constraints on WIMP dark matter from the high energy PAMELA \bar{p}/p data*, *Phys. Rev. Lett.* **102** (2009), 071301.
- [139] BICEP2 COLLABORATION, P. Ade et al., *Detection of B-mode polarization at degree angular scales by BICEP2*, *Phys. Rev. Lett.* **112** (2014), 241101.
- [140] BICEP2 COLLABORATION, PLANCK COLLABORATION, P. Ade et al., *A Joint Analysis of BICEP2/Keck Array and Planck Data*, *Phys. Rev. Lett.* **114** (2015), 101301.
- [141] M. Joyce, *Electroweak baryogenesis and the expansion rate of the universe*, *Phys. Rev. D* **55** (1997), 1875.
- [142] P. Salati, *Quintessence and the relic density of neutralinos*, *Phys. Lett. B* **571** (2003), 121.
- [143] P. Jordan, *Formation of the stars and development of the universe*, *Nature* **164** (1949), 637.
- [144] M. Fierz, *On the physical interpretation of P. Jordan's extended theory of gravitation*, *Helv. Phys. Acta* **29** (1956), 128.
- [145] C. Brans and R. H. Dicke, *Mach's principle and a relativistic theory of gravitation*, *Phys. Rev.* **124** (1961), 925.
- [146] J. D. Barrow, *Scalar-tensor cosmologies*, *Phys. Rev. D* **47** (1993), 5329.
- [147] T. Damour and K. Nordtvedt, *General relativity as a cosmological attractor of tensor-scalar theories*, *Phys. Rev. Lett.* **70** (1993), 2217.
- [148] T. Damour and K. Nordtvedt, *Tensor-scalar cosmological models and their relaxation toward general relativity*, *Phys. Rev. D* **48** (1993), 3436.

-
- [149] L. Randall and R. Sundrum, *Large mass hierarchy from a small extra dimension*, Phys. Rev. Lett. **83** (1999), 3370.
- [150] L. Randall and R. Sundrum, *An alternative to compactification*, Phys. Rev. Lett. **83** (1999), 4690.
- [151] N. Arkani-Hamed, S. Dimopoulos, and G. Dvali, *The hierarchy problem and new dimensions at a millimeter*, Phys. Lett. B **429** (1998), 263.
- [152] G. Dvali, G. Gabadadze, and M. Porrati, *4D gravity on a brane in 5D Minkowski space*, Phys. Lett. B **485** (2000), 208.
- [153] J. D. Barrow, *Massive particles as a probe of the early universe*, Nucl. Phys. B **208** (1982), 501.
- [154] M. Kamionkowski and M. S. Turner, *Thermal relics: do we know their abundances?*, Phys. Rev. D **42** (1990), 3310.
- [155] N. Okada and O. Seto, *Relic density of dark matter in brane world cosmology*, Phys. Rev. D **70** (2004), 083531.
- [156] R. Catena, N. Fornengo, A. Masiero, M. Pietroni, and F. Rosati, *Dark matter relic abundance and scalar-tensor dark energy*, Phys. Rev. D **70** (2004), 063519.
- [157] C. Pallis, *Quintessential kination and cold dark matter abundance*, JCAP **2005** (2005), 015.
- [158] N. Okada and S. Okada, *Gauss-Bonnet braneworld cosmological effect on relic density of dark matter*, Phys. Rev. D **79** (2009), 103528.
- [159] R. Catena, N. Fornengo, M. Pato, L. Pieri, and A. Masiero, *Thermal relics in modified cosmologies: bounds on evolution histories of the early universe and cosmological boosts for PAMELA*, Phys. Rev. D **81** (2010), 123522.
- [160] G. B. Gelmini, *Experimental signatures of non-standard pre-BBN cosmologies*, Nucl. Phys. Proc. Suppl. **194** (2009), 63.
- [161] M. Drees, H. Imminiyaz, and M. Kakizaki, *Constraints on the very early universe from thermal WIMP dark matter*, Phys. Rev. D **76** (2007), 103524.
- [162] N. Arkani-Hamed, A. Delgado, and G. Giudice, *The well-tempered neutralino*, Nuc. Phys. B **741** (2006), 108.
- [163] G. Busoni, A. De Simone, T. Jacques, E. Morgante, and A. Riotto, *Making the most of the relic density for dark matter searches at the LHC 14 TeV run*, JCAP **1503** (2015), 022.

- [164] G. B. Gelmini, P. Gondolo, A. Soldatenko, and C. E. Yaguna, *Direct detection of neutralino dark matter in nonstandard cosmologies*, Phys. Rev. D **76** (2007), 015010.
- [165] A. A. El Zant, S. Khalil, and H. Okada, *Dark matter annihilation and the PAMELA, FERMI, and ATIC anomalies*, Phys. Rev. D **81** (2010), 123507.
- [166] T. Basak, S. Mohanty, and G. Tomar, *Explaining AMS-02 positron excess and muon anomalous magnetic moment in dark left-right gauge model* (2015), arXiv:1501.06193.
- [167] F. Rosati, *Quintessential enhancement of dark matter abundance*, Phys. Lett. B **570** (2003), 5.
- [168] S. Profumo and P. Ullio, *SUSY dark matter and quintessence*, JCAP **0311** (2003), 006.
- [169] A. Arbey and F. Mahmoudi, *SUSY constraints from relic density: high sensitivity to pre-BBN expansion rate*, Phys. Lett. B **669** (2008), 46.
- [170] G. Steigman, B. Dasgupta, and J. F. Beacom, *Precise relic WIMP abundance and its impact on searches for dark matter annihilation*, Phys. Rev. D **86** (2012), 023506.
- [171] M. Schelke, R. Catena, N. Fornengo, A. Masiero, and M. Pietroni, *Constraining pre-big-bang nucleosynthesis expansion using cosmic antiprotons*, Phys. Rev. D **74** (2006), 083505.
- [172] R. Catena, N. Fornengo, A. Masiero, M. Pietroni, and M. Schelke, *Enlarging minimal-supergravity parameter space by decreasing pre-nucleosynthesis Hubble rate in scalar-tensor cosmologies*, J. High Energy Phys. **0810** (2008), 003.
- [173] G. B. Gelmini, J.-H. Huh, and T. Rehagen, *Asymmetric dark matter annihilation as a test of non-standard cosmologies*, JCAP **1308** (2013), 003.
- [174] T. Rehagen and G. B. Gelmini, *Effects of kination and scalar-tensor cosmologies on sterile neutrinos*, JCAP **1406** (2014), 044.
- [175] S.-Z. Wang, H. Iminiyaz, and M. Mamat, *Relic abundance of asymmetric dark matter in scalar-tensor model* (2015), arXiv:1503.06519.
- [176] A. Coc, K. A. Olive, J.-P. Uzan, and E. Vangioni, *Big bang nucleosynthesis constraints on scalar-tensor theories of gravity*, Phys. Rev. D **73** (2006), 083525.
- [177] M. Meehan, *Dark matter relic density in non-standard cosmologies* (Australian Institute of Physics National Congress, Canberra, December 2014).

- [178] M. T. Meehan and I. B. Whittingham, *Asymmetric dark matter in braneworld cosmology*, JCAP **1406** (2014), 018.
- [179] M. T. Meehan and I. B. Whittingham, *Dark matter relic density in Gauss-Bonnet braneworld cosmology*, JCAP **1412** (2014), 034.
- [180] T. Bringmann and S. Hofmann, *Thermal decoupling of WIMPs from first principles*, JCAP **0407** (2007), 016.
- [181] H.-Y. Chiu, *Symmetry between particle and antiparticle populations in the universe*, Phys. Rev. Lett. **17** (1966), 712.
- [182] S. Gershtein and Y. B. Zeldovich, *Rest mass of muonic neutrino and cosmology*, JETP Lett. **4** (1966), 120.
- [183] R. Cowsik and J. McClelland, *An upper limit on the neutrino rest mass*, Phys. Rev. Lett. **29** (1972), 669.
- [184] P. Hut, *Limits on masses and number of neutral weakly interacting particles*, Phys. Lett. B **69** (1977), 8.
- [185] B. W. Lee and S. Weinberg, *Cosmological lower bound on heavy-neutrino masses*, Phys. Rev. Lett. **39** (1977), 165.
- [186] D. A. Dicus, E. W. Kolb, and V. L. Teplitz, *Cosmological upper bound on heavy-neutrino lifetimes*, Phys. Rev. Lett. **39** (1977), 168.
- [187] G. Steigman, *Cosmology confronts particle physics*, Ann. Rev. Nucl. Part. Sci. **29** (1979), 313.
- [188] S. Wolfram, *Abundances of new stable particles produced in the early universe*, Phys. Lett. B **82** (1979), 65.
- [189] H. M. Georgi, S. L. Glashow, and S. Nussinov, *Unconventional model of neutrino masses*, Nucl. Phys. B **193** (1981), 297.
- [190] K. A. Olive, D. N. Schramm, and G. Steigman, *Limits on new superweakly interacting particles from primordial nucleosynthesis*, Nucl. Phys. B **180** (1981), 497.
- [191] K. A. Olive and M. S. Turner, *Cosmological bounds on the masses of stable, right-handed neutrinos*, Phys. Rev. D **25** (1982), 213.
- [192] L. M. Krauss, *New constraints on neutrino masses from cosmology*, Phys. Lett. B **128** (1983), 37.
- [193] E. W. Kolb and R. Slansky, *Dimensional reduction in the early universe: where have the massive particles gone?*, Phys. Lett. B **135** (1984), 378.

- [194] J. Bernstein, L. S. Brown, and G. Feinberg, *Cosmological heavy-neutrino problem*, Phys. Rev. D **32** (1985), 3261.
- [195] E. W. Kolb and M. S. Turner, *On the relic abundance of stable neutrinos*, Phys. Lett. B **159** (1985), 102.
- [196] V. Silveira and A. Zee, *Scalar phantoms*, Phys. Lett. B **161** (1985), 136.
- [197] E. W. Kolb and K. A. Olive, *Lee-Weinberg bound reexamined*, Phys. Rev. D **33** (1986), 1202.
- [198] M. Srednicki, R. Watkins, and K. A. Olive, *Calculations of relic densities in the early universe*, Nucl. Phys. B **310** (1988), 693.
- [199] P. Gondolo and G. Gelmini, *Cosmic abundances of stable particles: improved analysis*, Nucl. Phys. B **360** (1991), 145.
- [200] K. Griest and D. Seckel, *Three exceptions in the calculation of relic abundances*, Phys. Rev. D **43** (1991), 3191.
- [201] J. Edsjö and P. Gondolo, *Neutralino relic density including coannihilations*, Phys. Rev. D **56** (1997), 1879.
- [202] Y. B. Zel'dovich, L. B. Okun', and S. B. Pikel'ner, *Quarks: astrophysical and physicochemical aspects*, Sov. Phys. Uspekhi **8** (1966), 702.
- [203] S. Weinberg, *Cosmology* (Oxford University Press, Oxford, 2008).
- [204] C. M. Bender and S. Sarkar, *Asymptotic analysis of the Boltzmann equation for dark matter relics*, J. Math. Phys. **53** (2012), 103509.
- [205] J. Birrell, J. Wilkening, and J. Rafelski, *Boltzmann equation solver adapted to emergent chemical non-equilibrium*, J. Comput. Phys. **281** (2015), 896.
- [206] M. Cannoni, *Exact theory of freeze out*, Eur. Phys. J. C **75** (2015), 106.
- [207] H. Iminiyaz, M. Drees, and X. Chen, *Relic abundance of asymmetric dark matter*, JCAP **1107** (2011), 003.
- [208] R. Caldwell, R. Dave, and P. Steinhardt, *Cosmological imprint of an energy component with general equation of state*, Phys. Rev. Lett. **80** (1998), 1582.
- [209] B. Ratra and P. Peebles, *Cosmological consequences of a rolling homogeneous scalar field*, Phys. Rev. D **37** (1988), 3406.
- [210] K. Freese, F. C. Adams, J. A. Frieman, and E. Mottola, *Cosmology with decaying vacuum energy*, Nucl. Phys. B **287** (1987), 797.

- [211] A. R. Liddle and R. J. Scherrer, *Classification of scalar field potentials with cosmological scaling solutions*, Phys. Rev. D **59** (1998), 023509.
- [212] I. Zlatev, L. Wang, and P. Steinhardt, *Quintessence, cosmic coincidence, and the cosmological constant*, Phys. Rev. Lett. **82** (1999), 896.
- [213] M. Joyce and T. Prokopec, *Turning around the sphaleron bound: electroweak baryogenesis in an alternative post-inflationary cosmology*, Phys. Rev. D **57** (1998), 6022.
- [214] P. G. Ferreira and M. Joyce, *Cosmology with a primordial scaling field*, Phys. Rev. D **58** (1998), 023503.
- [215] M. Joyce and T. Prokopec, *Baryogenesis from ‘electrogenesis’ in a scalar field dominated epoch*, J. High Energy Phys. **2000** (2000), 030.
- [216] C. Pallis, *Kination-dominated reheating and cold dark matter abundance*, Nucl. Phys. B **751** (2006), 129.
- [217] S. Lola, C. Pallis, and E. Tzelati, *Tracking quintessence and cold dark matter candidates*, JCAP **0911** (2009), 017.
- [218] C. Pallis, *Cold dark matter in non-standard cosmologies, PAMELA, ATIC and Fermi-LAT*, Nucl. Phys. B **831** (2010), 217.
- [219] D. J. Chung et al., *Connecting LHC, ILC, and quintessence*, J. High Energy Phys. **0710** (2007), 016.
- [220] D. Grin, T. L. Smith, and M. Kamionkowski, *Axion constraints in nonstandard thermal histories*, Phys. Rev. D **77** (2008), 085020.
- [221] A. Arbey and F. Mahmoudi, *SUSY constraints, relic density, and very early universe*, J. High Energy Phys. **1005** (2010), 051.
- [222] M. Gomez, S. Lola, C. Pallis, and J. Rodriguez-Quintero, *Quintessential kination and thermal production of gravitinos and axinos*, JCAP **0901** (2009), 027.
- [223] L. Visinelli and P. Gondolo, *Axion cold dark matter in nonstandard cosmologies*, Phys. Rev. D **81** (2010), 063508.
- [224] W.-L. Guo and X. Zhang, *Constraints on dark matter annihilation cross section in scenarios of brane-world and quintessence*, Phys. Rev. D **79** (2009), 115023.
- [225] H. Iminiyaz and X. Chen, *Relic abundance of asymmetric dark matter in quintessence*, Astropart. Phys. **54** (2014), 125.

- [226] R. R. Caldwell and E. V. Linder, *Limits of quintessence*, Phys. Rev. Lett. **95** (2005), 141301.
- [227] E. V. Linder, *Quintessence's last stand?*, Phys. Rev. D **91** (2015), 063006.
- [228] N. A. Lima, A. R. Liddle, M. Sahlen, and D. Parkinson, *Reconstructing thawing quintessence with multiple datasets* (2015), arXiv:1501.02678.
- [229] P. Bergmann, *Comments on the scalar-tensor theory*, Int. J. Theor. Phys. **1** (1968), 25.
- [230] K. Nordtvedt, Jr., *Post-Newtonian metric for a general class of scalar-tensor gravitational theories and observational consequences*, Astrophys. J. **161** (1970), 1059.
- [231] R. V. Wagoner, *Scalar-tensor theory and gravitational waves*, Phys. Rev. D **1** (1970), 3209.
- [232] F. Perrotta, C. Baccigalupi, and S. Matarrese, *Extended quintessence*, Phys. Rev. D **61** (1999), 023507.
- [233] T. Kaluza, *Zum unitätsproblem der physik*, Sitzungsber. Preuss. Akad. Wiss. Berlin. (Math. Phys.) **1921** (1921), 45.
- [234] O. Klein, *Quantentheorie und fünfdimensionale Relativitätstheorie*, Z. Phys. **37** (1926), 895.
- [235] C. M. Will, *The confrontation between General Relativity and experiment*, Living Rev. Rel. **17** (2014), 4.
- [236] J. Khoury, *Theories of dark energy with screening mechanisms* (2010), arXiv:1011.5909.
- [237] P. Hamilton et al., *Atom-interferometry constraints on dark energy* (2015), arXiv:1502.03888.
- [238] T. Damour and B. Pichon, *Big bang nucleosynthesis and tensor-scalar gravity*, Phys. Rev. D **59** (1999), 123502.
- [239] J. Larena, J.-M. Alimi, and A. Serna, *Big bang nucleosynthesis in scalar tensor gravity: the key problem of the primordial ${}^7\text{Li}$ abundance*, Astrophys. J. **658** (2007), 1.
- [240] H. O. Silva, C. F. B. Macedo, E. Berti, and L. C. B. Crispino, *Slowly rotating anisotropic neutron stars in General Relativity and scalar-tensor theory* (2014), arXiv:1411.6286.

- [241] T. Damour and G. Esposito-Farèse, *Tensor-scalar gravity and binary-pulsar experiments*, Phys. Rev. D **54** (1996), 1474.
- [242] T. Damour and G. Esposito-Farèse, *Gravitational-wave versus binary-pulsar tests of strong-field gravity*, Phys. Rev. D **58** (1998), 042001.
- [243] P. C. Freire et al., *The relativistic pulsar–white dwarf binary PSR J1738+ 0333–II. The most stringent test of scalar–tensor gravity*, MNRAS **423** (2012), 3328.
- [244] B. Bertotti, L. Iess, and P. Tortora, *A test of general relativity using radio links with the Cassini spacecraft*, Nature **425** (2003), 374.
- [245] T. P. Sotiriou and V. Faraoni, *$f(R)$ theories of gravity*, Rev. Mod. Phys. **82** (2010), 451.
- [246] T. P. Sotiriou, *$f(R)$ gravity and scalar-tensor theory*, Classical Quant. Grav. **23** (2006), 5117.
- [247] K. S. Stelle, *Renormalization of higher-derivative quantum gravity*, Phys. Rev. D **16** (1977), 953.
- [248] J. D. Barrow, *The premature recollapse problem in closed inflationary universes*, Nucl. Phys. B **296** (1988), 697.
- [249] J. D. Barrow and S. Cotsakis, *Inflation and the conformal structure of higher-order gravity theories*, Phys. Lett. B **214** (1988), 515.
- [250] A. Starobinsky, *A new type of isotropic cosmological models without singularity*, Phys. Lett. B **91** (1980), 99.
- [251] W. Hu and I. Sawicki, *Models of $f(R)$ cosmic acceleration that evade solar system tests*, Phys. Rev. D **76** (2007), 064004.
- [252] P. Brax, C. van de Bruck, A.-C. Davis, J. Khoury, and A. Weltman, *Detecting dark energy in orbit: the cosmological chameleon*, Phys. Rev. D **70** (2004), 123518.
- [253] A. L. Erickcek, N. Barnaby, C. Burrage, and Z. Huang, *Catastrophic consequences of kicking the chameleon*, Phys. Rev. Lett. **110** (2013), 171101.
- [254] A. Coc, K. A. Olive, J.-P. Uzan, and E. Vangioni, *Nonuniversal scalar-tensor theories and big bang nucleosynthesis*, Phys. Rev. D **79** (2009), 103512.
- [255] K. Akama, *An early proposal of 'brane world'*, Lect. Notes Phys. **176** (1982), 267.
- [256] V. Rubakov and M. Shaposhnikov, *Do we live inside a domain wall?*, Phys. Lett. B **125** (1983), 136.

- [257] D. Langlois, *Brane cosmology: an introduction*, Prog. Theor. Phys. Suppl. **148** (2002), 181.
- [258] P. Brax and C. van de Bruck, *Cosmology and brane worlds: a review*, Class. Quant. Grav. **20** (2003), R201.
- [259] R. Durrer, *Braneworlds*, AIP Conf. Proc. **782** (2005), 202.
- [260] R. Maartens and K. Koyama, *Brane-world gravity*, Living Rev. Rel. **13** (2010), 5.
- [261] N. Arkani-Hamed, S. Dimopoulos, and G. Dvali, *Phenomenology, astrophysics, and cosmology of theories with submillimeter dimensions and TeV scale quantum gravity*, Phys. Rev. D **59** (1999), 086004.
- [262] A. Mazumdar, *Interesting consequences of brane cosmology*, Phys. Rev. D **64** (2001), 027304.
- [263] N. Okada and O. Seto, *Brane world cosmological solution to the gravitino problem*, Phys. Rev. D **71** (2005), 023517.
- [264] G. Panotopoulos, *Gravitino dark matter in brane-world cosmology*, JCAP **0705** (2007), 016.
- [265] N. Okada and O. Seto, *Gravitino dark matter from increased thermal relic particles*, Phys. Rev. D **77** (2008), 123505.
- [266] A. R. Liddle and A. J. Smith, *Observational constraints on braneworld chaotic inflation*, Phys. Rev. D **68** (2003), 061301.
- [267] S. Tsujikawa and A. R. Liddle, *Constraints on braneworld inflation from CMB anisotropies*, JCAP **0403** (2004), 001.
- [268] N. Okada and S. Okada, *Simple brane-world inflationary models in light of BICEP2* (2014), arXiv:1407.3544.
- [269] N. Okada and S. Okada, *Simple brane-world inflationary models: an update* (2015), arXiv:1504.00683.
- [270] T. Nihei, N. Okada, and O. Seto, *Neutralino dark matter in brane world cosmology*, Phys. Rev. D **71** (2005), 063535.
- [271] T. Nihei, N. Okada, and O. Seto, *Light W -ino dark matter in brane world cosmology*, Phys. Rev. D **73** (2006), 063518.
- [272] G. Panotopoulos, *Axino dark matter in brane world cosmology*, JCAP **0508** (2005), 005.

- [273] E. Abou El Dahab and S. Khalil, *Cold dark matter in brane cosmology scenario*, J. High Energy Phys. **0609** (2006), 042.
- [274] J. U. Kang and G. Panotopoulos, *Dark matter in supersymmetric models with axino LSP in Randall-Sundrum II brane model*, J. High Energy Phys. **0805** (2008), 036.
- [275] P. Binetruy, C. Deffayet, and D. Langlois, *Non-conventional cosmology from a brane universe*, Nucl. Phys. B **565** (2000), 269.
- [276] K. Ichiki, M. Yahiro, T. Kajino, M. Orito, and G. J. Mathews, *Observational constraints on dark radiation in brane cosmology*, Phys. Rev. D **66** (2002), 043521.
- [277] C. D. Hoyle et al., *Submillimeter test of the gravitational inverse-square law: a search for “large” extra dimensions*, Phys. Rev. Lett. **86** (2001), 1418.
- [278] J. Long et al., *Upper limits to submillimetre-range forces from extra space-time dimensions*, Nature **421** (2003), 922.
- [279] K.-i. Maeda and D. Wands, *Dilaton gravity on the brane*, Phys. Rev. D **62** (2000), 124009.
- [280] E. A. E. Dahab and S. Khalil, *Dark matter in brane cosmology*, Int. J. Mod. Phys. A **22** (2007), 5819.
- [281] J.-F. Dufaux, J. E. Lidsey, R. Maartens, and M. Sami, *Cosmological perturbations from braneworld inflation with a Gauss-Bonnet term*, Phys. Rev. D **70** (2004), 083525.
- [282] S. Tsujikawa, M. Sami, and R. Maartens, *Observational constraints on braneworld inflation: the effect of a Gauss-Bonnet term*, Phys. Rev. D **70** (2004), 063525.
- [283] G. Calcagni, S. Kuroyanagi, J. Ohashi, and S. Tsujikawa, *Strong Planck constraints on braneworld and non-commutative inflation*, JCAP **1403** (2014), 052.
- [284] I. P. Neupane, *Gauss-Bonnet assisted braneworld inflation in light of BICEP2 and Planck data*, Phys. Rev. D **90** (2014), 123534.
- [285] N. Okada and S. Okada, *Simple inflationary models in Gauss-Bonnet brane-world cosmology* (2014), arXiv:1412.8466.
- [286] M. Duff, J. T. Liu, and K. Stelle, *A supersymmetric type IIB Randall-Sundrum realization*, J. Math. Phys. **42** (2001), 3027.
- [287] D. J. Gross and J. H. Sloan, *The quartic effective action for the heterotic string*, Nucl. Phys. B **291** (1987), 41.

- [288] T. Clifton, P. G. Ferreira, A. Padilla, and C. Skordis, *Modified gravity and cosmology*, Phys. Rept. **513** (2012), 1.
- [289] C. Charmousis and J.-F. Dufaux, *General Gauss-Bonnet brane cosmology*, Classical Quant. Grav. **19** (2002), 4671.
- [290] S. C. Davis, *Generalized Israel junction conditions for a Gauss-Bonnet brane world*, Phys. Rev. D **67** (2003), 024030.
- [291] J. E. Lidsey and N. J. Nunes, *Inflation in Gauss-Bonnet brane cosmology*, Phys. Rev. D **67** (2003), 103510.
- [292] S. Profumo, K. Sigurdson, and M. Kamionkowski, *What mass are the smallest protohalos?*, Phys. Rev. Lett. **97** (2006), 031301.
- [293] J. M. Cornell, S. Profumo, and W. Shepherd, *Kinetic decoupling and small-scale structure in effective theories of dark matter*, Phys.Rev. **D88** (2013), 015027.
- [294] P. Gondolo, J. Hisano, and K. Kadota, *The effect of quark interactions on dark matter kinetic decoupling and the mass of the smallest dark halos*, Phys. Rev. D **86** (2012), 083523.
- [295] L. Visinelli and P. Gondolo, *Kinetic decoupling of WIMPs: analytic expressions* (2015), arXiv:1501.02233.
- [296] G. B. Gelmini and P. Gondolo, *Ultra-cold WIMPs: relics of non-standard pre-BBN cosmologies*, JCAP **0810** (2008), 002.
- [297] K. Freese, F. C. Adams, J. A. Frieman, and E. Mottola, *Cosmology with decaying vacuum energy*, Nucl. Phys. B **287** (1987), 797.
- [298] S. Basilakos, J. A. S. Lima, and J. Sola, *From inflation to dark energy through a dynamical Lambda: an attempt at alleviating fundamental cosmic puzzles*, Int. J. Mod. Phys. D **22** (2013), 1342008.
- [299] S. Weinberg, *Gravitation and Cosmology* (John Wiley and Sons, Inc., New York, 1972).
- [300] M. Hindmarsh and O. Philipsen, *Dark matter of weakly interacting massive particles and the QCD equation of state*, Phys. Rev. D **71** (2005), 087302.
- [301] H. Goldstein, C. Poole, and J. Safko, *Classical mechanics* (Addison Wesley, San Francisco, 2007).
- [302] D. Langlois, *Brane cosmology*, Prog. Theor. Phys. Supp. **148** (2002), 181.

-
- [303] W. Israel, *Singular hypersurfaces and thin shells in general relativity*, Nuovo Cim. B **44S10** (1966), 1.
- [304] P. Hořava and E. Witten, *Eleven-dimensional supergravity on a manifold with boundary*, Nucl. Phys. B **475** (1996), 94.

Appendix A

Review of General Relativity

A.1 Geodesics

In General Relativity test particles follow *geodesics* in curved spacetime. In essence, a geodesic is the generalization of a straight line in Euclidean space and is given by the "shortest" path between two points in curved spacetime. Formally, a geodesic is a curve \mathcal{C} , such that, for any two points on \mathcal{C} , P and P' , with coordinates x^α and $x^\alpha + dx^\alpha$ respectively, the unit tangent vector evaluated at P , when parallel transported to P' , is identical to the unit tangent vector at P' .

The interval between two points x^α and $x^\alpha + dx^\alpha$ is given by

$$ds^2 = g_{\mu\nu} dx^\mu dx^\nu \quad (\text{A.1})$$

where $g_{\mu\nu}$ is the metric tensor and the interval is related to the proper time, τ , via

$$d\tau^2 = -ds^2. \quad (\text{A.2})$$

Here, and throughout the text, we use the Lorentzian signature $(-, +, +, +)$.

The geodesic equation can be derived by extremizing the functional

$$D = \int_A^B d\tau = \int_A^B \frac{d\tau}{d\lambda} d\lambda = \int_A^B \sqrt{-g_{\mu\nu} \frac{dx^\mu}{d\lambda} \frac{dx^\nu}{d\lambda}} d\lambda \quad (\text{A.3})$$

where D is the length of a curve parameterized by λ (i.e. $x^\alpha \equiv x^\alpha(\lambda)$) between the points A and B . Using the formalism developed in Appendix D (see also, for example [299]), we find that

$$\frac{d^2 x^\rho}{d\lambda^2} + \Gamma_{\mu\nu}^\rho \frac{dx^\mu}{d\lambda} \frac{dx^\nu}{d\lambda} = 0 \quad (\text{A.4})$$

where the field $\Gamma_{\mu\nu}^{\rho}$ is the *affine connection* given by¹

$$\Gamma_{\mu\nu}^{\rho} = \frac{1}{2}g^{\rho\sigma}(\partial_{\mu}g_{\nu\sigma} + \partial_{\nu}g_{\sigma\mu} - \partial_{\sigma}g_{\mu\nu}), \quad (\text{A.6})$$

which is used to define the covariant derivative ∇_{μ} ,

$$\nabla_{\mu}V^{\nu} = \partial_{\mu}V^{\nu} + \Gamma_{\mu\lambda}^{\nu}V^{\lambda}; \quad \nabla_{\mu}\omega_{\nu} = \partial_{\mu}\omega_{\nu} - \Gamma_{\mu\nu}^{\lambda}\omega_{\lambda}. \quad (\text{A.7})$$

If we convert from the affine parameter λ to the *proper time* τ and introduce the four-velocity $u^{\mu} \equiv dx^{\mu}/d\tau$,² the geodesic equation can be written

$$\frac{du^{\rho}}{d\tau} + \Gamma_{\mu\nu}^{\rho}u^{\mu}u^{\nu} = 0. \quad (\text{A.9})$$

Multiplying through by m^2 we see that

$$mF^{\rho} = -\Gamma_{\mu\nu}^{\rho}p^{\mu}p^{\nu} \quad (\text{A.10})$$

where the four-momentum $p^{\mu} \equiv mu^{\mu}$ and

$$F^{\rho} = m\frac{d^2x^{\rho}}{d\tau^2}. \quad (\text{A.11})$$

The influence of gravity on test particles therefore manifests itself through the affine connection $\Gamma_{\mu\nu}^{\rho}$.

A.2 Cosmology

The field equations of General Relativity relate the curvature of spacetime to its matter-energy content and are given by³

$$R_{\mu\nu} - \frac{1}{2}g_{\mu\nu}R + g_{\mu\nu}\Lambda = 8\pi GT_{\mu\nu}. \quad (\text{A.13})$$

¹We adopt the notation

$$\partial_{\mu} \equiv \frac{\partial}{\partial x^{\mu}}. \quad (\text{A.5})$$

²According to the definition of the proper time,

$$d\tau^2 = -ds^2 = -g_{\mu\nu}dx^{\mu}dx^{\nu}, \quad (\text{A.8})$$

the four-velocity u^{μ} satisfies the normalization condition $g_{\mu\nu}u^{\mu}u^{\nu} = -1$.

³Einstein's field equations (A.13) can be derived from a variational principle applied to the action

$$S_{GR} = \frac{1}{16\pi G} \int_{\mathcal{M}} (R - 2\Lambda) d^4x + S_{\text{mat}}, \quad (\text{A.12})$$

as we show in section D.3.

Here $R_{\mu\nu}$ is the Ricci tensor

$$R_{\mu\nu} = \partial_\lambda \Gamma_{\mu\nu}^\lambda - \partial_\nu \Gamma_{\mu\lambda}^\lambda + \Gamma_{\mu\nu}^\rho \Gamma_{\lambda\rho}^\lambda - \Gamma_{\mu\lambda}^\rho \Gamma_{\nu\rho}^\lambda \quad (\text{A.14})$$

and R the Ricci scalar, $R = g^{\mu\nu} R_{\mu\nu}$, Λ is the cosmological constant, G is Newton's gravitational constant and $T_{\mu\nu}$ is the energy-momentum tensor. The field equations can be solved in a homogeneous and isotropic spacetime for which the invariant line element is given by the Robertson-Walker metric

$$ds^2 = -dt^2 + a^2(t) \left[\frac{d\xi^2}{1 - k\xi^2} + \xi^2 d\theta^2 + \xi^2 \sin^2 \theta d\phi^2 \right] \quad (\text{A.15})$$

where $k = -1, 0, +1$ for hyperbolic, flat and spheroidal curvature respectively.

It is convenient to write the spatial components g_{ij} in terms of the 3-space metric γ_{ij} where

$$g_{ij} = a^2(t) \gamma_{ij}. \quad (\text{A.16})$$

The non-vanishing components of the affine connections (A.6) are

$$\begin{aligned} \Gamma_{ij}^k &= \frac{1}{2} g^{kl} (\partial_i g_{jl} + \partial_j g_{li} - \partial_l g_{ij}) \\ &= \frac{1}{2} \gamma^{kl} (\partial_i \gamma_{jl} + \partial_j \gamma_{li} - \partial_l \gamma_{ij}), \end{aligned} \quad (\text{A.17})$$

$$\begin{aligned} \Gamma_{0j}^k &= \frac{1}{2} g^{kl} (\partial_j g_{0l} + \partial_0 g_{lj} - \partial_l g_{0j}) \\ &= \frac{1}{2} g^{kl} \partial_0 g_{jl} \\ &= \frac{\gamma^{kl}}{2a^2} \frac{\partial}{\partial t} (a^2 \gamma_{jl}) \\ &= \frac{\dot{a}}{a} \delta_j^k, \end{aligned} \quad (\text{A.18})$$

and

$$\begin{aligned} \Gamma_{ij}^0 &= \frac{1}{2} g^{0l} (\partial_i g_{jl} + \partial_j g_{li} - \partial_l g_{ij}) \\ &= \frac{1}{2} g^{00} (\partial_i g_{j0} + \partial_j g_{0i} - \partial_0 g_{ij}) \\ &= -\frac{1}{2} g^{00} \partial_0 g_{ij} \\ &= \frac{1}{2} \frac{\partial}{\partial t} (a^2 \gamma_{ij}) \\ &= a \dot{a} \gamma_{ij}. \end{aligned} \quad (\text{A.19})$$

Using (A.17)-(A.19), the components of the Ricci tensor can now be evaluated. The purely spatial components can be written

$$R_{ij} = {}^{(3)}R_{ij} + \gamma_{ij} (a\ddot{a} + 2\dot{a}^2) \quad (\text{A.20})$$

where, for a maximally symmetric 3-space, the Ricci tensor is [299]

$${}^{(3)}R_{ij} = 2k\gamma_{ij}, \quad (\text{A.21})$$

so that,

$$R_{ij} = \gamma_{ij} (2k + a\ddot{a} + 2\dot{a}^2). \quad (\text{A.22})$$

Similarly, the (0, 0) component is given by

$$R_{00} = -3\frac{\ddot{a}}{a}, \quad (\text{A.23})$$

and $R_{0j} = 0$. The Ricci scalar, $R = g^{\mu\nu} R_{\mu\nu}$, is then

$$R = 6 \left(\frac{\ddot{a}}{a} + \frac{\dot{a}^2}{a^2} + \frac{k}{a^2} \right). \quad (\text{A.24})$$

Combining (A.24) with (A.22) and (A.23) we can evaluate the various components of the Einstein tensor,

$$G_{\mu\nu} = R_{\mu\nu} - \frac{1}{2}g_{\mu\nu}R. \quad (\text{A.25})$$

The non-zero components are

$$G_{00} = 3 \left(\frac{\dot{a}^2}{a^2} + \frac{k}{a^2} \right), \quad (\text{A.26})$$

and

$$G_{ij} = -\gamma_{ij} (2a\ddot{a} + \dot{a}^2 + k). \quad (\text{A.27})$$

Assuming the energy momentum tensor takes the perfect fluid form,

$$T_{\mu\nu} = (\rho + p) u_\mu u_\nu + pg_{\mu\nu}, \quad (\text{A.28})$$

we can obtain the first Friedmann equation from the (0, 0) component of the field equations,

$$\frac{\dot{a}^2}{a^2} + \frac{k}{a^2} = \frac{8\pi G}{3}\rho + \frac{\Lambda}{3}. \quad (\text{A.29})$$

Similarly the second Friedmann equation is derived using the (i, j) components:

$$\frac{\ddot{a}}{a} = -\frac{4\pi G}{3}(\rho + 3p) + \frac{\Lambda}{3} \quad (\text{A.30})$$

where we have used the first Friedmann equation (A.29) to eliminate the $(\dot{a}/a)^2$ term.

Finally, if we differentiate the first Friedmann equation (A.29) and use the second Friedmann equation (A.30) to eliminate the \ddot{a} term, we obtain the continuity equation

$$\dot{\rho} + 3\frac{\dot{a}}{a}(\rho + p) = 0. \quad (\text{A.31})$$

This equation can also be derived from the Bianchi identity $\nabla_{\mu}G^{\mu\nu} = 0$, which, from the Einstein field equations (A.13), implies the conservation of energy-momentum condition $\nabla_{\mu}T^{\mu\nu} = 0$.

Appendix B

Thermodynamics of the Early Universe

B.1 Equilibrium

The extremely hot and dense conditions in the early universe ensure that the exotic particles present are frequently colliding and interacting such that we can safely assume that thermal equilibrium is established. The phase-space distribution function for a particle in kinetic equilibrium is given by the usual Fermi-Dirac or Bose-Einstein distribution (see for example [80]),

$$f(\vec{p}) = \{\exp [(E(\vec{p}) - \mu)/T] \pm 1\}^{-1}, \quad (\text{B.1})$$

where \vec{p} and m are the particle's momentum and rest mass respectively, $E(\vec{p}) = \sqrt{|\vec{p}|^2 + m^2}$ is the energy and μ is the chemical potential. The +1 and -1 correspond to fermions and bosons respectively. The number density is obtained by integrating the distribution function over momentum space,

$$n(T) = \frac{g}{(2\pi)^3} \int f(\vec{p}) d^3p, \quad (\text{B.2})$$

where g is the number of internal degrees of freedom of the particle. Similarly, the energy density, ρ , and pressure, P , are given respectively by

$$\rho(T) = \frac{g}{(2\pi)^3} \int E(\vec{p}) f(\vec{p}) d^3p, \quad (\text{B.3})$$

$$P(T) = \frac{g}{(2\pi)^3} \int \frac{|\vec{p}|^2}{3E(\vec{p})} f(\vec{p}) d^3p. \quad (\text{B.4})$$

In this appendix, we use a capital P to denote the pressure in order to distinguish it from the momentum \vec{p} . Substituting in the equilibrium distribution (B.1) we then have

$$n_{\text{eq}}(T) = \frac{g}{2\pi^2} \int_m^\infty \frac{(E^2 - m^2)^{1/2}}{\exp(E - \mu)/T \pm 1} E dE, \quad (\text{B.5})$$

$$\rho_{\text{eq}}(T) = \frac{g}{2\pi^2} \int_m^\infty \frac{(E^2 - m^2)^{1/2}}{\exp(E - \mu)/T \pm 1} E^2 dE, \quad (\text{B.6})$$

$$P_{\text{eq}}(T) = \frac{g}{6\pi^2} \int_m^\infty \frac{(E^2 - m^2)^{3/2}}{\exp(E - \mu)/T \pm 1} dE. \quad (\text{B.7})$$

Assuming the species is non-degenerate ($T \gg \mu$) then, in the relativistic limit ($T \gg m$), the expressions for n_{eq} , ρ_{eq} and P_{eq} simplify to

$$\begin{aligned} n_{\text{eq}}(T \gg m) &\simeq \frac{g}{2\pi^2} T^3 \int_0^\infty \frac{x^2}{e^x \pm 1} dx, \\ \rho_{\text{eq}}(T \gg m) &\simeq \frac{g}{2\pi^2} T^4 \int_0^\infty \frac{x^3}{e^x \pm 1} dx, \\ P_{\text{eq}}(T \gg m) &\simeq \rho_{\text{eq}}/3, \end{aligned} \quad (\text{B.8})$$

where $x = E/T$. The integrals

$$I_n^{(\pm)} \equiv \int_0^\infty \frac{x^n}{e^x \pm 1} dx \quad (\text{B.9})$$

are evaluated in terms of the standard integral

$$\int_0^\infty \frac{x^n}{e^{\mu x} - 1} dx = \frac{1}{\mu^{n+1}} \Gamma(n+1) \zeta(n+1) \quad (\text{B.10})$$

where $\zeta(n)$ is the Riemann Zeta function. Using

$$I_3^{(-)} = \int_0^\infty \frac{x^3 dx}{e^x - 1} = \Gamma(4) \zeta(4) = \frac{\pi^4}{15} \quad (\text{B.11})$$

and

$$I_3^{(+)} = \frac{7}{8} I_3^{(-)} = \frac{7\pi^4}{8 \cdot 15}, \quad (\text{B.12})$$

we then have,

$$n_{\text{eq}}(T \gg m) = \begin{cases} g (\zeta(3)/\pi^2) T^3, & \text{Boson,} \\ g (3/4) (\zeta(3)/\pi^2) T^3, & \text{Fermion.} \end{cases} \quad (\text{B.13})$$

$$\rho_{\text{eq}}(T \gg m) = \begin{cases} g (\pi^2/30) T^4, & \text{Boson,} \\ g (7/8) (\pi^2/30) T^4, & \text{Fermion} \end{cases} \quad (\text{B.14})$$

$$P_{\text{eq}}(T \gg m) = \rho_{\text{eq}}/3 \quad (\text{B.15})$$

where $\zeta(3) = 1.2020$. Similarly, in the non-relativistic limit ($T \ll m$), we have for both fermions and bosons

$$n_{\text{eq}}(T \ll m) = g \left(\frac{mT}{2\pi} \right)^{3/2} e^{-(m-\mu)/T}, \quad (\text{B.16})$$

$$\rho_{\text{eq}}(T \ll m) = mn, \quad (\text{B.17})$$

$$P_{\text{eq}}(T \ll m) = nT \ll \rho. \quad (\text{B.18})$$

The total energy density at early times is determined by summing the energy from each of the particle species i ,

$$\rho_{\text{tot}}(T) = \sum_i \rho_i(T). \quad (\text{B.19})$$

Since the energy and pressure of non-relativistic particles is exponentially suppressed, we need only consider the contribution from relativistic particles to the total energy density. Thus

$$\begin{aligned} \rho_{\text{tot}} &= \left(\sum_B g_B + \frac{7}{8} \sum_F g_F \right) \frac{\pi^2}{30} T^4 \\ &\equiv g_{*\rho}(T) \frac{\pi^2}{30} T^4 \end{aligned} \quad (\text{B.20})$$

where

$$g_{*\rho}(T) \equiv \sum_B g_B + \frac{7}{8} \sum_F g_F \quad (\text{B.21})$$

is the effective number of relativistic degrees of freedom. Note that if the various bosons and fermions are not in thermal equilibrium at the same temperature, then (B.21) is generalized to

$$g_{*\rho}(T) = \sum_B g_B \left(\frac{T_B}{T} \right)^4 + \frac{7}{8} \sum_F g_F \left(\frac{T_F}{T} \right)^4. \quad (\text{B.22})$$

For a given temperature T , the particles which contribute to $g_{*\rho}(T)$ are those for which $m < T$.

B.2 Entropy

From the first and second law of thermodynamics we have,

$$TdS(V, T) = dQ = dU + PdV = d(\rho_{\text{eq}}(T)V) + P_{\text{eq}}(T)dV \quad (\text{B.23})$$

where $S(V, T)$ is the entropy of particles in equilibrium at temperature T within a volume V . The integrability condition $\partial^2 S / \partial V \partial T = \partial^2 S / \partial T \partial V$ then gives

$$\frac{dP_{\text{eq}}(T)}{dT} = \frac{1}{T} [P_{\text{eq}}(T) + \rho_{\text{eq}}(T)]. \quad (\text{B.24})$$

Provided the particles in thermal equilibrium only interact with each other, their total energy and pressure satisfy the Einstein energy conservation relation (A.31) which can be written

$$a^3(t) \frac{dP_{\text{eq}}(t)}{dt} = \frac{d}{dt} \{a^3(t) [P_{\text{eq}}(t) + \rho_{\text{eq}}(t)]\}. \quad (\text{B.25})$$

Substituting in (B.24) we obtain

$$\frac{d}{dt} \left\{ \frac{a^3}{T} [P_{\text{eq}}(T) + \rho_{\text{eq}}(T)] \right\} = 0. \quad (\text{B.26})$$

The conservation law (B.26) has a simple interpretation in terms of entropy since, from (B.23),

$$\begin{aligned} dS(V, T) &= \frac{1}{T} [d(\rho_{\text{eq}}(T)V + P_{\text{eq}}(T)V) - dP_{\text{eq}}(T)V] \\ &= d \left[\frac{1}{T} \{P_{\text{eq}}(T) + \rho_{\text{eq}}(T)\} V \right]. \end{aligned} \quad (\text{B.27})$$

Hence up to an additive constant, the entropy is

$$S(V, T) = \frac{V}{T} [\rho_{\text{eq}}(T) + P_{\text{eq}}(T)] \quad (\text{B.28})$$

and therefore (B.26) indicates that the entropy in the volume $V = a^3(t)$ is conserved. Thus standard cosmology assumes that the universe expanded adiabatically. In this case, it is convenient to introduce the entropy density

$$s \equiv \frac{S(a^3, T)}{a^3} = \frac{1}{T} [\rho_{\text{eq}}(T) + P_{\text{eq}}(T)]. \quad (\text{B.29})$$

Recalling (B.14) and (B.15) for relativistic particles, then (B.29) gives

$$s = \frac{4}{3} \frac{\rho_{\text{eq}}}{T} = \frac{2\pi^2}{45} g_{*s}(T) T^3 \quad (\text{B.30})$$

where $g_{*s}(T)$ is the number of entropic degrees of freedom. For bosons and fermions in thermal equilibrium at different temperatures, $g_{*s}(T)$ is given by

$$g_{*s}(T) = \sum_B g_B \left(\frac{T_B}{T} \right)^3 + \frac{7}{8} \sum_F g_F \left(\frac{T_F}{T} \right)^3. \quad (\text{B.31})$$

Standard Model Particle Spectrum

	Particle	Mass (GeV)	g_i
Fermions	t	173.07	12
	b	4.18	12
	τ^\pm	1.78	4
	c	1.28	12
	μ^\pm	0.106	4
	s	0.095	12
	d	4.8×10^{-3}	12
	u	2.3×10^{-3}	12
	e^\pm	5.11×10^{-4}	4
	ν	-	6
Bosons	H	125.00	1
	Z	91.19	3
	W^\pm	80.39	6
	* π^0	0.140	1
	* π^\pm	0.135	2
	γ	-	2
	g	-	16

TABLE B.1: Properties of the Standard Model particle spectrum including mass (GeV) and number of spin degrees of freedom g_i . Composite particles are marked with an asterisk.

The number of degrees of freedom is tabulated in B.2 for the Standard Model particle spectrum whose properties are listed in table B.1. We also show, in figure B.1, the functions $g_{*s}(T)$ (solid blue curve) and $g_{*\rho}(T)$ (dashed red curve) which have been extracted directly from the DarkSUSY package [54] which uses the results from [300]. It is clear from figure B.1 that, for $T \gtrsim 10^{-3}$ GeV, $g_{*s}(T) = g_{*\rho}(T)$.

In terms of the entropy density, the conservation law (B.26) becomes

$$\frac{d}{dt}(a^3 s) = 0. \quad (\text{B.32})$$

which, using (B.30), gives

$$g_{*s}(T)T^3 a^3 = \text{const.} \quad (\text{B.33})$$

The temperature and scale factor are therefore related by

$$\left[\frac{g_{*s}(T)}{g_{*s}(T_0)} \right]^{1/3} \frac{T}{T_0} = \frac{a_0}{a}. \quad (\text{B.34})$$

Degrees of freedom

Temperature range	New Particles	g_B	g_F	$g_*(T)$
$T < m_e$	γ, ν	2	6	-
$m_e < T < m_\mu$	e^\pm		4	10.75
$m_\mu < T < m_\pi$	μ^\pm		4	14.25
$m_\pi < T < T_c^*$	$\pi^{\pm,0}$	3		17.25
$T_c^* < T < m_s$	u, d, g	16	24	51.25**
$m_s < T < m_c$	s		12	61.75
$m_c < T < m_\tau$	c		12	72.25
$m_\tau < T < m_b$	τ^\pm		4	75.75
$m_b < T < m_{W,Z}$	b		12	86.25
$m_{W,Z} < T < m_H$	W^\pm, Z	9		95.25
$m_H < T < m_t$	H	1		96.25
$T > m_t$	t		12	106.75

TABLE B.2: Total number of Standard Model degrees of freedom for varying temperature. Note that the fermionic contributions are weighted by a factor 7/8 as in (B.22) and (B.31) and we have omitted the value of $g_*(T)$ for $T < m_e$ since $g_{*\rho}$ and g_{*s} differ in this range. T_c^* is the confinement transition temperature between quarks and hadrons. **Subtract $\pi^{\pm,0}$ contributions for $T > T_c^*$.

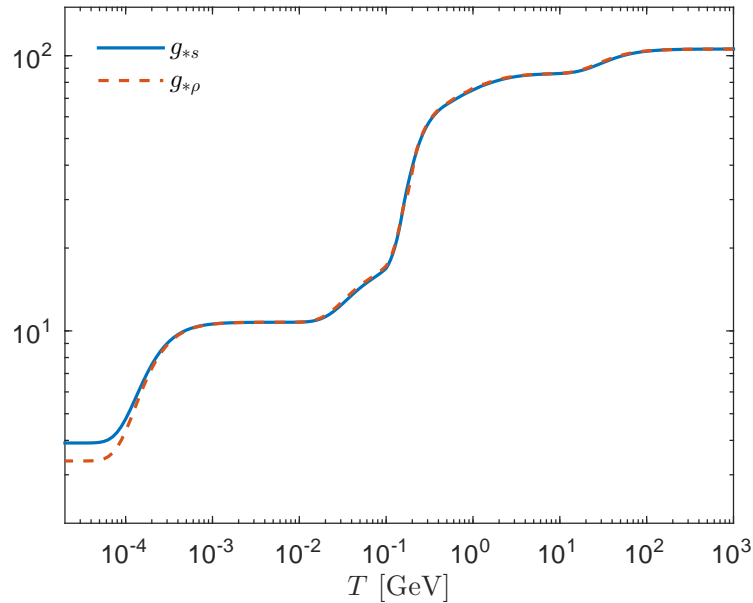


FIGURE B.1: Evolution of the number of entropic degrees of freedom $g_{*s}(T)$ (solid blue curve) and the number of relativistic degrees of freedom $g_{*\rho}(T)$ (dashed red curve) as a function of temperature T for the Standard Model particle spectrum.

When $g_{*s}(T)$ is constant the temperature falls as the inverse of the scale factor, $T \propto a^{-1}$. However, as particles decouple from the thermal plasma and $g_{*s}(T)$ decreases, the temperature falls less slowly than a^{-1} .

Appendix C

Rate Equation for Relic Abundance

C.1 Relativistic Boltzmann equation

The relic abundance of Dark Matter particles is determined from the Relativistic Boltzmann Equation which describes the evolution of the particles. For a system with phase space density $f(x^\mu, p^\mu)$ (where x^μ and $p^\mu = (E, \vec{p})$ are the position and momentum 4-vectors respectively) this equation is given by [80];

$$\hat{L}[f(x^\mu, p^\mu)] = \hat{C}[f(x^\mu, p^\mu)] \quad (\text{C.1})$$

where \hat{L} is the relativistic Liouville operator

$$\hat{L} \equiv p^\alpha \frac{\partial}{\partial x^\alpha} - \Gamma_{\beta\gamma}^\alpha p^\beta p^\gamma \frac{\partial}{\partial p^\alpha} \quad (\text{C.2})$$

and \hat{C} is the collision operator (to be discussed in section C.2). We can show that the relativistic Liouville operator reduces to the regular non-relativistic form by noting that, for a Robertson-Walker metric, the only non-vanishing affine connections, $\Gamma_{\beta\gamma}^0$, are (see (A.19))

$$\Gamma_{ij}^0 = \frac{\dot{a}}{a} g_{ij}. \quad (\text{C.3})$$

Hence

$$\hat{L} = p^i \frac{\partial}{\partial x^i} + E \frac{\partial}{\partial t} - \Gamma_{\beta\gamma}^i p^\beta p^\gamma \frac{\partial}{\partial p^i} - \frac{\dot{a}}{a} g_{ij} p^i p^j \frac{\partial}{\partial E}. \quad (\text{C.4})$$

Noting that $|\vec{p}|^2 = g_{ij}p^i p^j$ and that, from the geodesic equation (A.10), the connection between path curvature and the force acting is $mF^i = -\Gamma^i_{\beta\gamma} p^\beta p^\gamma$, then

$$\begin{aligned}\hat{L} &= p^i \frac{\partial}{\partial x^i} + E \frac{\partial}{\partial t} + mF^i \frac{\partial}{\partial p^i} - \frac{\dot{a}}{a} |\vec{p}|^2 \frac{\partial}{\partial E}, \\ &= \vec{p} \cdot \nabla_x + E \frac{\partial}{\partial t} + m\vec{F} \cdot \nabla_p - \frac{\dot{a}}{a} |\vec{p}|^2 \frac{\partial}{\partial E}.\end{aligned}\quad (\text{C.5})$$

We are interested in the case of a homogeneous and isotropic distribution function $f(x^\mu, p^\mu) = f(E, t)$ for which

$$\begin{aligned}\hat{L}[f(E, t)] &= \vec{p} \cdot \vec{\nabla} f(E, t) + E \frac{\partial}{\partial t} f(E, t) - \Gamma^i_{\beta\gamma} p^\beta p^\gamma \frac{\partial}{\partial p^i} f(E, t) - \frac{\dot{a}}{a} |\vec{p}|^2 \frac{\partial}{\partial E} f(E, t) \\ &= E \frac{\partial f}{\partial t} - \frac{\dot{a}}{a} |\vec{p}|^2 \frac{\partial f}{\partial E}.\end{aligned}\quad (\text{C.6})$$

The evolution of the number density $n(t)$, given by (B.2),

$$n(t) = \frac{g}{(2\pi)^3} \int d\vec{p} f(E, t), \quad (\text{C.7})$$

where g is the number of internal degrees of freedom, can be obtained by taking the zeroth moment of the Boltzmann equation (C.1):

$$\frac{g}{(2\pi)^3} \int d\vec{p} \frac{\hat{L}[f(E, t)]}{E} = \frac{g}{(2\pi)^3} \int d\vec{p} \frac{\hat{C}[f(E, t)]}{E}. \quad (\text{C.8})$$

The left hand side of this equation can be evaluated using (C.6). We then have

$$\begin{aligned}\frac{g}{(2\pi)^3} \int d\vec{p} \frac{\hat{L}[f(E, t)]}{E} &= \frac{g}{(2\pi)^3} \int d\vec{p} \frac{\partial f}{\partial t} - \frac{\dot{a}}{a} \frac{g}{(2\pi)^3} \int d\vec{p} \frac{|\vec{p}|^2}{E} \frac{\partial f}{\partial E} \\ &= \frac{dn}{dt} - \frac{\dot{a}}{a} \frac{g}{(2\pi)^3} \int d\Omega_p \int d|\vec{p}| \frac{|\vec{p}|^4}{E} \frac{\partial f}{\partial E}\end{aligned}\quad (\text{C.9})$$

where we have inserted the definition (C.7) for the number density. We can simplify the integral in (C.9) by using the relation

$$E^2 - |\vec{p}|^2 = m^2 \Rightarrow E dE = |\vec{p}| d|\vec{p}| \quad (\text{C.10})$$

so that

$$\frac{\dot{a}}{a} \frac{g}{(2\pi)^3} \int d\Omega_p \int d|\vec{p}| \frac{|\vec{p}|^4}{E} \frac{\partial f}{\partial E} = \frac{\dot{a}}{a} \frac{g}{(2\pi)^3} \int d\Omega_p \int dE |\vec{p}|^3 \frac{\partial f}{\partial E}. \quad (\text{C.11})$$

Integration by parts gives

$$\begin{aligned}
& \frac{\dot{a}}{a} \frac{g}{(2\pi)^3} \int d\Omega_p \left\{ \left[|\vec{p}|^3 f(E, t) \right]_0^\infty - 3 \int dE |\vec{p}|^2 \frac{d|\vec{p}|}{dE} f(E, t) \right\} \\
&= -3 \frac{\dot{a}}{a} \frac{g}{(2\pi)^3} \int d\Omega_p \int d|\vec{p}| |\vec{p}|^2 f(E, t) \\
&= -3 \frac{\dot{a}}{a} \frac{g}{(2\pi)^3} \int d\vec{p} f(E, t) \\
&= -3Hn(t).
\end{aligned} \tag{C.12}$$

The Boltzmann equation then becomes

$$\frac{dn}{dt} + 3Hn = \frac{g}{(2\pi)^3} \int \hat{C}(f) \frac{d\vec{p}}{E}. \tag{C.13}$$

C.2 Collision term

The derivation of the collision term presented here is based on Kolb and Turner [80] and Gondolo and Gelmini [199].

The collision term for the process $\chi + a + b + \dots \leftrightarrow i + j + \dots$ is given by [80]

$$\begin{aligned}
\frac{g}{(2\pi)^3} \int \hat{C}(f) \frac{d\vec{p}_\chi}{E_\chi} &= - \int d\Pi_\chi d\Pi_a d\Pi_b \dots d\Pi_i d\Pi_j \dots \times (2\pi)^4 \delta^4(p_\chi + p_a + p_b \dots - p_i - p_j \dots) \\
&\times [|\mathcal{M}|_{\chi+a+b+\dots \rightarrow i+j+\dots}^2 f_a f_b \dots f_\chi (1 \pm f_i)(1 \pm f_j) \dots \\
&\quad - |\mathcal{M}|_{i+j+\dots \rightarrow \chi+a+b+\dots}^2 f_i f_j \dots (1 \pm f_a)(1 \pm f_b) \dots (1 \pm f_\chi)]
\end{aligned} \tag{C.14}$$

where $f_i, f_j, f_a, f_b, \dots$ are the phase space densities of species i, j, \dots, a, b, \dots ; f_χ is the phase space density of the dark matter species χ ; the sign (+) applies to bosons; and (−) to fermions; and

$$d\Pi \equiv g \frac{1}{(2\pi)^3} \frac{d\vec{p}}{2E} \tag{C.15}$$

is the invariant phase space element. The four dimensional delta function enforces energy and momentum conservation, and the matrix element squared, $|\mathcal{M}|_{i+j+\dots \rightarrow \chi+a+b+\dots}^2$, for the process $i + j + \dots \rightarrow \chi + a + b + \dots$, is averaged over initial and final spins, and includes the appropriate symmetry factors for identical particles in the initial or final states.

The collision integral (C.14) simplifies considerably if we assume CP invariance, in which case the matrix element satisfies

$$|\mathcal{M}|_{i+j+\dots \rightarrow \chi+a+b+\dots}^2 = |\mathcal{M}|_{\chi+a+b+\dots \rightarrow i+j+\dots}^2 \equiv |\mathcal{M}|^2, \tag{C.16}$$

and if we neglect the Fermi-Dirac blocking or Bose-Einstein stimulated emission factors and use Maxwell-Boltzmann statistics for all species so that $1 \pm f_i \simeq 1$, where $f_i(E) = \exp[-(E - \mu)/T]$.

We will consider the case where only annihilation and inverse annihilation processes are possible,

$$\chi\bar{\chi} \leftrightarrow X\bar{X} \quad (\text{C.17})$$

and assume that all the species X, \bar{X} into which $\chi, \bar{\chi}$ annihilate have thermal distributions with zero chemical potential. Because these particles are lighter and will usually have additional interactions which are "stronger" than their interaction with the χ 's, the assumption of equilibrium for X 's is almost always a good one.

The factor $[\dots]$ in (C.14) then reduces to $|\mathcal{M}|^2 [f_\chi f_{\bar{\chi}} - f_X f_{\bar{X}}]$. Since X, \bar{X} are in thermal equilibrium and have zero chemical potential, their distribution functions are

$$f_X = \exp(-E_X/T), \quad f_{\bar{X}} = \exp(-E_{\bar{X}}/T). \quad (\text{C.18})$$

The energy part of the δ -function enforces $E_\chi + E_{\bar{\chi}} = E_X + E_{\bar{X}}$, so that

$$f_X f_{\bar{X}} = \exp[-(E_X + E_{\bar{X}})/T] = \exp[-(E_\chi + E_{\bar{\chi}})/T] = f_\chi^{\text{eq}} f_{\bar{\chi}}^{\text{eq}} \quad (\text{C.19})$$

since $f_\chi^{\text{eq}} \equiv \exp(-E_\chi/T)$ and $f_{\bar{\chi}}^{\text{eq}} \equiv \exp(-E_{\bar{\chi}}/T)$. Therefore, it follows that

$$[f_\chi f_{\bar{\chi}} - f_X f_{\bar{X}}] = [f_\chi f_{\bar{\chi}} - f_\chi^{\text{eq}} f_{\bar{\chi}}^{\text{eq}}]. \quad (\text{C.20})$$

The collision term now becomes

$$\begin{aligned} & - \int d\Pi_\chi d\Pi_{\bar{\chi}} d\Pi_X d\Pi_{\bar{X}} (2\pi)^4 \delta^4(p_\chi + p_{\bar{\chi}} - p_X - p_{\bar{X}}) |\mathcal{M}|^2 [f_\chi f_{\bar{\chi}} - f_X f_{\bar{X}}] \\ & = -4 \int d\Pi_\chi d\Pi_{\bar{\chi}} v_{\text{Møll}} E_\chi E_{\bar{\chi}} \sigma_{\chi\bar{\chi} \rightarrow X\bar{X}} [f_\chi f_{\bar{\chi}} - f_\chi^{\text{eq}} f_{\bar{\chi}}^{\text{eq}}] \end{aligned} \quad (\text{C.21})$$

where the collision cross section $\sigma_{\chi\bar{\chi} \rightarrow X\bar{X}}$ and the Møller relative velocity $v = v_{\text{Møll}} = [|\vec{v}_\chi - \vec{v}_{\bar{\chi}}|^2 - |\vec{v}_\chi \times \vec{v}_{\bar{\chi}}|^2]^{1/2}$ have been introduced using [199]

$$\int d\Pi_X d\Pi_{\bar{X}} |\mathcal{M}|^2 \delta^4(p_\chi + p_{\bar{\chi}} - p_X - p_{\bar{X}}) = 4v_{\text{Møll}} E_X E_{\bar{X}} \sigma_{\chi\bar{\chi} \rightarrow X\bar{X}}. \quad (\text{C.22})$$

The RHS of (C.21) is then

$$\begin{aligned} \text{RHS} & = -4 \int d\vec{p}_\chi \frac{g}{(2\pi)^3} \frac{1}{2E_\chi} d\vec{p}_{\bar{\chi}} \frac{g}{(2\pi)^3} \frac{1}{2E_{\bar{\chi}}} \sigma_{\chi\bar{\chi} \rightarrow X\bar{X}} v E_\chi E_{\bar{\chi}} [f_\chi f_{\bar{\chi}} - f_\chi^{\text{eq}} f_{\bar{\chi}}^{\text{eq}}] \\ & = - \int \sigma_{\chi\bar{\chi} \rightarrow X\bar{X}} v [dn_\chi dn_{\bar{\chi}} - dn_\chi^{\text{eq}} dn_{\bar{\chi}}^{\text{eq}}] \end{aligned} \quad (\text{C.23})$$

where

$$dn_\chi = \frac{g}{(2\pi)^3} f_\chi d\vec{p}_\chi. \quad (\text{C.24})$$

To find the total annihilation cross-section we must sum over all possible annihilation channels such that $\sigma_{\chi\bar{\chi} \rightarrow X\bar{X}}$ is replaced by [199]

$$\sigma_a = \sum \sigma_{\chi\bar{\chi} \rightarrow X\bar{X}}. \quad (\text{C.25})$$

The integrals over n_χ^{eq} and $n_{\bar{\chi}}^{\text{eq}}$ are just the thermally averaged annihilation cross section times relative velocity $\langle \sigma_a v \rangle$ [199]

$$\langle \sigma_a v \rangle = \frac{\int \sigma_a v dn_\chi^{\text{eq}} dn_{\bar{\chi}}^{\text{eq}}}{\int dn_\chi^{\text{eq}} dn_{\bar{\chi}}^{\text{eq}}}. \quad (\text{C.26})$$

However, the evaluation of the integrals over n_χ and $n_{\bar{\chi}}$ in (C.23) is not a trivial task and warrants some discussion. The species χ and $\bar{\chi}$ are maintained in kinetic equilibrium through their scattering with other numerous particles in the thermal bath during all of their evolution, even after their decoupling when they are out of chemical equilibrium. This scattering rate is much faster than their annihilation rate. It is then argued [199] that, from symmetry considerations, the distributions in kinetic equilibrium are proportional to those in chemical equilibrium, with a proportionality factor independent of momentum, that is $n_\chi = D n_\chi^{\text{eq}}$ and $n_{\bar{\chi}} = D' n_{\bar{\chi}}^{\text{eq}}$. Thus (C.23) becomes

$$\begin{aligned} \frac{g}{(2\pi)^3} \int \hat{C}(f) \frac{d\vec{p}_\chi}{E_\chi} &= - \left[\frac{n_\chi n_{\bar{\chi}}}{n_\chi^{\text{eq}} n_{\bar{\chi}}^{\text{eq}}} - 1 \right] \int \sigma_a v dn_\chi^{\text{eq}} dn_{\bar{\chi}}^{\text{eq}} \\ &= - (n_\chi n_{\bar{\chi}} - n_\chi^{\text{eq}} n_{\bar{\chi}}^{\text{eq}}) \langle \sigma_a v \rangle, \end{aligned} \quad (\text{C.27})$$

where in the last line we have used the definition for the thermally averaged annihilation cross section times relative velocity (C.26). Finally, combining (C.27) with (C.13), we obtain the Boltzmann equation describing the time evolution of the dark matter number density,

$$\frac{dn_\chi}{dt} + 3Hn_\chi = -\langle \sigma_a v \rangle [n_\chi n_{\bar{\chi}} - n_\chi^{\text{eq}} n_{\bar{\chi}}^{\text{eq}}]. \quad (\text{C.28})$$

If the species χ is symmetric, then $n_\chi = n_{\bar{\chi}}$, and the Boltzmann equation reduces to

$$\frac{dn_\chi}{dt} + 3Hn_\chi = -\langle \sigma_a v \rangle [n_\chi^2 - (n_\chi^{\text{eq}})^2]. \quad (\text{C.29})$$

Appendix D

Lagrangian Field Theory

D.1 Euler-Lagrange equations

In the Lagrangian formalism, the evolution of a dynamical system is derived from the principal of least action (see for example [301]).

Consider a system described by a set of continuous fields $\{\Phi^i\}$, where the $\Phi^i \equiv \Phi^i(x^\rho)$ are a function of the spacetime coordinate x^ρ . Note that because the manifold \mathcal{M} (and its coordinates) upon which the field theory is defined is arbitrary, the metric $g_{\mu\nu}$ of the manifold must be included in the set $\{\Phi^i\}$.¹

The covariant action integral is defined as

$$S = \int_{\mathcal{M}} d^4x \sqrt{-g} L(\Phi^i, \partial_\mu \Phi^i, \dots), \quad (\text{D.1})$$

where $L \equiv L(\Phi^i, \partial_\mu \Phi^i, \dots)$ is the *field Lagrangian*, which in general will be a function of the fields Φ^i and their first (and possibly higher order) derivatives. The integral is taken over the spacetime manifold \mathcal{M} and the covariant volume element $dV = \sqrt{-g} d^4x$, where g , the determinant of the metric $g_{\mu\nu}$, has been introduced so that S is a scalar under general coordinate transformations.

Introducing the arbitrary variation in the field(s) and their derivatives

$$\begin{aligned} \Phi^i(x^\rho) &\rightarrow \Phi'^i(x^\rho) = \Phi^i(x^\rho) + \delta\Phi^i(x^\rho), \\ \partial_\mu \Phi^i(x^\rho) &\rightarrow \partial_\mu \Phi'^i(x^\rho) = \partial_\mu \Phi^i(x^\rho) + \delta(\partial_\mu \Phi^i(x^\rho)), \end{aligned} \quad (\text{D.2})$$

¹Here, i labels the different fields in the set and should not be treated as a tensorial index.

where we have used the fact that the variation δ and the partial derivative ∂_μ commute,

$$\partial_\mu(\delta\Phi^i) = \partial_\mu(\Phi'^i - \Phi^i) = \partial_\mu\Phi'^i - \partial_\mu\Phi^i = \delta(\partial_\mu\Phi^i), \quad (\text{D.3})$$

then the variation in the action integral becomes

$$\delta S = \int_{\mathcal{M}} d^4x \delta(\sqrt{-g}L) = \int_{\mathcal{M}} d^4x \left[\frac{\partial(\sqrt{-g}L)}{\partial\Phi^i} \delta\Phi^i + \frac{\partial(\sqrt{-g}L)}{\partial(\partial_\mu\Phi^i)} \delta(\partial_\mu\Phi^i) \right]. \quad (\text{D.4})$$

To simplify the second term in (D.4), we first write it as

$$\int_{\mathcal{M}} d^4x \frac{\partial(\sqrt{-g}L)}{\partial(\partial_\mu\Phi^i)} \delta(\partial_\mu\Phi^i) = \int_{\mathcal{M}} d^4x \partial_\mu \left[\frac{\partial(\sqrt{-g}L)}{\partial(\partial_\mu\Phi^i)} \delta\Phi^i \right] - \int_{\mathcal{M}} d^4x \partial_\mu \left[\frac{\partial(\sqrt{-g}L)}{\partial(\partial_\mu\Phi^i)} \right] \delta\Phi^i. \quad (\text{D.5})$$

Using Stokes' theorem, the first term on the right hand side can be converted to an integral over the boundary, $\partial\mathcal{M}$, of the spacetime manifold \mathcal{M} , upon which we assume that $\delta\Phi^i$ vanishes. Therefore, this term will vanish. In general, this result implies that any term that can be written as a total divergence can be removed upon integration by parts and will not contribute to the resulting field equations.

Finally, substituting (D.5) back into (D.4) and setting $\delta S = 0$ for arbitrary $\delta\Phi^i$, we get the Euler-Lagrange (E-L) equations

$$\frac{\partial(\sqrt{-g}L)}{\partial\Phi^i} - \partial_\mu \left[\frac{\partial(\sqrt{-g}L)}{\partial(\partial_\mu\Phi^i)} \right] = 0. \quad (\text{D.6})$$

Repeating this procedure, it is straightforward to generalize (D.6) to the case where the Lagrangian density contains higher order derivatives of the fields Φ^i , i.e. $L \equiv L(\Phi^i, \partial_\mu\Phi^i, \partial_\mu\partial_\nu\Phi^i, \dots)$,

$$\frac{\partial(\sqrt{-g}\mathcal{L})}{\partial\Phi^i} - \partial_\mu \left[\frac{\partial(\sqrt{-g}\mathcal{L})}{\partial(\partial_\mu\Phi^i)} \right] + \partial_\mu\partial_\nu \left[\frac{\partial(\sqrt{-g}\mathcal{L})}{\partial(\partial_\mu\partial_\nu\Phi^i)} \right] - \partial_\mu\partial_\nu\partial_\rho \left[\frac{\partial(\sqrt{-g}\mathcal{L})}{\partial(\partial_\mu\partial_\nu\partial_\rho\Phi^i)} \right] + \dots = 0. \quad (\text{D.7})$$

D.2 Lagrangian formalism for a scalar field

As a simple illustration of the Lagrangian formalism we derive the field equations for a non-interacting scalar field $\phi(x^\rho)$ for which the Lagrangian density is given by

$$L_\phi = -\frac{1}{2}g^{\mu\nu}\partial_\mu\phi\partial_\nu\phi - V(\phi). \quad (\text{D.8})$$

The first term is a generalized 'kinetic' term and the second term is the self-interaction potential V . The equation of motion for the scalar field is derived using the Euler-Lagrange equations (D.6) derived in the previous section,

$$\frac{\partial(\sqrt{-g}L_\phi)}{\partial\phi} - \partial_\mu \left[\frac{\partial(\sqrt{-g}L_\phi)}{\partial(\partial_\mu\phi)} \right] = 0, \quad (\text{D.9})$$

where we treat ϕ as the independent field. Substituting in the Lagrangian (D.8), the first term in the E-L equations is simply

$$\frac{\partial(\sqrt{-g}L_\phi)}{\partial\phi} = -\sqrt{-g} \frac{\partial V(\phi)}{\partial\phi}, \quad (\text{D.10})$$

where the kinetic term in (D.8) does not contribute because it is a function of the field derivative only. Next we evaluate the second term in (D.9) to get

$$\partial_\mu \left[\frac{\partial(\sqrt{-g}L_\phi)}{\partial(\partial_\mu\phi)} \right] = \partial_\mu (-\sqrt{-g}g^{\alpha\mu}\partial_\alpha\phi) = -\sqrt{-g}\square\phi \quad (\text{D.11})$$

where we have used the identity

$$\square\phi \equiv \nabla_\mu \nabla^\mu \phi = \frac{1}{\sqrt{-g}} \partial_\mu (\sqrt{-g}g^{\mu\alpha}\partial_\alpha\phi) \quad (\text{D.12})$$

with the covariant derivative ∇_μ defined in (A.7). Combining (D.10) and (D.11) yields the equation of motion for the scalar field

$$\square\phi = \frac{\partial V}{\partial\phi}. \quad (\text{D.13})$$

If ϕ is homogeneous such that $\phi \equiv \phi(t)$, the left hand side of the equation of motion reduces to

$$\square\phi = g^{\mu\nu}\nabla_\mu\nabla_\nu\phi = g^{00}\partial_0\partial_0\phi - g^{ij}\Gamma_{ij}^0\partial_0\phi = -\ddot{\phi} - 3\frac{\dot{a}}{a}\dot{\phi} \quad (\text{D.14})$$

where we have used $g^{ij}\Gamma_{ij}^0 = 3\dot{a}/a$ (see Appendix A). The equation of motion becomes

$$\ddot{\phi} + 3H\dot{\phi} + \frac{\partial V}{\partial\phi} = 0. \quad (\text{D.15})$$

The energy-momentum tensor of the scalar field $\phi(x^\rho)$ is defined as

$$T_{\mu\nu}^\phi = -\frac{2}{\sqrt{-g}} \frac{\delta(\sqrt{-g}L_\phi)}{\delta g^{\mu\nu}}. \quad (\text{D.16})$$

The variation term is

$$\frac{\delta(\sqrt{-g}L_\phi)}{\delta g^{\mu\nu}} = -\frac{1}{2} \frac{\delta(\sqrt{-g}g^{\rho\sigma})}{\delta g^{\mu\nu}} \partial_\rho\phi\partial_\sigma\phi - \frac{\delta\sqrt{-g}}{\delta g^{\mu\nu}} V(\phi), \quad (\text{D.17})$$

which can be simplified using the identities

$$\begin{aligned}\delta g^{\rho\sigma} &= \frac{1}{2} (\delta_\mu^\rho \delta_\nu^\sigma + \delta_\nu^\rho \delta_\mu^\sigma) \delta g^{\mu\nu}, \\ \delta(\sqrt{-g}) &= -\frac{1}{2} \sqrt{-g} g_{\mu\nu} \delta g^{\mu\nu}.\end{aligned}\tag{D.18}$$

Substituting back into (D.16) yields

$$T_{\mu\nu}^\phi = \partial_\mu \phi \partial_\nu \phi - g_{\mu\nu} \left[\frac{1}{2} g^{\rho\sigma} \partial_\rho \phi \partial_\sigma \phi + V(\phi) \right].\tag{D.19}$$

Lastly, we can write the energy-momentum tensor (D.19) in the perfect fluid form

$$T_{\mu\nu}^\phi = (\rho_\phi + p_\phi) u_\mu^\phi u_\nu^\phi + p_\phi g_{\mu\nu}\tag{D.20}$$

where [299]

$$\rho_\phi = -\frac{1}{2} g^{\mu\nu} \partial_\mu \phi \partial_\nu \phi + V(\phi),\tag{D.21}$$

$$p_\phi = -\frac{1}{2} g^{\mu\nu} \partial_\mu \phi \partial_\nu \phi - V(\phi),\tag{D.22}$$

$$u_\mu^\phi = -[-g^{\rho\sigma} \partial_\rho \phi \partial_\sigma \phi]^{-1/2} \partial_\mu \phi.\tag{D.23}$$

D.3 Einstein's field equations from a variational principle

The field equations of General Relativity can also be derived from the principle of least action using the Einstein-Hilbert (EH) action,

$$S_{\text{EH}} = \frac{1}{2\kappa^2} \int_{\mathcal{M}} d^4x \sqrt{-g} R,\tag{D.24}$$

where $R = g^{\mu\nu} R_{\mu\nu}$ is the Ricci scalar and the constant $\kappa^2 = 8\pi G$ will be required when we introduce matter fields. Varying this action with respect to the metric field $g^{\mu\nu}$, yields

$$\delta S_{\text{EH}} = \int_{\mathcal{M}} d^4x \left[\delta(\sqrt{-g}) R + \sqrt{-g} R_{\mu\nu} \delta g^{\mu\nu} + \sqrt{-g} g^{\mu\nu} \delta R_{\mu\nu} \right].\tag{D.25}$$

The first term can be evaluated using (D.18) and the second term already contains the variation $\delta g^{\mu\nu}$, so we turn our attention to the final term $\sqrt{-g} g^{\mu\nu} \delta R_{\mu\nu}$. After a considerable amount of algebra, we find that

$$g^{\mu\nu} \delta R_{\mu\nu} = \nabla_\mu \nabla_\nu (g^{\mu\nu} g_{\rho\sigma} \delta g^{\rho\sigma} - \delta g^{\mu\nu}).\tag{D.26}$$

Hence, the final term in (D.25) is a total divergence and will not contribute to the field equations.² Therefore, substituting in the identity (D.18) and setting $\delta S_{\text{EH}} = 0$, we obtain Einstein's field equations in a vacuum,

$$G_{\mu\nu} \equiv R_{\mu\nu} - \frac{1}{2}g_{\mu\nu}R = 0. \quad (\text{D.27})$$

We extend this result by including matter fields and a cosmological constant Λ so that the total action becomes

$$S_{\text{GR}} = \frac{1}{2\kappa^2} \int_{\mathcal{M}} d^4x \sqrt{-g} (R - 2\Lambda) + S_{\text{mat}}. \quad (\text{D.28})$$

Variation with respect to the metric field then yields the Einstein equations of General Relativity

$$R_{\mu\nu} - \frac{1}{2}g_{\mu\nu}R + g_{\mu\nu}\Lambda = \kappa^2 T_{\mu\nu} \quad (\text{D.29})$$

where the energy-momentum tensor of the matter fields $T_{\mu\nu}$ is defined as

$$T_{\mu\nu} = -\frac{2}{\sqrt{-g}} \frac{\delta S_{\text{mat}}}{\delta g^{\mu\nu}}. \quad (\text{D.30})$$

²We could have arrived at the same result if we had instead considered the variation in $R_{\mu\nu}$ in a locally geodesic coordinate system and then transformed to an arbitrary reference frame.

Appendix E

Equations of Scalar-tensor gravity

E.1 Jordan frame field equations

In this appendix we derive the cosmological equations in scalar-tensor gravity models, i.e. the modified Friedmann equation (4.22) and the scalar field time evolution equation (4.24).

To begin we write the Jordan frame action integral (4.4) as

$$S_{\text{tot}} = S_g + S_\varphi + S_{\text{mat}}$$

where

$$S_g = \frac{1}{16\pi G_*} \int d^4x \sqrt{-g} F(\varphi) R,$$
$$S_\varphi = -\frac{1}{16\pi G_*} \int d^4x \sqrt{-g} [g^{\mu\nu} Z(\varphi) \partial_\mu \varphi \partial_\nu \varphi + 2U(\varphi)],$$

and $S_{\text{mat}} \equiv S_{\text{mat}}[g_{\mu\nu}; \Psi_{\text{mat}}]$. The gravitational field equations in this frame can be derived by varying each term with respect to the Jordan frame metric $g^{\mu\nu}$. Beginning with the gravitational action S_g we have

$$\begin{aligned} \delta S_g &= \frac{1}{16\pi G_*} \int d^4x F(\varphi) [\delta(\sqrt{-g})R + \sqrt{-g}\delta R], \\ &= \frac{1}{16\pi G_*} \int d^4x F(\varphi) \left[-\frac{1}{2}\sqrt{-g}g_{\mu\nu}\delta g^{\mu\nu}R + \sqrt{-g}(R_{\mu\nu}\delta g^{\mu\nu} + g^{\mu\nu}\delta R_{\mu\nu}) \right], \\ &= \frac{1}{16\pi G_*} \int d^4x \sqrt{-g} F(\varphi) \left[\left(R_{\mu\nu} - \frac{1}{2}g_{\mu\nu}R \right) \delta g^{\mu\nu} + \nabla_\mu \nabla_\nu (g^{\mu\nu} g_{\alpha\beta} \delta g^{\alpha\beta} - \delta g^{\mu\nu}) \right], \end{aligned}$$

where we have used the identities (D.18) and (D.26) given in Appendix D. Integrating the second term by parts twice and neglecting boundary terms, we finally get

$$\delta S_g = \frac{1}{16\pi G_*} \int \sqrt{-g} \left[F(\varphi) \left(R_{\mu\nu} - \frac{1}{2} g_{\mu\nu} R \right) - (\nabla_\mu \nabla_\nu - g_{\mu\nu} \square) F(\varphi) \right] \delta g^{\mu\nu}$$

where the D'Alembertian \square is defined in (D.12). Combining this result with the variations δS_φ and δS_{mat} , which we can determine straightforwardly using the formalism developed in sections D.2 and D.3 respectively, we get

$$F(\varphi) G_{\mu\nu} - (\nabla_\mu \nabla_\nu - g_{\mu\nu} \square) F(\varphi) = 8\pi G_* (T_{\mu\nu} + T_{\mu\nu}^\varphi) \quad (\text{E.1})$$

where the scalar field energy momentum tensor is given by (cf. (D.19))

$$\begin{aligned} T_{\mu\nu}^\varphi &= -\frac{2}{\sqrt{-g}} \frac{\delta S_\varphi}{\delta g^{\mu\nu}}, \\ &= \frac{1}{8\pi G_*} \left\{ Z(\varphi) \partial_\mu \varphi \partial_\nu \varphi - g_{\mu\nu} \left[\frac{1}{2} g^{\alpha\beta} Z(\varphi) \partial_\alpha \varphi \partial_\beta \varphi + U(\varphi) \right] \right\}, \end{aligned} \quad (\text{E.2})$$

and the matter energy momentum tensor is

$$T_{\mu\nu} = -\frac{2}{\sqrt{-g}} \frac{\delta S_{\text{mat}}}{\delta g^{\mu\nu}}.$$

E.2 Conformal transformation to the Einstein frame

To simplify the gravitational field equations we transform to the Einstein conformal frame by applying a conformal transformation of the form

$$g_{\mu\nu}^* = \Omega^2(x) g_{\mu\nu}, \quad (\text{E.3})$$

where $\Omega(x)$ is an arbitrary function of the spacetime coordinates, and we use the notation Ω^2 to preserve the sign of the line element $ds_*^2 = \Omega^2 ds^2$. In this case, the relevant quantities transform according to

$$\begin{aligned} \sqrt{-g_*} &= \Omega^4 \sqrt{-g}, \\ R &= \Omega^2 R_* + 6\square_*(\log \Omega) - 6g_*^{\mu\nu} \nabla_\mu(\log \Omega) \nabla_\nu(\log \Omega), \end{aligned} \quad (\text{E.4})$$

where R is the Ricci scalar and an asterisk denotes quantities defined using the metric $g_{\mu\nu}^*$. Taking $\Omega(x) = F^{1/2}(\varphi)$ so that

$$g_{\mu\nu}^* = F(\varphi) g_{\mu\nu}, \quad (\text{E.5})$$

the Jordan frame action integral (4.4) can be written

$$S_{\text{tot}} = \frac{1}{16\pi G_*} \int d^4x \sqrt{-g_*} \left\{ R_* - g_{\mu\nu}^* \left[\frac{3}{2F^2} \left(\frac{dF}{d\varphi} \right)^2 + \frac{Z}{F} \right] \partial_\mu \varphi \partial_\nu \varphi - \frac{2U}{F^2} \right\} \\ + S_{\text{mat}}[F^{-1}(\varphi)g_{\mu\nu}^*; \Psi_{\text{mat}}]$$

where we have omitted the divergence term from (E.4) since it will not contribute to the resulting field equations (see Appendix D).

We can simplify this expression by introducing the field redefinitions

$$\left(\frac{d\varphi_*}{d\varphi} \right)^2 = \frac{3}{4} \left(\frac{d \log F}{d\varphi} \right)^2 + \frac{Z}{2F}, \\ 2V(\varphi_*) = \frac{U(\varphi)}{F^2(\varphi)}, \\ A(\varphi_*) = F^{-1/2}(\varphi),$$

so that the Einstein frame action integral becomes

$$S_{\text{tot}} = \frac{1}{16\pi G_*} \int d^4x \sqrt{-g_*} [R_* - 2g_*^{\mu\nu} \partial_\mu \varphi_* \partial_\nu \varphi_* - 4V(\varphi_*)] + S_{\text{mat}}[A^2(\varphi_*)g_{\mu\nu}^*; \Psi_{\text{mat}}], \\ = S_g^* + S_{\varphi_*} + S_{\text{mat}}[A^2(\varphi_*)g_{\mu\nu}^*; \Psi_{\text{mat}}]. \quad (\text{E.6})$$

Before deriving the field equations in the Einstein conformal frame we first determine the relationship between the Einstein frame energy momentum tensor $T_{\mu\nu}^*$ and the Jordan frame energy momentum tensor $T_{\mu\nu}$,

$$T_{\mu\nu}^* = -\frac{2}{\sqrt{-g_*}} \frac{\delta S_{\text{mat}}[A^2(\varphi_*)g_{\mu\nu}^*; \Psi_{\text{mat}}]}{\delta g_*^{\mu\nu}}, \quad (\text{E.7})$$

$$= -\frac{2}{A^{-4}(\varphi_*)\sqrt{-g}} \frac{\delta S_{\text{mat}}[g_{\mu\nu}; \Psi_{\text{mat}}]}{A^2(\varphi_*)\delta g^{\mu\nu}}, \\ = A^2(\varphi_*)T_{\mu\nu}. \quad (\text{E.8})$$

Contracting both sides with $g_*^{\mu\nu} = A^{-2}(\varphi_*)g_{\mu\nu}$, we see that the Einstein frame energy density and pressure are related to their Jordan frame counterparts via

$$\rho_* = A^4(\varphi_*)\rho, \quad p_* = A^4(\varphi_*)p. \quad (\text{E.9})$$

E.3 Einstein frame field equations

Varying the Einstein frame action integral (E.6) with respect to the Einstein frame metric $g_*^{\mu\nu}$ we obtain the gravitational field equations¹

$$G_{\mu\nu}^* = 8\pi G_* (T_{\mu\nu}^* + T_{\mu\nu}^{\varphi_*}) \quad (\text{E.10})$$

where the scalar field energy momentum tensor is now given by (cf. (D.19) and (E.2))

$$\begin{aligned} T_{\mu\nu}^{\varphi_*} &= -\frac{2}{\sqrt{-g_*}} \frac{\delta S_{\varphi_*}}{\delta g_*^{\mu\nu}}, \\ &= \frac{1}{4\pi G_*} \left\{ \partial_\mu \varphi_* \partial_\nu \varphi_* - g_{\mu\nu}^* \left[\frac{1}{2} g_*^{\alpha\beta} \partial_\alpha \varphi_* \partial_\beta \varphi_* + V \right] \right\}. \end{aligned}$$

and the Einstein frame matter energy momentum tensor is defined in (E.7).

Assuming a Robertson-Walker line element,

$$ds_*^2 = -dt_*^2 + a_*^2(t_*) \gamma_{ij}^* dx_i^* dx_j^*, \quad (\text{E.11})$$

the (0,0) component of (E.10) gives (using (A.26))

$$3 \left(\frac{\dot{a}_*^2}{a_*^2} + \frac{k}{a_*^2} \right) = 8\pi G_* \rho_* + \dot{\varphi}_*^2 + 2V(\varphi_*), \quad (\text{E.12})$$

and the (i,j) components gives (using (A.27)),

$$-3 \frac{\ddot{a}_*}{a_*} = 4\pi G_* (\rho_* + 3p_*) + 2\dot{\varphi}_*^2 - 2V(\varphi_*). \quad (\text{E.13})$$

Additionally, the scalar field equation of motion can be derived using the results presented in section D.2. Defining

$$L_{\varphi_*} = -\frac{1}{4\pi G_*} \left[\frac{1}{2} g_*^{\mu\nu} \partial_\mu \varphi_* \partial_\nu \varphi_* + V(\varphi_*) \right], \quad (\text{E.14})$$

we then have

$$\frac{\delta L_{\varphi_*}}{\delta \varphi_*} = -\frac{1}{4\pi G_*} \left[\frac{dV}{d\varphi_*} - \square \varphi_* \right]. \quad (\text{E.15})$$

¹See section D.3 for more details.

Moreover, the variation of the matter action with respect to φ_* is given by

$$\begin{aligned} \frac{\delta S_{\text{mat}}}{\delta \varphi_*} &= \frac{\delta S_{\text{mat}}[A^2(\varphi_*)g_{\mu\nu}^*; \Psi_{\text{mat}}]}{\delta(A^2(\varphi_*)g_{\mu\nu}^*)} \frac{\partial(A^2(\varphi_*)g_{\mu\nu}^*)}{\partial \varphi_*}, \\ &= \left(\frac{1}{A^2(\varphi_*)} \frac{\delta S_{\text{mat}}}{\delta g_{\mu\nu}^*} \right) \left(2A(\varphi_*)g_{\mu\nu}^* \frac{dA(\varphi_*)}{d\varphi_*} \right), \\ &= -\sqrt{-g_*} \alpha(\varphi_*) g_{\mu\nu}^* T_*^{\mu\nu}, \end{aligned} \quad (\text{E.16})$$

where $\alpha(\varphi_*)$ is defined as

$$\alpha(\varphi_*) = \frac{d \log A(\varphi_*)}{d\varphi_*}. \quad (\text{E.17})$$

Assuming the scalar field φ_* is a function of time of only, the D'Alembertian becomes (see (D.14)) $\square \varphi_* = -\ddot{\varphi}_* - 3H_* \dot{\varphi}_*$, and the equation of motion can be written

$$\ddot{\varphi}_* + 3H_* \dot{\varphi}_* + \frac{\partial V}{\partial \varphi_*} = -4\pi G_* \alpha(\varphi_*) (\rho_* - 3p_*), \quad (\text{E.18})$$

where we have also used $g_{\mu\nu}^* T_*^{\mu\nu} = (\rho_* - 3p_*)$.

Finally, the Einstein frame energy conservation equation can be determined by differentiating the first Friedmann equation and substituting in the second Friedmann equation to get

$$4\pi G_* [\dot{\rho}_* + 3H_* (\rho_* + p_*)] = \left[\ddot{\varphi}_* + 3H_* \dot{\varphi}_* + \frac{\partial V}{\partial \varphi_*} \right] \dot{\varphi}_*. \quad (\text{E.19})$$

Using the scalar field equation of motion we finally have

$$\dot{\rho}_* + 3H_* (\rho_* + p_*) = \alpha(\varphi_*) (\rho_* - 3p_*) \dot{\varphi}_*. \quad (\text{E.20})$$

Appendix F

Braneworld Field Equations

F.1 Field equations

The derivation of the Randall-Sundrum braneworld field equation presented here is based on Binetruy *et al* [275] and Langlois [302].

The total action for the five dimensional braneworld scenario can be written

$$S_{\text{tot}} = S_{\mathcal{M}} + S_{\text{mat}} + S_{\Sigma} \quad (\text{F.1})$$

where $S_{\mathcal{M}}$ is the bulk action integral taken over the five dimensional manifold \mathcal{M} given by

$$S_{\mathcal{M}} = \frac{1}{2\kappa_5^2} \int_{\mathcal{M}} d^5x \sqrt{-g} (R - 2\Lambda_5), \quad (\text{F.2})$$

S_{mat} is the action integral incorporating the matter fields on the brane,

$$S_{\text{mat}} = - \int_{\partial\mathcal{M}} d^4x \sqrt{-h} L_{\text{mat}} \quad (\text{F.3})$$

and S_{Σ} contains the boundary terms required to compensate those generated by the presence of the brane. We have used g and h to denote the determinants of the bulk and brane metrics, g_{AB} and $h_{\mu\nu}$, respectively. The quantity R is the five dimensional Ricci scalar constructed from the bulk metric g_{AB} , i.e. $R = g^{AB}R_{AB}$. Note that in this appendix we use capital Latin indices for the five bulk spacetime coordinates, Greek indices for the four brane spacetime coordinates and lower case Latin indices for the three braneworld spatial coordinates. This is in contrast to chapters 5 and 6 where lower case Latin indices are used to span the bulk spacetime coordinates.

In five dimensional spacetime, the general metric which guarantees homogeneity and isotropy on a four dimensional slice of spacetime is given by

$$ds^2 = -n(t, y)^2 dt^2 + a(t, y)^2 \gamma_{ij} dx^i dx^j + dy^2 \quad (\text{F.4})$$

where γ_{ij} is the familiar spatial 3-metric (A.16) and y is a new coordinate spanning the additional bulk spatial dimension.

We will model the brane (our universe) as an infinitely thin surface located at the origin of the fifth dimension ($y = 0$), in which case the induced metric on the surface of the brane satisfies

$$ds_{\text{brane}}^2 = -n(t, 0)^2 dt^2 + a(t, 0)^2 \gamma_{ij} dx^i dx^j. \quad (\text{F.5})$$

If t is the proper time on the brane then $n(t, 0) = 1$ and $a(t, 0)$ is the braneworld scale factor. The brane metric $h_{\mu\nu}$ is therefore related to the bulk metric g_{AB} via

$$h_{\mu\nu}(x^\mu) = g_{AB}(x^\mu, 0). \quad (\text{F.6})$$

The braneworld field equations are derived by varying the total action (F.1) with respect to the bulk metric g_{AB} . In order to do so we first rewrite the matter action (F.3) as

$$S_{\text{mat}} = - \int_{\mathcal{M}} d^5x \sqrt{-h} L_{\text{mat}} \delta(y), \quad (\text{F.7})$$

where the distributional factor signifies the discontinuity introduced by the brane at $y = 0$. Varying the bulk and brane actions with respect to the bulk metric g_{AB} gives

$$\delta S_{\mathcal{M}} = \frac{1}{2\kappa_5^2} \int_{\mathcal{M}} d^5x \sqrt{-g} \left(R_{AB} - \frac{1}{2} g_{AB} R + g_{AB} \Lambda_5 \right) \delta g^{AB}$$

and

$$\delta S_{\text{mat}} = - \int_{\mathcal{M}} d^5x \sqrt{-h} \frac{\delta L_{\text{mat}}}{\delta h^{\mu\nu}} \delta_A^\mu \delta_B^\nu \delta(y) \delta g^{AB} \quad (\text{F.8})$$

where we have used

$$\delta h^{\mu\nu} = \delta g^{AB} \delta_A^\mu \delta_B^\nu. \quad (\text{F.9})$$

Setting $\delta S_{\text{tot}} = 0$, and noting that, for the metric (F.4), $\det(g_{AB}) = \det(h_{\mu\nu})$, yields

$$G_{AB} \equiv R_{AB} - \frac{1}{2} g_{AB} R = \kappa_5^2 T_{AB} - g_{AB} \Lambda_5, \quad (\text{F.10})$$

where the five dimensional energy-momentum tensor T_{AB} is given by

$$T_{AB} = T_{\mu\nu} \delta_A^\mu \delta_B^\nu \delta(y) \quad (\text{F.11})$$

and

$$T_{\mu\nu} = -\frac{2}{\sqrt{-g}} \frac{\delta S_{\text{mat}}}{\delta h^{\mu\nu}}. \quad (\text{F.12})$$

F.2 Cosmological solution

The presence of the brane introduces a discontinuity in the Einstein field equations (F.10). To solve the field equations we could invoke the formalism developed by Israel [303] to derive the so-called junction conditions. Instead, we follow the method outlined in [275].

Firstly, we note that we require the bulk metric and its components to be continuous across the brane surface located at $y = 0$, i.e. $g_{AB}(x^\mu, y = 0^-) = g_{AB}(x^\mu, y = 0^+)$. Therefore, the first derivative of the metric $g'_{AB}(x)$,¹ can contain at most a Heaviside step function and that the second derivative will contain a Dirac delta (distribution) function. Thus any quantity containing second derivatives of the bulk metric (including the Einstein tensor) can be expanded as the sum of its non-distributional and distributional components [275],

$$a'' = \hat{a}'' + [a']\delta(y) \quad (\text{F.13})$$

where \hat{a}'' denotes the non-distributional component and the square brackets denote the 'jump' in a quantity at the location of the brane, defined as

$$[a'] = a'(y = 0^+) - a'(y = 0^-). \quad (\text{F.14})$$

The junction conditions needed to solve the five dimensional field equations can then be determined by equating the distributional components of the Einstein tensor G_{AB} with the brane energy momentum tensor, which is expressed as

$$T_{\mu\nu} = (\rho_b + p_b)u_\mu u_\nu + p_b h_{\mu\nu}, \quad (\text{F.15})$$

where ρ_b and p_b are the energy density and pressure of the braneworld matter fields.

¹We use a dash to denote differentiation with respect to the y coordinate and overdots denote differentiation with respect to t .

From the bulk metric g_{AB} defined in (F.4) the various components of the five dimensional Einstein tensor are given by

$$G_{00} = 3\frac{\dot{a}^2}{a^2} - 3n^2 \left(\frac{a''}{a} + \frac{a'^2}{a^2} \right) + 3k\frac{n^2}{a^2}, \quad (\text{F.16})$$

$$G_{ij} = a^2\gamma_{ij} \left(2\frac{a''}{a} + \frac{n''}{n} + \frac{a'^2}{a^2} + 2\frac{a'n'}{an} \right) + \frac{a^2}{n^2}\gamma_{ij} \left(-2\frac{\ddot{a}}{a} - \frac{\dot{a}^2}{a^2} + 2\frac{\dot{a}\dot{n}}{an} \right) - k\gamma_{ij}, \quad (\text{F.17})$$

$$G_{04} = 3 \left(\frac{n'\dot{a}}{na} - \frac{\dot{a}'}{a} \right), \quad (\text{F.18})$$

$$G_{44} = 3 \left(\frac{a'^2}{a^2} + \frac{a'n'}{an} \right) - \frac{3}{n^2} \left(\frac{\ddot{a}}{a} + \frac{\dot{a}^2}{a^2} - \frac{\dot{a}\dot{n}}{an} \right) - 3\frac{k}{a^2}. \quad (\text{F.19})$$

Splitting G_{AB} up into

$$G_{AB} = \widehat{G}_{AB} + \widetilde{G}_{AB}, \quad (\text{F.20})$$

where \widetilde{G}_{AB} and \widehat{G}_{AB} denote the distributional and non-distributional components, we can read off the $(0,0)$ and (i,j) components of \widetilde{G}_{AB} from Eqs. (F.16) and (F.17),

$$\widetilde{G}_{00} = -3\frac{n^2}{a}[a']\delta(y), \quad \widetilde{G}_{ij} = a^2\gamma_{ij} \left(2\frac{[a']}{a} + \frac{[n']}{n} \right) \delta(y). \quad (\text{F.21})$$

Equating these two expressions with the distributional part of the right hand side of the field equations then gives the junction conditions

$$\frac{[a']}{a} = -\frac{\kappa_5^2}{3}\rho_b, \quad \frac{[n']}{n} = \frac{\kappa_5^2}{3}(3p_b + 2\rho_b). \quad (\text{F.22})$$

Motivated by the Horava-Witten model [304], a Z_2 symmetry is imposed across the brane, so that we identify $y \rightarrow -y$ and $g_{AB}(x^\mu, -y) = g_{AB}(x^\mu, y)$. The 'jump' in a quantity can then be replaced by twice the function evaluated at the location of the brane, i.e.

$$[a'] = 2a'|_{y=0^+}. \quad (\text{F.23})$$

The junction conditions (F.22) then become

$$\frac{a'}{a} \Big|_{y=0^+} = -\frac{\kappa_5^2}{6}\rho_b, \quad \frac{n'}{n} \Big|_{y=0^+} = -\frac{\kappa_5^2}{6}(3p_b + 2\rho_b). \quad (\text{F.24})$$

The junction conditions can now be used to solve the Einstein field equations. Firstly, we look at the $(0,4)$ component of the field equations which reads

$$G_{04} = \widehat{G}_{04} = 3 \left(\frac{n'\dot{a}}{na} - \frac{\dot{a}'}{a} \right) = 0. \quad (\text{F.25})$$

Integrating this equation with respect to y gives

$$\dot{a}(t, y) = \nu(t) n(t, y). \quad (\text{F.26})$$

We can also evaluate the equation (F.25) directly by inserting the junction conditions (F.24), which gives

$$(3p_b + 2\rho_b) \frac{\dot{a}_0}{a_0} + \dot{\rho}_b + \rho_b \frac{\dot{a}_0}{a_0} = 0 \quad (\text{F.27})$$

where we have used a subscript 0 to denote quantities evaluated on the brane, i.e. $a_0(t) = a(t, 0)$. Defining the Hubble factor as $H \equiv \dot{a}_0/a_0$, the standard energy conservation law is recovered on the brane,

$$\dot{\rho}_b + 3H(\rho_b + p_b) = 0. \quad (\text{F.28})$$

Finally, we can equate the non-distributional part of the (0, 0) component of the field equations

$$\widehat{G}_{00} = -g_{00}\Lambda_5, \quad (\text{F.29})$$

to get

$$3\frac{\dot{a}^2}{a^2} - 3n^2 \left(\frac{a''}{a} + \frac{a'^2}{a^2} \right) + 3k \frac{n}{a^2} = n^2 \Lambda_5. \quad (\text{F.30})$$

Substituting in the result (F.26), we can rewrite this equation as

$$\nu^2 + k - (a\nu)' = \frac{\Lambda_5}{3} a^2. \quad (\text{F.31})$$

Integrating with respect to a^2 and substituting in the junction condition (F.24) yields

$$H^2 \equiv \frac{\dot{a}_0^2}{a_0^2} = \frac{\kappa_5^4}{36} \rho_b^2 + \frac{\Lambda_5}{6} - \frac{k}{a^2} + \frac{C}{a^4}. \quad (\text{F.32})$$

This is the modified Friedmann equation in the braneworld scenario.